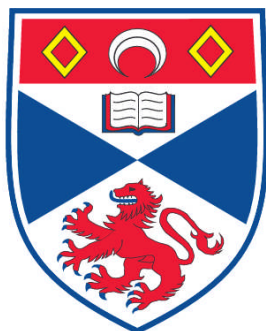


ULTRAFAST PHOTOPHYSICS OF IRIDIUM COMPLEXES

Gordon James Hedley

A Thesis Submitted for the Degree of PhD
at the
University of St. Andrews



2012

Full metadata for this item is available in
Research@StAndrews:FullText
at:

<http://research-repository.st-andrews.ac.uk/>

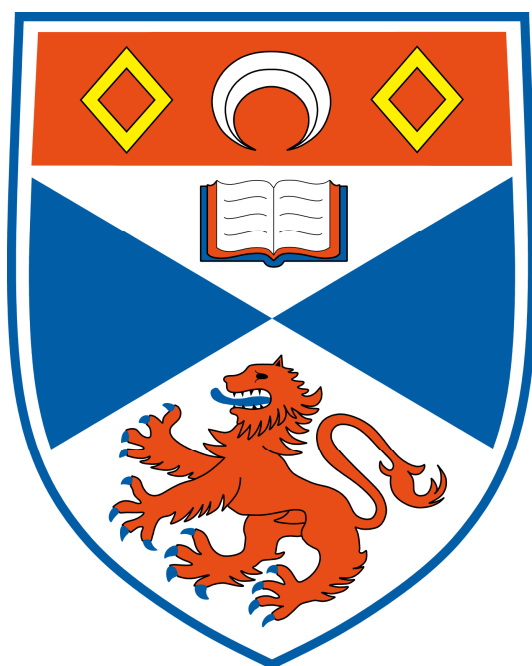
Please use this identifier to cite or link to this item:

<http://hdl.handle.net/10023/1981>

This item is protected by original copyright

ULTRAFAST PHOTOPHYSICS OF IRIDIUM COMPLEXES

Gordon James Hedley



A thesis submitted to the School of Physics and Astronomy,
University of St Andrews, for the degree of Doctor of
Philosophy

April 2010

Abstract

This thesis presents ultrafast photophysical measurements on a number of phosphorescent iridium complexes and establishes relationships between the relaxation rates and the vibrational properties of the material.

When ultrafast luminescence is measured on the peak of the phosphorescence spectrum and on its red-side, 230 fs and 3 ps decay time constants were observed in all materials studied, and this was attributed to population redistribution amongst the three electronic substates of the lowest triplet metal-ligand charge transfer (MLCT) state.

The observation of luminescence at higher values of energy embodied ultrafast dissipation of excess energy by intramolecular vibrational redistribution (IVR) and it was found that the dissipation channels and rate of IVR could be modified by chemical modification of the emitting molecule. This was tested in two ways. Firstly by adding electronically inactive dendrons to the core, an increase in the preference for dissipation of excess energy by IVR rather than by picosecond cooling to the solvent molecules was found, but this did not change the rate of IVR. The second method of testing was by fusing a phenyl moiety directly onto the ligand, this both increased the rate of IVR and also the preference for dissipation by it rather than by picosecond cooling.

Fluorescence was recorded in an iridium complex for the first time and a decay time constant of 65 fs was found, thus allowing a direct observation of intersystem crossing (ISC) to be made.

In a deep red emitting iridium complex internal conversion (IC) and ISC were observed and the factors controlling their time constants deduced. IC was found

to occur by dissipation of excess energy by IVR. The rate of IC was found to be dependent on the amount of vibrational energy stored in the molecule, with IC fast (< 45 fs) when < 0.6 eV of energy is stored and slower (~ 70 fs) when the value is > 0.6 eV. The rate of ISC agreed with these findings, indicating that the very process of ISC may be thought of as closely analogous to that of IC given the strongly spin-mixed nature of the singlet and triplet MLCT states.

Declaration

I, Gordon James Hedley, hereby certify that this thesis, which is approximately 45,000 words in length, has been written by me, that it is the record of work carried out by me and that it has not been submitted in any previous application for a higher degree.

I was admitted as a research student in September 2006 and as a candidate for the degree of Doctor of Philosophy in September 2006; the higher study for which this is a record was carried out in the University of St Andrews between 2006 and 2010.

Gordon J. Hedley April 1, 2010

I hereby certify that the candidate has fulfilled the conditions of the Resolution and Regulations appropriate for the degree of Doctor of Philosophy in the University of St Andrews and that the candidate is qualified to submit this thesis in application for that degree.

Ifor D.W. Samuel April 1, 2010

Copyright Declaration

In submitting this thesis to the University of St Andrews we understand that we are giving permission for it to be made available for use in accordance with the regulations of the University Library for the time being in force, subject to any copyright vested in the work not being affected thereby. We also understand that the title and the abstract will be published, and that a copy of the work may be made and supplied to any bona fide library or research worker, that my thesis will be electronically accessible for personal or research use unless exempt by award of an embargo as requested below, and that the library has the right to migrate my thesis into new electronic forms as required to ensure continued access to the thesis. We have obtained any third-party copyright permissions that may be required in order to allow such access and migration or have requested the appropriate embargo below.

Gordon J. Hedley April 1, 2010

Ifor D.W. Samuel April 1, 2010

Embargo

The following is an agreed request by candidate and supervisor regarding the electronic publication of this thesis:

Access to all of the printed copy but embargo of all of the electronic publication of thesis for a period of 1 year on the following ground: publication would preclude future publication.

Gordon J. Hedley April 1, 2010

Ifor D.W. Samuel April 1, 2010

Acknowledgements

Few achievements are made without the great help, support and encouragement of others, and this PhD has benefited immensely from all three qualities provided by those around me.

Our ability to practice good science, learn, develop and enjoy is instructed not just by what we do, but by what those around us do, and the research group I have been a part of for the duration of my PhD, the Organic Semiconductor Optoelectronics Group, has been a very good home to achieve all of these things – my sincerest thanks are made to Prof. Ifor Samuel for his guidance, expertise and supervision, and to Dr Graham Turnbull for ably assisting – thanks are also made to all OSO members, past and present, for their contributions, either to the work documented here or in making my “PhD experience” a very satisfying and enjoyable one. Research is rarely a solitary business, and whether in the lab, office or pub a special mention must be made here to Dimali, Paul and Georgios, all three of whom have made my PhD a great deal of fun – excusing the pun, I think we were on the same wavelength, and that kind of resonance is always very rewarding.

Virtually no research would happen in Physics without the support staff, who are a major not minor cog in the engine of science, so my thanks are made to George, Steve, Scott, Les, Chris and Paul for providing first class support no matter how hard the challenges that were posed.

Lastly, there is one acknowledgement and thanks that stands above all others, and that is to Dr Arvydas Ruseckas. To fully define the breadth and scope of the thanks that are made here to Arvydas is to define the breadth and scope of this very body of work – none of this research would have been possible without Arvydas’s very valuable expertise, assistance and encouragement that was given throughout, I am deeply, humbly and forever in his debt.

This work is dedicated to my parents and my sister,

For Ellis, George and Sarah

“Science is a very human form of knowledge. We are always at the brink of the known; we always feel forward for what is to be hoped. Every judgment in science stands on the edge of error and is personal. Science is a tribute to what we can know although we are fallible.”

Jacob Bronowski, *Knowledge or Certainty, The Ascent of Man*, 1973

Contents

Abstract	i
Declaration	v
Copyright Declaration	vii
Embargo	ix
Acknowledgements	xi
Dedication	xiii
1 Introduction	1
1.1 References	9
2 Theory of Emissive Organic Semiconducting Materials	13
2.1 Introduction	13
2.2 Organic Conjugated Systems	14
2.3 Photophysical Properties of Organic Conjugated Systems	20
2.4 Transition Metal Complexes	28
2.4.1 Chemical Structure	28
2.4.2 Electronic and Photophysical Properties	29
2.4.3 Ultrafast Processes in Transition Metal Complexes	34
2.4.4 Intramolecular Vibrational Redistribution	36
2.5 References	39
3 Experimental Methods	45
3.1 Introduction	45

3.2	Sample Preparation	46
3.3	Steady State Photophysical Measurements	49
3.4	Ultrafast Light Sources	50
3.4.1	Titanium Sapphire Oscillator	50
3.4.2	Regenerative Amplification	53
3.4.3	Non-Collinear Parametric Amplification	55
3.5	Luminescence Upconversion Spectroscopy	56
3.5.1	FOG100 by CDP Systems	58
3.5.2	The Raman Problem	64
3.5.3	The Instrument Response	65
3.5.4	Detecting Luminescence from Phosphorescent Complexes	66
3.5.5	Detection Wavelength Intensity Correction	69
3.6	Transient Absorption Spectroscopy	70
3.7	Temporal Fitting	77
3.8	References	80
4	Femtosecond Dynamics of Ir(ppy)₃	83
4.1	Introduction	83
4.2	Photophysical Properties of Ir(ppy) ₃	84
4.3	Ultrafast Luminescence Dynamics	88
4.4	Ultrafast Transient Absorption Dynamics	94
4.5	Interpretation of Ultrafast Dynamics	98
4.6	Conclusions	104
4.7	References	105
5	Effect of Structural Modification on Ultrafast Dynamics in Iridium Dendrimers	109
5.1	Introduction	109
5.2	Dendrimers: A Modular Chemical Concept	110
5.3	Intramolecular Vibrational Redistribution	114

5.4	Photophysical Properties of Iridium Cored Dendrimers	114
5.5	Ultrafast Luminescence Dynamics	118
5.6	Ultrafast Transient Absorption Dynamics	122
5.7	Interpretation of Ultrafast Dynamics	124
5.8	Conclusions	129
5.9	References	130
6	Ultrafast Intersystem Crossing in an Iridium Complex	133
6.1	Introduction	133
6.2	Intersystem Crossing in Transition Metal Complexes	134
6.3	Photophysical Properties of a Red Emitting Iridium Complex	135
6.4	Ultrafast Luminescence Dynamics of Ir(piq) ₃	138
6.5	Ultrafast Transient Absorption Dynamics of Ir(piq) ₃	145
6.6	Interpretation of Ultrafast Dynamics	148
6.7	Conclusions	155
6.8	References	156
7	Intramolecular Vibrational Redistribution Controls Internal Conversion in an Iridium Complex	159
7.1	Introduction	159
7.2	Internal Conversion: Non-radiative Electronic Relaxation	160
7.3	Photophysical Properties of a Deep Red Emitting Iridium Complex	165
7.3.1	The Material Under Investigation	165
7.3.2	Spectral Fitting	167
7.4	Calculated Transition Dipole Moments: Assignment of Spectral Features	171
7.5	Ultrafast Luminescence Measurements	174
7.5.1	Proposed Model: Consecutive Relaxation	174

7.5.2	Global Fitting to Luminescence Data	176
7.5.3	Decay Associated Fluorescence Spectra	181
7.5.4	Error Analysis	184
7.5.5	Variation of Excitation Wavelength	188
7.6	Internal Conversion: Mediated by Energy Stored In The Molecule	191
7.7	Conclusions	199
7.8	References	200
8	Conclusions	205
8.1	References	211
	Appendix: Publications Arising from this Work	213

1

Introduction

Misled by fancy's meteor ray,
By passion driven;
But yet the light that led astray
Was light from heaven.

Robert Burns, *The Vision*, 1786

Human comprehension tends to view timescales and the advances made during them in small quanta – fractions of an average individual lifespan rather than on longer timescales, such as fractions of a species lifespan. The pace, and perhaps more crucially, the *acceleration* of human scientific and technological advancement is, when one views the situation on such longer timescales, breathtaking. Listing all advancements would of course be impossible, and even detailing a select few would be a monograph in its own right, but one just has to look all around to see the ever increasing degrees of change that occur in ever shortening periods of time.

Scientific ideas, whether they are based on the quest to turn base metal into gold, to identify the luminiferous aether or to settle the question of whether objects are particles or waves, have periods of dominance before being superseded by newer, more precise ideas, which are themselves then dominant before later being dethroned. The new more precise ideas (better defined as paradigms)¹ are often created and defined by new and more precise measurements or by the discovery of new materials or processes. This work sits within the paradigm of ultrafast molecular photophysics:^{2,3} utilising ultrafast light pulses to observe the behaviour of molecules on the femtosecond timescale.

A little over fifty years ago the advanced development and industrialisation of plastics – polymerised carbon base materials – ushered in perceptible societal changes and quickly became ubiquitous in almost all areas of life. What could not be envisaged then was the great potential that these materials could have when small chemical modifications were made to enable them to conduct electricity and emit light. Since the discovery of these new properties in polymers in 1977^{4,5} and earlier work on similar chemically structured small molecule materials in the 1960's⁶ the field of organic semiconductors has grown and expanded to explore almost every avenue of these novel materials and their unique features.

Organic semiconductors, as the name implies, are organic materials with semiconducting properties. The organic nature of the materials, either as small molecules or long chain polymers, give these materials great potential advantages over traditional silicon based semiconducting systems which have specific requirements of purity and crystallinity. The potential greater control over device functions, forms, fabrication and applications lead to obvious advantages for organic semiconductors.

The invention of a number of different organic semiconductor devices has shown that there exists a wide variety of uses for these materials, particularly with regard to their light emitting properties. Initial work in the 1960's on deriving light emission under electrical excitation from organic materials concentrated on the small molecule acene family (specifically anthracene and tetracene),^{6,7} however the requirement of using crystals of the materials limited the amount of light that could be generated, needing hundreds of volts to drive the devices. The first practical organic light emitting diode (OLED) was invented by Tang and Van Slyke⁸ in the 1980's and used the small organic molecule *tris*(8-hydroxyquinoline)aluminium sandwiched between a cathode and anode with suitable electron and hole transporting layers to ensure that charges met in the organic layer and so emitted light. Later work in 1990 with a polymer rather than a small molecule by Burroughes et al. led to the first reported conjugated polymer

OLED.⁹ The third significant event in the development of OLEDs was the reporting in 1998 of the use of an organometallic material (initially a platinum porphyrin,¹⁰ but later with an iridium complex¹¹) in an OLED device to enable efficient phosphorescence, thus allowing theoretically much greater (approximately three times) internal device efficiencies than were possible with fluorescent materials. The fourth development of note in OLEDs was the use of light emitting dendrimers, enabling solution processable phosphorescent devices to be made.¹²

OLED device technologies are aimed towards the realisation of affordable efficient light sources for use in both lighting and displays. With substantial commercial backing both areas of technological development have grown markedly over the last twenty years or so since the beginnings of the field in scientific laboratories. Indeed OLED displays, offering richer colours, far higher contrast ratios and lower power consumption than LCD alternatives, are now becoming commonplace in mobile phones, a statement that, even just five years ago, would have been purely a prediction rather than a reality.

A second promising area of research using organic semiconductors is the harnessing of light emission from organic materials to induce lasing. Of course laser dyes have been common for many years, but the utilisation of conjugated polymers or dendrimers enables the realisation of solid state organic lasers^{13, 14} rather than solution based ones. Currently such devices are optically pumped by means of a second laser, and the ultimate aim of this field is electrical pumping, but for the moment a more promising route involves indirect electrical pumping, using an inorganic LED to pump the organic laser.¹⁵

Another key use of organic semiconductors has been in the invention of organic solar cells – essentially attempting to reverse the concept developed with OLEDs to instead absorb light and produce a flow of charge.¹⁶ More recently the development of organic field effect transistors (FETs),¹⁷ light emitting FETs¹⁸ and

phosphorescent FETs¹⁹ have highlighted the range of possible future applications for organic semiconducting materials.

It is clear from the short sampling of research areas that employ conjugated organic materials provided above that they are a vibrant source of novel properties, potentially leading to significant new inventions and devices. To lead to new devices or applications, however, one needs to understand the chemical physics of the materials that are used – how do they function at a molecular level and can any of the processes that occur there be influenced or controlled?

As mentioned above, organometallic transition metal complexes have become a recent focus of activity in light emitting devices for their display of efficient room temperature phosphorescence. Structurally the complexes consist of a central heavy transition metal ion which is co-ordinated to a number of conjugated ligand moieties. Initially platinum complexes were used¹⁰ but the centre of research gravity quickly shifted to iridium based materials that show very efficient emission of light.²⁰ Iridium based complexes are superior to platinum materials due to their shorter radiative lifetimes, this leads to a reduction in any losses associated with non-radiative decay and a reduction in the probabilities of triplet-triplet annihilation that sees two triplet states combine to form one singlet state (an effective loss of emission) – if the radiative lifetime is shorter then the chance of annihilation is reduced. Efficient room temperature phosphorescence is unexpected in organic materials as triplet emission is forbidden by spin statistics, hence it has a very low probability attached to it.^{21, 22} In transition metal complexes however strong mixing between the spin-allowed singlet and formally spin-forbidden triplet states is caused by the central co-ordinating heavy metal ion induced through spin-orbit coupling.^{23, 24} This mixing is strongest in metal-ligand charge transfer states (MLCT) where an electron moves from the metal orbital out onto the ligand – here the metal character of the excited state enables strong singlet/triplet mixing and therefore leads to efficient phosphorescence. An almost barrierless gradient down to the lowest triplet MLCT state is formed due to this mixing and a high density and small separation of excited electronic states²⁵⁻²⁷

leads to a very fast excited state evolution.²⁸⁻³¹ This very fast relaxation is somewhat unique and the process of and factors controlling it are not well understood. Surprisingly given their widespread use in OLEDs ultrafast studies of iridium complexes have received very little attention, with only one study being reported.³²

This was the area of enquiry that was defined for the work undertaken during the course of this PhD. A number of phosphorescent iridium based organometallic transition metal complexes were studied and understanding of their ultrafast processes was sought. As mentioned above, understanding of the very fast processes that occur in the excited state evolution in transition metal complexes is poorly understood, hence it was conceived that the highly emissive nature of iridium complexes could be capitalised upon to aid in understanding. Observing luminescence in particular was focussed upon as detection of emission on a femtosecond timescale and can greatly aid in observing how and why fast relaxation occurs. By looking at different iridium complexes and at different detection wavelengths understanding of all parts of the excited state decay: internal conversion, intersystem crossing and vibrational relaxation, was sought.

In Chapter 2 I provide a comprehensive background to the theory of emissive organic semiconducting materials. Starting with the orbital arrangements of the carbon bonds that give rise to electron delocalisation through the π bond molecular orbitals I will then discuss bonding and anti-bonding orbitals and spin-selection rules before moving on to the photophysical properties of conjugated systems. There I explain the processes of optical absorption and emission, discussing the Franck-Condon principle and probabilities and the Stokes shift. The photophysical picture will then be redrawn with respect to time and the processes occurring, looking at vibrational relaxation within an electronic state, non-radiative relaxation between electronic states (internal conversion) and intersystem crossing (ISC) from singlet to triplet states. Finally the photophysics of transition metal complexes is presented in detail, explaining the chemical structure of this class of materials and the characteristic features of their

photophysical processes, with special attention paid to the work already reported on their ultrafast dynamics and energy dissipation mechanisms. This is followed in Chapter 3 with an outline of the experimental methods, looking at sample preparation, ultrafast light sources and a detailed discussion of the two main ultrafast spectroscopic techniques that were used in this thesis: upconversion spectroscopy and transient absorption pump probe spectroscopy.

In Chapter 4 results of ultrafast measurements on the prototypical iridium complex *fac*-tris(2-phenylpyridine) iridium(III) (denoted Ir(ppy)₃) are presented. Observation of emission from the primary lowest triplet (³MLCT) state shows a decay of 230 fs and 3 ps and is attributed to relaxation between three closely spaced ($\sim 100 \text{ cm}^{-1}$) electronic substates of the lowest ³MLCT state, with the decay amplitudes found to conform to the expected Boltzmann distribution for the three states' energy separations. Complementary transient absorption measurements confirmed that the process of ISC from the singlet to triplet MLCT manifolds is very fast, less than 100 fs.

Chapter 5 extends the work done on Ir(ppy)₃ by comparing its relaxation dynamics at 140 meV of excess excited state energy against two Ir(ppy)₃ cored dendrimers. An introduction to dendrimers – highly branched macromolecules that enable extra material to be added to the molecule without affecting its electronic properties – is provided and luminescence dynamics are compared, showing decays of 150 fs and 3 ps. It is found that dissipation of excess energy is facilitated by intramolecular vibrational redistribution (IVR) – the spatial and frequency redistribution of vibrations within a molecule – and that while the rate of IVR does not measurably increase with the increased size of the dendrimers compared to Ir(ppy)₃ (both are 150 fs) more dissipation takes place by this mechanism than slower picosecond cooling to the surrounding solvent molecules, indicating that the dendrons act as a heat sink to take excess energy away from the emissive core of the dendrimer.

In Chapter 6 a red emitting iridium complex tris(1-phenylisoquinoline)iridium(III) (denoted as Ir(piq)₃) is the focus of inquiry. Ultrafast luminescence and transient absorption dynamics were measured. The favourable red emitting properties of this material enabled direct observation of fluorescence to be made on an iridium complex for the first time, with a decay time constant of 65 ± 5 fs found, representing intersystem crossing from the singlet to triplet MLCT states. Transient absorption dynamics also showed an imprint of the ISC process, with time constants that confirmed the fluorescence measurements. Contrasting with Chapter 5 discussed above, an increase in the rate of relaxation at 140 meV of excess energy was observed in Ir(piq)₃ when compared to Ir(ppy)₃ (150 fs down to 95 fs). The molecule consists of an extra phenyl fused onto the pyridine when compared to Ir(ppy)₃, and it is this direct connection to the ligand structure that gives both the red emission and faster dissipation of vibrational energy by IVR.

Chapter 7 represents the culmination of the studies into ultrafast iridium complexes presented here, and provides a detailed study of the deep red emitting heteroleptic iridium complex bis(2-(9,9-dibutylfluorenyl)-1-isoquinoline(acetylacetonate) iridium (III), (denoted as Ir(dbfliq)₂acac). The deep red emitting spectral properties of this material have the benefit of red-shifting high energy electronic states to lower energy, thus enabling these states to be studied in the spectral window accessible with upconversion spectroscopy. Three ¹MLCT states were identified from absorption features and fluorescence from them was recorded. Global analysis was used to fit a sequential relaxation model to the data, giving decay times from the three singlet states of < 20 fs, 65 fs and 75 fs. The relationship between the rate of decay and the amount of vibrational energy stored inside the molecule is then established, indicating that stored vibrational energy controls the rate of IVR, and hence the rate of internal conversion (IC) between the singlet states.

The work outlined in this thesis therefore looks at all stages of the excited state cascade of the population as it evolves in iridium complexes: from very fast IC between ¹MLCT states, then ISC from singlet to triplet MLCT states before

relaxation within the $^3\text{MLCT}$ manifold and finally redistribution within the three electronic substates of the lowest $^3\text{MLCT}$ state.

1.1 References

- [1] T.S. Kuhn, *The Structure of Scientific Revolutions*. 1970: University of Chicago Press.
- [2] A.H. Zewail, *The Journal of Physical Chemistry*, 1993. **97**(48): p. 12427-12446.
- [3] A.H. Zewail, *The Journal of Physical Chemistry A*, 2000. **104**(24): p. 5660-5694.
- [4] H. Shirakawa, E.J. Louis, A.G. Macdiarmid, C.K. Chiang, and A.J. Heeger, *Journal of the Chemical Society-Chemical Communications*, 1977(16): p. 578-580.
- [5] C.K. Chiang, C.R. Fincher, Y.W. Park, A.J. Heeger, H. Shirakawa, E.J. Louis, S.C. Gau, and A.G. Macdiarmid, *Physical Review Letters*, 1977. **39**(17): p. 1098-1101.
- [6] M. Pope, H.P. Kallmann, and P. Magnante, *The Journal of Chemical Physics*, 1963. **38**(8): p. 2042-2043.
- [7] W. Helfrich and W.G. Schneider, *Physical Review Letters*, 1965. **14**(7): p. 229.
- [8] C.W. Tang and S.A. Van Slyke, *Applied Physics Letters*, 1987. **51**(12): p. 913-915.
- [9] J.H. Burroughes, D.D.C. Bradley, A.R. Brown, R.N. Marks, K. Mackay, R.H. Friend, P.L. Burns, and A.B. Holmes, *Nature*, 1990. **347**(6293): p. 539-541.
- [10] M.A. Baldo, D.F. O'Brien, Y. You, A. Shoustikov, S. Sibley, M.E. Thompson, and S.R. Forrest, *Nature*, 1998. **395**(6698): p. 151-154.
- [11] M.A. Baldo, S. Lamansky, P.E. Burrows, M.E. Thompson, and S.R. Forrest, *Applied Physics Letters*, 1999. **75**(1): p. 4-6.
- [12] S.C. Lo, N.A.H. Male, J.P.J. Markham, S.W. Magennis, P.L. Burn, O.V. Salata, and I.D.W. Samuel, *Advanced Materials*, 2002. **14**(13-14): p. 975-979.
- [13] F. Hide, M.A. Diaz-Garcia, B.J. Schwartz, M.R. Andersson, Q. Pei, and A.J. Heeger, *Science*, 1996. **273**(5283): p. 1833-1836.

- [14] I.D.W. Samuel and G.A. Turnbull, *Chemical Reviews*, 2007. **107**(4): p. 1272-1295.
- [15] Y. Yang, G.A. Turnbull, and I.D.W. Samuel, *Applied Physics Letters*, 2008. **92**(16): p. 163306.
- [16] R.N. Marks, J.J.M. Halls, D.D.C. Bradley, R.H. Friend, and A.B. Holmes, *Journal of Physics: Condensed Matter*, 1994(7): p. 1379.
- [17] H. Koezuka, A. Tsumura, and T. Ando, *Synthetic Metals*, 1987. **18**(1-3): p. 699-704.
- [18] A. Hepp, H. Heil, W. Weise, M. Ahles, R. Schmechel, and H. von Seggern, *Physical Review Letters*, 2003. **91**(15): p. 157406.
- [19] E.B. Namdas, B.B.Y. Hsu, Z. Liu, S.-C. Lo, P.L. Burn, and I.D.W. Samuel, *Advanced Materials*, 2009. **21**(48): p. 4957-4961.
- [20] C. Adachi, M.A. Baldo, M.E. Thompson, and S.R. Forrest, *Journal of Applied Physics*, 2001. **90**(10): p. 5048-5051.
- [21] M. Kasha, *Chemical Reviews*, 1947. **41**(2): p. 401-419.
- [22] M. Pope and C.E. Swenberg, *Electronic Processes in Organic Crystals and Polymers*. 2nd ed. 1999: Oxford University Press.
- [23] R.L. Ake and M. Gouterman, *Theoretica Chimica Acta*, 1969. **15**(1): p. 20-42.
- [24] A. Harriman, *Journal of the Chemical Society-Faraday Transactions II*, 1981. **77**: p. 1281-1291.
- [25] P.J. Hay, *Journal of Physical Chemistry A*, 2002. **106**(8): p. 1634-1641.
- [26] K. Nozaki, *Journal of the Chinese Chemical Society*, 2006. **53**(1): p. 101-112.
- [27] T. Matsushita, T. Asada, and S. Koseki, *Journal of Physical Chemistry C*, 2007. **111**(18): p. 6897-6903.
- [28] N. Damrauer, G. Cerullo, A. Yeh, T. Boussie, C. Shank, and J. McCusker, *Science*, 1997. **275**(5296): p. 54-57.
- [29] A.T. Yeh, C.V. Shank, and J.K. McCusker, *Science*, 2000. **289**(5481): p. 935-938.
- [30] A.C. Bhasikuttan, M. Suzuki, S. Nakashima, and T. Okada, *Journal of the American Chemical Society*, 2002. **124**(28): p. 8398-8405.

- [31] A. Cannizzo, A.M. Blanco-Rodriguez, A. El Nahhas, J. Sebera, S. Zalis, J.A. Vlcek, and M. Chergui, *Journal of the American Chemical Society*, 2008. **130**(28): p. 8967-8974.
- [32] K.C. Tang, K.L. Liu, and I.C. Chen, *Chemical Physics Letters*, 2004. **386**(4-6): p. 437-441.

2

Theory of Emissive Organic Semiconducting Materials

In reasoning on the peculiar coloured dispersion operated on a portion of a beam of white light intromitted into a solution of sulphate of quinine, it occurred to me as a subject well worthy of enquiry.

J.F.W. Herschel, 1845

2.1 Introduction

Traditional definitions within science label metals as good electrical conductors and non-metals as poor. Organic based materials (those containing large amounts of carbon) such as almost all biological compounds, alkanes, alkenes and plastics are thus traditionally assigned as being electrical insulators. Metals of course show very good electrical conduction and so have found implementation in many situations. Intermediary elements between metal and non-metals, such as silicon, can show semiconducting properties when suitably prepared by doping or other means, however they generally have specific properties that can create restrictions on their applicability when preparing materials for devices (such as the creation of light emitting diodes, transistors or integrated circuits). These properties (such as the material's crystallinity) facilitate semiconducting and light emitting behaviour, but also restrict the material's use (a silicon based integrated circuit cannot be flexible). Organic based systems, on the other hand, can show a wide variety of properties – compounds can be synthesised with specific characteristics in mind,

and a variety of classes of materials exist such as small organic molecules, polymers or dendrimers, each with different and unique properties. The semiconducting and light emitting qualities of organic materials could therefore be widely employed in a diverse range of systems free of the restrictions imposed by traditional highly crystalline silicon based devices.

This chapter presents the established theories on organic semiconductor materials, looking at organic conjugated systems (Section 2.2), their photophysical properties (Section 2.3) and transition metal complexes (Section 2.4).

2.2 Organic Conjugated Systems

Conjugated organic systems can show semiconductor like behaviour when suitably prepared. Conjugated polymers, first synthesised by Heeger and co-workers in 1977^{1, 2} and later the subject of the award of the Nobel Prize for Chemistry in the year 2000, are at their most simple are alternating single and double carbon bonds along a chain, as shown in Figure 2.1.

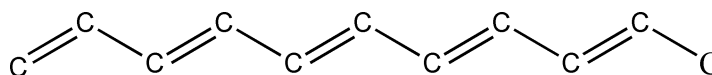


Figure 2.1. Chemical structure of a conjugated backbone, consisting of alternating double and single carbon bonds.

In order to understand these semiconducting properties, it is first necessary to consider the electronic structure of the carbon atom. Examination of the electronic orbital structure gives good reasons for the observed electrical conduction. The carbon atom has a charge $Z=6$ and these six electrons are configured within various electronic orbitals. From lowest to highest energy the 1s, 2s and 2p orbitals are filled, leaving full 1s and 2s orbitals with two electrons each and two unpaired electrons in the 2p orbital: denoted as having an electronic configuration of $1s^2 2s^2 2p^2$. The spatial configuration of the orbitals are shown in

Figure 2.2, with the s orbital showing a spherical distribution and the p orbitals (in the x, y and z axis) showing dumbbell like shapes.³

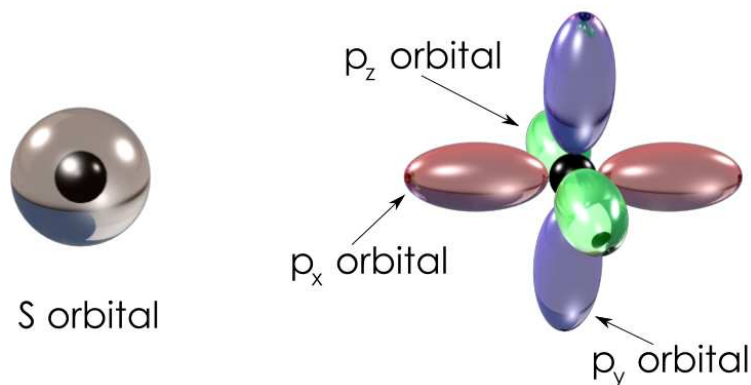


Figure 2.2. Spatial distribution of s and p orbital clouds for carbon. The s orbital presents a single spherical shape around the nucleus, providing capacity for two electrons. The p orbitals show x, y and z axis dumbbell shapes, providing capacity for three pairs of electrons.

In organic molecules the orbitals can mix, or to use chemical terminology *hybridise*, with each other upon specific bond formations, producing an entirely new orbital structure with composites of both originating orbitals.³ Hybridisation occurs because the resultant hybridised orbital shapes enable stronger bonding than the originating orbitals alone would otherwise give. The exact orbital configuration is dependent on the bonding of the atoms. If the 2s orbital combines with two of the three 2p orbitals then sp^2 hybridisation is produced, leading to three hybrid sp^2 orbitals and one unmodified 2p orbital on each carbon atom. The three sp^2 orbitals sit in a plane, 120° apart from each other, while the unmodified p orbital sits orthogonal to the sp^2 plane, with lobes above and below. Sp^2 hybridisation is found in C=C based systems, and leads to two types of molecular bonding orbitals, σ and π . The simplest alkene, ethene – C_2H_4 – can act as a good exemplar of sp^2 hybridisation. Shown on the left in Figure 2.3 are the two carbon atoms with their three sp^2 orbitals and one p orbital when held apart from each other, unbonded. When the double bond between the two carbon atoms forms then molecular bonding orbitals are created, shown on the right in Figure 2.3. A single hybridised sp^2 orbital from both C atoms come together to form an

in plane σ bond molecular orbital while the second C-C bond is formed by the 2p orbitals from both carbon atoms to give rise to a π bond molecular orbital. Since the originating 2p orbitals of the π bond sit out of plane so does the π bond molecular orbital, and it leaves the forming electrons further away and delocalised over a larger region of space in the π bond when compared to the σ bond. It is this increased delocalisation that leads to electronic conducting properties in conjugated organic based structures.

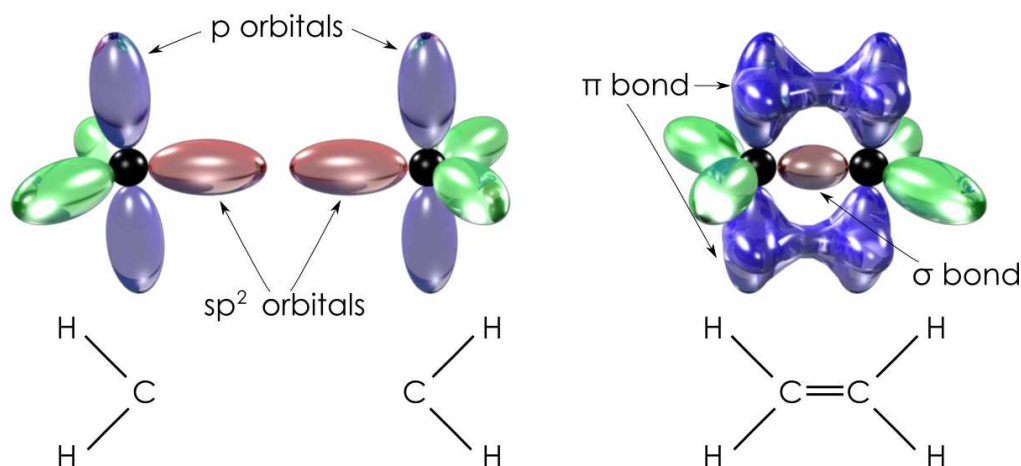


Figure 2.3. Spatial distribution of electron orbitals for ethene. Shown on the left are two sp^2 hybridised carbons before ethene forms, with one s orbital and two p orbitals hybridised to form sp^2 orbitals ready to bond, and one p orbital left free. On the right is the formed ethene molecule, with the two sp^2 orbitals now joined to form a σ bond molecular orbital in plane with the rest of the bonds, while the two p orbitals have joined together out of plane to form a π bond molecular orbital. Figure inspired by reference 3.

Electrical conduction due to the molecular orbital distribution in an organic semiconductor is perhaps best observed by looking at the molecule anthracene, structure, Figure 2.4, which consists of three fused benzene rings – essentially the molecule can be thought of as a long conjugated carbon chain that has been joined up into small rings.

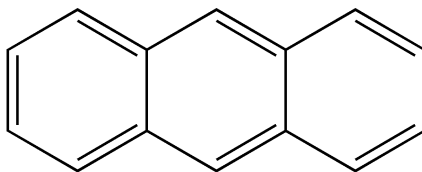


Figure 2.4. The chemical structure of anthracene, consisting of three fused benzene rings.

For benzene alone, in consideration of the sp^2 orbital bonding discussed above it is clear there for each double bond there will be a π bond orbital sitting out of plane, and in such a tight ring the π bond orbitals actually join up to form a single “ring like” orbital above and below the plane of each benzene ring, as shown in Figure 2.5.

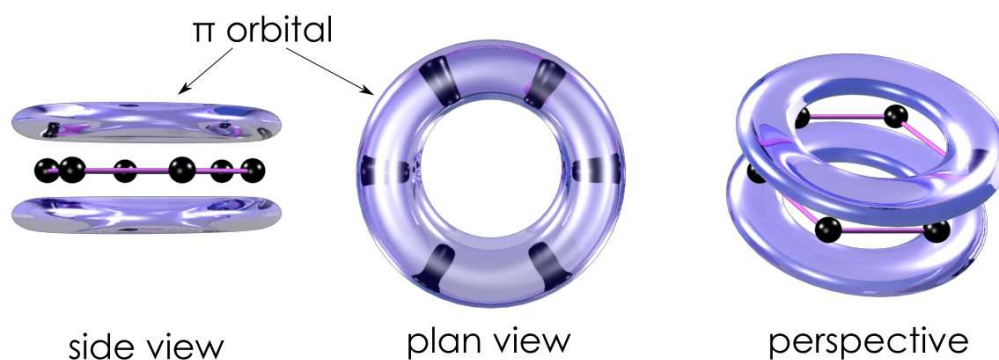


Figure 2.5. Representation of the delocalised nature of the π molecular orbitals that form for benzene, with side plan and perspective views shown. All other orbitals have been removed for clarity. In benzene the π orbitals from each carbon double bond join up to form a ring above and below the molecule.

Thus when three benzene rings are fused together as in anthracene one ends up with a continuous π bond orbital region, enabling electrical conduction, as shown in Figure 2.6.

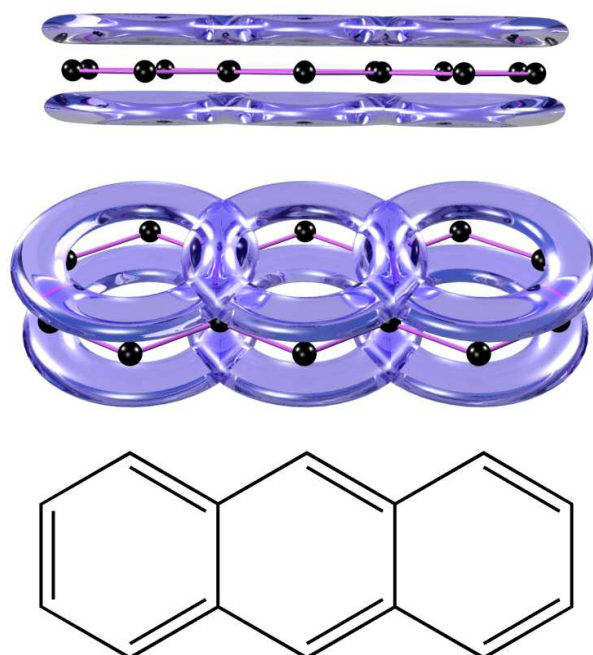


Figure 2.6. Side (top) and perspective (centre) views of the π molecular orbitals in anthracene (structure bottom). The π bond orbitals from each of the rings join up, leading to a continuous π molecular orbital sitting above and below the molecule.

Electrical conduction is therefore possible, but how do these chemical structures enable electronic transitions, i.e. excited states? It is easiest to return again to ethene, C_2H_4 , for an explanation.

Upon formation of the sp^2 hybridised system the two 2p orbitals of the carbon atoms combine. Combining two orbitals will produce two molecular orbitals, denoted bonding and anti-bonding orbitals, as shown in Figure 2.7 – the lowest energy orbital will form in-phase, this is the π orbital as previously described, and the higher energy orbital will form out-of-phase, denoted as the π^* orbital. The energy separation of these two bonding states gives rise to electronic transitions where, with suitable excitation, an electron moves from the π to the π^* molecular orbital.⁴ In an organic system the analogy to the top of the valence band is given by denoting the highest occupied molecular orbital (HOMO), while the bottom of the conduction band is analogised by denoting it as the lowest unoccupied molecular orbital (LUMO). HOMO-LUMO hence gives the energy gap between

the states, and hence what the transition energy will be when one electron moves from the π to the π^* orbital.

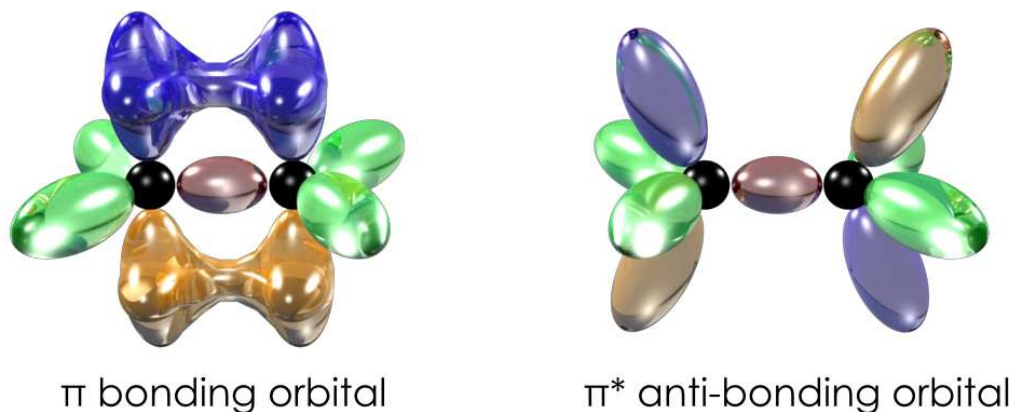


Figure 2.7. Representation of the lower energy π bonding and higher energy π^* anti-bonding molecular orbitals for ethene. Figure inspired by reference 4.

Control of the energy gap between the electronic states is achieved by modifying the molecular orbital distribution. Increasing the conjugation length leads to larger spatial distributions of the π molecular orbital region, increasing electron delocalisation. As the conjugation length is increased the HOMO-LUMO energy gap decreases, thus facilitating lower energy transitions between the π and π^* orbitals.

One final consideration in these systems is the spin of the electrons. As already mentioned, upon formation of the excited electronic states one electron of the two in the π orbital moves to the π^* orbital. Relaxation therefore occurs with that electron moving back down from π^* to join the unpaired electron in the π orbital.

Considering the spin of an electron (+1/2 or -1/2) we can define two regimes, that where the electron spins are anti-parallel ($S = 0$) and that where the spins are parallel ($S = 1$), hence the number of allowed states ($2S+1$) is thus either 1 for the anti-parallel case (defined as a singlet) or 3 for the parallel case (defined as triplets).

The ability for singlet or triplet states to form or relax is defined by spin-selection rules.⁵ The selection rules which govern the allowed transitions can be thought of in terms of Fermi's Golden rule, namely that the transition rate t can be defined by equation 2.1:

$$t \propto \langle \psi_i | D | \psi_f \rangle^2 \rho_f \quad [2.1]$$

where ψ_i is the initial wavefunction of the electron, D the dipole matrix operator, ψ_f the final wavefunction of the electron and ρ_f is the density of states of the final state. The dipole moment D is an odd function and the final wavefunction (the ground state) is even. The singlet wavefunction is an odd function while the triplet is even. This set of definitions allows the selection rules of the excited state to be fully quantified. If the excited state is a singlet then the matrix element will consist of $\langle \text{odd} | \text{odd} | \text{even} \rangle$ and will equal a non-zero number, hence the transition is fully spin-allowed. If the excited state is a triplet then the matrix element will be $\langle \text{even} | \text{odd} | \text{even} \rangle$ and so will equal zero, hence the transition will be spin-forbidden.

Spin-selection rules hence enforce that only transitions to or from excited singlet states will be spin-allowed, with triplet states formally spin-forbidden.

2.3 Photophysical Properties of Organic Conjugated Systems

Conjugated organic molecules therefore show distinctive electronic states and electronic transitions from the ground state to excited states. Under the right conditions these electronic transitions can be radiatively accessed, i.e. absorb a photon to reach the excited state (optical absorption) and/or then subsequently emit a photon to decay back to the ground state (luminescence). The observation of optical absorption and luminescence in organic materials has long been known⁶ and occurs naturally in pigments such as chlorophylls, carotenoids and melanin.⁷⁻

¹⁰ A detailed treatment of all of these photophysical processes would be a

monograph in its own right, and indeed publication of such works has been made by others.^{5, 11} Presented here is but a brief overview of the key aspects of merit.

As mentioned above in Section 2.2, increasing the conjugation length decreases the HOMO-LUMO gap, so lowering the energy of the electronic transition.

The dependence of the optical properties on the conjugation length is best exemplified by looking at the acenes family. The principal value of the absorption wavelength is shown for increasing numbers of fused benzene rings in Table 2.1.

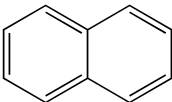
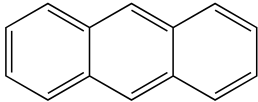
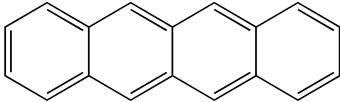
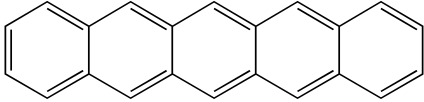
Molecule	Structure	Absorption Region (nm)
Benzene		255
Napthalene		315
Anthracene		380
Tetracene		480
Pentacene		580

Table 2.1. The increase in the absorption peak wavelength with the increase in the conjugation length for the acenes family of materials.⁵ As delocalisation increases the $S_0 \rightarrow S_1$ energy gap decreases.

Optical transitions in conjugated organic materials are, however, not single wavelength transitions such as would be found in atomic spectra. They are instead broadened and contain imprints caused by the structure of the emitting molecule and may show the effects of the host solvent or local environment. This

broadening, characterised as both homogeneous and inhomogeneous broadening,⁵ leads to Gaussian *bands* of emission as a function of energy rather than a single value of an energy delta function.

One might expect that optical absorption and emission spectra for an organic conjugated molecule would therefore just be a single Gaussian function and that both spectra should be the same, this however is not the case, and instead a typical set of spectra for an organic material is as shown in Figure 2.8.

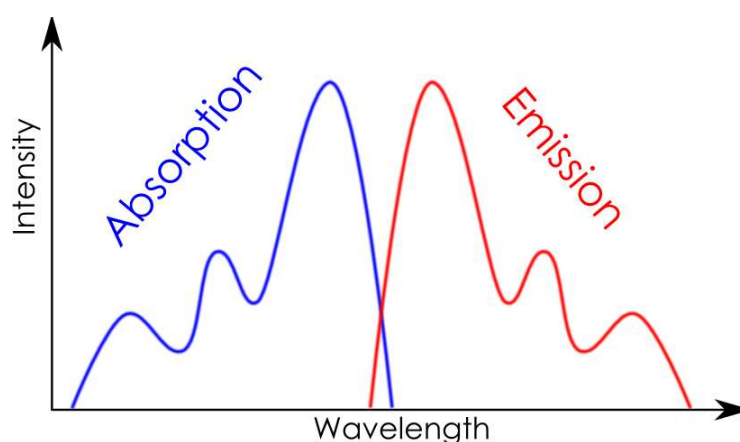


Figure 2.8. Typical absorption and emission spectra of a conjugated organic material. Absorption is found to be at higher energy than emission. Both spectra show internal structure and are the mirror image of each other.

The complex nature of the optical spectra are explained by the nature of the excited states in organic materials and how they influence the optical transitions. Firstly it is useful to present a schematic of the energy levels under consideration and their applicable properties, as shown in Figure 2.9.

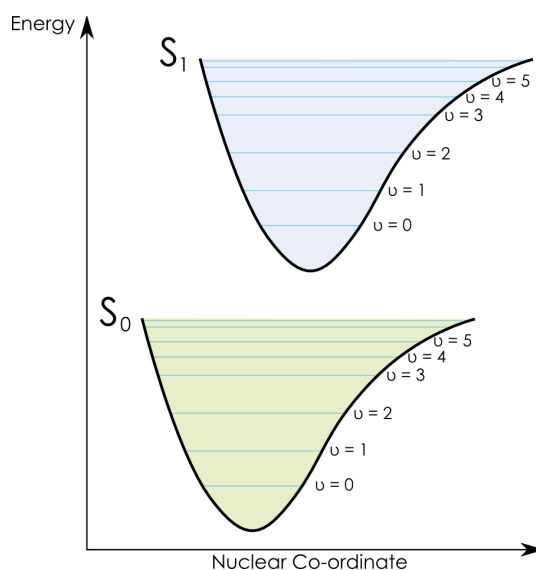


Figure 2.9. Schematic of Morse-like potential wells of the electronic ground state (S_0) and first excited state (S_1). The vibrational states within each potential are shown, from the lowest energy, $v = 0$, upwards.

Each excited state consists of a Morse-like potential well, the energy levels of which correspond to vibrational states ($v = 0 \dots v = n$) – caused by the vibrational motion of the molecule and its interaction with the surroundings. Upon excitation the system is moved from the electronic ground state, S_0 , into an excited state (this could be any higher state S_n , but for simplicity let us denote it as S_1). The S_1 state is offset in the nuclear co-ordinate with respect to S_0 due to a geometry change in the molecule that exists between the two states' configurations. Electronic (and hence in our case optical) transitions occur very quickly compared to the motion of the nucleus, denoted as the Born–Oppenheimer approximation.¹² Therefore electronic transitions are treated as being vertical in nature and hence the vibrational states are unchanged (i.e. the S_1 potential well does not move horizontally with respect to S_0 during the timeframe of an electronic transition). This leads to the formulation of the Franck-Condon principle¹³⁻¹⁵ that establishes the relationship between optical absorption and emission. Briefly, the principle states that the vibrational overlap between ground and excited state wavefunctions dictates the probability (the Franck-Condon factor) of such a transition taking place and is shown diagrammatically in Figure 2.10.

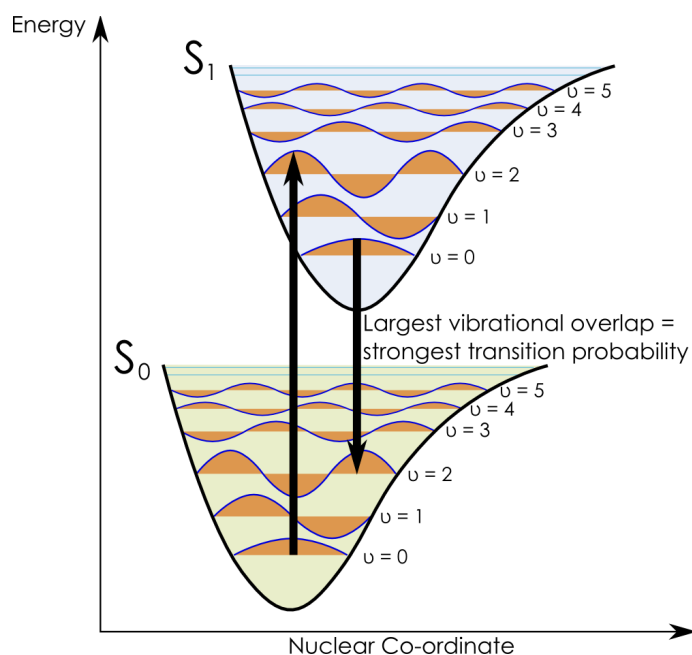


Figure 2.10. Schematic illustrating the Franck-Condon principle, where probabilities of absorption and emission are defined by the overlap of vibrational wavefunctions between the two states. Accordingly the strongest absorption and emission transitions are shown.

From a relaxed system in the $v = 0$ vibrational state of S_0 , optical absorption leads to the population of the S_1 vibrational state with the largest wavefunction overlap – generally this is a higher vibrational level due to the offset of S_1 compared to S_0 in the nuclear co-ordinate, as an excited state has different electronic configuration and so different excited state geometry. Optical absorption transitions of lower probabilities will occur to lower and higher vibrational states in S_1 , leading to a characteristic spectrum. Emission is just a mirror image of this process – transitions from $S_1 \rightarrow S_0$ will occur where the overlap of the vibrational wavefunctions is greatest. Naturally one would thus presume that the emission spectrum should therefore just be the same as the absorption, but very fast relaxation occurs within S_1 ($\sim 10^{-12}$ s or faster),¹¹ much shorter than the time required for radiative decay ($\sim 10^{-9}$ s), hence the population will generally always reach the $v = 0$ vibrational state of S_1 before it emits any light. Hence overlap of the $v = 0$ wavefunction of S_1 with the vibrational levels of S_0 will dictate what the emission spectrum looks like. Overall there is therefore a loss of energy when comparing the principal absorption wavelength for a two state situation with the

principal emission wavelength. This energy loss is called the Stokes Shift¹⁶ and is indicative of the vibrational overlap between the initial and final states when comparing absorption and emission. Characteristic absorption and emission spectra produced as a result of consideration of the above discussion are shown in Figure 2.11.

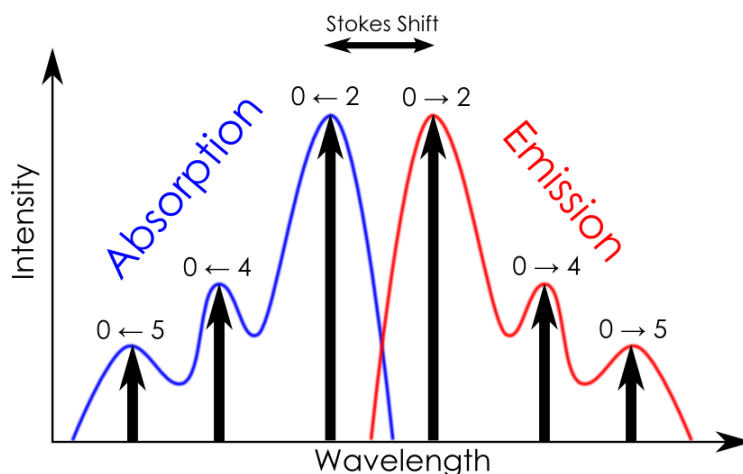


Figure 2.11. Characteristic absorption and emission spectra for a conjugated organic material. With vibrational overlaps as depicted in Figure 2.10 the associated vibronic peaks are produced. The Stokes Shift between absorption and emission is also shown.

It is thus clear from the outlined discussion that the characteristic absorption and emission spectra in conjugated organic materials are well understood. This discussion has presented optical transitions in what one would call the *steady state* regime, i.e. long lived in nature (typically on the order of 10^{-9} s or longer). What is therefore of interest is to recast the above discussion in a temporal light, i.e. characterise the excited state and the processes that occur there in terms of the time and nature of those processes. This is traditionally achieved by sketching a Jablonski diagram,¹⁷ as shown in Figure 2.12.

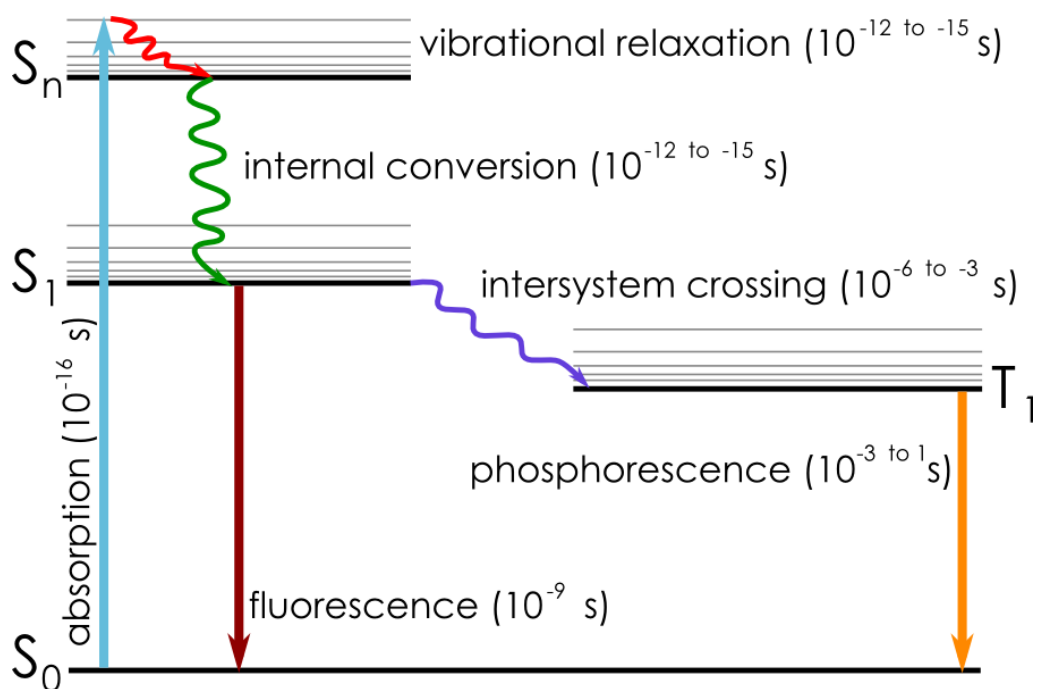


Figure 2.12. Jablonski diagram showing the various processes that occur upon excitation and their characteristic timescales for a conjugated organic material, as discussed in the text.

Some of the features may look familiar, but have now been schematically drawn to highlight the differing nature of the processes. Upon photoexcitation a higher excited state, S_n is accessed. From here *internal conversion* (IC), the very fast non-radiative relaxation to lower electronic states, occurs ($\sim 10^{-12}$ to 10^{-15} s),^{18, 19} hence emission is generally observed from the lowest singlet state, S_1 due to this fast IC, this is known as Kasha's rule.²⁰ Once in the lowest state, S_1 , the population will undergo *vibrational relaxation* through the vibrational levels ($\sim 10^{-12}$ to 10^{-15} s) to reach the lowest vibrational state in S_1 .²¹ Here it is possible for the excited state population to undergo *intersystem crossing* (ISC) to the triplet manifold, however as this requires a spin-flip of an electron it has a low probability in traditional conjugated organic materials. From either S_1 or T_1 radiative decay can occur and collectively this is known as luminescence. For $T_1 \rightarrow S_0$ this process is termed *phosphorescence*.²² Since phosphorescence requires another spin-flip (to return to the singlet ground state) this has a low probability and long radiative lifetime ($\sim 10^{-3}$ to 10^1 s), hence a low emission strength. For S_1

→ S_0 luminescence takes the form of *fluorescence* and is fully spin-allowed, hence strong emission can be observed and lead to short lifetimes ($\sim 10^{-9}$ s).

Non-radiative decay pathways compete with luminescence, potentially reducing the photoluminescence quantum yield (PLQY) – defined as the number of photons emitted divided by the number of photons absorbed²³ – due to deactivation occurring by vibrational rather than radiative dissipation. Therefore when measuring lifetimes of emissive samples the observed natural lifetime (τ) is related to the radiative (k_r) and non-radiative (k_{nr}) rates by equation 2.2:

$$\tau = \frac{1}{k_r + k_{nr}} \quad [2.2]$$

The rate of a process (e.g. the radiative rate) is simply related to its lifetime by:

$$\tau_r = \frac{1}{k_r} \quad [2.3]$$

Thus the PLQY is defined as:

$$PLQY = \frac{\tau}{\tau_r} \quad [2.4]$$

It is hence clear that when looking at phosphorescence in conventional organic materials k_r is small, thus k_{nr} dominates and the PLQY is very low.

One can rightfully ask why this is a problem, as if the probability of reaching T_1 via ISC is low anyway why should the low efficiencies of phosphorescence there matter either? Under photoexcitation this is true, as $S_0 \rightarrow S_n$ transitions are initially optically accessed, however under electrical excitation this is not the case.

Utilisation of conjugated organic materials in organic light emitting diodes (OLEDs) was pioneered in the 1980's using small molecules²⁴ and in the early 1990's using conjugated polymers.²⁵ Detailed discussion of OLED device architectures and operating methodologies is beyond the scope of the work presented here, with extensive literature available for further reading in this large area.²⁶⁻³⁰ Briefly, however, electrons and holes are injected into a device stack, meeting in the organic layer to form an exciton (a bound electron-hole pair). The excitons form with an unbiased spin selection, so generally conform to the overall deduced singlet/triplet ratio as detailed in Section 2.2, i.e. 25% singlet and 75% triplet. There is currently a small amount of debate as to whether this ratio is truly fixed or can be somewhat manipulated,³¹ but it is generally accepted that the 1:3 relation is very frequently going to be the resultant singlet/triplet ratio under electrical excitation. When the exciton decays (producing luminescence) it will do so according to whatever spin-state it is in. Hence, given the very low efficiencies of phosphorescence, it is clear that traditional OLED devices can only reach a maximum internal efficiency of 25%, with overall external efficiencies being substantially lower (due to light extraction losses). It would, therefore, be highly advantageous to find some way of improving internal efficiencies, and this was pioneered by modifying the organic materials used to include a transition metal ion to enable efficient phosphorescence.

2.4 Transition Metal Complexes

2.4.1 Chemical Structure

Transition metal complexes are, as the name implies, comprised of a central transition metal ion, complexed with an organic ligand. Also referred to as organometallic complexes, this class of materials show unique properties due to the somewhat unconventional integration of heavy metal ions with light organic molecular structures. A typical organometallic complex is shown in Figure 2.13, with a central metal ion, M, co-ordinated with three bi-pyridine ligands.

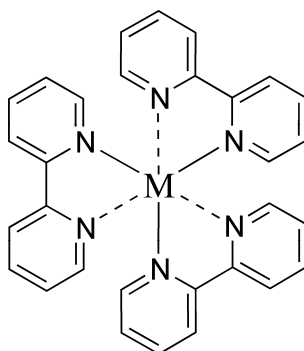


Figure 2.13. Typical chemical structure of an organometallic complex. A metal (M) is surrounded by co-ordinated ligands, in this case three bi-pyridine ligands are shown.

The unique properties that organometallic complexes display has led to numerous natural and synthetic uses for this class of materials. Many biological processes function through the use of metal complexes – generally through complex metalloprotein structures – to carry out material transport,³² signalling³³ or enzyme functions.³⁴ One of the more fundamental organometallic complexes found in nature is the iron complex haemoglobin, which enables the transport of oxygen in red blood cells.³⁵ The dye that absorbs sunlight in the process of photosynthesis, chlorophyll, is an organometallic complex, with a magnesium ion at the middle of a porphyrin moiety.³⁶ Synthetic uses for organometallic complexes include their extensive use as catalysts in chemical reactions³⁷⁻³⁹ and in recent years have included the use of ruthenium complexes in dye-sensitised solar cells⁴⁰ and platinum and iridium complexes in organic light emitting diodes to enable triplet emission.⁴¹⁻⁴³

2.4.2 Electronic and Photophysical Properties

The unique properties of transition metal complexes with conjugated ligands can lead to novel electronic properties when compared with traditional conjugated systems as already discussed earlier. In addition to the expected π - π^* electronic structures forming on the conjugated ligands there now exists the potential for

electrons to move between the central metal ion and the ligand, creating charge transfer states. Depending on the appropriate choice of the metal ion, its oxidation level, and the ligand structure either ligand-metal charge transfer (LMCT)⁴⁴ or metal-ligand charge transfer (MLCT)⁴⁵ states can form. The formation of MLCT states will be the focus of attention here since these are the formed and observed electronic states in the materials studied in this thesis.

In MLCT states an electron moves from the d orbital (the 5d orbital in the case of iridium complexes) out onto one of the ligands of the complex forming the charge transfer state, as shown in Figure 2.14. The MLCT transition can form for numerous electronic transitions (states) and these tend to form at energies of 1-3 eV, i.e. spanning the visible wavelength region of the electromagnetic spectrum.⁴⁶ MLCT transition have lower oscillator strengths than fully allowed π - π^* transitions owing to the charge transfer character of the states.

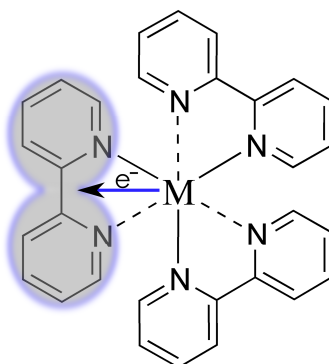


Figure 2.14. The formation of a metal-ligand charge transfer state. An electron from the d orbital of the metal moves out onto the ligand forming an excited state localised on one ligand.

Traditional assignments^{45, 47} are made of the formed electronic states in transition metal complexes based on the observed features in their optical absorption spectrum. These assignments are shown below in Figure 2.15 for the prototypical iridium phenylpyridine complex. Given the small conjugated ligand size of a phenyl and pyridine moiety the π - π^* absorption bands are in the ultra-violet due to confined electron delocalisation. Singlet MLCT (denoted ¹MLCT) states form at

lower energy, with multiple assigned singlet states. The lowest triplet MLCT (denoted $^3\text{MLCT}$) state is visible in these complexes, as indicated, and is a remarkable fact in itself given the formally forbidden nature of the transition. As discussed below, mixing with the fully allowed $^1\text{MLCT}$ state is responsible for the partially allowed nature of the $S_0 \rightarrow ^3\text{MLCT}$ transition.

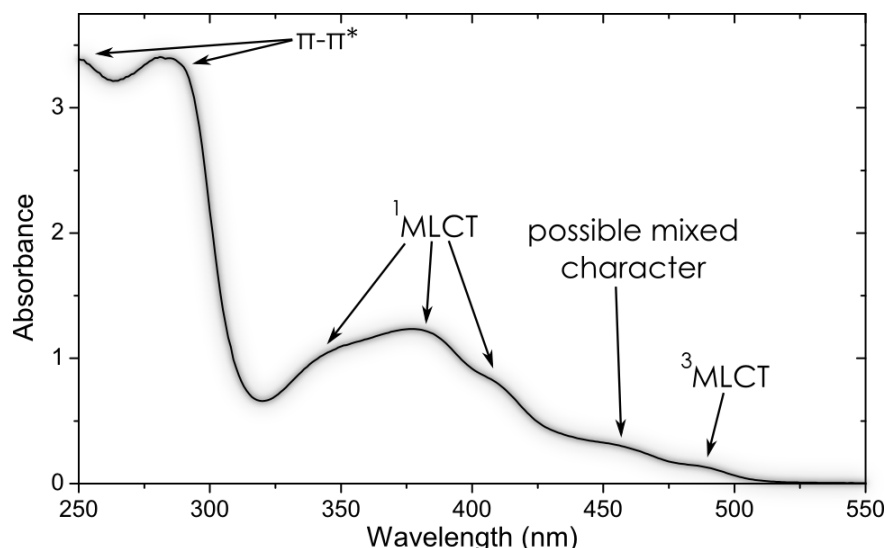


Figure 2.15. Typical assignment of the features in the absorption spectrum of the transition metal complex *fac*-tris(2-phenylpyridine) iridium(III). A $^3\text{MLCT}$ state is formed at the lowest energy and is the weakest feature, indicating the partially allowed nature of the transition. A band of intermediary strength $^1\text{MLCT}$ states forms at higher energy before strongly absorbing $\pi\text{-}\pi^*$ transitions on the ligand form in the ultra-violet.

To complicate matters a little, theoretical treatments find,⁴⁸⁻⁵⁰ however, that the charge transfer states are not pure states, but rather mixtures of MLCT and $\pi\text{-}\pi^*$ character. Essentially the states can be thought of as having dual character of MLCT and $\pi\text{-}\pi^*$. This mixed nature exists due to the nature of the originating HOMO and LUMOs. The HOMO is found to be comprised of dual 5d iridium and π ligand character while the LUMO is found to be purely π^* ligand character.

While the formation of partial charge transfer states somewhat alters the traditional picture of electronic structures in conjugated organic systems, and enables novel uses of the materials, the main effect that is of importance here is

the effect of the heavy metal ion itself through the manifestation of spin-orbit coupling (SOC).

Spin-orbit coupling is the effect of the angular momentum of a spin of an electron (S) interacting, or in other words being coupled, with the orbital angular momentum of the electron around the nucleus (L). Two regimes exist, Russell-Saunders (LS) coupling and jj-coupling.⁵¹ The former, LS, involves simple separate summation of the individual spin (s_i) and orbital (l_i) components of angular momentum, giving total S and L values, and then defining the total angular momentum $J = L+S$. Stronger coupling exists with jj-coupling, where the individual s_i and l_i components are themselves added together before being summed over all i leading to a total J.

In conventional conjugated systems comprised of 2p originating π molecular orbitals SOC is very weak, leading to very low probabilities of ISC and phosphorescence.⁵² In transition metal complexes such as ruthenium, platinum and iridium based materials, however, the co-ordinating metal leads to heavy metal effects that induce strong SOC.^{53, 54}

SOC in transition metal complexes has been assigned to both LS⁵⁵ and jj-coupling.⁵⁶ The effect of large SOC in transition metal complexes is to couple the singlet states to the triplet states, in effect a singlet state is partially mixed with a triplet state.^{47, 57}

Radiative decay of triplet states, phosphorescence, is as discussed in Section 2.2, formally forbidden by spin-selection rules. When phosphorescence is observed in traditional organic light emitting materials it is with a very long radiative lifetime (milliseconds to seconds) and is this long because emission is reliant upon random spin flips of the excited state to enable radiative decay. The long radiative lifetime hence leads to very inefficient emission due to non-radiative losses that occur much faster. In transition metal complexes SOC enables mixing of singlet character into triplet states and therefore phosphorescence becomes a partially

spin-allowed process. The spin-allowed nature of the triplet states in transition metal complexes also leads to intersystem crossing to the triplet manifold becoming allowed. The result of this is to produce an excited state gradient, funnelling the population to the lowest triplet state (which is lower in energy than the lowest singlet) where it will then remain and radiatively decay back to the ground state as phosphorescence. SOC therefore enables efficient phosphorescence from transition metal complexes with comparatively short microsecond lifetimes at room temperature.

It can thus be seen that transition metal complexes, properly designed, can lead to very efficient emission of light and fulfil the criterion that was laid out at the end of Section 2.3 for fabricating light emitting devices that can have very high internal efficiencies. Indeed such an OLED device using an iridium complex has been reported to have essentially a 100% internal quantum efficiency,⁴³ with the only associated losses related to light extraction and as such it becomes an engineering optical design problem rather than one necessarily related to the emissive material itself. Further novel properties of these materials have also been exploited. Very fast relaxation immediately down to the lowest ³MLCT state, coupled with absorption from deep in the UV up to ~ 600 nm in some complexes gives the opportunity to capitalise on the large spectral separation of absorption and emission, for example a complex excited at 300 nm can give emission at 650 nm, a separation of ~ 2 eV. This downconversion was recently used to enable a low-cost concentration of solar light for electrical generation in a device with a platinum porphyrin complex, absorbing the light across visible wavelengths and in effect “funnelling” it to phosphorescence at ~ 800 nm, keeping the self-absorption effects of the emitted light far lower than could be achieved with purely organic materials.⁵⁸

The unique properties of transition metal complexes can therefore be useful in their own right in applied physics; however it is the unique photophysical properties of the materials themselves that pique the interest within the field of ultrafast chemical physics. The funnelling effect discussed above with the

movement to the lowest triplet state occurs on very fast timescales (predominantly 10^{-15} s)⁵⁹⁻⁶¹ – movement through ¹MLCT states, intersystem crossing to ³MLCT states and relaxation to the lowest ³MLCT state are allowed processes and so can be very fast. The high density of electronic states leads to significant ultrafast processes occurring and hence transition metal complexes can give insight into these femtosecond processes that, in other materials, either do not exist or would be difficult or even impossible to observe.

2.4.3 Ultrafast Processes in Transition Metal Complexes

In this thesis the focus of the work has been on iridium complexes with phenylpyridine ligands because of their relatively simple chemical structures and importance in OLEDs, where they have found widespread use as efficient phosphorescent emitters.

As intimated above at the end of Section 2.4.2, ultrafast processes dominate the relaxation pathways from higher excited states to the lowest ³MLCT state in transition metal complexes owing to strong spin-orbit coupling. Different techniques on different materials have been used to try and gain insight on these processes and are described here to provide background and context for the later work that is presented, with the movements and processes summarised in Figure 2.16.

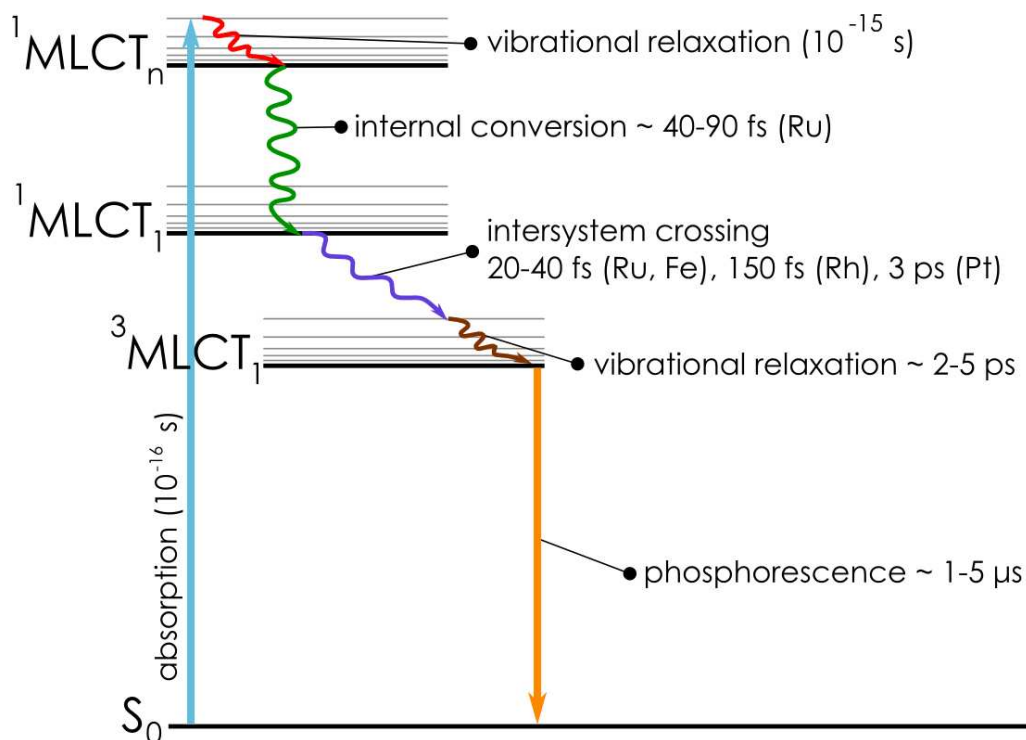


Figure 2.16. Jablonski diagram summarising the observed processes in a typical transition metal complex. The essential difference with a traditional Jablonski picture of relaxation is the very fast nature of relaxation to the lowest $^3\text{MLCT}$ state, which leads to large amounts of dissipation of excess energy in very short amounts of time. Typical relaxation times for some of the processes are noted for ruthenium, iron, rhenium and platinum complexes.

Three main processes can be identified and their time constants discerned. Firstly upon excitation to a high energy $^1\text{MLCT}$ state very fast internal conversion down to lower singlet states is likely, with only one study reporting on this process. Looking at a ruthenium complex, Bhasikuttan and Okada⁶² indicated that internal conversion between $^1\text{MLCT}$ states may occur with time constants in the 40-90 fs region, although unfortunately strong supporting evidence to aid in their assignments was lacking. Movement from the singlet to triplet manifold – intersystem crossing – has, however, been a frequently studied process in transition metal complexes. Very fast decay of fluorescence from singlet MLCT states in ruthenium^{60, 61} and iron⁶³ complexes, with time constants of 40 fs or less, have been reported, and were attributed to ISC. Slightly slower ISC has been observed in rhenium⁶⁴ complexes on the 150 fs timescale. When studying ISC in rhenium, Chergui and co-workers observed a correlation between the ISC rate and

the vibrational periods of the metal-ligand modes, implying that the rate could be controlled by low-frequency skeletal vibrations.⁶⁴ In ultrafast transient absorption studies by McCusker and co-workers excited state localisation in a ruthenium complex was found to occur in 60 fs and was attributed to nondiffusive solvation dynamics,⁶⁵ while evolution of the primary singlet MLCT state to the lowest excited ³MLCT state was found to occur on a timescale of 100 fs.⁵⁹ Recent work using both ultrafast luminescence⁶³ and x-ray spectroscopy⁶⁶ have looked at the ultrafast dynamics of an iron complex and found a 120 fs time constant for the population to leave the ³MLCT state for a quintet state. Once in the ³MLCT state vibrational cooling to the surrounding environment has been reported on the 2-5 ps time range.^{67, 68}

Ultrafast dissipative mechanisms to enable non-radiative relaxation primarily rely on processes within the molecule – interaction with the surrounding environment generally occurs on longer timescales. The key process for dissipation of excess energy inside the molecule is intramolecular vibrational redistribution.

2.4.4 Intramolecular Vibrational Redistribution

Intramolecular vibrational redistribution (IVR), the process of both redistribution of vibrations from high to low frequency modes in a molecule and spatial spreading of those vibrations around the molecule,^{21, 69-72} is an important ultrafast dissipative mechanism for energy that plays a role in the making and breaking of chemical bonds,⁷³ charge transfer reactions⁷⁴ and biological processes.⁷⁵

IVR has been assigned as a dissipating agent in femtosecond relaxation processes in transition metal complexes.^{59, 61} IVR acts as a dissipating agent because it allows energy to be redistributed *within* a molecule, transforming localised high frequency vibrations that are prepared by the formation of an excited state by laser pulse excitation to spatially and frequency distributed vibrations. The concept can be visualised simply with a ball-and-spring model of a molecule as shown in

Figure 2.17, where a preliminary vibration on one bond shows initial local motion before moving towards redistributed motion over the whole molecule.

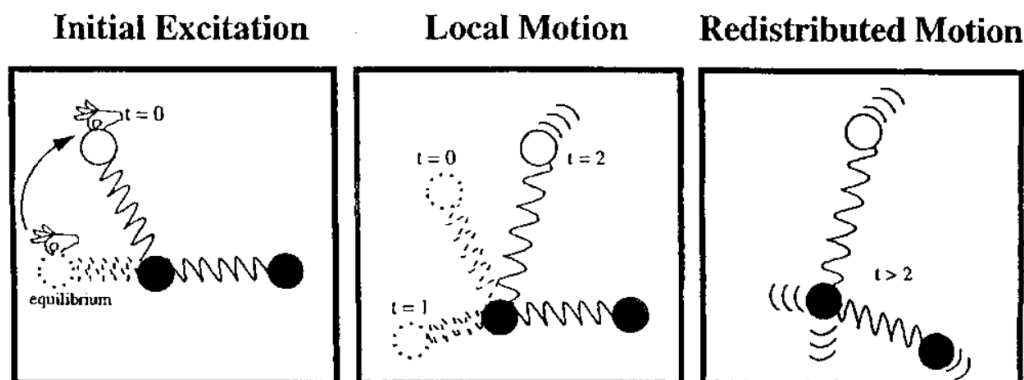


Figure 2.17. Classical description of intramolecular vibrational redistribution, as originally presented by Nesbitt & Field.⁶⁹ The first panel shows the initial excitation (creation of an energetic potential) in a simple three atom ball-and-spring molecule. The second panel shows local motion of the excited atom before the third panel shows the redistributed motion to the third atom caused by IVR. Figure from reference 69. Reproduced with permission of the rights holder.

This is a simple analogy and one that belies a large amount of subtle detail at a quantum mechanical level that defines an entire field of science, but it is one that efficiently communicates the basic concept of IVR.

Vibrations spread through a molecule due to the nature of how atoms bonded together can move with respect to each other. Various vibrational motions are possible. Atoms can, amongst other movements, stretch, twist, bend and flex with respect to each other. These movements are linked – one atom will have a twist constrained if the other atom it is twisting with respect to is stretching further away. This connectivity leads to a number of *normal modes* in a molecule, such that the vibrations of atoms with respect to each other are occurring in harmony – defined such that each of the atom's movements reach their maximum, minimum and equilibrium positions at the same time. The number of such normal modes for a non-linear molecule is defined as:⁷⁶

$$3N - 6$$

[2.5]

where N is the number of atoms in the molecule. It is thus clear that with large polyatomic systems the situation very quickly becomes very complicated. H_2O has three normal modes, ethene has 12 and the simplest iridium complex studied in this thesis, $\text{Ir}(\text{ppy})_3$, has 177 normal modes.

IVR, as stated, involves the redistribution of energy from higher to lower frequency modes inside the molecule, and is not confined to normal modes. To give an analogy, *Inter*-molecular vibrational cooling in the condensed phase involves energy flow from the molecule to surrounding molecules (the bath) – in IVR the bath can be thought of as being the molecule itself. IVR exists in two states, *restricted* and *dissipative*. In restrictive IVR, also known as the small molecule case, there is small but non-zero spacing between vibrational energy levels and IVR proceeds in a limited stepwise manner. In larger molecules, however, dissipative IVR is possible, where a continuum of vibrational states exists and hence energy flow can proceed down through them with few limitations. These cases can be generalised by considering the density of vibrational states, which will increase with larger molecules and with larger values of vibrational energy present within the molecule.⁷⁷

Treatments, both classical and quantum mechanical on IVR have been given by others and are provided for further reading.^{71, 77-79}

Self-evidently descriptions of IVR are difficult enough in simple small molecules such as benzene, let alone in large polyatomic ones. Transition metal complexes, with their high degree of spin-mixing and very fast dissipation of large amounts of excess energy may provide an opportunity to study IVR in large molecular systems.

2.5 References

- [1] H. Shirakawa, E.J. Louis, A.G. Macdiarmid, C.K. Chiang, and A.J. Heeger, *Journal of the Chemical Society-Chemical Communications*, 1977(16): p. 578-580.
- [2] C.K. Chiang, C.R. Fincher, Y.W. Park, A.J. Heeger, H. Shirakawa, E.J. Louis, S.C. Gau, and A.G. Macdiarmid, *Physical Review Letters*, 1977. **39**(17): p. 1098-1101.
- [3] J. McMurry, *Organic Chemistry*. 6th ed. 2004: Brooks/Cole.
- [4] J. Clayden, N. Greeves, S. Warren, and P. Wothers, *Organic Chemistry*. 2008: Oxford University Press.
- [5] M. Pope and C.E. Swenberg, *Electronic Processes in Organic Crystals and Polymers*. 2nd ed. 1999: Oxford University Press.
- [6] J.F.W. Herschel, *Philosophical Transactions of the Royal Society of London*, 1845. **135**: p. 147-153.
- [7] N. Kollias and A. Baqer, *Journal of Investigative Dermatology*, 1985. **85**(1): p. 38-42.
- [8] H.K. Lichtenthaler, *Methods in Enzymology*, 1987. **148**: p. 350-382.
- [9] T. Polivka and V. Sundstrom, *Chemical Reviews*, 2004. **104**(4): p. 2021-2071.
- [10] J.F. Wintermans and A. de Mots, *Biochim Biophys Acta*, 1965. **109**(2).
- [11] J.R. Lakowicz, *Principles of Fluorescence Spectroscopy*. 2nd ed. 1999: Kluwer Academic.
- [12] M. Born and R. Oppenheimer, *Annalen der Physik*, 1927. **84**: p. 457.
- [13] J. Franck and E.G. Dymond, *Transactions of the Faraday Society*, 1926. **21**: p. 536-542.
- [14] E.U. Condon, *Physical Review*, 1926. **28**(6): p. 1182.
- [15] E.U. Condon, *Physical Review*, 1928. **32**(6): p. 858.
- [16] G.G. Stokes, *Philosophical Transactions of the Royal Society of London*, 1852. **142**: p. 463-562.
- [17] A. Jablonski, *Zeitschrift fur Physik*, 1935. **94**: p. 38-46.
- [18] R. Englman and J. Jortner, *Molecular Physics*, 1970. **18**(2): p. 145-164.

- [19] P. Avouris, W.M. Gelbart, and M.A. Elsayed, *Chemical Reviews*, 1977. **77**(6): p. 793-833.
- [20] M. Kasha, *Discussions of the Faraday Society* 1950. **9**: p. 14-19.
- [21] T. Elsaesser and W. Kaiser, *Annual Review of Physical Chemistry*, 1991. **42**: p. 83-107.
- [22] M. Kasha, *Chemical Reviews*, 1947. **41**(2): p. 401-419.
- [23] I.D.W. Samuel, G. Rumbles, and R.H. Friend, *Primary Photoexcitations in Conjugated Polymers: Molecular Excitation Versus Semiconductor Band Model*, ed. N.S. Sariciftci. 1998: World Scientific Publishing Company.
- [24] C.W. Tang and S.A. Van Slyke, *Applied Physics Letters*, 1987. **51**(12): p. 913-915.
- [25] J.H. Burroughes, D.D.C. Bradley, A.R. Brown, R.N. Marks, K. Mackay, R.H. Friend, P.L. Burns, and A.B. Holmes, *Nature*, 1990. **347**(6293): p. 539-541.
- [26] K.Y. Law, *Chemical Reviews*, 1993. **93**(1): p. 449-486.
- [27] J.R. Sheats, H. Antoniadis, M. Hueschen, W. Leonard, J. Miller, R. Moon, D. Roitman, and A. Stocking, *Science*, 1996. **273**(5277): p. 884-888.
- [28] A. Kraft, A.C. Grimsdale, and A.B. Holmes, *Angewandte Chemie-International Edition*, 1998. **37**(4): p. 402-428.
- [29] U. Mitschke and P. Bauerle, *Journal of Materials Chemistry*, 2000. **10**(7): p. 1471-1507.
- [30] M.T. Bernius, M. Inbasekaran, J. O'Brien, and W.S. Wu, *Advanced Materials*, 2000. **12**(23): p. 1737-1750.
- [31] J.S. Wilson, A.S. Dhoot, A.J.A.B. Seeley, M.S. Khan, A. Kohler, and R.H. Friend, *Nature*, 2001. **413**(6858): p. 831.
- [32] F.A. Armstrong, H.A. Heering, and J. Hirst, *Chemical Society Reviews*, 1997. **26**(3): p. 169-179.
- [33] K.M.F. Khan and D.J. Falcone, *Journal of Biological Chemistry*, 1997. **272**(13): p. 8270-8275.
- [34] D.W. Christianson, *Advances in Protein Chemistry*, 1991. **42**: p. 281-355.
- [35] P.J. Steinbach, A. Ansari, J. Berendzen, D. Braunstein, K. Chu, B.R. Cowen, D. Ehrenstein, H. Frauenfelder, J.B. Johnson, D.C. Lamb, S.

- Luck, J.R. Mourant, G.U. Nienhaus, P. Ormos, R. Philipp, A.H. Xie, and R.D. Young, *Biochemistry*, 1991. **30**(16): p. 3988-4001.
- [36] S.A. Green and N.V. Blough, *Limnology and Oceanography*, 1994. **39**(8): p. 1903-1916.
- [37] C.A. Tolman, *Chemical Reviews*, 1977. **77**(3): p. 313-348.
- [38] T.M. Trnka and R.H. Grubbs, *Accounts of Chemical Research*, 2001. **34**(1): p. 18-29.
- [39] J. Dupont, R.F. de Souza, and P.A.Z. Suarez, *Chemical Reviews*, 2002. **102**(10): p. 3667-3691.
- [40] B. O'Regan and M. Gratzel, *Nature*, 1991. **353**(6346): p. 737-740.
- [41] M.A. Baldo, D.F. O'Brien, Y. You, A. Shoustikov, S. Sibley, M.E. Thompson, and S.R. Forrest, *Nature*, 1998. **395**(6698): p. 151-154.
- [42] M.A. Baldo, S. Lamansky, P.E. Burrows, M.E. Thompson, and S.R. Forrest, *Applied Physics Letters*, 1999. **75**(1): p. 4-6.
- [43] C. Adachi, M.A. Baldo, M.E. Thompson, and S.R. Forrest, *Journal of Applied Physics*, 2001. **90**(10): p. 5048-5051.
- [44] C.R. Johnson, W.W. Henderson, and R.E. Shepherd, *Inorganic Chemistry*, 1984. **23**(18): p. 2754-2763.
- [45] S. Sprouse, K.A. King, P.J. Spellane, and R.J. Watts, *Journal of the American Chemical Society*, 1984. **106**(22): p. 6647-6653.
- [46] S. Lamansky, P. Djurovich, D. Murphy, F. Abdel-Razzaq, H.E. Lee, C. Adachi, P.E. Burrows, S.R. Forrest, and M.E. Thompson, *Journal of the American Chemical Society*, 2001. **123**(18): p. 4304-4312.
- [47] M.G. Colombo, A. Hauser, and H.U. Gudel, *Inorganic Chemistry*, 1993. **32**(14): p. 3088-3092.
- [48] P.J. Hay, *Journal of Physical Chemistry A*, 2002. **106**(8): p. 1634-1641.
- [49] K. Nozaki, *Journal of the Chinese Chemical Society*, 2006. **53**(1): p. 101-112.
- [50] E. Jansson, B. Minaev, S. Schrader, and H. Agren, *Chemical Physics*, 2007. **333**(2-3): p. 157-167.
- [51] P.W. Atkins, *Molecular Quantum Mechanics*. 2nd ed. 1983: Oxford University Press.

- [52] S.P. McGlynn, T. Azumi, and M. Kinoshita, *The Molecular Spectroscopy of the Triplet State*. 1969, New York: Prentice-Hall.
- [53] R.L. Ake and M. Gouterman, *Theoretica Chimica Acta*, 1969. **15**(1): p. 20-42.
- [54] A. Harriman, *Journal of the Chemical Society-Faraday Transactions II*, 1981. **77**: p. 1281-1291.
- [55] M.A. Baldo, M.E. Thompson, and S.R. Forrest, *Pure and Applied Chemistry*, 1999. **71**(11): p. 2095-2106.
- [56] D. Wasserberg, *Triplet states - triplet fates: phosphorescence and energy transfer in functional molecules*, in *Department of Chemical Engineering*. 2006, Technische Universiteit Eindhoven: Eindhoven.
- [57] Y. Komada, S. Yamauchi, and N. Hirota, *Journal of Physical Chemistry*, 1986. **90**(24): p. 6425-6430.
- [58] M.J. Currie, J.K. Mapel, T.D. Heidel, S. Goffri, and M.A. Baldo, *Science*, 2008. **321**(5886): p. 226-228.
- [59] N. Damrauer, G. Cerullo, A. Yeh, T. Boussie, C. Shank, and J. McCusker, *Science*, 1997. **275**(5296): p. 54-57.
- [60] A.C. Bhasikuttan, M. Suzuki, S. Nakashima, and T. Okada, *Journal of the American Chemical Society*, 2002. **124**(28): p. 8398-8405.
- [61] A. Cannizzo, F. van Mourik, W. Gawelda, G. Zgrablic, C. Bressler, and M. Chergui, *Angewandte Chemie-International Edition*, 2006. **45**(19): p. 3174-3176.
- [62] A.C. Bhasikuttan and T. Okada, *Journal of Physical Chemistry B*, 2004. **108**(34): p. 12629-12632.
- [63] W. Gawelda, A. Cannizzo, V.T. Pham, F. vanMourik, C. Bressler, and M. Chergui, *Journal of the American Chemical Society*, 2007. **129**(26): p. 8199-8206.
- [64] A. Cannizzo, A.M. Blanco-Rodriguez, A. El Nahhas, J. Sebera, S. Zalis, J.A. Vlcek, and M. Chergui, *Journal of the American Chemical Society*, 2008. **130**(28): p. 8967-8974.
- [65] A.T. Yeh, C.V. Shank, and J.K. McCusker, *Science*, 2000. **289**(5481): p. 935-938.

- [66] C. Bressler, C. Milne, V.T. Pham, A. ElNahhas, R.M. van der Veen, W. Gawelda, S. Johnson, P. Beaud, D. Grolimund, M. Kaiser, C.N. Borca, G. Ingold, R. Abela, and M. Chergui, *Science*, 2009. **323**(5913): p. 489-492.
- [67] B. Dietzek, D. Akimov, W. Kiefer, S. Rau, J. Popp, and M. Schmitt, *Laser Physics Letters*, 2007. **4**(2): p. 121-125.
- [68] S.A. McFarland, F.S. Lee, K.A.W.Y. Cheng, F.L. Cozens, and N.P. Schepp, *Journal of the American Chemical Society*, 2005. **127**(19): p. 7065-7070.
- [69] D.J. Nesbitt and R.W. Field, *Journal of Physical Chemistry*, 1996. **100**(31): p. 12735-12756.
- [70] K.K. Lehmann, G. Scoles, and B.H. Pate, *Annual Review of Physical Chemistry*, 1994. **45**(1): p. 241-274.
- [71] M. Gruebele and P.G. Wolynes, *Accounts of Chemical Research*, 2004. **37**(4): p. 261-267.
- [72] D. Boyall and K.L. Reid, *Chemical Society Reviews*, 1997. **26**(3): p. 223-232.
- [73] A.H. Zewail, *Journal of Physical Chemistry*, 1996. **100**(31): p. 12701-12724.
- [74] G. Benko, J. Kallioinen, J.E.I. Korppi-Tommola, A.P. Yartsev, and V. Sundstrom, *Journal of the American Chemical Society*, 2002. **124**(3): p. 489-493.
- [75] Q. Wang, R.W. Schoenlein, L.A. Peteanu, R.A. Mathies, and C.V. Shank, *Science*, 1994. **266**(5184): p. 422-424.
- [76] E.B. Wilson, J.C. Decius, and P.C. Cross, *Molecular vibrations: the theory of infrared and Raman vibrational spectra*. 1980: Courier Dover Publications.
- [77] A. Tramer, C. Jungen, and F. Lahmani, *Energy dissipation in molecular systems*. 2005: Springer.
- [78] T. Uzer and W.H. Miller, *Physics Reports-Review Section of Physics Letters*, 1991. **199**(2): p. 73-146.
- [79] M. Quack, *Annual Review of Physical Chemistry*, 1990. **41**: p. 839-874.

3

Experimental Methods

The Science of Colours becomes a Speculation as truly mathematical as any other part of Opticks. I mean, so far as they depend on the Nature of Light, and are not produced or alter'd by the Power of Imagination, or by striking or pressing the Eye.

Sir Isaac Newton, *Opticks*, 4th Ed., 1730

3.1 Introduction

This chapter presents a description of the equipment and experimental methodologies employed in this work. Ultrafast light sources were used to enable observation of femtosecond processes in iridium complexes with two principal techniques; luminescence upconversion spectroscopy and transient absorption pump probe experiments.

In Section 3.2 I provide a description of sample preparation methods and in Section 3.3 I describe the steady state photophysical measurements that were performed to give basic characterisation of the materials under study. In Section 3.4 I give the background and descriptions of operation of the ultrafast light sources that were used in this work, detailing the Ti:Sapphire oscillator, regenerative amplifier and non-collinear parametric amplifier equipment. In Section 3.5 I discuss in some detail the upconversion setup that was the primary spectroscopic method that was employed during the PhD – this experiment

enables the detection of luminescence with femtosecond resolution and I present the optical setup and operating methodologies of upconversion spectroscopy. In Section 3.6 I discuss the optical layout and operating conditions of the amplified pump probe experiment that was used to record transient absorption dynamics. Finally in Section 3.7 I discuss the temporal fitting methodologies that were used to fit exponential functions to the kinetics recorded with the spectroscopic setups already detailed.

3.2 Sample Preparation

The studies performed in this work were made on solutions of various iridium complexes. Materials were purchased from American Dye Source Inc. and were used without further purification. The dendrimers studied in Chapter 5 were synthesised by the group of Prof. Paul Burn according to published methods.¹ All materials were stored in oxygen free conditions until their use for the preparation of a solution.

Materials were dissolved in either toluene or tetrahydrofuran (spectrophotometric grade, Sigma Aldrich Co.), depending on the compound under investigation and the experimental technique used. THF was found to be better at dissolving material; however this came at a small cost of the stability of the solution. It was ensured that fresh solvents were used, particularly with THF, which, lacking stabilisers, would become unusable after the seal on the bottle had been broken for two or more weeks. Some of the limitations of measurements described in later chapters are caused by the poor solubility of some iridium complexes and different solvents were experimented with. Chlorinated solvents (dichloromethane for example) provided very high solubility but displayed very poor photostability, visibly degrading in minutes under laser light. This was unsuitable for the femtosecond measurements that were to be taken, as solutions were regularly required to be under femtosecond high repetition rate laser

excitation for tens of hours or more. Hence the solvent range was limited to toluene and THF.

The solutions themselves were prepared under ambient air clean room conditions, typically in volumes of 1 or 2 ml at whatever concentration (e.g. 2 mg/ml) was appropriate. The solute generally dissolved without assistance though some stirring or shaking for a couple of minutes was often provided to ensure full dissolution.

Once a solution was made it was then pipetted into the sample cell. The cell is a custom solution cell that enables it to be rotated to avoid sample degradation, and is shown in an exploded diagram in Figure 3.1. It consists of two pieces of fused silica (each 2 mm thick) with a Teflon spacer ring sandwiched between them. Different spacer rings of varying thickness can be used (to vary the optical path length of the solution under investigation). Filling of the cell is achieved by sliding the stack of the three pieces slightly apart and pipetting in the solution before sliding the glass back. The three piece stack is held inside an aluminium base structure, the stack pressed together with a metal top piece that is screwed in place to ensure none of the solution can escape or evaporate over time. Typically a 0.5 mm spacer was used in all studies performed and was thinnest available – it was found that thicker spacers, with associated longer optical path lengths, caused temporal broadening with upconversion spectroscopy, so degrading the resolution of measurements.

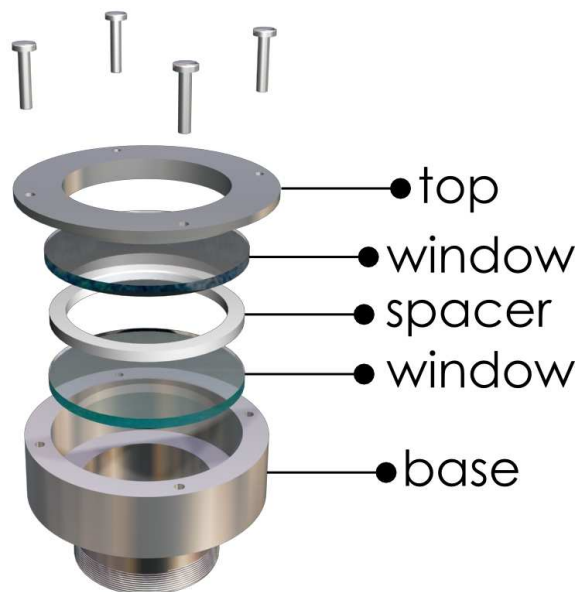


Figure 3.1. Exploded diagram of the rotating sample cell used in this work. A Teflon spacer (0.5 mm thick) is sandwiched between two fused silica windows (each 2 mm thick) and this “stack” is then held inside an aluminium base with a metal top piece screwed in place.

All ultrafast measurements were performed with the sample cell rotating, achieved by a rubber band looping around a groove in the cell and onto a motor drive shaft. The motor was 12 V D.C. and it was estimated that the sample cell rotated at ~ 200 revolutions per minute.

As mentioned above, solutions have the potential to photodegrade under the intense laser excitation that they are subjected to in the undertaken ultrafast experiments. Monitoring of solutions for stability was achieved by a number of means. Firstly the ultrafast dynamics themselves can be tracked. Dynamics tended to be composed of numerous scans averaged together – a change in the dynamics across this series of datasets can give evidence of changes, although once the safe laser exposure limits of a material had been roughly defined this then just acted as a confirmation of stability – a final check. The main method of stability checking was to monitor the steady state absorption and photoluminescence spectra of the sample for any changes when compared to a fresh solution. Absorption checks were found to be the most sensitive – looking

for a loss of absorption across multiple features is easier than a loss of luminescence from just one (the steady state phosphorescence peak). After gaining experience with a number of materials a good guide for exposure limits was defined, generally in the region of 200 hours of laser exposure. Accordingly fresh solutions were prepared well before this exposure time was reached and great care was always taken to ensure the recorded dynamics were free of any unwanted substances or effects.

Upon changing to a fresh solution or new material all components of the sample cell were thoroughly cleaned by sonication in acetone. The deconstructable nature of the rotating sample cell enables comprehensive cleaning to be performed – a must if small changes in time constants or intensities are being monitored.

All solutions were created in open air. Oxygen quenching (triplet-triplet annihilation) reduces the natural lifetime from microseconds to nanoseconds,² but this is not a concern with the femto/picosecond timescales that are of interest here.

3.3 Steady State Photophysical Measurements

Steady state photophysical measurements were performed to enable basic characterisation of the materials under investigation. Spectra were typically taken of the actual solution in the rotating cell that was used in ultrafast measurements to ensure full consistency in what was being observed.

Absorption of light in a sample occurs as detailed in Chapter 2. The absorbance (A) is defined as:

$$A = -\log_{10}(T) \quad [3.1]$$

where T is the transmittance of light through a sample (the light that passes through the sample divided by the light entering the sample, I/I_0). The absorbance

of the sample depends on the concentration and optical path length over which the absorption is measured. These variable properties can be removed by defining the molar absorption coefficient, ϵ :

$$\epsilon = \frac{A}{cl} \quad [3.2]$$

where A is the absorbance, c is the concentration and l is the optical path length.

Absorption spectra were recorded with the Varian Cary 300 Bio UV-Vis spectrophotometer, the spectrum of just the solvent being recorded separately and subtracted (though in practice there was no absorption from the solvent above 300 nm, which was the region of interest).

Photoluminescence spectra were recorded with the Fluoromax 2 fluorimeter. Light is produced in the instrument by a xenon bulb and a monochromator is used to select the wavelength that is used for excitation. Emission is collected, and since the rotating sample cell was used custom positioning of the cell was made with a collection angle of close but not exactly 45° with respect to the excitation, ensuring no excitation light was reflected into the emission monochromator. A scanning emission monochromator is used to record the intensities of light produced by the sample at different wavelengths on a photomultiplier tube (PMT). The recorded emission spectra were corrected for the reduced sensitivity of the PMT at longer wavelengths (> 600 nm).

3.4 Ultrafast Light Sources

3.4.1 Titanium Sapphire Oscillator

Examination of ultrafast photophysical processes generally requires an ultrafast (i.e. femtosecond) source of light to achieve the stated goal. This used to be achieved with passively modelocked dye lasers, an unstable and high maintenance

technology that limited the amount and location of research that could take place. This was overcome by the invention of self-modelocking (also known as kerr-lens modelocking) in Titanium Sapphire (Ti:Sapphire) lasers in 1991 by Spence, Kean and Sibbett here in St Andrews.³ This simple and low-maintenance technology allowed commercialised ultrafast laser solutions to be created, rapidly expanding the availability of ultrafast light sources for photophysical research.

Ultrafast experiments reported in this thesis were carried out at the Femtosecond Laser Amplifier Facility, part of the Organic Semiconductor Centre at the University of St Andrews. The starting point of ultrafast equipment at the facility is a Ti:Sapphire laser, the Spectra-Physics Mai Tai oscillator. The Mai Tai consists of two components, a continuous-wave (CW) pump and Ti:Sapphire cavity. The CW pump is itself comprised of two components, with inorganic red semiconductor laser diodes used to pump neodymium ions (Nd^{3+}) in a yttrium vanadate (Nd:YVO_4) matrix gain medium. The crystalline Nd:YVO_4 matrix has a strong absorption peak ~ 815 nm and two banks of laser diodes pump the material at this wavelength, producing > 10 W of 1064 nm laser output. This emission is frequency doubled in a lithium triborate (LBO) nonlinear crystal, producing green 532 nm laser light – all CW.

Titanium ions doped into Al_2O_3 (sapphire) and formed into a rod are the gain medium in the second component of the Mai Tai system. The absorption and emission spectrum of the Ti:Sapphire rod is shown below in Figure 3.2.

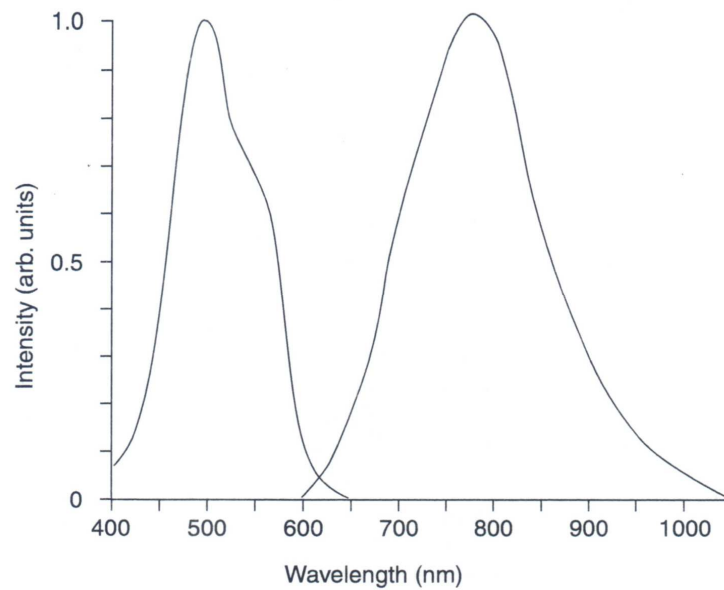


Figure 3.2. Absorption (left) and emission (right) of the titanium doped sapphire rod used as a gain medium in the Mai Tai oscillator. The gain medium is pumped at 532 nm and gain is available in the 670-950 nm region. The spectra are from the Mai Tai manual.⁴

Pumping with the 532 nm light gives lasing in the 670-950 nm region – due to various conditions the actual tuneability of the ultrafast output of the Mai Tai oscillator is 750-850 nm. CW lasing can thus be achieved, but it is the special properties of the Ti:Sapphire rod itself that enables the generation of femtosecond pulses. Self, or Kerr-lens modelocking (KLM) – the intensity dependence of the nonlinear refractive index of the gain medium – is the mechanism that gives rise to self-modelocking in Ti:Sapphire systems.^{3, 5} In addition to KLM the Mai Tai also uses acousto-optic modulation (AOM) – the generation of an acoustic wave inside a modulator placed in the cavity to establish a time-dependent refractive index grating – to provide greater stability.

The Mai Tai is therefore able to produce stable ultrafast pulsed laser emission. Pulse widths are nominally 100 fs full-width half-maximum (FWHM) and the oscillator is tuneable from 750-850 nm by simple PC based control software at a repetition rate of 80 MHz. Output powers are dependent on the configuration and wavelength, but the full output of the oscillator would generally give ~ 600 mW,

though around 50% of this is used to pump the regenerative amplifier that will be discussed next in Section 3.4.2, leaving in the region of 300 mW available for use in luminescence upconversion spectroscopy as discussed in Section 3.5.

3.4.2 Regenerative Amplification

While the Mai Tai oscillator, as discussed above, gives short (100 fs FWHM) pulses with an average power of 300-800 mW the high repetition rate of the system (80 MHz) is a consequence of the cavity length:

$$\text{repetition rate} = \frac{2L}{c} \quad [3.3]$$

where L is the cavity length and c is the speed of light. This means that a laser pulse is produced every 12 ns. For some spectroscopic measurements this can be a benefit, but for others it can be a nuisance, limiting the range of times that can be measured, giving the possibility of accumulating long-lived excitations and increasing the average power on the sample. It is therefore desirable to have lower repetition rates (kHz), however in consideration of equation 3.3 above it is clear that cavity lengths would hence need to be on the order of 10^{12} m, which is not possible. A requirement for some spectroscopic techniques is the ability to produce a wide variety of wavelengths, and very high pulse energies enable this through parametric amplification as will be discussed in Section 3.4.3. A second requirement for some spectroscopic measurements is the ability to have very high peak power intensities. With 300 mW average power at 80 MHz each pulse is therefore ~ 4 nJ, however peak pulses on the order of microjoules or higher are sometimes desirable.

The two outlined desires – low repetition rate and high peak power – are commensurate with each other, and are achieved by a process known as regenerative amplification. Increasing the peak power of each ultrafast pulse is, one would imagine, a straightforward step – just simply increase the pumping

energy of the Ti:Sapphire cavity, so achieving higher powers. Optical components are, however, not that accommodating, and femtosecond pulses with energies in the microjoule regime or higher will lead to potential problems, with self-focussing in the gain medium leading to extremely high energy intensities and thus catastrophic damage occurring. The solution, therefore, is to stretch the pulse temporally, so reducing its peak power before amplification, a technique known as chirped pulse amplification (CPA).⁶

The main CPA that occurs in the ultrafast facility is via the Spectra Physics Hurricane, an integrated regenerative amplifier that provides a single box solution to ultrafast laser requirements, containing the Mai Tai oscillator and taking ~ 50% of its output to be amplified, leaving the rest for high repetition rate experiments. CPA is achieved in the Hurricane by firstly temporally stretching the 100 fs pulse with a pair of diffraction gratings. 100 fs laser pulses contain a range of wavelengths of light, indeed the time-bandwidth relation acts as an embodiment of the uncertainty principle – as the width (time) of the pulse decreases the bandwidth (spread of wavelengths) increases, hence short 100 fs pulses have a high bandwidth (9 nm). Diffracting the pulses off of a pair of gratings has the effect of splitting these wavelengths up, blue wavelengths are delayed compared to red wavelengths and thus the pulse becomes “smeared” out in time to ~ 100 ps, hence reducing the overall peak power. With a stretched pulse the next step is to amplify it to higher intensities. This is achieved by use of a diode pumped solid state laser (Spectra Physics Evolution, 532 nm, ~ 200 ns (FWHM), 5 kHz, 10 W) to pump a Ti:Sapphire gain medium. Since amplification only occurs when both the seed pulse and the pump pulse are temporally aligned the amplified output has a repetition rate of 5 kHz rather than 80 MHz (the 5 kHz pump is loosely synchronised to the 80 MHz seed to ensure that the 100 ps seed pulse arrives in the gain medium at roughly the same amount of time after the pump each time to ensure consistent amplification of each pulse). Pockels cells on both the seed input and amplified output control both the seed pulse entry to the Ti:Sapphire gain medium and the number of roundtrips that the amplified pulse makes through it before being allowed to leave the cavity. After amplification the resultant pulse

is then put through pulse compression diffractive gratings (operating in reverse compared to the pulse stretcher already discussed) and the final resultant 100 fs FWHM, 5 kHz, 1 W output is then able to be used for experiments that require lower repetition rate and higher peak energy pulses.

3.4.3 *Non-Collinear Parametric Amplification*

The tuning range of the Mai Tai oscillator enables 80 MHz low peak power femtosecond pulses to be generated in the 750-850 nm region. Frequency doubling opens up another window in the 375-425 nm region, and tripling another in the 250-285 nm region. These are useful wavelength ranges, and many organic semiconductors have optical absorption in the 375-425 nm range, enabling femtosecond photoexcitation and spectroscopy to be performed. It is however desirable to have a wider range of ultrafast wavelengths for different spectroscopic techniques, both for excitation and measurement of the resulting excited states. Amplified pulses have even less tuneability when produced by the Hurricane as amplification is preset for 800 nm – hence only 800, 400 and 266 nm are available. It is, however, the high peak energy of amplified pulses that can enable a very wide range of femtosecond wavelengths through different parametric amplification techniques.

The parametric amplification setup that was utilised in the transient absorption setup was the TOPAS-White-IR system by Light Conversion, a non-collinear optical parametric amplifier.

An optical parametric amplifier (OPA) amplifies light by taking advantage of non-linear mechanisms rather than building gain as in a traditional laser amplification stage. A white light continuum is generated by focussing a small amount of incident 800 nm amplified light onto a sapphire plate. This light is then fed onto a Beta Barium Borate (BBO) non-linear crystal along with the originating pump and amplification of the selected wavelength of the white light continuum take place based on the crystal angle, generating signal and idler

beams. Amplification occurs in two stages, a pre-amplification and a power amplification stage. The resultant power-amplified beam is then delivered out of the OPA for use. The TOPAS-White is a non-collinear OPA, indicating that the configuration of the setup is in a non-collinear geometry – this produces very high bandwidth pulses and therefore enables their compression to very short pulse durations – typically < 50 fs. The output wavelength range of the system that was used as the probe beam in transient absorption studies, as discussed in Section 3.6, was 500-1000 nm.

Inclusion of an optical setup diagram for the internal arrangement of the TOPAS-White system would, due to its compact and highly configured nature, not aid in clarification, but reference can be provided to the user's manual for more information.⁷

3.5 Luminescence Upconversion Spectroscopy

All the femtosecond light sources discussed above represent the culmination of many years of research and commercialisation of these technologies, delivering stable and (relatively) affordable ultrafast sources. While the physics of ultrafast light generation and manipulation is in itself engrossing, it is the application of that light to physical systems that is of most interest to the work described in this thesis. The light acts like both a metaphorical and, to some extent, literal beacon, illuminating molecules and uncovering their inner workings.

By far the most unambiguous technique to understand excited state processes in light emitting materials is to look at the light emission itself, for light emitted from an electronic state shows temporal behaviour that embodies the nature of the excited state, how quickly it forms, its coupling to the ground state, an imprint of its local environment and the factors controlling its radiative and non-radiative decay. Temporally resolved detection of luminescence began in the nanosecond time domain with flash lamp based systems, quickly evolving towards the

picosecond regime with time correlated single photon counting and streak cameras.⁸ Even the highest time resolution of these techniques, however, could not reach far or at all into the femtosecond time domain, due in no small part to the electronic jitter that plagues detection for times shorter than a few picoseconds. Thus the femtosecond domain remained out of reach for luminescence detection until the development of upconversion spectroscopy in the 1970's and 80's, best summarised by the review of Shah in 1988.⁹ It is worth noting that while these techniques were developed quite some time ago it has only been in the last ten or so years that they have become more widely used.

Upconversion spectroscopy removes all of the problems associated with electronic jitter in obtaining very high temporal resolutions as it is an all optical technique. It is therefore the properties of the light pulses and their guiding optics that defines the resolution of the instrument, not electronics. Upconversion is based on the process of sum-frequency generation (SFG) inside a non-linear crystal between two incident light beams.^{10, 11}

SFG is utilised in upconversion spectroscopy by generating the sum frequency between luminescence and a gating pulse. Temporal resolution is achieved with movement of a delay line on the gating pulse, thus changing the temporal point of SFG creation with respect to the luminescence. Key to the ability to record femtosecond dynamics is that the excitation pulse (and hence the origin of luminescence in time) and the gating pulse originate from the same initial pulse – so removing any jitter problems, as exact delays on the gating pulse can be made with respect to the luminescence by mechanical means with a delay line.

Femtosecond dynamics can then be recorded by simple movement of an optical delay line. Upconverted light will only be generated when the gate and luminescence are both present on the SFG crystal, so if the gate delay line is scanned out (increasing the path length of the gate arm and hence forcing the gate to arrive later with respect to the luminescence) temporal dynamics will be recorded. The sequence for recording dynamics is that the delay line moves some

distance (e.g. $1\ \mu\text{m} = 3.33\ \text{fs}$) then stops and the PMT count rate is recorded, then the delay line moves again and stops before another count reading is taken. The process is as depicted in Figure 3.3.

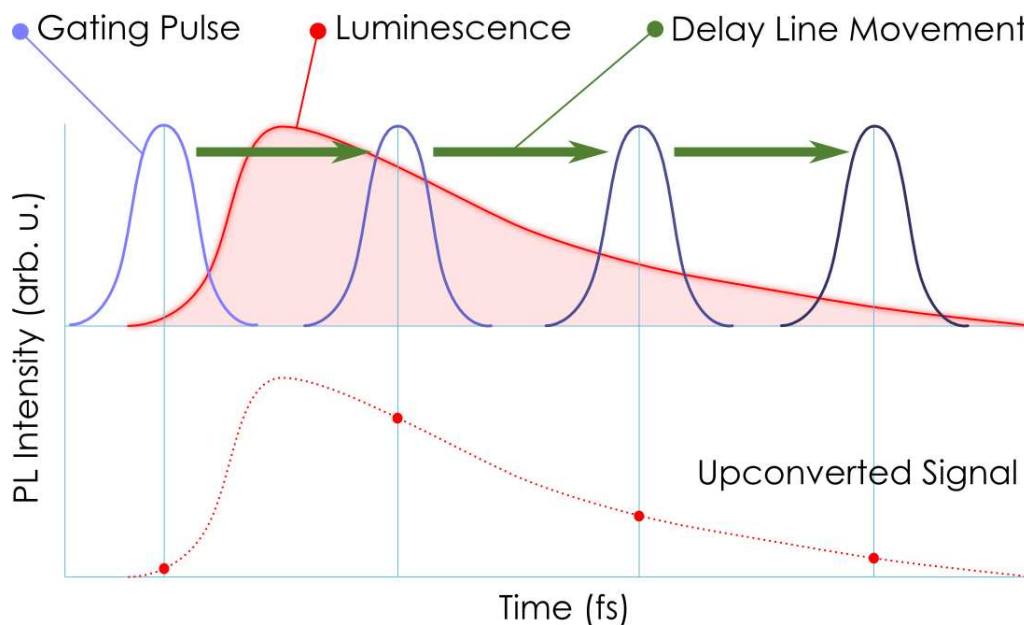


Figure 3.3. Schematic of the principle behind upconversion spectroscopy. Temporal overlap between a gating pulse and luminescence produces an upconverted signal. Moving the gating pulse in time with respect to the luminescence with a delay line leads to different parts of the luminescence temporal profile being upconverted, thus enabling the kinetics of an emitting sample to be recorded.

3.5.1 FOG100 by CDP Systems

The setup that was used in this work was a purpose built system, the “FOG100”, and was designed and manufactured by CDP Systems. A purpose built setup has the advantages of enabling fully customised optical components that give best upconversion performance (both in its signal to noise and temporal resolution) when compared with compromises that may be made when using off-the-shelf optical components in a home-built setup. A full diagram of the optical arrangement of the upconversion setup used is shown in Figure 3.4.

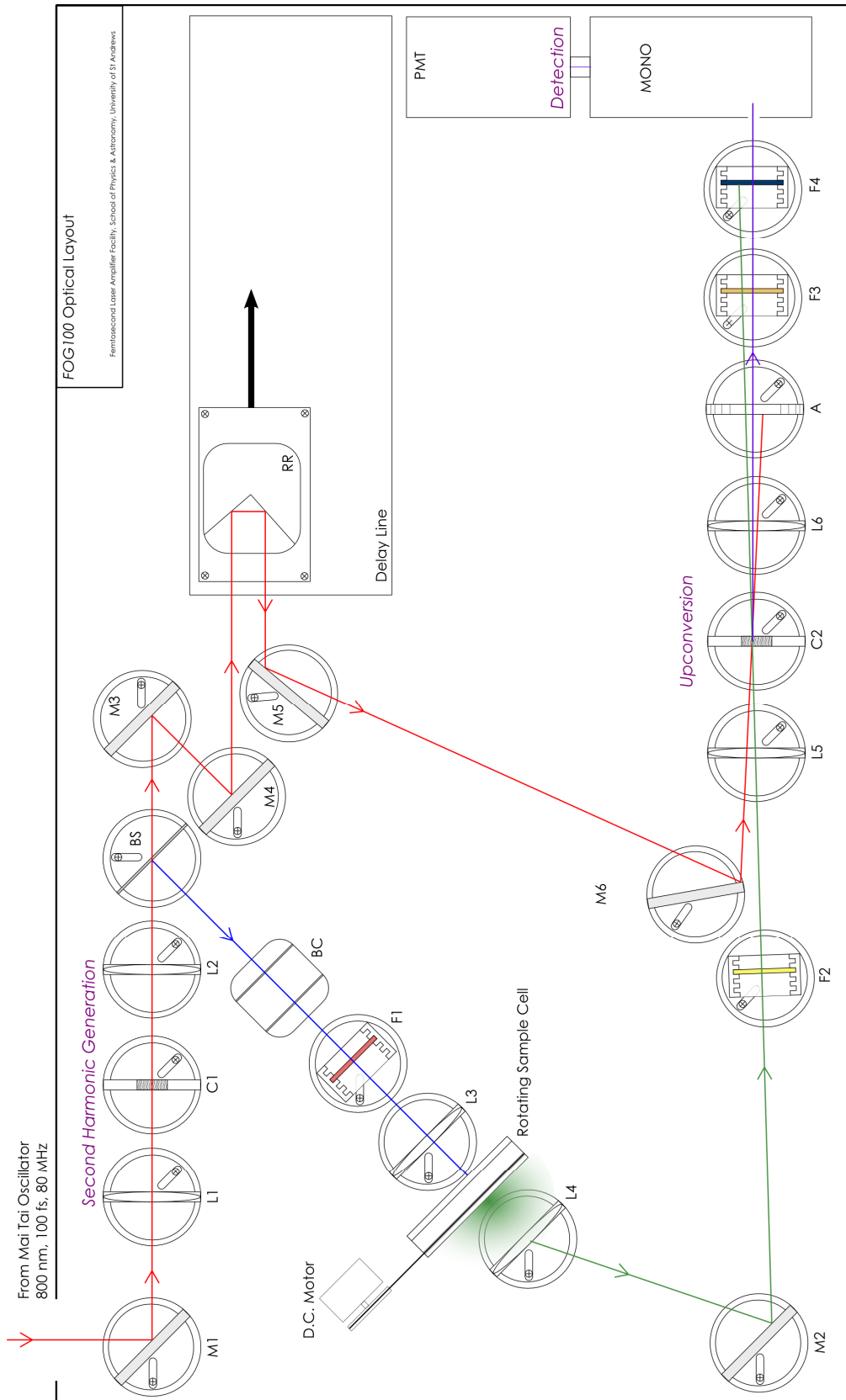


Figure 3.4. The optical layout of the upconversion setup used in the work reported here. The configuration of the optical components are discussed in the text.

Discussing the setup in stages, firstly second harmonic generation and beam splitting takes place. The 100 fs 80 MHz output of the Mai Tai is fed into the FOG100 setup (M1), 750-850 nm is available but for simplicity 800 nm will be presumed for this description, with requirements for other excitation wavelengths being very similar. The 800 nm laser light is focussed by a 6 cm lens (L1) onto a type 1 Beta Barium Borate (BBO) non-linear crystal (1 mm thickness) (C1). Around 100 mW of 400 nm second harmonic and 200 mW of residual 800 nm are produced and these are collimated with a second 6 cm lens (L2) before being brought onto a dichroic beamsplitter (BS) which reflects 400 nm along the excitation path and transmits 800 nm along the gating path.

Dealing with the excitation path first, the 400 nm is passed through a Berek's compensator (BC) to provide polarisation control of the excitation (generally set at the magic angle of 54.7°) and then on through a cut-off filter (F1) with a red Schott glass filter chosen to transmit 400 nm and absorb \sim 800 nm to remove any residual gate that was reflected down the excitation path from the beamsplitter. The 400 nm light is then focussed onto the sample space with a 4 cm achromatic lens (L3). The focussing is made as tight as possible to generate the highest intensity of luminescence, and this is usually checked by optimising with low intensity excitation on a dye solution, observing with binoculars and moving the lens to get as small an excitation spot as possible – estimated to be \sim 20-40 μ m. As already discussed in Section 3.2, the solution under investigation is held in a rotating sample cell and its optical path length is 0.5 mm. Upon excitation strong emission is therefore produced – the amount of absorption of the 400 nm excitation will determine some of the later luminescence dynamics that are able to be observed due to generation of Raman signals from the solvent, as will be discussed in more detail in Section 3.5.2. Luminescence is emitted from the solution in all directions and is collected on-axis by an achromatic 4 cm lens (L4) – this can be off-axis collection if one wants to avoid collecting residual 400 nm excitation (at the cost of a small reduction in amount of collected luminescence). The collected luminescence is then directed with a steering mirror (M2) towards

the upconversion region of the setup, passing through a yellow Schott glass cut-off filter (F2) to remove any 400 nm excitation that has been collected.

The gating arm of the setup simply involves spatial movement of the residual 800 nm beam on and off a delay line. Mirrors (M3,4) provide alignment control to enable a straight beam to be brought onto the gold coated retroreflector (RR) of an optical delay line. The delay line itself is stepper motor driven and is controlled by electronics and PC based software, as discussed later, and is capable of moving out to 1.7 ns in steps as small as 6.25 fs. A micrometer screw is provided for initial setting movements. The returned beam is then reflected (M5) down towards a folding mirror (M6) that directs it into the upconversion region to join the collected luminescence.

Alignment of the delay line is made to ensure that the beam is perfectly parallel with the delay path, i.e. as the delay line is scanned out there is no horizontal or vertical “wandering” of the returned beam. This is achieved by using mirrors M3 and M4 to control the alignment – an initial configuration is made and then the delay line is scanned out to its maximum length. A picking mirror is placed between M5 & M6 to reflect the gate out of the upconversion setup and the beam is monitored on a target far away (2-3 meters). At such large path lengths very small movements of the gate can be easily monitored. Appropriate adjustments are then made to the alignment with M3 & M4 before rescanning the delay line. This process is repeated until no visible movement of the gate pulse is observed on the distant target when scanning the delay out.

The upconversion region is where the all optical nature of luminescence detection becomes apparent. As outlined above, both the luminescence and the 800 nm gate have been brought spatially to the same position and are now both focussed with an 8 cm achromatic lens (L5) onto a second type 1 BBO crystal (0.5 mm thickness), (C2), this is required for sum frequency generation (SFG). Both beams are spatially overlapped on the crystal (M2 providing steering of the luminescence to give overlap) and are brought onto the crystal at $\sim 10^\circ$ to each

other (see Figure 3.5) so that the upconverted beam is spatially separated from the other beams. The C2 crystal angle in the horizontal axis is varied with a micrometer screw to give the correct phase-matching conditions for the gate and desired detected luminescence wavelength for SFG. The sum frequency light that is generated is in the ultraviolet and is produced angularly halfway between the luminescence and gate, as depicted in Figure 3.5.

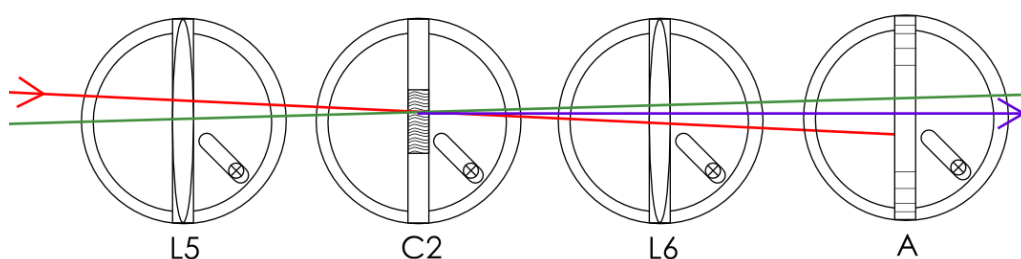


Figure 3.5. The overlap of the gate (red) and luminescence (green) beams on the SFG crystal (C2) and the resultant UV sum frequency (purple) beam that is produced. The incident beams are brought in at an angle to each other to aid in subsequent filtering of them from the sum frequency light.

After generation of the UV light all three beams are then collected with an 8 cm lens (L6) which is moved to provide focussing of the UV light on the monochromator (MONO) slit at the end of the detection line. Filtering of unwanted light is then the next key challenge, ~ 200 mW of 800 nm gate and significant quantities of luminescence represent the vast majority of the light after the SFG crystal, but only the very small quantities of UV sum frequency light are of interest, hence everything else now needs to be filtered out. This was the rationale for bringing both the luminescence and gate in at a $\sim 10^\circ$ with respect to each other, as after the crystal they propagate away from the desired UV light. However, significant fractions are still caught by the collecting lens (L6) and so require removal, which is done firstly spatially with an aperture (A) and then spectrally with two filters. The first filter (F3) is a dielectric designed to reflect any excitation light ~ 400 nm – if on-axis collection with L4 is used on a sample that does not absorb all excitation light then this also gets through to the detection region of the setup. The second filter (F4) is a UV-pass Schott glass filter

designed to pass light in the 250-400 nm region and absorb in the 750-850 nm region, with transmission essentially 0% at 800 nm, though some transmission is present below 790 nm. After these filtering mechanisms the upconverted UV light is passed into the monochromator (MONO). This is a Solar/TII single monochromator (CDP Systems model 2022) and wavelength selection is achieved by turning a micrometer screw to the correct position for the required wavelength (the control software indicates the screw position that should be set for the desired visible wavelength based on the UV upconversion wavelength needed for the monochromator).

Once the UV light is spectrally filtered in the monochromator it is then passed on to a photomultiplier tube (PMT). PMT counting and delay line movement are controlled by PC software provided by CDP Systems (“Lumex” Version 4.0.1.0).

A summary of the specifications of the upconversion setup, indicating excitation and detection ranges is shown in Table 3.1.

Upconversion Setup:	
Excitation Wavelength Range:	380-425 nm
Repetition Rate:	80 MHz
Pulse Width (FWHM):	100 fs
Detection Range:	390-790 nm
Upconversion Range:	260-400 nm

Table 3.1. Specification of excitation and detection spectral parameters for the FOG100 luminescence upconversion setup used in this work.

3.5.2 The Raman Problem

Phase-matching of the SFG crystal enables all wavelengths across the visible region to be upconverted, from 390-790 nm, thus complete characterisation of visible light emitting materials should be possible giving upconverted light in the range 260-400 nm. For solutions of materials with poor solubility, however, a challenge was discovered. Essentially in low concentration solutions that do not completely absorb the excitation light (generally solutions that have optical density < 2) some of that excitation light is instead generating Raman signals from the solvent itself. Typical Raman shifts in common solvents used to dissolve organic materials are $\sim 3000\text{ cm}^{-1}$, therefore with 400 nm excitation a Raman peak exists at $\sim 455\text{ nm}$. Raman signals are instantaneous “emission” hence on the femtosecond timescales observed with upconversion they show up as instrument limited kinetics – a significant problem if one is interested in processes on a similar timescale as one cannot be separated from the other. If these were single wavelength problems then this would be manageable, however spectral broadening leads to a wide region that is off-limits, with evidence of Raman features up to $\sim 470\text{ nm}$ being observed. Thus when looking at materials that did not have good dissolution properties 480 nm was the shortest wavelength that could safely be observed, an unhappy coincidence when in some of the key materials looked at the 450-480 nm region was the one of greatest interest!

Two solutions were found to this problem. The first was to find and use materials with better solubility or solvents better at dissolving materials. As discussed in Section 3.2 chlorinated solvents were found to be very good at dissolving iridium complexes, however they photodegraded so quickly under laser excitation as to be of essentially no use. Some specific iridium complexes with better solubility were available, but generally not with the spectral or material properties that were desirable. The best outcome for finding better materials was to utilise dendrimers, highly functionalised macromolecules with solubilised surface groups (Chapter 5) to enable high concentration solutions to be prepared. The second solution to the Raman problem was to shift the excitation wavelength to higher energy. While

375 nm (750 nm) was as high as one could go, higher pump energy was deliverable with 380 nm (760 nm) and this was instead used. This shift enabled Raman free luminescence detection down to 460 nm and satisfied the problem. Unfortunately this excitation shift also introduced a new problem that limited its usage, namely the final UV pass filter (F4), which was an almost perfect blocker of 800 nm, was less than perfect at 760 nm – hence much more spatial filtering was required with the aperture to ensure that the gate light did not overwhelm the upconverted signal of interest – this inevitably meant that some of the upconverted light was lost due to harsh spatial filtering. Unfortunately no better UV pass filter could be found; hence 380 nm excitation was the best solution to give access to higher energy detection, but at the cost of poorer signal to noise.

3.5.3 *The Instrument Response*

It is required when fitting femtosecond luminescence dynamics to have an instrument response function (IRF) that indicates what the exact temporal response of the upconversion setup is. This is needed when fitting exponential functions to the kinetics as reconvolution is used as part of the fit, as discussed in more detail in Section 3.7. It is therefore required to have some process that shows an instantaneous response, something shorter than the system can measure, so the limit of the system itself can be recorded. Commensurate with Section 3.5.2 above Raman signals are a useful tool to do this, being instantaneous virtual emission events. The IRF of the upconversion setup varied both with excitation wavelength and due to changes in the setup (e.g. changing or moving lenses or crystals) thus no one IRF was used throughout. The IRF was recorded by filling a sample cell solely with a solvent (water or THF were commonly used) and then detecting on the peak of the strongest longest Raman shift (for 400 nm excitation this was typically 450-460 nm). The upconversion setup was left to scan across the Raman signal and then the scans were averaged into a final dataset. The final dataset was typically essentially Gaussian in its form, therefore to produce a smooth IRF for fitting generally a Gaussian was fitted and used as the IRF. IRFs for 380 and 400 nm excitation (the only two wavelengths used in almost all work

presented here) were found to be between 220 and 280 fs (FWHM) for 400 nm excitation and 310 fs for 380 nm excitation. The most commonly used IRFs at 400 and 380 nm excitation are plotted in Figure 3.6.

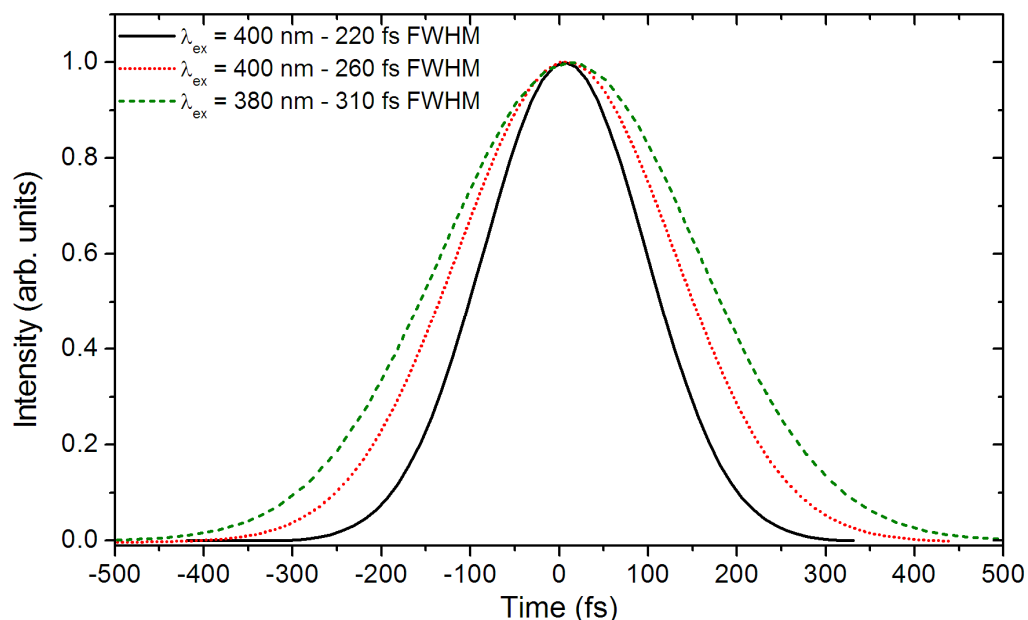


Figure 3.6. Instrument response functions (IRFs) for the upconversion setup. The black line is the IRF with 400 nm excitation and a 220 fs full-width half maximum (FWHM). The red dotted line is also 400 nm excitation and shows a FWHM of 260 fs. The green dashed line is with 380 nm excitation and has a FWHM of 310 fs.

3.5.4 Detecting Luminescence from Phosphorescent Complexes

Upconversion spectroscopy has been in frequent use for the last 15 years or so. For a technique that relies on generating the sum frequency of luminescence with a gating pulse it can, on highly fluorescent materials, give very good signal to noise (S/N) – typically 500 to 1 on a strongly emissive laser dye solution, hence frequently on such materials only one scan of the delay line is required to record kinetics suitable for fitting. Highly fluorescent materials have high radiative rates (typically on the order of 10^8 s^{-1}) and so there is a substantial photon flux for upconversion. In phosphorescent materials such as transition metal complexes as discussed in Chapter 2, however, radiative rates are a few orders of magnitude

lower (typically 10^5 or 10^6 s⁻¹) and hence the photon flux is also much lower. This poses something of a challenge for measuring femtosecond luminescence dynamics as the S/N is now significantly reduced (in two ways, as will be discussed later). Consequently the difficulty of measuring femtosecond luminescence dynamics in phosphorescent transition metal complexes means it is a relatively recent activity, with the first report in ruthenium based materials being made only in the year 2000,¹² followed by only a few other reports in the years since.^{13, 14}

To acquire kinetic traces suitable for fitting of the iridium complexes used in this work a number of steps were taken, briefly detailed here. To begin with the required detection wavelength was first selected and then the upconversion setup was optimised (luminescence overlap with the gate on the SFG crystal, SFG crystal angle and setting of delay line time-zero) with a strongly emitting laser dye solution. Once optimised the sample cell with the iridium complex under investigation was swapped into the setup – this was acceptable as both the laser dye cell and the iridium cell were identical, thus no timing or alignment issues should occur. To achieve any visibility on the kinetics 10 seconds PMT integration per data point was required for phosphorescent materials, hence for an 80 point dataset around 15 minutes was required per scan. To avoid large amounts of wasted time an initial “setting scan” was completed consisting of two or three scans to give visibility of the main features of the decay (to check that the decay was indeed visible and covered by the correct delay line step sizing, typically 12.5 or 25 fs per step for femtosecond processes). The control software would remember the previously used step sizes for the next scan and could be instructed to rescan the same region for as many times as required. Once everything was as required the upconversion setup was then left to scan the set region continuously, typically overnight, and although times varied dependent on the material and detection wavelength looked at, total scanning time for a single wavelength would be in the region of 12 to 24 hours. Weak high energy states or excitation/observation combinations that have inherently poor S/N may require significant scanning – the longest ever completed was ~ 100 hours for a single

wavelength. The requirement for such long integration periods is obvious when one looks at a typical single scan (10 seconds integration per point), as shown in Figure 3.7.

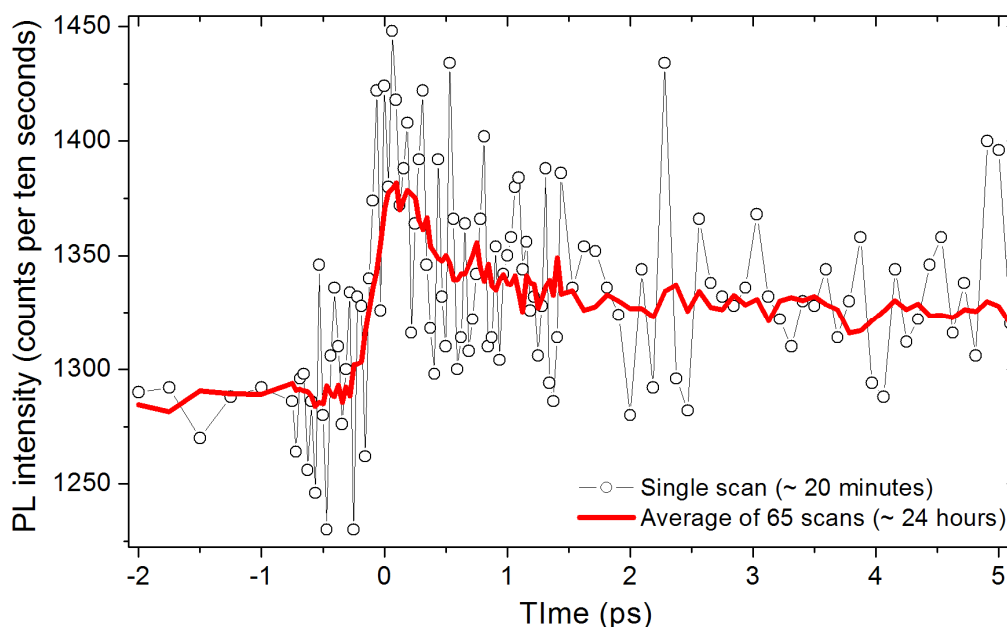


Figure 3.7. Typical upconversion data for a phosphorescent complex – Ir(dbfliq)₂acac studied in Chapter 7 on the peak of its phosphorescence spectrum, 660 nm. All scans were with 10 seconds integration per point. A single scan is shown as the connected open circles and black line and would take around 20 minutes to record, while the final average of 65 scans (taking around 24 hours) is shown as a thick solid red line.

Not only is the low radiative rate of the emitting materials as discussed above the reason for such low S/N, but it is also the high background level that is inherent in microsecond emitters such as transition metal complexes. The excitation of these samples occurs at 80 MHz, therefore there is an excitation pulse every 12 ns incident upon a material with a lifetime of $\sim 1 \mu\text{s}$. Upon excitation the sample is thus going to emit a significant fraction of its light *after* the first 12 ns, but at that point another excitation pulse will have arrived at the sample, generating more light – it is thus a consequence that all emission from the sample longer than 12 ns is upconverted as a constant background, with the kinetics $< 12 \text{ ns}$ on top of it. It is therefore clear that the lower radiative rates of transition metal complexes makes it doubly difficult to detect ultrafast luminescence, not only reducing the

signal in the S/N but adding to the noise as well. With 400 nm excitation counts on the PMT for a typical sample consisted of ~ 10 counts per second of 800 nm gate, 100 cps of background luminescence (dependent on wavelength and sample) and 0-6 cps of dark noise. The upconverted signal would typically account for ~ 10 cps.

After significant scanning the complete set of scans are averaged together and the final decay is background corrected and then ready to fit, as detailed in Section 3.7.

3.5.5 *Detection Wavelength Intensity Correction*

The efficiency of upconverted emission at each detection wavelength is not the same, and instead the upconversion setup shows a spectral dependence of its recorded emission intensity. If one is interested only in the kinetics at each wavelength, not how strong they are, then that is not a problem, but if the aim is to reconstruct spectra of transient species then clearly the emission strength at, for example 500 nm, needs to be related to the emission strength at another wavelength in order to reproduce a valid reconstructed spectrum. This requires calibration of the upconversion efficiency and the results were used in spectral reconstruction of multiple singlet states in Chapter 7.

Calibration was achieved with a Bentham IL7 150 W xenon lamp, producing light across the 200-1000 nm region. The output from the lamp was focussed onto the SFG crystal along with the 800 nm gate and the upconverted intensity was recorded in the 420-610 nm window in 10 nm steps. It was then a simple exercise to divide the recorded intensities by the lamp spectrum to produce a correction factor, as shown below in Figure 3.8, with the lamp spectrum recorded with an Ocean Optics “USB2000” fibre spectrometer.

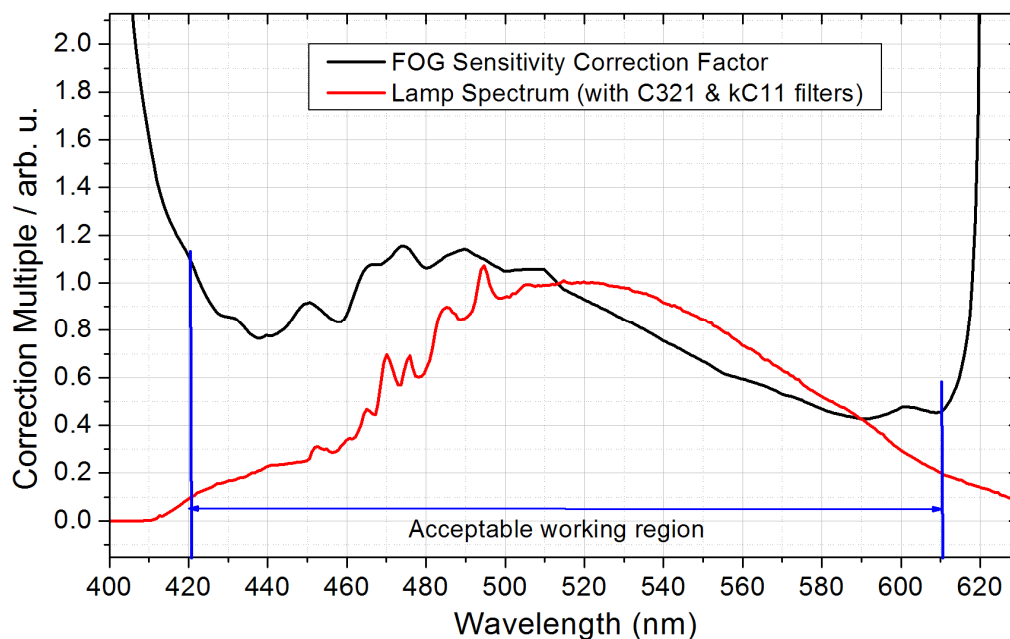


Figure 3.8. Recorded upconversion wavelength sensitivity dependence (black line) and the lamp spectrum (red line) used to deduce it.

3.6 Transient Absorption Spectroscopy

Transient absorption (TA) pump probe spectroscopy is a technique to look at the excited state dynamics of a material, capitalising on ultrafast light sources to pump the material into its excited state, and then delivering a second beam some variable amount of time later to probe the formed state, monitoring how much of the probe is absorbed in the sample. Varying the delay between the pump and the probe and/or the probe wavelength can therefore give temporal and spectral dynamics of excited state processes. This is graphically demonstrated in Figure 3.9.

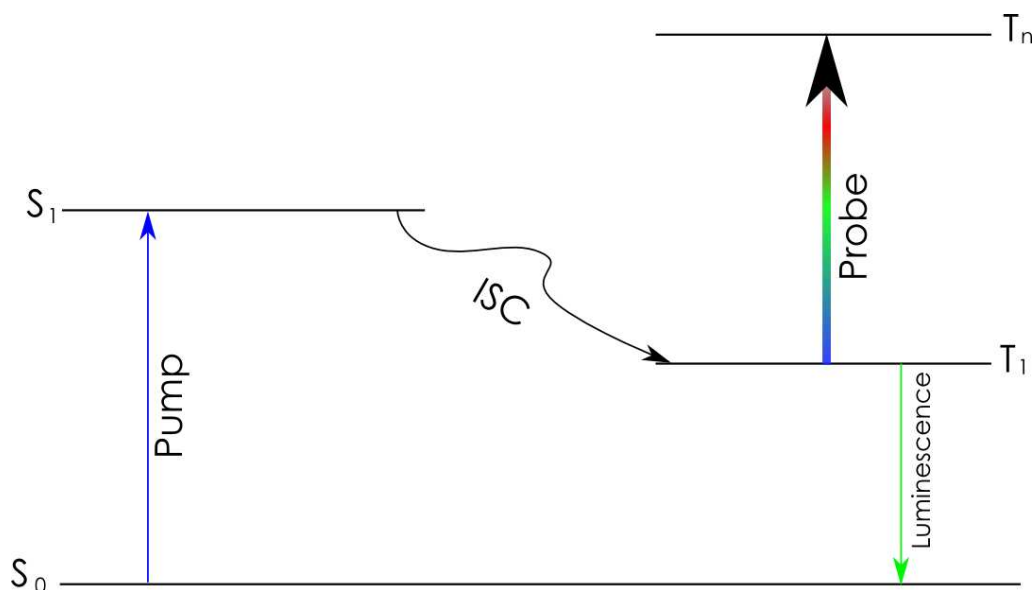


Figure 3.9. Jablonski schematic showing the processes probed by transient absorption pump probe spectroscopy in transition metal complexes. Initial pumping of the $S_0 \rightarrow S_1$ transition is followed by fast intersystem crossing (ISC) to the triplet manifold. The variable wavelength probe is then observing excited state absorption processes to higher lying states.

Generation of variable probe wavelengths is achieved with the TOPAS-White amplified source as discussed in Section 3.4.3, giving < 50 fs FWHM, 5 kHz pulses in the 500-1000 nm window with pulse energies in the nJ range.

A TA setup was built for this work and is shown in Figure 3.10.

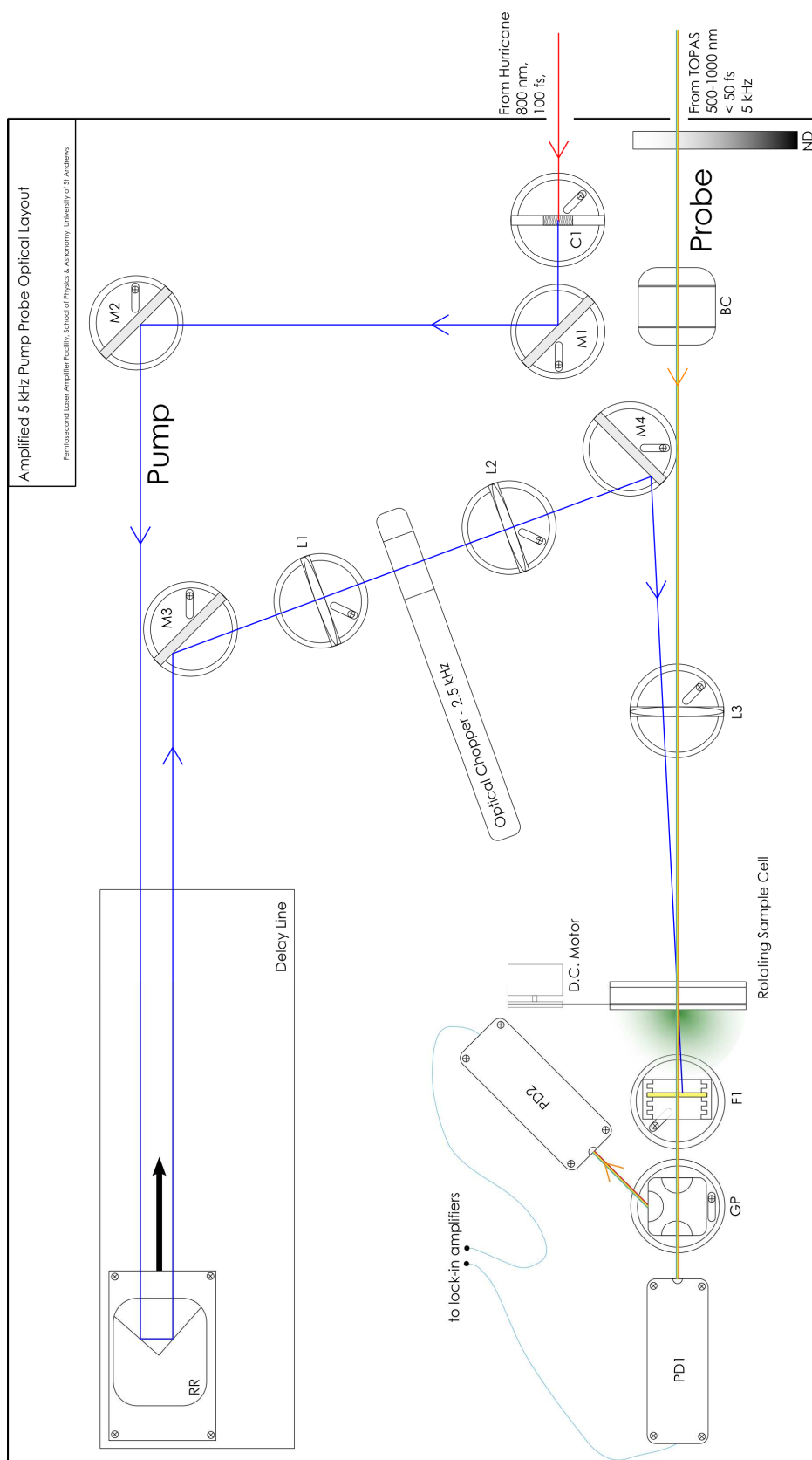


Figure 3.10. Optical layout of the transient absorption pump probe setup that was built and used in this work. The configuration is discussed in the text.

Described briefly, the output of the TOPAS-White includes the variable wavelength probe and residual amplified 800 nm (100 fs FWHM, 5 kHz, 3 μ J per pulse). The 800 nm is frequency doubled in a type 1 Beta Barium Borate (BBO) non-linear crystal (1 mm thickness) (C1) before being steered (M1,2) onto a retroreflector (RR) of a computer controlled delay line – moving the delay line has the effect of shortening the pump path, i.e. making the probe arrive increasingly later than the pump. After returning from the retroreflector the beam is moved (M3) onto a 20 cm lens (L1) to focus the pump onto an optical chopper. This chopper is synchronised with the amplified laser pulses and chops at exactly half the repetition rate, 2.5 kHz, i.e. one pulse is rejected and one pulse is passed. After the chopper the beam is recollimated (L2) and moved onto the sample line with a steering mirror (M4), passing through a 12.5 cm lens (L3) to gently focus onto the rotating sample cell – tight focussing is not required due to the amplified nature of the pulses, as such tight focussing would generally induce white light continuum generation on the sample cell windows. After the sample the 400 nm pump is required to be filtered out to avoid detection, and this is achieved with a yellow Schott glass filter (F1, 5 mm thickness), absorbing everything below 450 nm.

The probe is taken as generated from the TOPAS-White amplifier and firstly passed through a neutral density wheel (ND) to ensure that the same intensity of probe light was being used at each probe wavelength (the intensity output from the TOPAS varied across its operating region). The light was then passed through a Berek's compensator (BC) to enable control of its polarisation. The probe's journey is relatively simple, and it just passes through the same sample focussing lens (L3) onto the rotating sample cell. Spatial overlap of the pump and probe beams on the sample is achieved by moving the pump with the steering mirror (M4), visually aided by a pair of binoculars. After the sample the probe is split by a glan polariser (GP) into two orthogonal components that are detected using two silicon photodiodes (PD1,2). The probe wavelength is changed by computer control of the TOPAS-White, with a program provided to type in the desired

wavelength and automatic movement of the TOPAS crystals and optics would be made. Checking of the actual probe wavelength generated compared to what was requested was achieved with an Ocean Optics “USB2000” fibre spectrometer.

Detection is achieved by the lock-in technique. Three Stanford Research Systems lock-in amplifiers (models SR830) are used to record the signals from the TA setup – one reference and two measurement. This is shown diagrammatically in Figure 3.11, with a description given below.

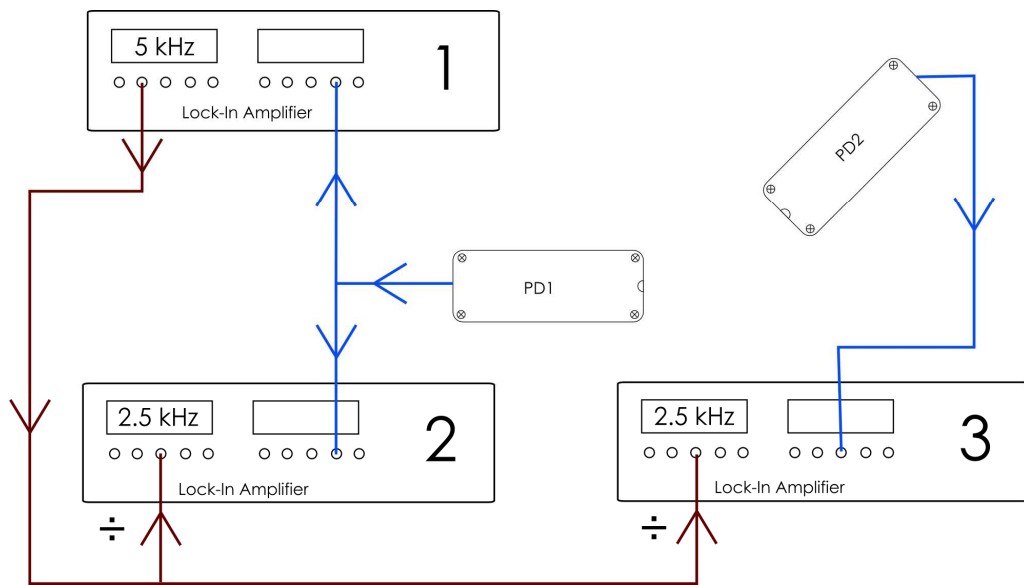


Figure 3.11. Schematic of the configuration of the detectors and lock-in amplifiers. Two photodiodes (PD 1 & 2) give output, with one split between lock-in 1 (detecting at 5 kHz, the reference) and 2 (detecting 2.5 kHz, the signal). Lock-in 3 also operates at 2.5 kHz and just records the output from the second photodiode. The signals of the photodiodes on lock-ins 2 and 3 are divided by the 5 kHz reference value from lock-in 1 to aid in the recorded signal to noise.

Two detection frequencies are used to aid in the stability of the measurements. The probe beam is operated at a 5 kHz repetition rate, while the pump is synchronously chopped at 2.5 kHz. A 5 kHz TTL triggering output is provided by the Hurricane and this fed into a homebuilt frequency divider to give a 2.5 kHz output. The lock-in amplifiers are configured as follows: the signal taken from one of the photodiodes (it does not matter which one) is split, with one signal going to lock-in 1 at 5 kHz (triggered from the Hurricane TTL) to be used as a

reference and the other signal going to lock-in 2 for measurement at 2.5 kHz (triggered from the frequency divided Hurricane TTL). The signal from the second photodiode is wired directly to lock-in 3 for measurement at 2.5 kHz. Variation in the probe intensity is a known difficulty in these measurements – generation of such a wide variation of possible ultrafast probe wavelengths does not lend itself to extremely stable intensity of the pulse trains. Consequently the recorded 5 kHz signal from lock-in 1 is used as a reference – the signal being fed to lock-ins 2 and 3 and the measured 2.5 kHz values divided by the 5 kHz value, hence removing the probe variability from the noise. Integration on all lock-in amplifiers was 30 ms, with a sensitivity of 50 μV on the detection lock-ins and 500 μV on the reference. The probe energy was kept constant at ~ 3 nJ per pulse to ensure that any comparison of transient absorption signals across different probe wavelengths was fairly made.

TA measurements consist of simply reading the signal of the probe recorded on the photodiode and moving the delay line to record how that probe signal changes with time. Control of the delay line and recoding of the photodiode intensities is made with a home-built labview program. Setting of the delay line scanning parameters was made on an initial scan – finding the regions of interest to scan with small step sizes and those that can be scanned with large steps, and then the labview software was instructed to scan this region and save the data. Typically between two and five scans were needed to give acceptable signal to noise, though this varied with probe wavelength as the TOPAS was more stable at some wavelengths than at others.

Polarisation measurements were automatically made with the setup as both signals parallel and perpendicular to the pump beam polarisation are automatically made, with the Berek's compensator set each time to give a balanced signal from both photodiodes. Magic angle (54.7°) kinetics can quickly be reconstructed when both the parallel (I_{para}) and perpendicular (I_{perp}) kinetics are recorded by use of equation 3.4:

$$I(MA) = I_{para} + 2I_{perp} \quad [3.4]$$

The instrument response function (IRF) of the TA setup was recorded by using a BBO crystal to give sum frequency generation (SFG) between the 400 nm pump and a 550 nm probe beam. Scanning the delay line would move the pump through the probe beam and give UV SFG when the two beams are temporally overlapped. The TA IRF was found to be 185 fs FWHM and is shown in Figure 3.12.

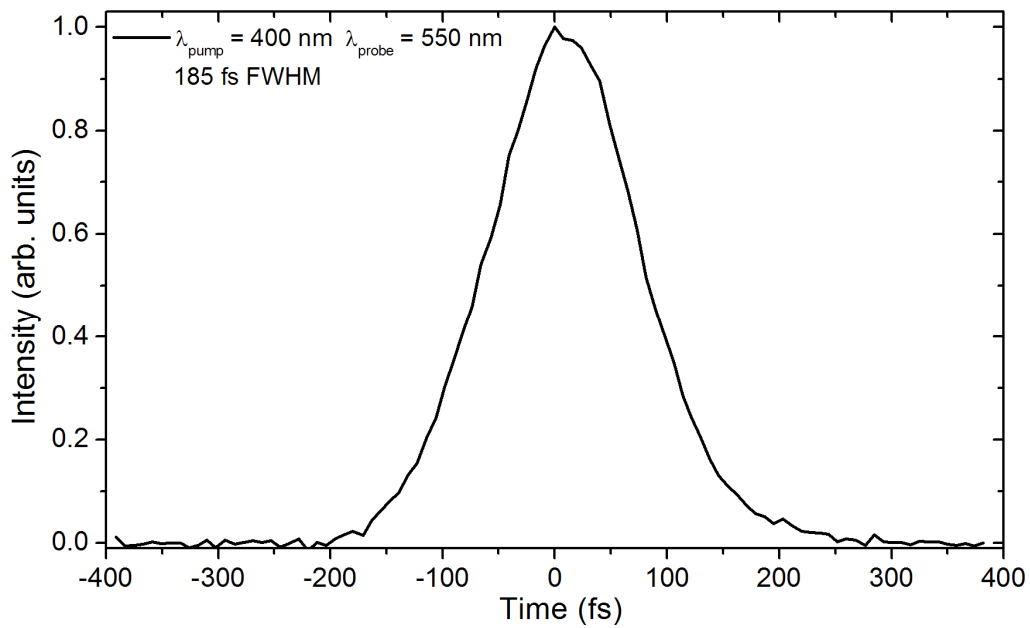


Figure 3.12. Instrument response function (185 fs FWHM) of the transient absorption setup, recorded by the generation of sum-frequency light between the 400 nm pump and 550 nm probe in a BBO crystal.

The specifications of the pump and probe beams used in the TA setup are shown in Table 3.2.

Transient Absorption Setup:

Excitation Wavelength:	400 nm
Repetition Rate:	5 kHz
Excitation Pulse Width (FWHM):	100 fs
Probe Wavelength Range:	500-1000 nm
Probe Pulse Width (FWHM):	< 50 fs

Table 3.2. Specification of pump and probe spectral parameters for the homebuilt transient absorption setup used in this work.

3.7 Temporal Fitting

The experimental techniques discussed in Sections 3.5 and 3.6 give time based kinetics and fitting decay functions to these kinetics was required to identify the photophysical processes and record their time constants.

Relaxation processes in organic luminescent materials generally show exponential decay like behaviour⁸ of the form:

$$I(t) = I_0 e^{\frac{-t}{\tau}} \quad [3.5]$$

where I is the total intensity, I_0 is a pre-exponential multiplication factor, t is the time and τ is the time constant (otherwise known as the natural lifetime). If I_0 is positive then the function leads to population reduction with time (a decay) and if I_0 is negative then population building is the result (a rise-time).

For a multiexponential decay the total intensity generally becomes a sum of individual decay components:

$$I(t) = \sum_n I_n e^{\frac{-t}{\tau_n}} \quad [3.6]$$

Fitting procedures for the ultrafast luminescence kinetics involved taking the final averaged and background corrected dataset and then fitting a single or sum of exponential functions to it. The trial exponential function is mathematically convolved with the instrument response function and then compared against the actual dataset, with chi-square values used as a test of goodness of fit. Iteration of the variables takes place until the lowest chi-squared value can be obtained and these are the values that are then reported as the best-fit parameters. Care is taken with decays of time constant less than 200 fs (i.e. less than the FWHM of the IRF) to ensure that the fitted value is valid. With a 260 fs FWHM IRF the absolute lower limit on the decay time constant that can be fitted with a perfect signal to noise is $\sim \tau = 40$ fs. Shown below in Figure 3.13 is a comparison of 40, 60 and 80 fs time constants convolved with the IRF, indicating that the two become almost identical at ~ 40 fs.

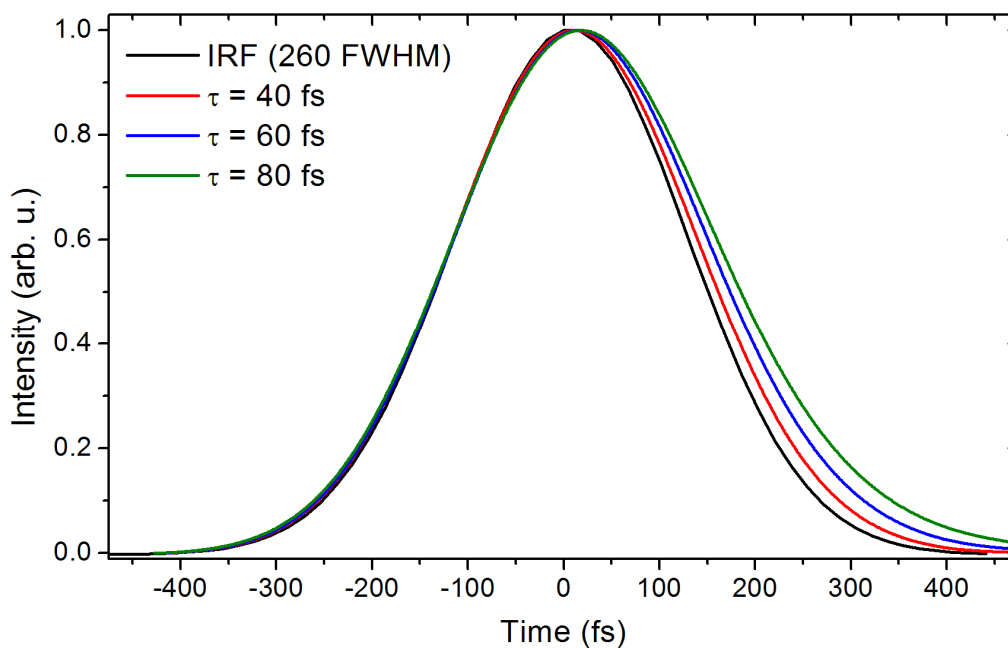


Figure 3.13. The comparison of simulated decay kinetics against an instrument response function of 260 fs (FWHM), black line. A decay of 40 fs (red line) is very similar to the IRF, while 60 fs (blue line) and 80 fs (green line) are both measurably longer.

Iterative reconvolution analysis on datasets was completed with a number of software packages including the DAS6 program by Horiba and Globals WE developed at the Laboratory for Fluorescence Dynamics at the University of Illinois at Urbana-Champaign.¹⁵

3.8 References

- [1] S.C. Lo, E.B. Namdas, P.L. Burn, and I.D.W. Samuel, *Macromolecules*, 2003. **36**(26): p. 9721-9730.
- [2] W. Holzer, A. Penzkofer, and T. Tsuboi, *Chemical Physics*, 2005. **308**(1-2): p. 93-102.
- [3] D.E. Spence, P.N. Kean, and W. Sibbett, *Optics Letters*, 1991. **16**(1): p. 42-44.
- [4] Spectra-Physics, *Mai Tai User's Manual*. 2001.
- [5] P.G. Kryukov, *Quantum Electronics*, 2001. **31**(2): p. 95-119.
- [6] J.V. Rudd, G. Korn, S. Kane, J. Squier, G. Mourou, and P. Bado, *Optics Letters*, 1993. **18**(23): p. 2044-2046.
- [7] Light-Conversion, *TOPAS-White User's Manual*. 2004.
- [8] J.R. Lakowicz, *Principles of Fluorescence Spectroscopy*. 2nd ed. 1999: Kluwer Academic.
- [9] J. Shah, *IEEE Journal of Quantum Electronics*, 1988. **24**(2): p. 276-288.
- [10] F. Zernike and J.E. Midwinter, *Applied Nonlinear Optics*. 1973, New York: Wiley.
- [11] Y.R. Shen, *The Principles of Nonlinear Optics*. 1984, New York: Wiley.
- [12] A.C. Bhasikuttan, M. Suzuki, S. Nakashima, and T. Okada, *Journal of the American Chemical Society*, 2002. **124**(28): p. 8398-8405.
- [13] A. Cannizzo, F. van Mourik, W. Gawelda, G. Zgrablic, C. Bressler, and M. Chergui, *Angewandte Chemie-International Edition*, 2006. **45**(19): p. 3174-3176.
- [14] W. Gawelda, A. Cannizzo, V.T. Pham, F. vanMourik, C. Bressler, and M. Chergui, *Journal of the American Chemical Society*, 2007. **129**(26): p. 8199-8206.
- [15] J.M. Beechem and E. Gratton, *Proceedings of SPIE*, 1988. **909**: p. 77-81.

4

Femtosecond Dynamics of Ir(ppy)₃

That is the artist's job: take mineral rock from dark silent earth, transform it into shining light-reflecting form from sky.

Philip K. Dick, *The Man in the High Castle*, 1962

4.1 Introduction

This chapter presents a series of ultrafast luminescence and transient absorption measurements that were completed on the prototypical iridium complex Ir(ppy)₃. Intersystem crossing in this material was found to be very fast (< 100 fs) and femtosecond and picosecond decay processes were observed and assigned to relaxation amongst the electronic substates of the lowest ³MLCT state.

In Section 4.2 I summarise the basic photophysical and electronic properties of the material under investigation and discuss the relevant background literature on Ir(ppy)₃. In Section 4.3 I introduce the principal ultrafast luminescence measurements that were completed and in Section 4.4 I show the transient absorption results. In section 4.5 I discuss all the presented results and provide interpretation of the data leading to the generation of a schematic of the likely ultrafast processes occurring in this material. Finally in Section 4.6 I provide the conclusions that are drawn in this piece of work.

4.2 Photophysical Properties of Ir(ppy)₃

The study of ultrafast dynamics in transition metal complexes can give new insights into how they behave and help aid in the understanding of how their photophysical properties can be controlled. As has already been discussed in Chapter 2, the ultrafast photophysics of transition metal complexes – primarily ruthenium and iron centred complexes – have been studied in some detail.¹⁻⁸ It was surprising therefore that the ultrafast processes in iridium complexes, with their advantageous light emitting properties for use in organic light emitting diodes (OLEDs), had not received a great deal of attention, with only a solitary transient absorption measurement having been reported.⁹

The prototypical iridium complex *fac*-tris(2-phenylpyridine) iridium(III) [Ir(ppy)₃], its structure shown in Figure 4.1a, is a good candidate material to begin understanding the ultrafast dynamics of these complexes. The relatively simple chemical structure of the ligands, a connected phenyl and pyridine moiety, coupled with its wide usage in high efficiency green OLED devices¹⁰ gives rise to a strong interest in the properties of this material.

The chemical structure of the Ir(ppy)₃ molecule itself is found to exist in two isomers, facial and meridional, as shown in Figure 4.1. The material is found to be more thermodynamically stable in the facial isomer which is fortuitous as the meridional isomer has very low luminescence efficiency and is thus of less use in photophysical studies and devices.¹¹ The facial isomer is exclusively the one that is used in these studies. The molecule itself forms a three-fold symmetry three bladed “propeller shape”.¹²

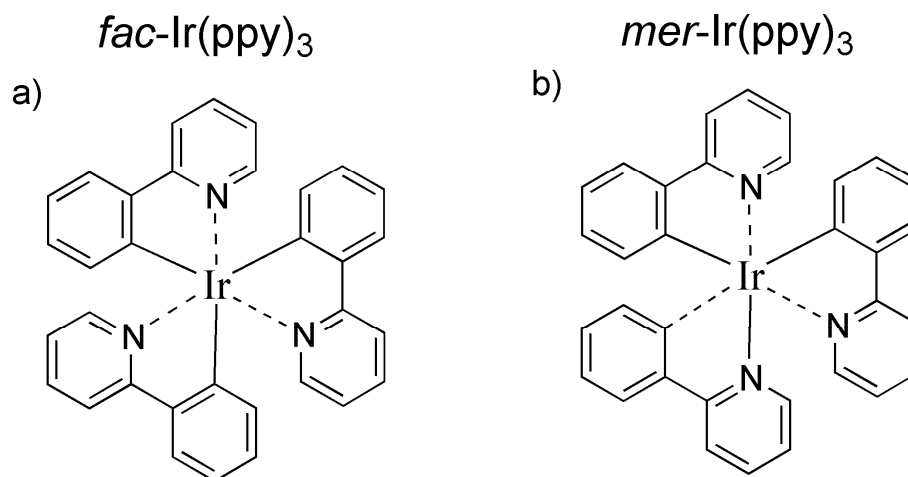


Figure 4.1. Chemical structure of the two isomers of Ir(ppy)₃. **a)** facial tris(2-phenylpyridine) iridium(III) and **b)** meridional tris(2-phenylpyridine) iridium(III). The complex used exclusively in these studies is the facial isomer due to greater thermodynamic stability and high luminescence efficiency.

The steady state optical absorption and photoluminescence (PL) spectra of Ir(ppy)₃ dissolved in tetrahydrofuran are shown in Figure 4.2. The absorption spectrum shows features typical of a transition metal complex, with strong ultraviolet absorption features (< 300 nm) assigned to π - π^* ligand centred transitions, a weaker absorption band (325-450 nm) representing singlet metal-ligand charge transfer (¹MLCT) transitions and finally the weakest absorption feature (475-525 nm) is assigned as a triplet ³MLCT transition, weak because it is only partially spin-allowed.¹²⁻¹⁶ The PL spectrum of Ir(ppy)₃ shows a relatively featureless emission band lacking any significant vibronic structure with a PL peak at 505 nm.

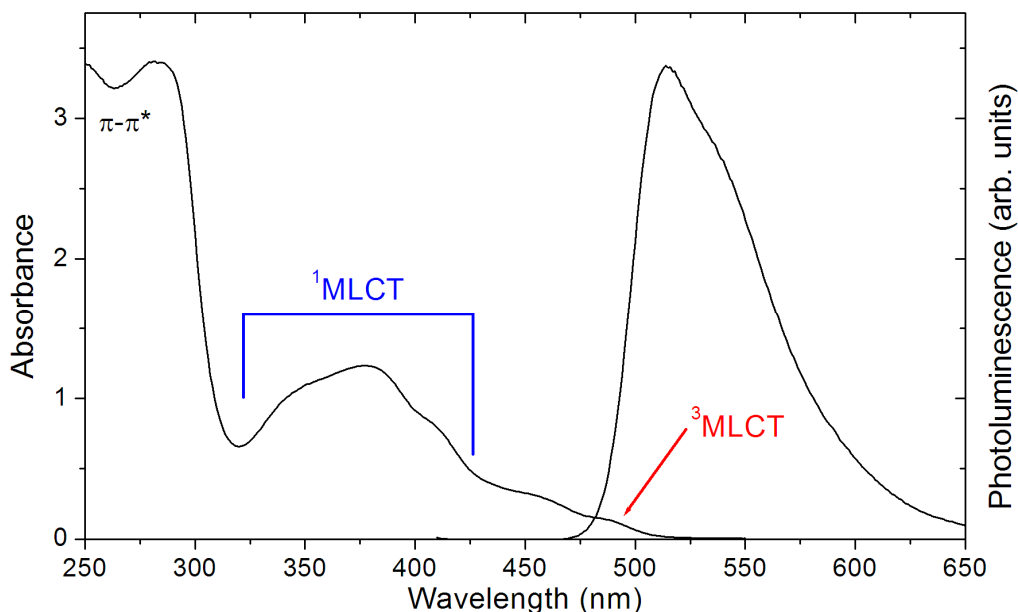


Figure 4.2. Absorption and photoluminescence spectra of Ir(ppy)₃ in THF at room temperature. Traditional assignments of the main absorption features are shown, from high to low energy: 250-300 nm π - π^* ligand centred transitions, 325-425 nm singlet metal-ligand charge transfer transitions and finally 475-525 nm partially spin-allowed triplet metal-ligand charge transfer transitions.

Upon formation of the metal-ligand charge transfer state with optical excitation a 5d orbital iridium electron moves out onto one of the ligands of the molecule. Theoretical calculations show that the lowest unoccupied molecular orbital in Ir(ppy)₃ tends to localise on one ligand¹⁷ and this is consistent with experimental results found in a similar ruthenium complex.⁵ Time-dependent density functional theory (TDDFT) calculations on Ir(ppy)₃¹⁷⁻²⁰ show a very high density of excited electronic states exist (70 states in the first eV). These calculations provide a more nuanced attribution of electronic states than are nominally experimentally assigned, where definitive π - π^* , ¹MLCT or ³MCLT transitions are generally specified as in Figure 4.2 above. The TDDFT work indicates that instead the MLCT states are in fact best represented by a mixture of states of different character. In Ir(ppy)₃ the MLCT states are calculated to have only around 50% iridium 5d electron character with the other half coming from π atomic orbitals on the ligand, best viewed as the highest occupied molecular orbital consisting of mixed 5d and π character while the lowest unoccupied molecular orbital is purely π^* .^{17, 18} Efficient phosphorescence is facilitated due to

strong spin-mixing between allowed singlet and formally forbidden triplet MLCT states. In Ir(ppy)₃ calculations indicate that the lowest ³MLCT state comprises 20-50% ¹MLCT character and 50-80% triplet character.¹⁹

Upon photoexcitation of the ¹MLCT state the population quickly moves to the lowest ³MLCT state before emitting on the microsecond timescale with a natural lifetime of 1.1 μs.²¹ The photoluminescence quantum yield (PLQY) of the material in dilute solution has been found to be very high, 90%,²¹ hence the natural lifetime is also very close to the radiative lifetime. In studies by Finkinzellar and Yersin the electronic structure of the lowest ³MLCT state was observed with very high spectral resolution at low temperatures and high magnetic fields to observe the zero-field splitting (ZFS) that occurs due to spin-orbit coupling (SOC).²² They observed that the lowest ³MLCT state in Ir(ppy)₃ was in fact made up of three electronic substates, III, II and I – with state II sitting 70 cm⁻¹ below III and state I 13.5 cm⁻¹ below II, as shown in Figure 4.3. The top substate, III, was found to be responsible for observed room temperature phosphorescence, with the radiative rates of the lower and lowest states being ten and one hundred times slower respectively.

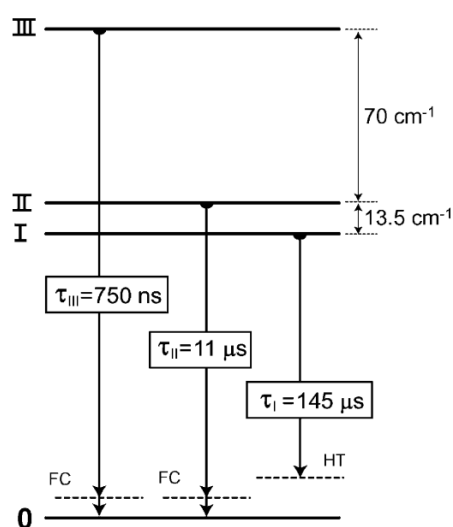


Figure 4.3. Schematic of the three electronic substates of the lowest ³MLCT state, indicating energy spacing (in wavenumbers) and radiative rates of the three substates. Figure from reference 22. Reproduced with permission of the rights holder.

As already mentioned, previous ultrafast studies of Ir(ppy)₃ have been scarce, however one study by Tang and co-workers⁹ observed that the formation of the ³MLCT state was completed within or with around a time constant of 100 fs, i.e. this is an upper limit on the time constant of intersystem crossing (ISC).

4.3 Ultrafast Luminescence Dynamics

In the work conducted ultrafast luminescence dynamics were recorded in Ir(ppy)₃ using the upconversion technique as described in Chapter 3, with all measurements performed at room temperature. Solutions of the material were prepared by dissolving 0.25 mg/ml of the material in toluene and 1 mg/ml in THF, the higher concentration in THF being accounted for by the higher solubility of Ir(ppy)₃ in this solvent. Absorption and PL spectra of both solutions are shown in Figure 4.4. All measurements were done in fully aerated solutions, i.e. not degassed to remove oxygen. Presence of oxygen in iridium complex solutions leads to quenching due to triplet-triplet energy transfer between the ³MLCT state of the excited iridium complex and the ground state of oxygen.²¹ Quenching leads to a reduction in the excited state lifetime from 1.1 μs to a few nanoseconds, however this is of no consequence for the time ranges that are being studied here as oxygen quenching occurs on much longer timescales. In addition to the practical problems introduced by degassing solutions (rotating sample cells are filled by hand and would be difficult to manage in an oxygen free environment) the long-lived luminescence quenching is of benefit to the measurements being performed as it actually helps increase the signal to noise on the time-scales of interest. Excitation of the solutions is performed with an 80 MHz pump, i.e. a pulse arrives to excite the sample every 12 ns. In the upconversion technique all luminescence that is longer than 12 ns is upconverted at all times (i.e. when the next excitation pulse arrives luminescence derived from the previous one is still being produced) and hence appears as a constant background on all ultrafast dynamics. The less long lived background (with its associated noise) there is the better the S/N of the femtosecond dynamics being measured will be.

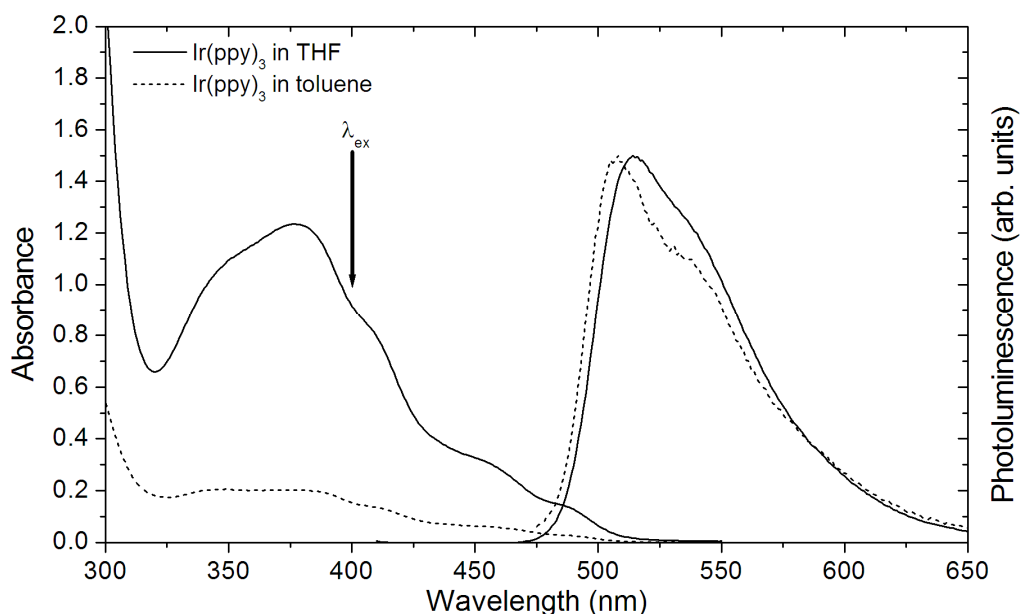


Figure 4.4. Steady state absorption and normalised photoluminescence spectra ($\lambda_{ex} = 400$ nm, arrow) of Ir(ppy)₃ solutions in tetrahydrofuran (solid lines) and toluene (dashed lines) on samples used in ultrafast experiments.

Variation of the solution concentration of the samples being studied was also checked, with no difference in observed ultrafast kinetics found for toluene from 0.25 mg/ml down to 0.04 mg/ml, as shown in Figure 4.5 for ultrafast luminescence measured at 480 nm – the lower signal to noise on the low concentration sample is as a result of the difficulty in measuring such low levels of light, demonstrating why higher concentrations were generally preferred.

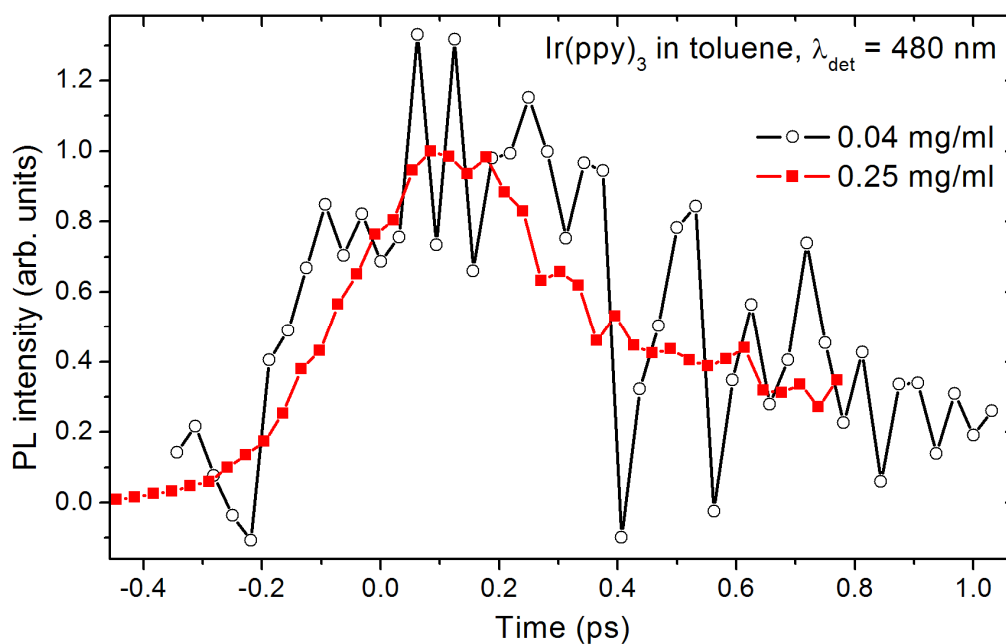


Figure 4.5. Comparison of ultrafast luminescence detected at 480 nm of Ir(ppy)₃ in toluene for two different concentrations, 0.04 mg/ml (open circles and black line) and 0.25 mg/ml (closed squares and red line). The two are, within noise limits, showing the same kinetic profile, indicating that the concentration in this range has no effect on ultrafast dynamics.

With 400 nm excitation the ¹MLCT manifold is accessed and decay dynamics are observed at a number of wavelengths. Luminescence kinetics at 500 nm (peak of the steady state PL spectrum) and at 560 nm (red-side of PL) in THF are shown in Figure 4.6. Firstly it is noted that dynamics at 500 and 560 nm are the same, indicating that the same emitting species is responsible for ultrafast luminescence at both wavelengths, therefore kinetics in this window can be averaged to give better signal to noise. Fitting to an average of all kinetics recorded in the 500-560 nm window is shown as a solid line when convolved with the instrument response function (IRF) (dotted line). Three characteristic features can be seen in the kinetics, there is an initial fast decay component which fits best to a time constant of 230 fs (with a pre-exponential factor of 49%, i.e. 49% of total amplitude), a slower decay component of 3 ps (24%) and finally substantially slower nanosecond emission (27%).

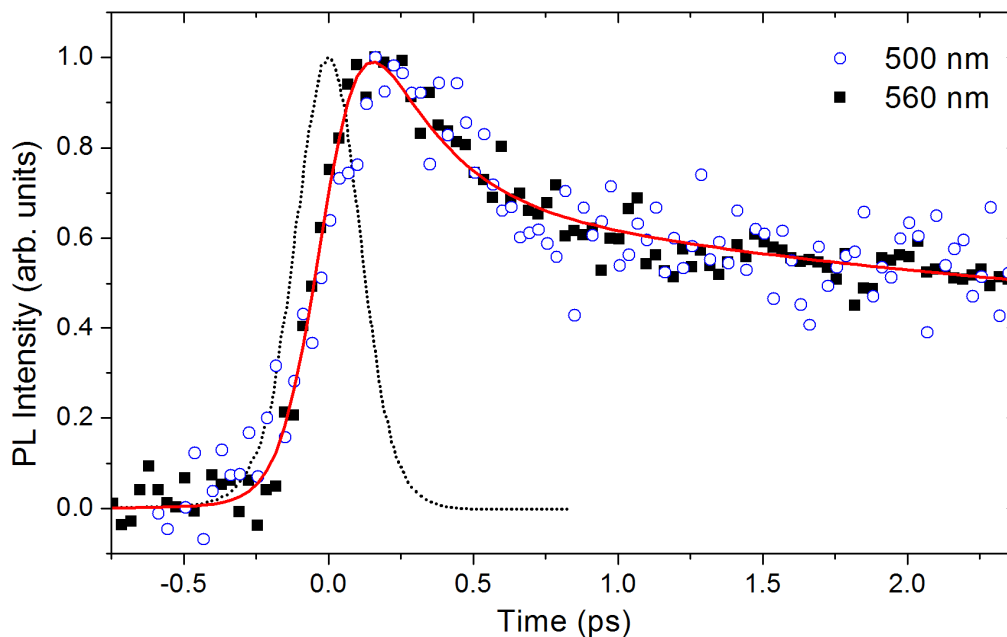


Figure 4.6. Ultrafast luminescence kinetics of Ir(ppy)₃ dissolved in THF at $\lambda_{\text{ex}} = 400$ nm. Dynamics are recorded at 500 nm (open circles) and 560 nm (closed squares). The dotted line indicates the instrument response function, IRF, (222 fs FWHM). The solid line indicates the best-fit of 230 fs (49% of total amplitude), 3 ps (24%) and a nanosecond offset (27%) when convolved with the IRF.

When one observes dynamics at slightly higher energy, however, the situation is substantially changed. Shown in Figure 4.7 are the luminescence kinetics observed at 490 nm, and it can be seen that the fast decay has become faster and now accounts for a larger amount of the overall decay amplitude. Fitting to the 490 nm data (solid line) indicates that the fast component is now 150 fs and represents 88% of the overall decay and a slower 3 ps component which exists with 12% of the total amplitude.

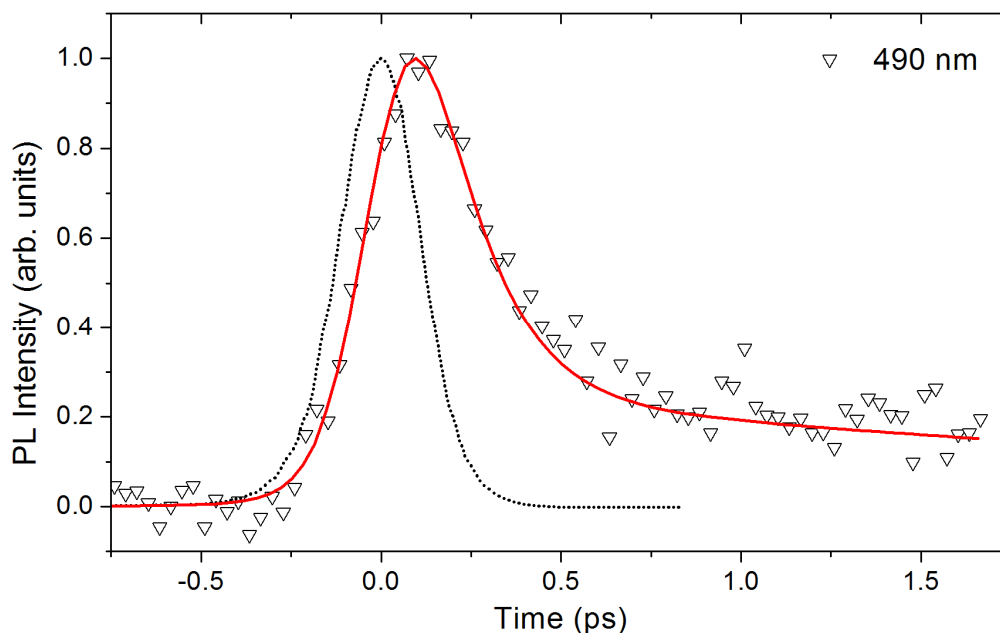


Figure 4.7. Ultrafast luminescence kinetics of Ir(ppy)₃ dissolved in THF at $\lambda_{\text{ex}} = 400$ nm. The dynamics are recorded at 490 nm with the IRF shown as a dotted line (222 fs FWHM). The solid line indicates the best-fit decay of 150 fs (88%) and 3 ps (12%) when convolved with the IRF.

To identify if the solvent had any effect on the ultrafast dynamics toluene was used and the same wavelengths were recorded. Comparison between the toluene and THF data in the window corresponding to steady state emission (500-560 nm) in the first 3 ps is shown in Figure 4.8 and out to 18 ps in Figure 4.9. It can be seen that no differences in dynamics are observed, with the data from both solvents fitting to the same decay time constants and amplitudes.

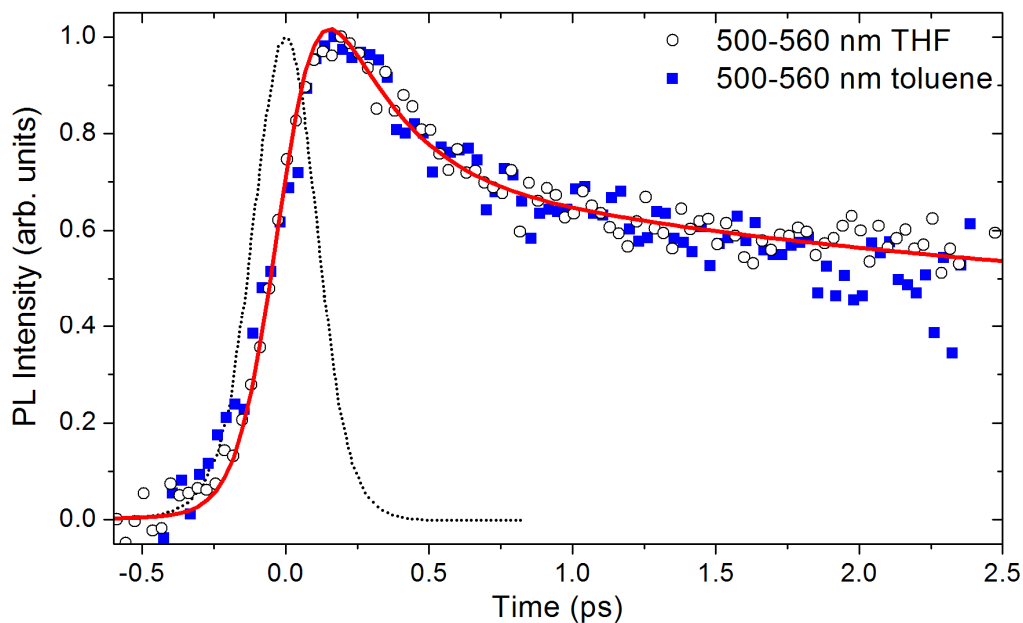


Figure 4.8. Averaged luminescence kinetics of Ir(ppy)₃ at $\lambda_{\text{ex}} = 400$ nm in the 500-560 nm detection window (data averaged from 500, 520 and 560 nm scans) representing steady state PL. The open circles show data for Ir(ppy)₃ dissolved in THF and the closed squares show it dissolved in toluene. The dotted line represents the IRF (222 fs FWHM). The solid line indicates the best-fit when the overall averaged data is convolved with the IRF and has decay time constants of 230 fs, 3 ps and a nanosecond offset as previously quoted.

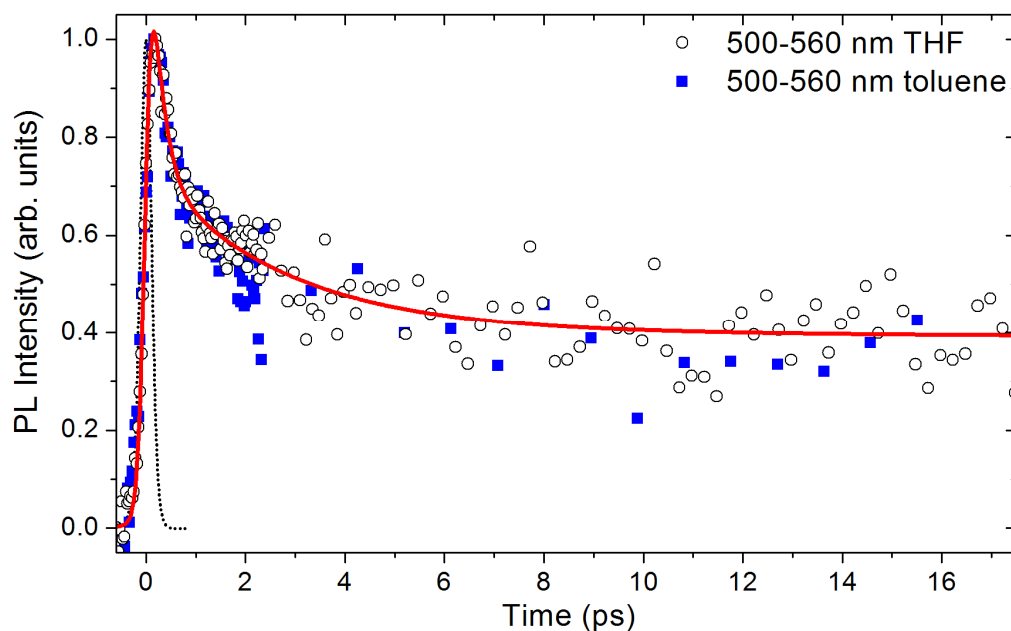


Figure 4.9. Averaged luminescence kinetics of Ir(ppy)₃ at $\lambda_{\text{ex}} = 400$ nm in the 500-560 nm detection window, as detailed above in Figure 4.8, out to 18 ps.

Comparison of dynamics in toluene and THF was also made at higher detection energy, 490 nm in THF and 480 nm in toluene, with the kinetics and fit shown in Figure 4.10. No discernable difference can be made between the two sets of decays.

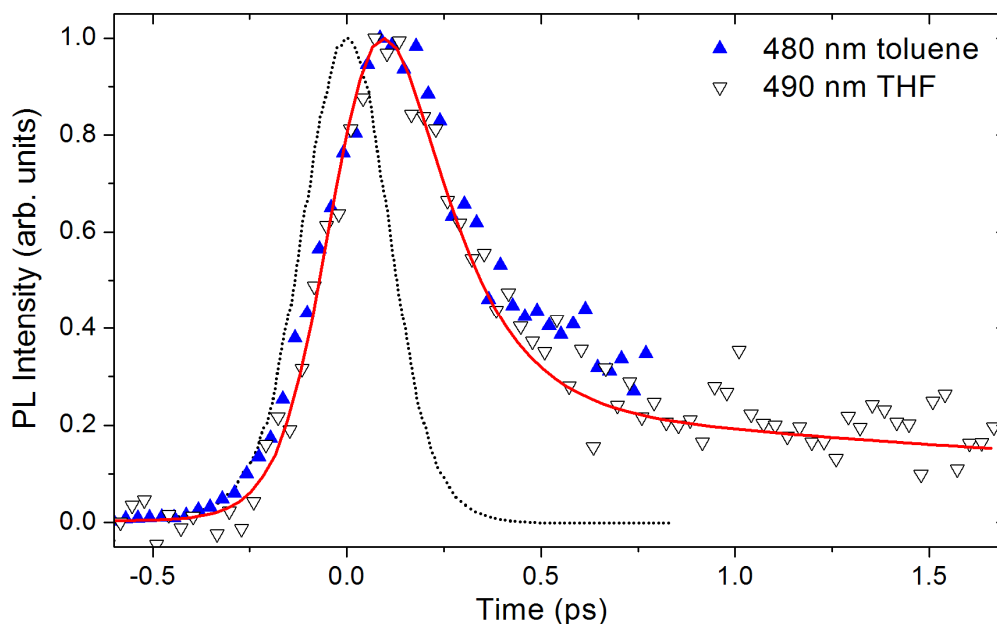


Figure 4.10. Comparison of luminescence kinetics on the high energy side of the steady state PL of Ir(ppy)₃ dissolved in toluene (open triangles) and THF (closed triangles). The solid line is the best-fit when the data is convolved with the IRF and represents decays of 150 fs (88%) and 3 ps (12%).

4.4 Ultrafast Transient Absorption Dynamics

Pump probe techniques can give detailed insight into the excited state dynamics occurring in optically active materials. It was of strong interest to complement the information derived from luminescence studies on a material with transient absorption measurements to enable better assignment of the observed dynamics. The pump probe transient absorption setup used in this work has been described in detail in Chapter 3. The rotating sample cell used in these studies was the same

as used in the luminescence work and enabled direct comparisons between the two techniques to be made on the same solution.

Ultrafast transient absorption dynamics of Ir(ppy)₃ dissolved in THF were of interest to see if any of the same features that are observed in the ultrafast luminescence work appear in the TA measurements. Pumping at 400 nm and probing at a range of wavelengths in the 500-950 nm region always produced a positive signal, i.e. an increase in the sample's absorption, indicative of excited state absorption (ESA) from the excited state to higher optically active states.

Observed TA signals in the first 2 ps with 500 and 900 nm probe wavelengths are shown in Figure 4.11, the absolute absorbance values are deduced by noting the absolute signal values at 5 kHz and 2.5 kHz on the lock-in amplifiers. The transient state at both probe wavelengths is found to form within the instrument limit of the setup (i.e. < 100 fs) and there are then no further dynamics recorded. A stable transient state thus appears to form and TA signals at longer times indicate that it is then completely stable, with dynamics (or rather lack of them) out to 40 ps shown in Figure 4.12.

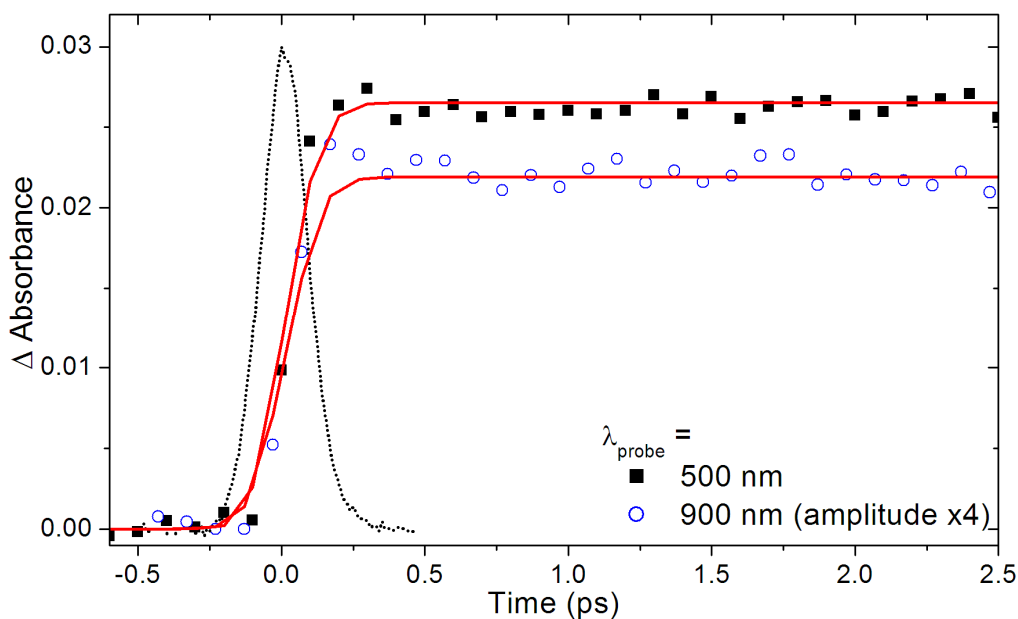


Figure 4.11. Ultrafast transient absorption kinetics of Ir(ppy)₃ dissolved in THF recorded with $\lambda_{\text{pump}} = 400$ nm and probe wavelengths of 500 nm (closed squares) and 900 nm (open circles). The 900 nm probe data amplitudes have been multiplied by 4 to enable easier plotting. The instrument response function of the TA setup is shown as a dotted line, 185 fs FWHM.

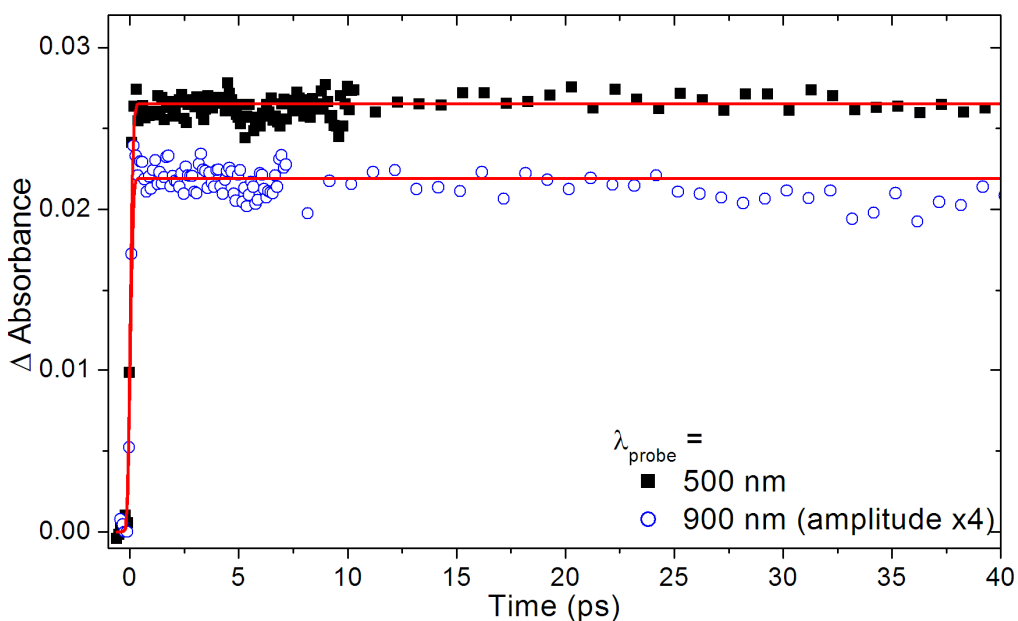


Figure 4.12. Transient absorption kinetics out to 40 ps recorded with $\lambda_{\text{pump}} = 400$ nm and probe wavelengths of 500 nm (closed squares) and 900 nm (open circles). The 900 nm probe data amplitudes have been multiplied by 4 to enable easier plotting. The transient state is found to be unchanging out to at least 40 ps.

While there is no change observed between 500 and 900 nm probe wavelengths there is a notable difference in the signal strength, with 500 nm signal levels being approximately 4 times higher than at 900 nm. Recording the signal levels with different probe wavelengths can therefore enable the excited state absorption spectrum to be reconstructed, and this is shown in Figure 4.13.

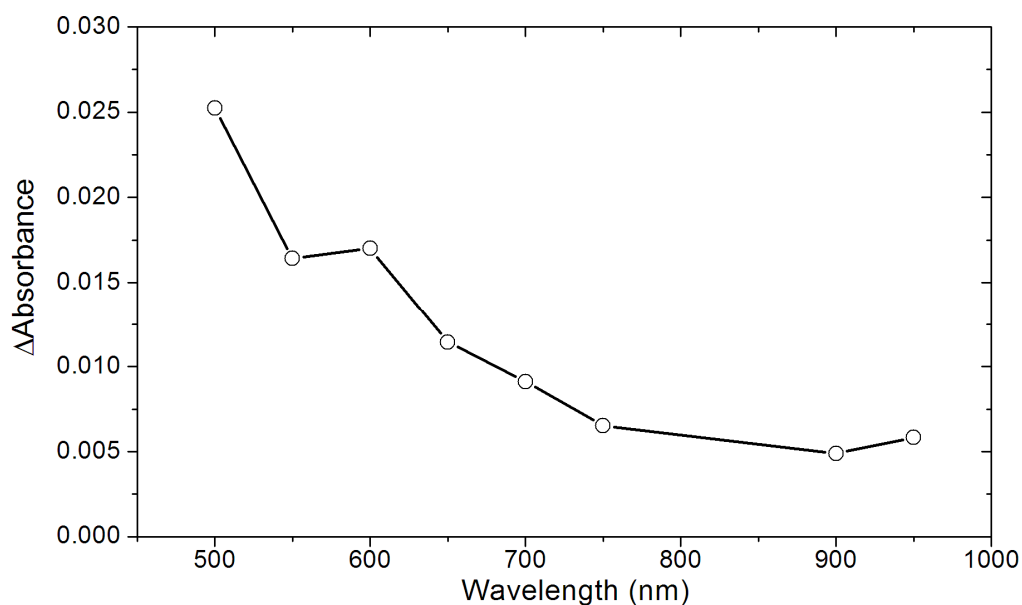


Figure 4.13. Reconstructed excited state absorption spectrum of Ir(ppy)₃ in THF with $\lambda_{\text{pump}} = 400$ nm. The probe wavelengths are varied and the signal intensity at each is recorded to enable reconstruction of the ESA spectrum.

It can be seen that the ESA spectrum shows a strong absorption at short wavelengths. This reduces consistently as one moves out to longer wavelengths before leaving a long tail of residual ESA out in the infra-red.

4.5 Interpretation of Ultrafast Dynamics

The recorded measurements in femtosecond luminescence and transient absorption experiments give a significant amount of information on the processes occurring in the first moments after excitation in Ir(ppy)₃.

With 400 nm excitation the absorption spectrum (Figure 4.4) indicates that the ¹MLCT state is directly accessed. The intersystem crossing event from the singlet to triplet MLCT states is anticipated to be fast.⁹ Instantaneous formation of the transient signal is found and then no change is observed on a long timescale, far longer than the ISC time would be. Two possible interpretations of this data can be presented, either the ISC event occurs inside the instrument response time of the transient absorption setup, (i.e. less than 100 fs), or there is significant overlap of the singlet and triplet MLCT excited state absorption spectra, i.e. no dynamics would be visible in the TA signal of the ISC event.

Comparison with luminescence data provides a stark contrast, where two distinct decay processes are clearly visible, one fast (femtosecond) and one slower (picosecond). The immediate question to pose, therefore, is what these processes represent. The first thing to note is the instantaneous rise of the luminescence detected at all wavelengths, indicating that there is no process slower than ~100 fs feeding the emitting states – this is especially telling on the 500-560 nm steady state PL window which consists of ³MLCT emission, and so indicates that the ISC event will be fast. The similarity of the 230 fs decay across the steady state PL spectrum, with the same decay found at both 500 and 560 nm in two different solvents (Figure 4.6, Figure 4.8 and Figure 4.9) indicate that this decay must represent some process within the ³MLCT manifold. One might anticipate that there could be some residual imprint of ¹MLCT emission on the peak of the PL spectrum, but it would seem highly unlikely that there could be any ¹MLCT emission at over 0.5 eV from the nearest singlet state at 560 nm – since with fast ISC with a time constant of < 100 fs the population of the ¹MLCT state would be depleted before emission with a time constant of 230 fs could occur. ¹MLCT

emission even on the peak of the PL can be ruled out when the amplitudes of the femtosecond decay are taken into account – being identical to those at 560 nm, i.e. if there was additional emission it should show up as enhanced amplitude of femtosecond decay. It is therefore concluded that the 230 fs decay represents some process occurring within the ³MCLT manifold.

The slower picosecond process is consistently found to have a time constant of 3 ps and can be assigned to vibrational cooling of the hot ³MLCT state to the surrounding solvent molecules. No dynamics on the picosecond timescale are observed in the transient absorption data, giving further support to this process being vibrational rather than electronic. The observed 3 ps time constant was found to be independent of whether toluene or THF was used, indicating that the cooling time is insensitive to the local solvent structure due to polarity. Picosecond time constants similar to the value reported here that were assigned to vibrational cooling to the surrounding solvent molecules have been found in ruthenium complexes.^{3, 23, 24}

The femtosecond and picosecond processes have therefore been identified as representing dissipation events within the ³MCLT manifold. Closer inspection of the nature of the lowest ³MLCT state, consisting of three closely spaced electronic substates due to zero-field splitting of the lowest ³MCLT state, can allow assignment of the decay features. As previously mentioned in Section 4.2, the energy spacing between the substates have been reported²² and it was found that only the top substate is responsible for observed emission, the two lower substates being essentially storage wells for the excited state population. With a general cascade model, as shown in Figure 4.14, the relaxation to the lowest ³MLCT state proceeds in an orderly manner. The population will initially access the ¹MLCT state and then proceed across to the triplet manifold before, it is presumed, initially filling the top electronic substate, III.

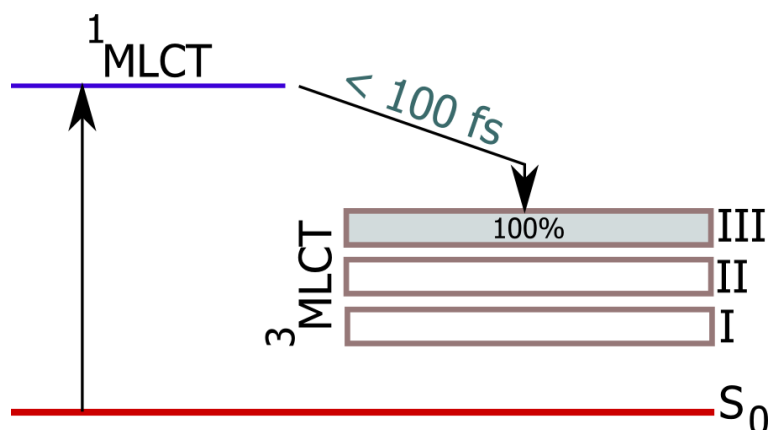


Figure 4.14. Cascade energy level schematic showing that following excitation to the ¹MLCT state, rapid (< 100 fs) population of the top substate (III) of the lowest ³MLCT state will occur.

The excited state population is not going to remain completely in this substate with two lower and energetically close substates, II & I, available to fill. Therefore the population will redistribute to these two lower substates. If one were to apply Boltzmann statistics (equation 4.1) to the outlined situation at room temperature and given the known energy spacing between the states the population should redistribute with 26% in the top substate, 36% in substate II and 38% in the bottom substate, as shown on the right-hand side of Figure 4.15.

$$F(E) = e^{-\left(\frac{E}{k_B T}\right)} \quad [4.1]$$

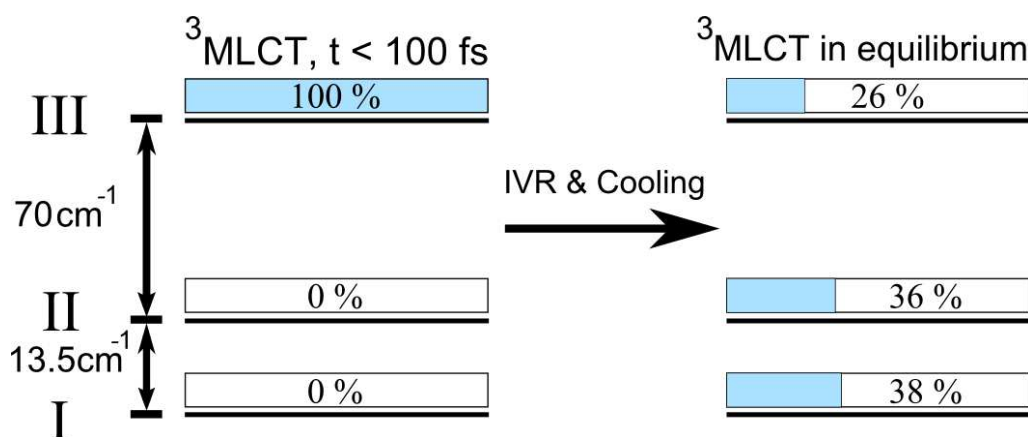


Figure 4.15. Population redistribution from the initially fully populated top substate, III, will occur. The final populations in each substate would be expected to follow a Boltzmann distribution, with values as indicated on the right-hand side. Intramolecular vibrational redistribution (IVR) and vibrational cooling on a 230 fs and 3 ps timescale respectively will facilitate this population redistribution.

There should be, therefore, population redistribution, reducing substate III from 100% to only 26%. The examination of substate dynamics by Finkinzellar and Yersin in a closely related iridium complex,²⁵ again at low temperatures and high magnetic fields, helps to confirm the processes observed here. In the reported case relaxation from the top substate to the lower two was found to be instrument limited in their experiments (less than 50 ns) at 1.5 K and relaxation amongst the lower two states was found to be on the microsecond timescale and was achieved by spin-lattice relaxations, again at 1.5 K.

The dynamics observed here, specifically the self-similarity of dynamics across the steady state PL region, give good evidence that the 230 fs and 3 ps decay processes are likely to be responsible for the relaxation from the top electronic substate to the lower two. Both processes contribute to the dissipation of excess energy, dissipation that is required to enable filling of the lower two substates, as indicated in Figure 4.15.

It is intriguing that the 230 fs decay process is as slow as it is – the ISC process (< 100 fs) indicates that very fast relaxation is possible in this complex. The 230 fs time constant has also been observed in other iridium complexes, as detailed in

Chapters 5, 6 and 7, and hence appears to be something of a characteristic relaxation time from within the lowest ³MLCT state. When one views the amount of energy that is required to be dissipated, however, the explanation becomes clear. Relaxation from substate III to I is only a small amount of energy, ~ 100 cm⁻¹. Femtosecond dissipation of energy can occur by intramolecular vibrational redistribution (IVR),^{26, 27} the process of redistribution of energy from high to low frequency vibrational modes within a molecule. When such a small amount of energy is required to be dissipated the dissipation will be forced to occur through IVR amongst lower frequency vibrational modes, and will thus be slower, explaining the measured 230 fs time constant. It is not possible to separate the contributions that the 230 fs and the 3 ps processes will make to facilitate the population redistribution amongst the three electronic substates other than to say that it is likely that both will contribute.

Long lived phosphorescence in Ir(ppy)₃ therefore occurs from the top substate, III, of the lowest ³MLCT state, with the population of this state being fed and maintained via thermal activation from the two lower, essentially non-emissive substates.

Ultrafast luminescence detected at higher energy, above the steady state PL peak, Figure 4.10, provides insight into fast relaxation to the lowest ³MLCT state. It is not clear what specific state this relaxation is from, it is possible, given the high density of electronic states in iridium complexes¹⁹ that this decay is from a higher ³MLCT state, or it could be just from a vibrationally hot lowest ³MLCT state. The specific decay parameters – a faster femtosecond time constant of 150 fs and a larger amplitude of femtosecond decay of 88% – indicate that more dissipation is occurring by IVR. The IVR process itself appears to be able to occur faster because the relaxation is higher in energy (and thus is dissipating more energy). Detection wavelengths on this higher energy side are ~ 1100 cm⁻¹ above the steady state PL peak, hence there is a greater amount of energy that is to be dissipated, and hence can proceed by IVR amongst higher frequency vibrational modes. If the IVR is able to proceed faster then it can dissipate more energy, and

hence less energy is required to be dissipated by slower picosecond vibrational cooling to the surrounding solvent molecules, explaining the lower amplitude of picosecond decay. Unfortunately luminescence dynamics at even higher detection energies (< 480 nm), which would provide direct luminescence information on ISC and singlet MLCT processes, were not accessible in Ir(ppy)₃ owing to strong Raman signals from the solvents that were produced due to the relatively poor solubility of the complex therefore meaning that the solvent scattered more excitation light. Direct luminescence detection at higher energy would have enabled a more surefooted assignment of what the 150 fs faster component that was detected at 480/490 nm represents, and this was a subject that was pursued further with more suitable materials in Chapters 6 and 7.

A general schematic outlining the main observed processes in Ir(ppy)₃ can be produced as shown, in Figure 4.16.

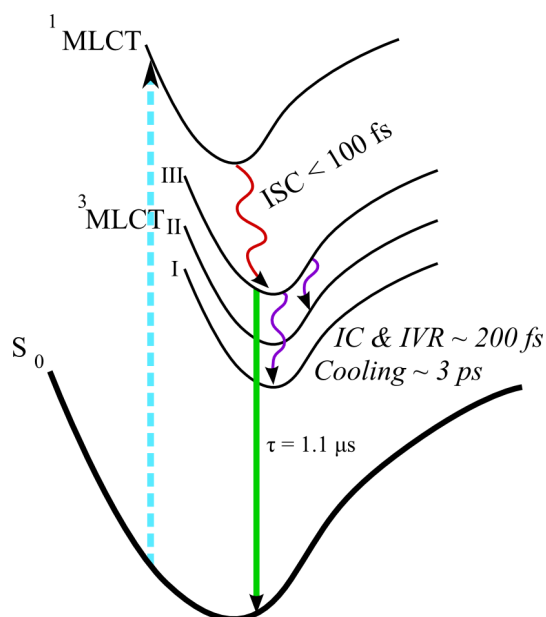


Figure 4.16. General schematic outlining the main observed ultrafast processes occurring in Ir(ppy)₃. After initial excitation into the ¹MCLT state the population undergoes intersystem crossing to the ³MLCT manifold in less than 100 fs. After it reaches the ³MLCT state population redistribution amongst the three electronic substates will occur by IVR on a 200 fs timescale and by vibrational cooling to the surrounding solvent molecules on a 3 ps timescale. Finally sitting in the ³MCLT state the population will radiatively decay to the electronic ground state with a lifetime of 1.1 μs.

4.6 Conclusions

The results presented here have allowed the earliest moments of the relaxation in the triplet MLCT manifold in an iridium complex to be understood for the first time. The material Ir(ppy)₃ was chosen as it is a prototypical example of an iridium complex and is widely used in OLED devices as an emissive organic material.

After initial excitation to the ¹MLCT state intersystem crossing to populate the ³MLCT manifold is found to be very fast (< 100 fs) and is a timescale that is consistent with a high degree of mixing between the singlet and triplet MLCT states facilitating fast crossing. After the population moves into the triplet manifold it rapidly relaxes to the lowest ³MLCT state. This was observed by looking at the luminescence on the high energy side of the steady state PL peak, with the vast majority of the decay (88%) there represented by a time constant of ~ 150 fs, embodying intramolecular vibrational redistribution (IVR) from high to lower frequency vibrational modes to facilitate dissipation of excess energy.

Once in the lowest ³MLCT state the population still shows ultrafast dynamics with two decays present, one of 230 fs (49%) and one of 3 ps (12%) with a further nanosecond offset (27%). These dynamics – both their time constants and amplitudes – are consistent out onto the red-side of the steady state PL spectrum indicating that they are a manifestation of a process from the lowest ³MLCT state and not from any higher energy state. Assignment of these dynamics takes into account the fact that the lowest ³MLCT state is actually comprised of three closely spaced electronic substates due to zero-field splitting – separated from top to bottom substate by ~ 100 cm⁻¹. Initially the top substate will be fully populated and the lower two substates will be empty. The 230 fs process thus represents dissipation of excess energy by IVR and the 3 ps process vibrational cooling to the surrounding solvent molecules, both enabling relaxation of the population from the top substate to the lower two.

4.7 References

- [1] N. Damrauer, G. Cerullo, A. Yeh, T. Boussie, C. Shank, and J. McCusker, *Science*, 1997. **275**(5296): p. 54-57.
- [2] N.H. Damrauer and J.K. McCusker, *Journal of Physical Chemistry A*, 1999. **103**(42): p. 8440-8446.
- [3] A.C. Bhasikuttan, M. Suzuki, S. Nakashima, and T. Okada, *Journal of the American Chemical Society*, 2002. **124**(28): p. 8398-8405.
- [4] A. Cannizzo, F. van Mourik, W. Gawelda, G. Zgrabcic, C. Bressler, and M. Chergui, *Angewandte Chemie-International Edition*, 2006. **45**(19): p. 3174-3176.
- [5] A.T. Yeh, C.V. Shank, and J.K. McCusker, *Science*, 2000. **289**(5481): p. 935-938.
- [6] W. Gawelda, A. Cannizzo, V.T. Pham, F. vanMourik, C. Bressler, and M. Chergui, *Journal of the American Chemical Society*, 2007. **129**(26): p. 8199-8206.
- [7] A. Cannizzo, A.M. Blanco-Rodriguez, A. El Nahhas, J. Sebera, S. Zalis, J.A. Vlcek, and M. Chergui, *Journal of the American Chemical Society*, 2008. **130**(28): p. 8967-8974.
- [8] C. Bressler, C. Milne, V.T. Pham, A. ElNahhas, R.M. van der Veen, W. Gawelda, S. Johnson, P. Beaud, D. Grolimund, M. Kaiser, C.N. Borca, G. Ingold, R. Abela, and M. Chergui, *Science*, 2009. **323**(5913): p. 489-492.
- [9] K.C. Tang, K.L. Liu, and I.C. Chen, *Chemical Physics Letters*, 2004. **386**(4-6): p. 437-441.
- [10] C. Adachi, M.A. Baldo, M.E. Thompson, and S.R. Forrest, *Journal of Applied Physics*, 2001. **90**(10): p. 5048-5051.
- [11] A.B. Tamayo, B.D. Alleyne, P.I. Djurovich, S. Lamansky, I. Tsyba, N.N. Ho, R. Bau, and M.E. Thompson, *Journal of the American Chemical Society*, 2003. **125**(24): p. 7377--7387.
- [12] M.G. Colombo, T.C. Brunold, T. Riedener, H.U. Gudel, M. Fortsch, and H.B. Burgi, *Inorganic Chemistry*, 1994. **33**(3): p. 545-550.

- [13] S. Sprouse, K.A. King, P.J. Spellane, and R.J. Watts, *Journal of the American Chemical Society*, 1984. **106**(22): p. 6647--6653.
- [14] K. King, P. Spellane, and R. Watts, *Journal of the American Chemical Society*, 1985. **107**(5): p. 1431-1432.
- [15] K. Ichimura, T. Kobayashi, K.A. King, and R.J. Watts, *Journal of Physical Chemistry*, 1987. **91**(24): p. 6104-6106.
- [16] G.A. Crosby, *Accounts of Chemical Research*, 1975. **8**(7): p. 231-238.
- [17] E. Jansson, B. Minaev, S. Schrader, and H. Agren, *Chemical Physics*, 2007. **333**(2-3): p. 157-167.
- [18] P.J. Hay, *Journal of Physical Chemistry A*, 2002. **106**(8): p. 1634-1641.
- [19] K. Nozaki, *Journal of the Chinese Chemical Society*, 2006. **53**(1): p. 101-112.
- [20] T. Matsushita, T. Asada, and S. Koseki, *Journal of Physical Chemistry C*, 2007. **111**(18): p. 6897-6903.
- [21] W. Holzer, A. Penzkofer, and T. Tsuboi, *Chemical Physics*, 2005. **308**(1-2): p. 93-102.
- [22] W.J. Finkenzeller and H. Yersin, *Chemical Physics Letters*, 2003. **377**(3-4): p. 299-305.
- [23] B. Dietzek, D. Akimov, W. Kiefer, S. Rau, J. Popp, and M. Schmitt, *Laser Physics Letters*, 2007. **4**(2): p. 121-125.
- [24] S.A. McFarland, F.S. Lee, K.A.W.Y. Cheng, F.L. Cozens, and N.P. Schepp, *Journal of the American Chemical Society*, 2005. **127**(19): p. 7065-7070.
- [25] W.J. Finkenzeller, M.E. Thompson, and H. Yersin, *Chemical Physics Letters*, 2007. **444**(4-6): p. 273-279.
- [26] D.J. Nesbitt and R.W. Field, *Journal of Physical Chemistry*, 1996. **100**(31): p. 12735-12756.
- [27] T. Elsaesser and W. Kaiser, *Annual Review of Physical Chemistry*, 1991. **42**: p. 83-107.

5

Effect of Structural Modification on Ultrafast Dynamics in Iridium Dendrimers

There are two kinds of light – the glow that illuminates, and the glare that obscures.

James Thurber, *Lanterns and Lances*, 1963

5.1 Introduction

This chapter presents ultrafast luminescence measurements of iridium complexes and dendrimers. Emission from the prototypical iridium complex Ir(ppy)₃ was compared with two Ir(ppy)₃ cored dendrimers, and the differences in the relaxation rates were monitored. Dissipation of excess energy is facilitated by intramolecular vibrational redistribution (IVR), and it was found that the larger dendrimers helped to dissipate more vibrational energy inside the molecule, leaving less to be dissipated to the surrounding solvent molecules.

In Section 5.2 I give a conceptual introduction to the dendrimer class of materials that have been utilised in these studies. In Section 5.3 I give a brief outline of the mechanism of intramolecular vibrational redistribution and discuss the traditional techniques that are used to observe it. In Section 5.4 I present and discuss the basic photophysical properties of the dendrimers that have been used, and this then follows with the presentation of the main ultrafast luminescence measurements in Section 5.5 and pump-probe measurements in Section 5.6. In Section 5.7 I give interpretation and provide discussion on the ultrafast dynamics

and the implications for the study of IVR in large polyatomic molecules. Finally in Section 5.8 I provide the conclusions found in this piece of work.

5.2 Dendrimers: A Modular Chemical Concept

Dendrimers are a class of materials that utilise significant branching of common units in their molecular design to enable the realisation of unique chemical structures. The design of the molecules can be thought of as similar to a tree-branch-like patterning, with dendrons rapidly branching away from a central core, with each branch branching again, with the number of levels of branching being called the “generation” number. Dendritic structures can be found in nature, with the symmetrical branching structure of some snow crystals, Figure 5.1, being emblematic of the form.



Figure 5.1. Photograph of a snow crystal, entitled “Snow Crystal 13” by Wilson Bentley,¹ representing the branching dendritic nature of some water ice crystals. Colour inverted for ease of reproduction.

In applying the dendritic principles to light emitting materials the idea is to capitalise on the advantageous control of properties that dendrimer molecules provide to enable design of materials that have modular and customisable properties. The basic modular structure of a light emitting dendrimer can be broken down into three components, as shown in Figure 5.2, namely a core (1)

that defines the light emitting properties, dendrons (2) that provide spatial separation between cores, controlling the core-core interactions, and surface groups (3) that define how the molecule interacts with its environment, e.g. to aid solubility, give chemical sensing of the local environment or to attract or repel other dendrimer molecules surrounding it.

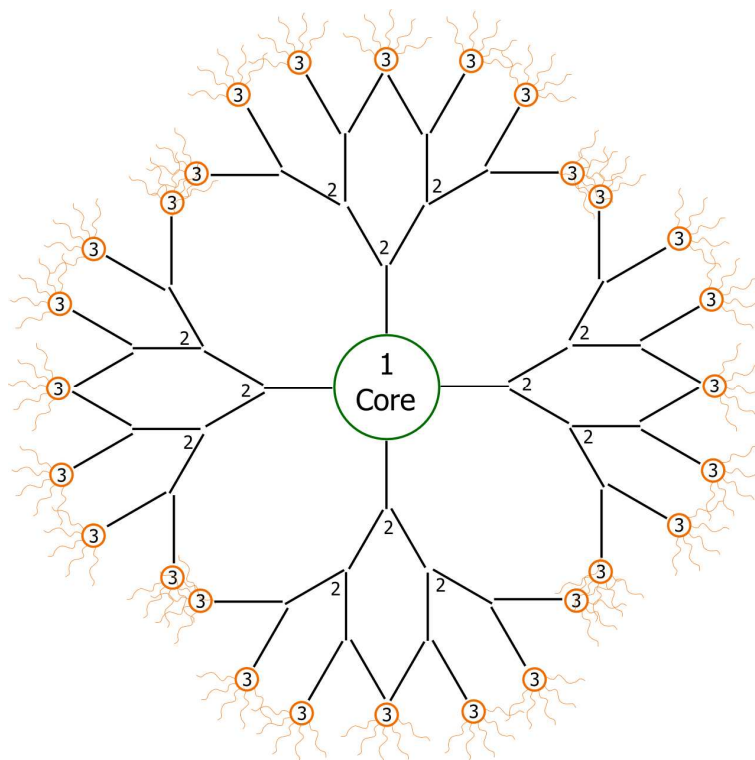


Figure 5.2. Schematic of the constituent parts of a dendrimer molecule. (1) The core at the centre, in light emitting materials this is generally the emitting component. (2) Dendrons providing the branches that define core-core spacing and interactions. (3) Surface groups that control how the dendrimer interacts with its environment.

The application of dendrimer chemical structures to light emitting materials was first pursued by Samuel and Burn, initially with fluorescent materials² and then subsequently with phosphorescent transition metal complexes.³⁻⁶ The motivations for using phosphorescent dendrimers are numerous. Small molecule iridium complexes traditionally used in phosphorescent organic light emitting diodes have limited solubility and thus are conventionally thermally evaporated onto device substrates, a potentially time-consuming and complex process, especially when

the aim is to impart a high degree of detail in a device such as would be found with pixel patterning in a high resolution display. Dendrimers offer up the ability to attain high material solubility by choosing surface groups that enable high solution concentrations to be prepared. With high concentration solutions the material can then be solution processed and be deposited onto the substrate by spin-casting or ink jet printing methods, offering the ability to lay down organic material with high levels of intricacy in a fast, cheap and efficient manner, maintaining control of the film-forming properties, intermolecular interactions and solubility by simple chemical modification of the dendrimer. These advantages have enabled the worlds most efficient solution processable OLED to be fabricated utilising a dendrimer as the emissive material.⁶ The other key advantage of dendrimers is the ability to control the intermolecular spacing between chromophores. Traditionally the emissive material in an OLED is doped in a host matrix to reduce self-quenching of generated excitons. In dendrimers there is the ability to control how close each light emitting core is to its nearest neighbour by controlling the length and chemical nature of the spacing dendrons on the molecule.³ Charge transport and morphological properties of the dendrimer can also be controlled by chemical engineering of the dendrons.⁷⁻⁹

Looking specifically at phosphorescent iridium dendrimers, the general chemical structure of a first generation iridium dendrimer is shown in Figure 5.3, the Ir(ppy)₃ core is shown in green, the bi-phenyl dendrons in blue and the 2-ethylhexyloxy surface groups in red.

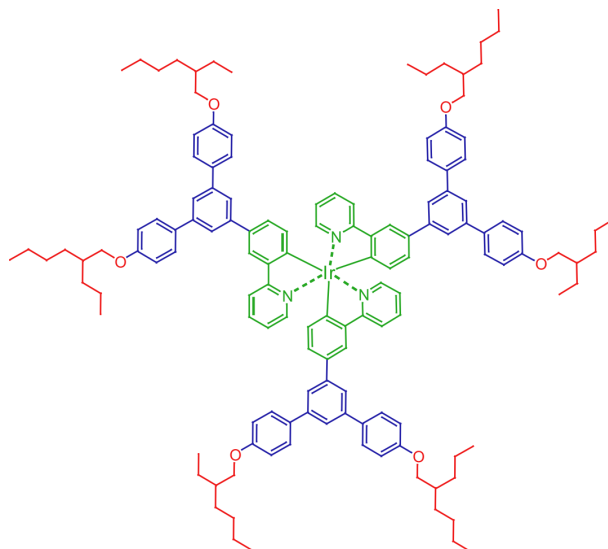


Figure 5.3. Assignment of iridium cored dendrimer components. Shown in green is the central light emitting iridium core. In blue are the dendrons that spatially separate the cores, and in red are the surface groups that control solubility and environmental interactions.

In this work the key advantages of the dendrimer materials is the ability to make chemical additions to the molecule without necessarily changing the excited state electronic properties of the material, and their high solubility. As briefly touched upon in Chapter 4, limited solubility of iridium complexes can hamper the ultrafast photophysics that is able to be observed. Low concentration solutions lead to the unfortunate and unintended generation of a significant amount of Raman signals from the solvent, hence with 400 nm excitation measurements of ultrafast luminescence are restricted to wavelengths of 480 nm and longer unless the dynamics observed < 480 nm are significantly slower than the instantaneous signals generated by Raman shifts to enable separation of the two components. Since luminescence becomes faster as one moves to higher energy in iridium complexes this precluded any ability to look < 480 nm. Iridium cored dendrimers, however offer up the possibility of creating high concentration solutions that can enable the observation of Raman free luminescence dynamics at wavelengths below 480 nm.

5.3 Intramolecular Vibrational Redistribution

An introduction to intramolecular vibrational redistribution (IVR) is provided in Chapter 2, but to briefly restate, IVR is a (predominantly) ultrafast vibrational dissipative mechanism that involves redistributing vibrational energy, both spatially over the molecule and from high to lower frequency vibrational modes. Methods of observing IVR in the time-domain have generally relied on complex experimental techniques, principally in the gas phase. Time-resolved fluorescence,¹⁰ pump-probe spectroscopy,¹¹ time-resolved stimulated emission pumping¹²⁻¹⁴ and Raman spectroscopy^{15, 16} have all been applied to the study of IVR. Ultrafast luminescence measurements have made use of the dynamical shift of the photoluminescence (PL)¹⁷ as well as directly detected luminescence¹⁸ to monitor IVR. The aforementioned techniques suffer from assignment difficulties, especially in the condensed phase, where spectral dynamics can easily be affected by solvation or matrix reorganisation. In large many atom molecules broad spectral features make assignment using these techniques even more difficult owing to the small changes being looked for amongst broad features.

As described in Chapter 4, however, IVR can be identified and easily observed in iridium complexes. Observation of the ultrafast luminescence in iridium complexes can thus provide a simple unambiguous methodology for observing IVR, contrasting with the complex and specific treatments described above. This concept drove the work described in this chapter, where iridium dendrimers were used to observe how IVR changes with the addition of the dendrons as compared to the Ir(ppy)₃ core alone.

5.4 Photophysical Properties of Iridium Cored Dendrimers

Two first generation iridium cored dendrimers were studied, G1M and G1P, and were compared against Ir(ppy)₃, the parent core that is also part of them both. All three chemical structures are shown in Figure 5.4. G1M and G1P are different

only in the attachment of the dendrons onto the phenyl moiety of the Ir(ppy)₃ core, with M attaching at the *meta* position and P at the *para*. It was of interest to see what, if any, difference the connection point would make to the ultrafast dynamics.

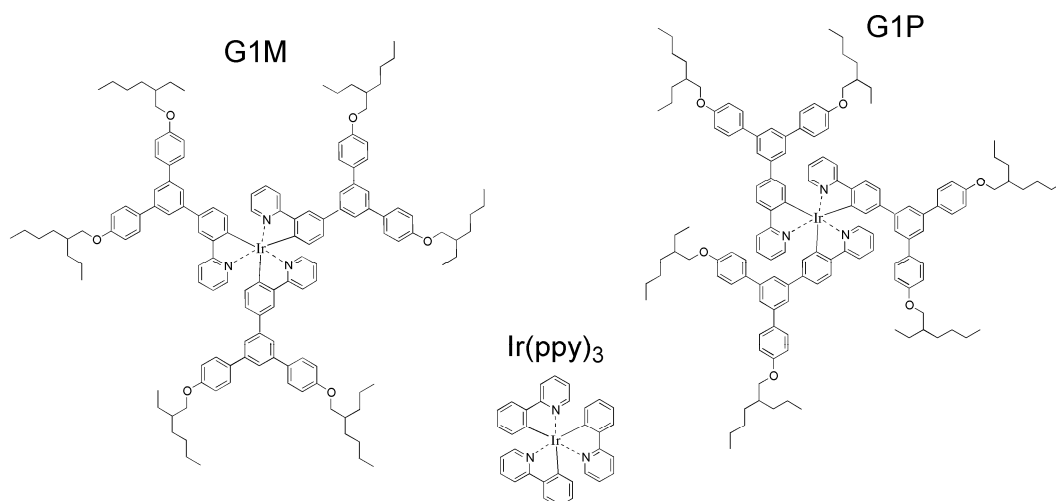


Figure 5.4. Chemical structures of the three iridium complexes under investigation. The first generation Ir(ppy)₃ cored dendrimers, G1M and G1P are shown, with the only difference being the bi-phenyl dendron connection to the ligand phenyl, either at *meta* (M) or *para* (P) positioning. The Ir(ppy)₃ core is also shown.

The materials were dissolved in THF and concentrations used for the dendrimers were 3 mg/ml for G1M and 4 mg/ml for G1P. These concentrations were chosen to have similar absorbance to the 1 mg/ml Ir(ppy)₃ solution that they were being compared with. As already discussed, dendrimers have the advantage of being able to be dissolved to much higher concentrations, and this was utilised in studies on the high energy side (< 480 nm) where concentrations of ~ 10 mg/ml were used. The ultrafast luminescence from the high concentrations used here were checked against lower concentration solutions of the same dendrimer materials and dynamics were found to be identical, indicating that there were no additional effects caused by the high concentration, as shown in Figure 5.5, where G1M in THF is compared at three concentrations at a detection wavelength of 490 nm, with no difference in kinetics being observed.

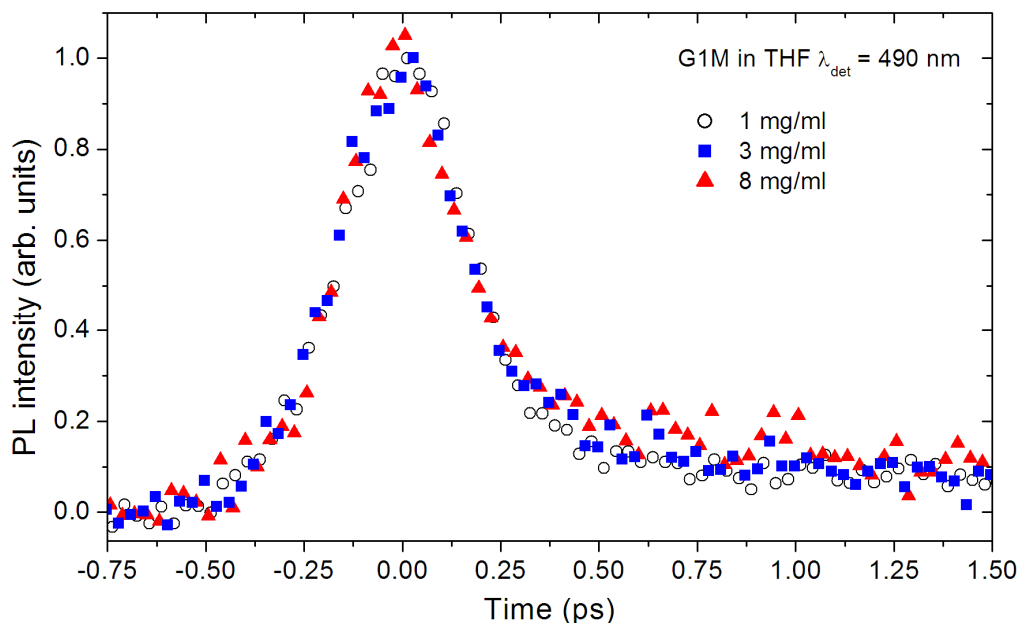


Figure 5.5. Comparison of ultrafast luminescence kinetics for G1M in THF at a detection wavelength of 490 nm with variation of solution concentration. Open circles represent 1 mg/ml, closed squares 3 mg/ml and closed triangles 8 mg/ml. No differences in the kinetics are observed across this concentration range.

Optical absorption and photoluminescence spectra of the three materials under investigation are presented in Figure 5.6. It can be seen that G1M shows very similar spectral features to Ir(ppy)₃, with only a slight shift in the PL peak (5 nm) which can likely be accounted for by solvatochromic shifting – the larger dendrimer and its surface groups will interact slightly differently with the surrounding THF solvent molecules. G1P, however, does show different spectral features, there is a more featureless absorption spectrum in the ¹MCLT region – this is shown more clearly in a normalised plot in Figure 5.7 for comparison – and a red-shifted PL (10 nm from G1M). The changes in G1P compared to G1M can be accounted for due to the structural alteration. In G1M the dendron connected at *meta* leads to a 72° angle between the phenyl of the ligand and the bi-phenyl of the dendron, mostly breaking electron delocalisation and therefore confining the excited state to the core, giving rise to the observed Ir(ppy)₃ like spectral properties. In G1P, however, the dendron is connected at *para*, and so there is linearity between the phenyls of the core and dendron. This allows the excited

state delocalisation to extend a little onto the dendron, explaining the slightly red-shifted PL and altered electronic properties.

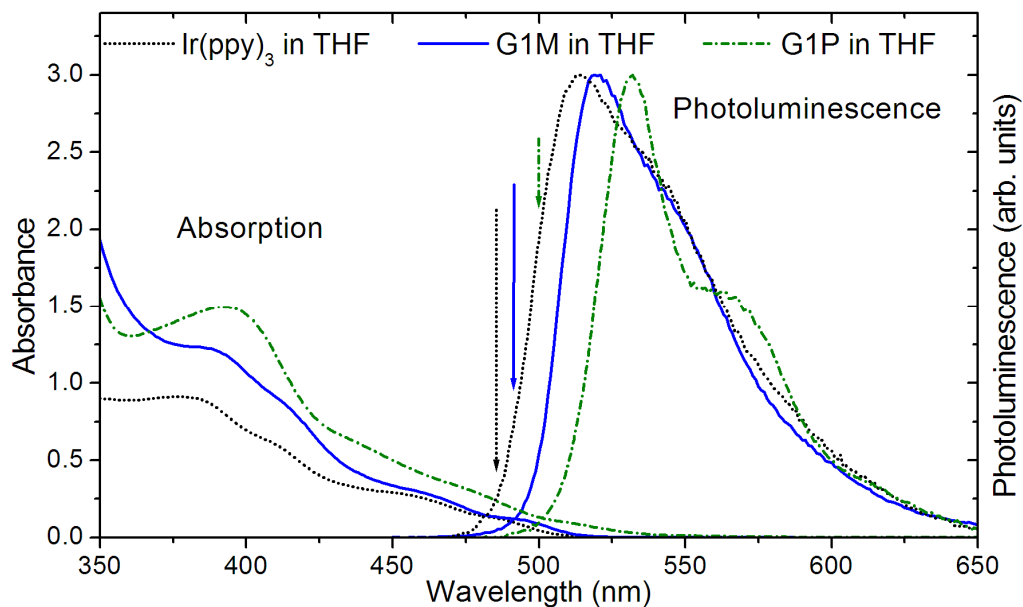


Figure 5.6. Optical absorption and photoluminescence spectra for the three complexes under study. Ir(ppy)₃ is shown as black dotted lines, G1M as solid blue lines and G1P as green dot-dashed lines. All materials are dissolved in THF at concentrations quoted in the text. The arrows indicate the detection wavelength at 140 meV above the PL peak for each material.

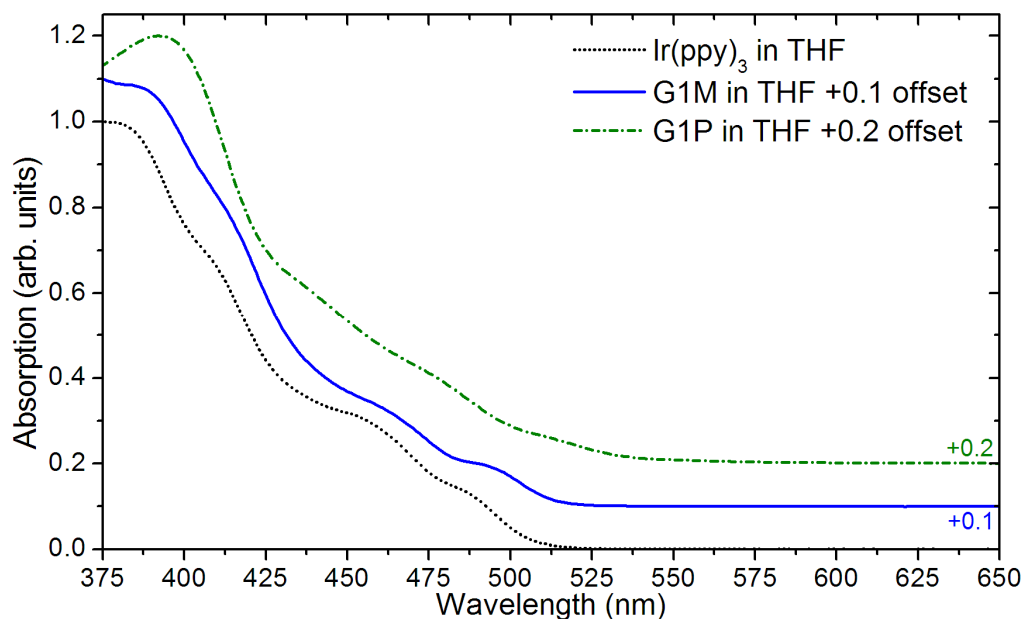


Figure 5.7. Normalised optical absorption spectra for the three materials under study. Ir(ppy)₃ is shown as a dotted line, G1M (solid) + 0.1 offset in the y-axis for clarity and G1P (dot-dashed) + 0.2 offset.

5.5 Ultrafast Luminescence Dynamics

Observation of ultrafast luminescence with the two studied dendrimers can allow relaxation mechanisms in iridium complexes to be better understood. To establish the processes that were occurring luminescence was monitored on the peak of the PL spectrum and on the red-side for both G1M and G1P and was found to behave identically to the dynamics observed in Ir(ppy)₃ that were detailed in Chapter 4, namely a decay of 230 fs representing 49% of the total decay, 3 ps (27%) and a nanosecond offset (24%). Kinetics on the peak of the PL for G1M and G1P are shown in Figure 5.8.

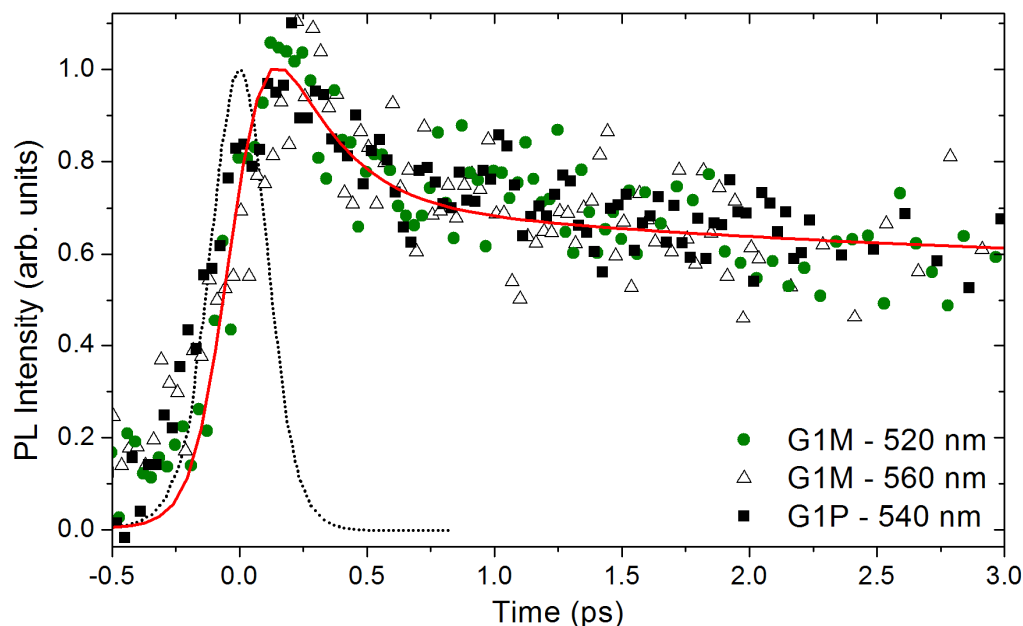


Figure 5.8. Ultrafast luminescence measurements in the steady state PL region of G1M (closed circles, 520 nm, and open triangles, 560 nm) and G1P (closed squares, 540 nm). The dotted line indicates the instrument response function (260 fs FWHM). The solid line indicates the best-fit when the kinetics are convolved with the IRF, and gives time constants of 230 fs (49% of amplitude), 3 ps (27%) and a nanosecond offset (24%).

Features on the peak of the PL, representing emission from the lowest $^3\text{MLCT}$ state can be easily compared across different materials as it is certain that the same state is being looked at. At higher energy, however, a standard metric needs to be established to enable comparison. Raman signals in $\text{Ir}(\text{ppy})_3$ define that ~ 480 nm is as high a detection energy that can be safely recorded in this material, and so this provided an upper bound on detection energies when wanting to compare dynamics in the dendrimers against $\text{Ir}(\text{ppy})_3$. A value of energy above the PL peak of ~ 140 meV, i.e. emission from a position 140 meV above the relaxed $^3\text{MLCT}$ state, was chosen as a standard comparison value across the three materials. This equates to 485 nm detection wavelength in $\text{Ir}(\text{ppy})_3$ and so should not show any Raman signals. A comparison of the ultrafast luminescence dynamics of $\text{Ir}(\text{ppy})_3$ (at 485 nm), G1M (490 nm) and G1P (500 nm), all dissolved in THF, at 140 meV above the PL peak is shown in Figure 5.9.

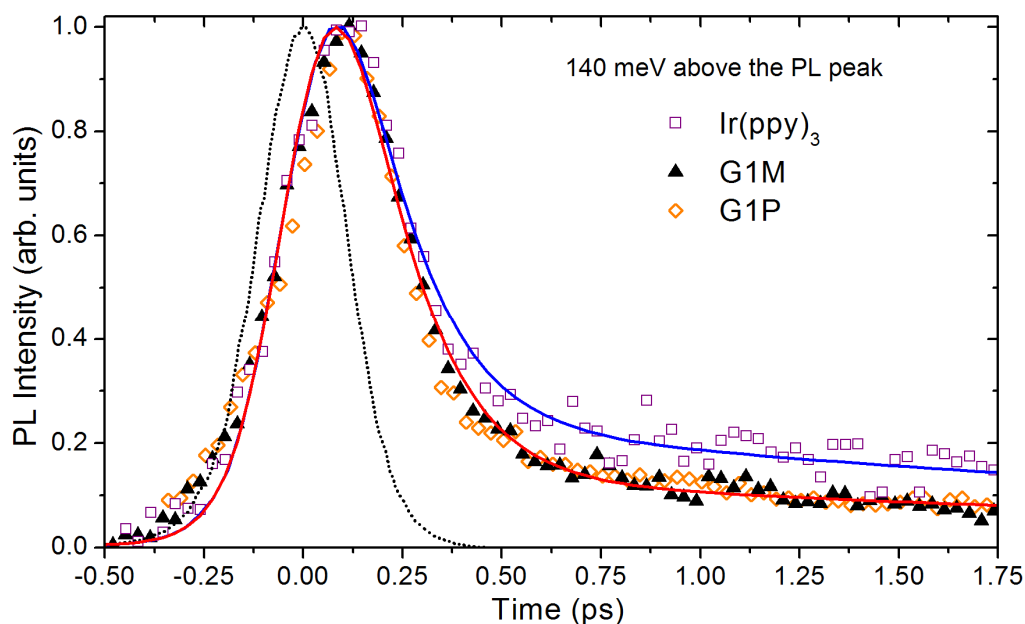


Figure 5.9. Ultrafast luminescence recorded at detection energies of 140 meV above the PL peaks of Ir(ppy)₃ (open squares), G1M (closed triangles) and G1P (open diamonds), all in THF. The dashed line is the IRF (260 fs FWHM). The solid lines indicate the best-fits for the two datasets, with time constants of 150 fs and 3 ps fitting to both systems. The amplitudes, however, vary, with Ir(ppy)₃ giving 150 fs (88%) and 3 ps (12%) while for the dendrimers 150 fs (94%) and 3 ps (6%). Copyright American Chemical Society 2008,¹⁹ reproduced with permission of the rights holder.

Kinetics in the dendrimers best fit to time constants of 150 fs and 3 ps, the same as Ir(ppy)₃, however the amplitudes are different, with 94% of the amplitude constituting the femtosecond decay in the dendrimers with the remainder consisting of the picosecond decay, whereas in Ir(ppy)₃ only 88% of the total amplitude is represented by the femtosecond component. To test for any solvent dependence of dynamics the luminescence was recorded at 140 meV above the PL peak in G1P in toluene and the kinetics were found to be identical to those in THF, with a comparison shown in Figure 5.10.

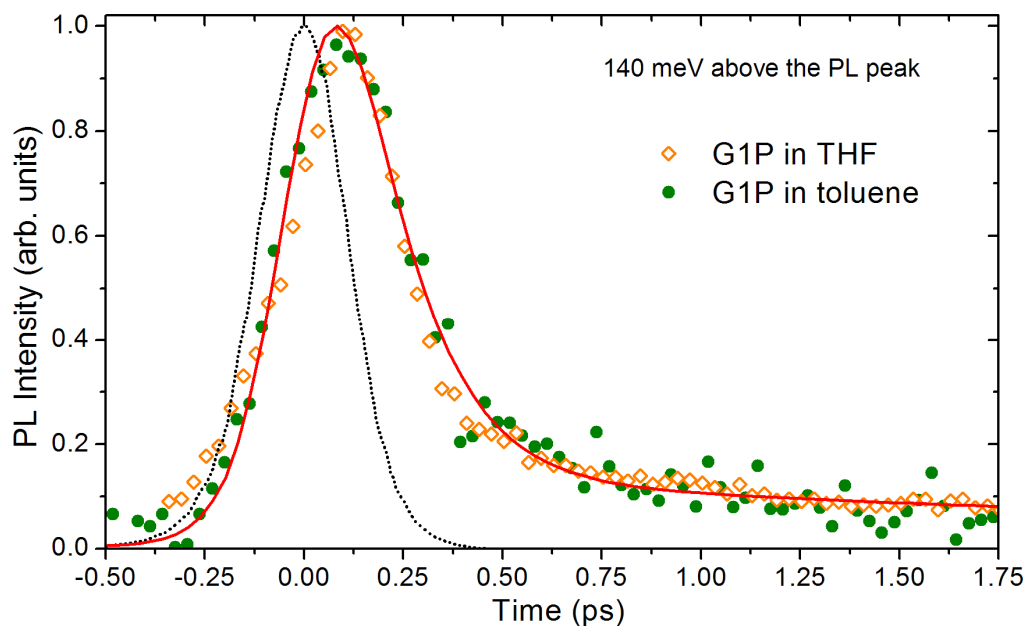


Figure 5.10. Ultrafast luminescence at a detection energy of 140 meV above the PL peak of G1P dissolved in THF (open diamonds) and toluene (closed circles). The dotted line indicates the IRF (260 fs FWHM). The solid line indicates the best-fit, with dynamics best represented by 150 fs (94%) and 3 ps (6%) decays.

As previously mentioned, a significant advantage of dendrimers in this study is the ability to produce high concentration solutions, therefore enabling Raman free observations at higher energy. It was thus possible to confidently observe luminescence at higher energies, and this was done in G1P and G1M at 480, 470 and 460 nm in solutions that were typically ~ 10 mg/ml. Dynamics at 460 nm are shown for G1M in THF in Figure 5.11.

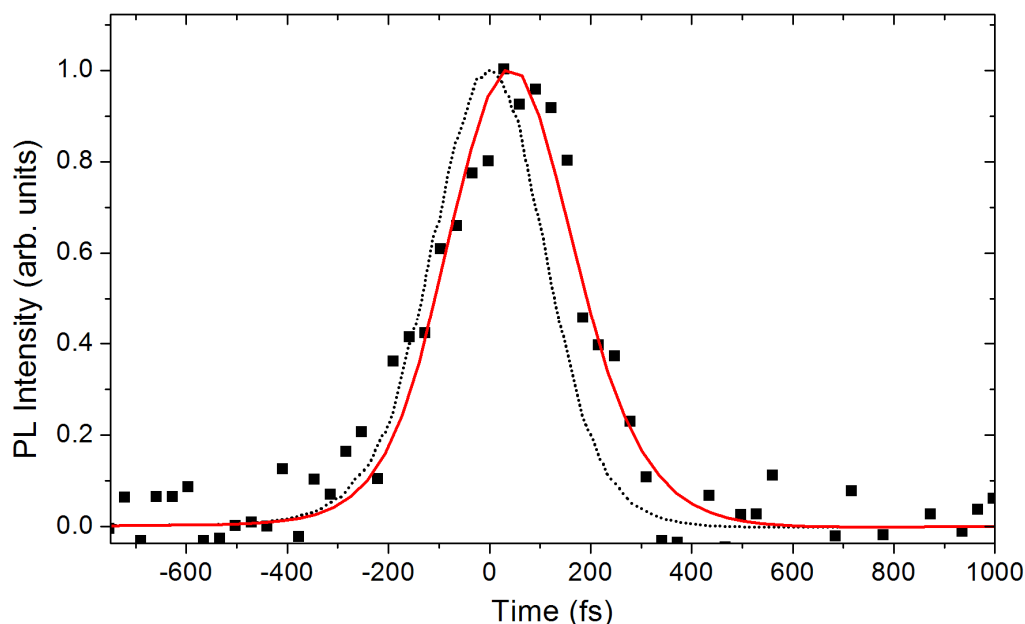


Figure 5.11. Ultrafast luminescence dynamics at 460 nm detection in G1M. The dotted line is the IRF (260 fs FWHM) and the solid line is the best-fit, giving a decay of 70 ± 20 fs.

The kinetics at 460 nm best fit to a time constant of ~ 70 fs, representing 100% of the decay, however the signal to noise is such that this number cannot be stated with a high degree of confidence, with time constants ± 20 fs giving an acceptable fit.

5.6 Ultrafast Transient Absorption Dynamics

Pump probe experiments were carried out with an experimental setup as described in Chapter 3 on G1M to see if any of the luminescence dynamics could be observed in transient absorption processes. Shown in Figure 5.12 is a typical transient signal ($\lambda_{\text{pump}} = 400$ nm, $\lambda_{\text{probe}} = 500$ nm), with a positive amplitude indicating excited state absorption rather than stimulated emission. The dynamics (or rather lack of them) are found to be the same as $\text{Ir}(\text{ppy})_3$, as discussed in Chapter 4, namely an instantaneous formation of the excited state followed by a long lived transient signal out to at least 100 ps (not shown). Instantaneous formation of the transient indicates that the absorbing state(s) form in < 100 fs.

The strong similarity of the observed dynamics here is not surprising given how similar the electronic structures of G1M and Ir(ppy)₃ are.

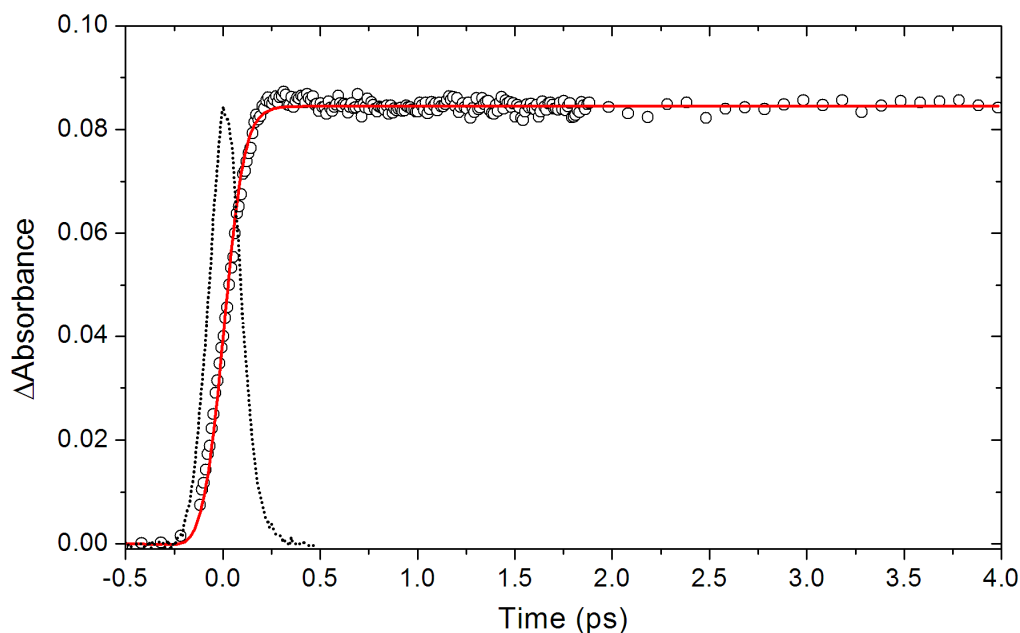


Figure 5.12. Transient absorption dynamics ($\lambda_{\text{pump}} = 400 \text{ nm}$, $\lambda_{\text{probe}} = 500 \text{ nm}$) for G1M in THF. Positive signal indicates excited state absorption. The kinetics fit to an instantaneous rise in the signal followed by long lived (nanosecond) decay, with the fit shown as a solid line. The instrument response function (185 fs FWHM) is shown as a dotted line.

Monitoring the transient signal at different probe wavelengths allows the excited state absorption spectrum to be reconstructed, as shown in Figure 5.13. The spectrum shows features similar to Ir(ppy)₃, namely stronger absorption at higher energy, weakening to a long tail into the infra-red.

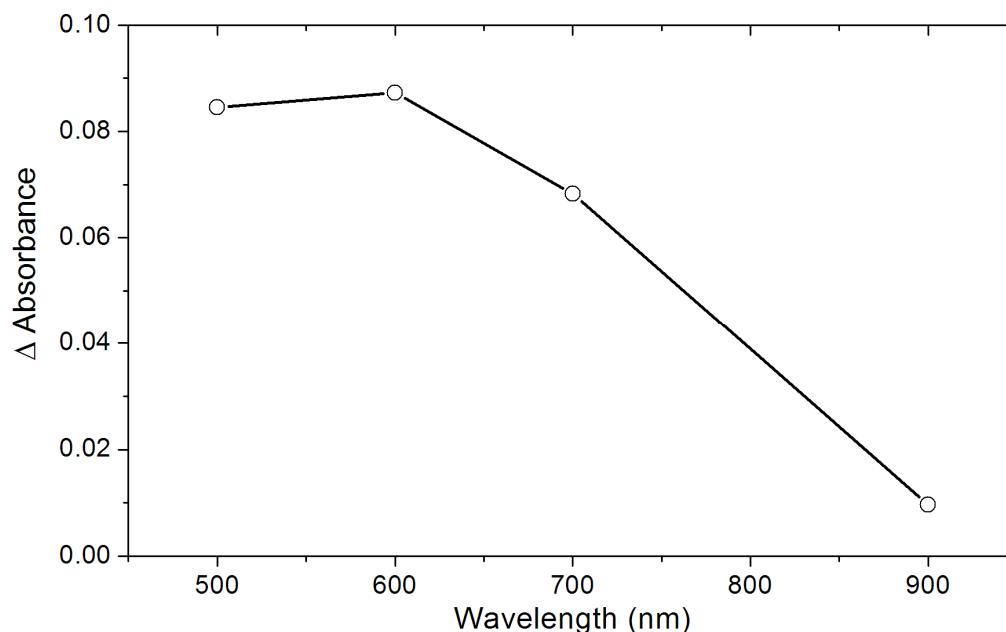


Figure 5.13. Reconstructed excited state absorption spectrum for G1M in THF with $\lambda_{\text{pump}} = 400$ nm and when varying the probe.

5.7 Interpretation of Ultrafast Dynamics

The presented femtosecond luminescence measurements enable the ultrafast processes in the chosen iridium dendrimers to be compared against their parent $\text{Ir}(\text{ppy})_3$ core.

Firstly, luminescence across the steady state PL region in the two studied dendrimers is found to be the same as in $\text{Ir}(\text{ppy})_3$, namely 230 fs and 3 ps decays, and assignment of these are made to the same processes, namely IVR and vibrational cooling from the top electronic substate of the lowest $^3\text{MLCT}$ state to the two lower substates.²⁰ It is completely understandable that G1M and $\text{Ir}(\text{ppy})_3$ show identical features on this process as they are essentially electronically the same, however it is interesting that G1P, with its definite altered electronic structure, also shows the exact same redistribution times and amplitudes amongst the lowest $^3\text{MLCT}$ substates. This indicates that the redistribution time is relatively insensitive to the specific excited state electronic structure. It is

imagined that what instead would play a larger role in altering the time constants of these processes would be the amount of zero-field splitting between the substates. The energy spacing between the substates defines how much dissipation is required, and so complexes with the same central co-ordinating metal and general ligand structure will likely show similar splitting and hence similar redistribution times.

Detecting luminescence at 140 meV above the PL peak in the three materials can help elucidate the nature and controlling factors of energy dissipation in iridium complexes. IVR is assigned as the dissipating agent due to the increase in the decay rate that is observed as one moves to higher energies (230 fs to 150 fs to 70 fs). The identical nature of the decays in solvents of different polarities also rules out solvation as a major contributor to the observed decay processes. At 140 meV of excess energy both dendrimers are found to decay with the same time constants (150 fs & 3 ps) as in Ir(ppy)₃ (Figure 5.9) however the amplitudes are different, with 94% of the decay now occurring by the femtosecond process and only 6% by picosecond cooling to the solvent – versus 88% and 12% in Ir(ppy)₃. This indicates that while the rate of IVR does not appear to increase in the dendrimers the *amount* of energy that is able to be dissipated by IVR does, hence leaving less excess energy to be dissipated by the slower picosecond process. With the addition of the dendrons to the molecule one might expect that the rate of IVR should increase – more physical matter is available for vibrations to spread to within the molecule, and thus the rate should be faster. Indeed the increase in the amount of dissipation by IVR versus vibrational cooling to the surrounding solvent molecules does indeed indicate that the extra matter in the dendrimers allows greater intramolecular dissipation of energy – the dendrons acting as an extra vibrational storage well for excess energy. The reason however for the lack of the observed increase of the rate of IVR can be explained when one looks at how the extra matter, the dendrons, that have been added to the Ir(ppy)₃ core are connected. Linkage between the phenyl ring of the core and the bi-phenyl of the dendron is by a single C-C bond. The energy of a C-C stretch vibration is ~ 170 meV, higher than the 140 meV of excess energy that is being dissipated here. To

deduce what percentage of the C-C stretch vibrational will be thermally activated one can apply Boltzmann statistics on the relative energies and it is found that only around one-quarter of the C-C stretch vibrations will be activated and thus would have a faster rate of IVR. As this faster rate of IVR would correspond to lifetimes < 150 fs, and given that time constants are deconvolved with the instrument response function, it would be difficult to fit such a faster time constant for 25% of the femtosecond decay with any great degree of confidence. The rate increase may exist, but it may just be that the amplitude of emission is much more sensitive to the change than the fitted time constants, therefore what is observed is mainly an increase in the pre-exponential factor of the femtosecond component rather than a shortening of its time constant.

The relaxation rate in G1P is found to be identical to G1M, despite the clearly altered excited state electronic structure in G1P. This gives good support to the assignments made here, namely that the relaxation is vibrationally dissipative in nature – had this relaxation been dependent on the intersection, number, position and structure of excited electronic states this would have presumably showed up in the observed dynamics of G1P given its differing electronic properties. The second conclusion that can be drawn from the G1P observations is that the vibrational flow is likely dependent on the C-C bond connecting the core to the biphenyl of the dendron. G1P still has that C-C connection, but it is now at *para* position on the phenyl of the ligand, indicating that it is not the *meta* positioning in G1M that stops the increase in the rate of IVR, but rather the connecting C-C bond itself.

The dendrimer systems can thus be thought of as giving extra physical matter for the acceptance of vibrational energy within the molecule, and a schematic of the vibrational energy flow out onto the dendrons is shown in Figure 5.14.

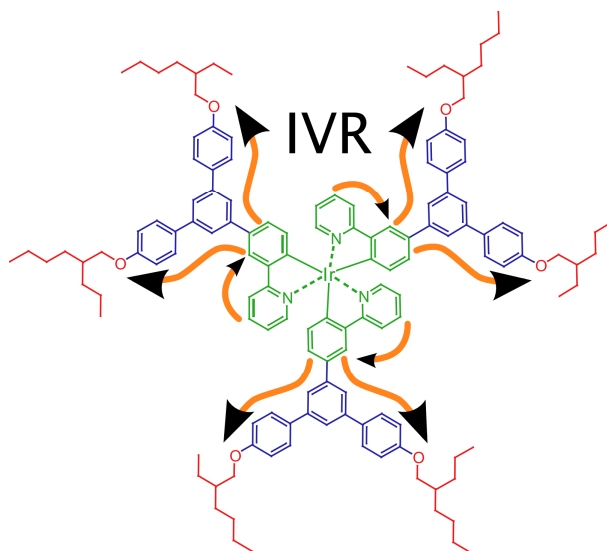


Figure 5.14. Schematic of vibrational energy flow in G1M, with arrows showing the flow of vibrational energy within the phenyl-pyridine ligand and then out onto the bi-phenyl dendron.

The utilised technique of ultrafast luminescence measurements with iridium complexes can therefore provide a straight forward and unambiguous methodology for observing and interpreting IVR in large polyatomic molecules. Simple chemical modification of the structure – that either does or does not alter the excited state electronic properties of the material – such as that which occurs in dendrimer systems, can enable the flow of vibrational energy to be monitored.

As mentioned previously, the higher solubility of the dendrimer materials allowed larger concentrations to be made and so higher energy dynamics (< 480 nm) to be explored, free from Raman signals. Dynamics at 460 nm in G1M, Figure 5.11, show a decay that is $\sim 70 \pm 20$ fs. Looking at the absorption spectrum for this detection wavelength in G1M, Figure 5.6, shows a pronounced shoulder ~ 460 nm, indicating a second electronic state. The stronger absorption, coupled with the higher energy would give good supporting evidence that this state is likely to be more singlet in character than the lowest absorption feature (which is assigned as the $^3\text{MLCT}$ state). It is thus likely that the luminescence that is observed at 460 nm originates from the lowest $^1\text{MLCT}$ state and hence the 70 fs time constant embodies the rate of intersystem crossing (ISC), and indeed this time correlates

with a instantaneous formation of the excited state absorption that is observed in pump-probe measurements, indicating a formation time of < 100 fs (Figure 5.12). However definitive evidence for the exact time constant of ISC is unfortunately lacking here.

Monitoring the rate of IVR at different values of excess energy (i.e. values of energy above the lowest $^3\text{MLCT}$ state – represented by $\lambda_{\text{det}} - \lambda_{\text{PL peak}}$) can enable the construction of a plot of excess energy versus IVR rate, as shown in Figure 5.15.

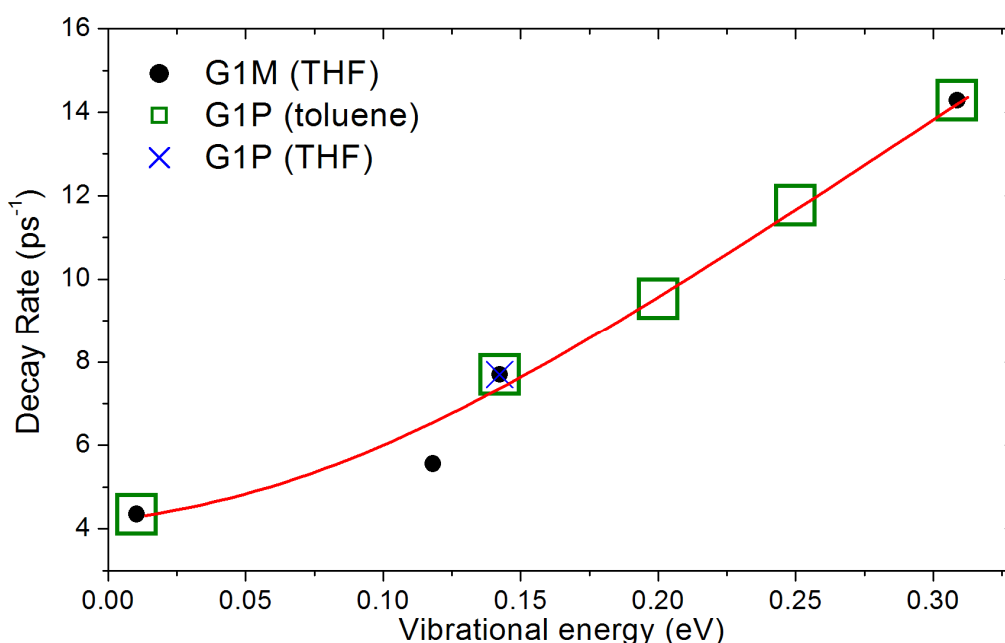


Figure 5.15. Scatter plot of excess vibrational energy ($\lambda_{\text{det}} - \lambda_{\text{PL peak}}$) versus IVR decay rate for the dendrimers under investigation. The red line is a guide for the eye. Copyright American Chemical Society 2008,¹⁹ reproduced with permission of the rights holder.

An increase in the rate of IVR is found as one moves to larger values of excess energy and in the range 0.1-0.3 eV of excess energy a linear fit of $43 \text{ ps}^{-1} \text{ eV}^{-1}$ can be made. As the values of excess energy increase the vibrational density of states will also increase²¹ and this explains the increase in the rate of IVR.

5.8 Conclusions

The results presented here have allowed the observation and monitoring of vibrational energy flow in a molecule. IVR, the redistribution of vibrations from high to low frequency modes in a molecule, has important roles in a number of ultrafast chemical processes. What controls IVR and how the relaxation process can be monitored or influenced is of importance in the field of chemical physics and femtochemistry. Using a series of iridium cored dendrimers it has been possible to monitor IVR and track how the dissipation of excess energy is altered with the addition of extra physical matter to an Ir(ppy)₃ core. The addition of dendrons does not noticeably increase the rate of IVR when monitored at 140 meV of excess energy that requires dissipation. At this energy the C-C stretch vibration of the bond that connects the phenyl of the core to the bi-phenyl of the dendron will only be one-quarter thermally activated and therefore the increase in the rate will not be enough to be visible or to be confident in any fitted increase. What can be stated with confidence is the increase in the *amount* of dissipation of excess energy by IVR when compared with just the Ir(ppy)₃ core at 140 meV of excess energy. In just the Ir(ppy)₃ core 88% of the dissipation was achieved by femtosecond IVR with 12% by picosecond cooling to the surrounding solvent molecules, however in the Ir(ppy)₃ cored dendrimers the amount of dissipation achieved by IVR increased to 94%, with only 6% left to be dissipated by picosecond vibrational cooling. This result, tested carefully in two different dendrimers and with two different solvents, indicates that the extra matter added to the molecule in the dendrimers enables more vibrational energy to be dissipated by IVR, the dendrons of the molecule acting as heat sinks for the excess energy.

Viewing the dissipation by IVR at higher values of excess energy enabled a relationship between the values of excess energy and the rate of IVR to be established, with a linear fit in the range 0.1-0.3 eV of excess energy of 43 ps⁻¹ eV⁻¹ being made.

5.9 References

- [1] W. Bentley,
http://commons.wikimedia.org/wiki/File:Bentley_Snowflake13.jpg
- [2] H. Mounir, N.G.P. Jonathan, D.W.S. Ifor, and L.B. Paul, *Advanced Materials*, 1999. **11**(5): p. 371-374.
- [3] J.M. Lupton, I.D.W. Samuel, M.J. Frampton, R. Beavington, and P.L. Burn, *Advanced Functional Materials*, 2001. **11**(4): p. 287-294.
- [4] S.C. Lo, E.B. Namdas, P.L. Burn, and I.D.W. Samuel, *Macromolecules*, 2003. **36**(26): p. 9721-9730.
- [5] P.L. Burn, S.-C. Lo, and I.D.W. Samuel, *Advanced Materials*, 2007. **19**(13): p. 1675-1688.
- [6] S.C. Lo, N.A.H. Male, J.P.J. Markham, S.W. Magennis, P.L. Burn, O.V. Salata, and I.D.W. Samuel, *Advanced Materials*, 2002. **14**(13-14): p. 975-979.
- [7] J.M. Lupton, I.D.W. Samuel, R. Beavington, M.J. Frampton, P.L. Burn, and H. Bässler, *Physical Review B*, 2001. **63**(15): p. 155206.
- [8] T.D. Anthopoulos, J.P.J. Markham, E.B. Namdas, J.R. Lawrence, I.D.W. Samuel, S.-C. Lo, and P.L. Burn, *Organic Electronics*, 2003. **4**(2-3): p. 71-76.
- [9] J.P.J. Markham, I.D.W. Samuel, S.-C. Lo, P.L. Burn, M. Weiter, and H. Bassler, *Journal of Applied Physics*, 2004. **95**(2): p. 438-445.
- [10] J.A. Syage, P.M. Felker, and A.H. Zewail, *The Journal of Chemical Physics*, 1984. **81**: p. 4706.
- [11] A. Laubereau, A. Seilmeier, and W. Kaiser, *Chemical Physics Letters*, 1975. **36**(2): p. 232-237.
- [12] M.J. Côté, J.F. Kauffman, P.G. Smith, and J.D. McDonald, *The Journal of Chemical Physics*, 1989. **90**: p. 2865.
- [13] J.F. Kauffman, M.J. Côté, P.G. Smith, and J.D. McDonald, *The Journal of Chemical Physics*, 1989. **90**: p. 2874.
- [14] Q. Zhong, Z. Wang, Y. Sun, Q. Zhu, and F. Kong, *Chemical Physics Letters*, 1996. **248**(3-4): p. 277-282.

- [15] A. Laubereau and W. Kaiser, *Reviews of Modern Physics*, 1978. **50**: p. 607-665.
- [16] Z. Wang, A. Pakoulev, and D.D. Dlott, *Science*, 2002. **296**(5576): p. 2201-2203.
- [17] A. Mokhtari, A. Chebira, and J. Chesnoy, *Journal of the Optical Society of America B*, 1990. **7**(8): p. 1551-1557.
- [18] S. Akimoto, I. Yamazaki, S. Takaichi, and M. Mimuro, *Chemical Physics Letters*, 1999. **313**(1-2): p. 63-68.
- [19] G.J. Hedley, A. Ruseckas, Z. Liu, S.-C. Lo, P.L. Burn, and I.D.W. Samuel, *Journal of the American Chemical Society*, 2008. **130**(36): p. 11842–11843.
- [20] G.J. Hedley, A. Ruseckas, and I.D.W. Samuel, *Chemical Physics Letters*, 2008. **450**(4-6): p. 292-296.
- [21] K.K. Lehmann, G. Scoles, and B.H. Pate, *Annual Review of Physical Chemistry*, 1994. **45**(1): p. 241-274.

6

Ultrafast Intersystem Crossing in an Iridium Complex

Gie me ae spark o' Nature's fire,
That's a' the learning I desire.

Robert Burns, *First Epistle to John Lapraik*, 1785

6.1 Introduction

This chapter presents ultrafast luminescence and transient absorption measurements that were completed on the red-emitting iridium complex Ir(piq)₃. Red-shifted electronic features enabled fluorescence to be observed in this class of materials for the first time, enabling the rate of intersystem crossing to be measured. At lower luminescence detection energies the time constant for dissipation of excess energy by intramolecular vibrational redistribution (IVR) was observed and it was found that Ir(piq)₃ could dissipate excess energy faster by IVR than the smaller prototypical Ir(ppy)₃ complex.

In Section 6.2 I discuss in detail the work that has already been published on the process of intersystem crossing in transition metal complexes. In Section 6.3 I provide basic photophysical results on the material under study, presenting details of its optical absorption and emission features. In Section 6.4 I present the principal ultrafast luminescence measurements that have been performed and in Section 6.5 I follow this up with presentation of the ultrafast pump probe results. In Section 6.6 I provide discussion on the ultrafast luminescence observations and give interpretation of the pump probe dynamics. Finally in Section 6.7 I give the conclusions deduced in this piece of work.

6.2 Intersystem Crossing in Transition Metal Complexes

Intersystem crossing (ISC) from singlet to triplet excited states in transition metal complexes generally shows very fast behaviour and has thus been an area of significant experimental work in recent years. The strong spin-orbit coupling (SOC) caused by the heavy central metal ion leads to very efficient ISC.¹ The rates of ISC in transition metal complexes have yet to be fully understood. Categorising ISC from fast to slow, the process has been found to be in the time range of 15-40 fs for ruthenium complexes,^{2, 3} ≤ 20 fs in iron complexes,^{4, 5} and slower dynamics of 3 ps in platinum complexes⁶ and 15 ps in copper complexes.⁷

One might assume that the rate of ISC would correlate with the mass of the central ion – the heavier the co-ordinating metal, the faster the ISC. However, it has been found that while this is correct as a broad approximation (ISC in copper is certainly slower than in ruthenium) it is not always the case, as ISC in ruthenium has been found to be faster than in platinum. It has therefore been speculated that at some certain mass SOC becomes saturated, and the rates of ISC are then dependent on some other controlling variable.

Others have even questioned to what extent ISC can actually be an identifiable process with such fast relaxation processes in such strongly spin-mixed materials, where the lowest triplet state can have significant degrees of singlet character.⁸ Some of the most recent work on ISC in transition metal complexes by Chergui and co-workers attempted to perform a detailed study on how the rate of ISC changed when one of the ligands was altered with different halide atoms.⁹ What was found helped to establish the emerging consensus, that in heavy metal complexes where SOC is saturated it is the structure of the molecule itself that controls ISC, as the time constant of ISC was found to vary from 85 to 150 fs with variation of a halide ligand from chlorine to iodine. Analysis of the vibrational properties of the material indicated that the ISC rates correlated with the

frequency of the metal-halide ligand stretch vibration, giving support to the view that it is the molecular structure – and specifically vibrational mechanisms – that may control ISC.

Relaxation of higher excited states plays a crucial role in energy and charge transfer processes,¹⁰ and understanding the nature and rates of relaxation from such ¹MLCT states may enable more efficient extraction of energy from systems employing transition metal complexes. Intersystem crossing in iridium complexes has not been much explored. Formation of the lowest ³MLCT state has been found to be very fast^{11, 12} when looking at transient absorption data. Ultrafast luminescence experiments – which would give a much clearer assignment of ISC – have been limited in iridium complexes due to the generally higher emission energy, hence forcing observation of singlet emission to wavelengths that were experimentally difficult. The development and interest in iridium complexes for use in organic light emitting diodes (OLEDs) has driven the synthesis of materials that can cover the entire visible spectrum,¹³ therefore red emitting iridium materials are available for study.¹⁴ This was the pursued direction to enable observation of fluorescence, and hence the deduction of ISC rates in iridium materials; as if the material has red-shifted emission and all excited state electronic features are also red-shifted then the singlet emission region should become observable with upconversion spectroscopy.

6.3 Photophysical Properties of a Red Emitting Iridium Complex

The material chosen for the study of ISC in iridium complexes was the homoleptic compound tris(1-phenylisoquinoline)iridium(III) – denoted as Ir(piq)₃, structure shown on the left in Figure 6.1 – which was purchased from American Dye Sources Inc.. This material has been successfully used in efficient OLED device structures due to its high luminescence efficiency (10% external quantum efficiency in a device)¹⁴ and appropriate spectral properties for attaining deep red

emission suitable for use in full colour displays (Commission Internationale de L'Eclairage coordinates 0.68, 0.32).¹⁴

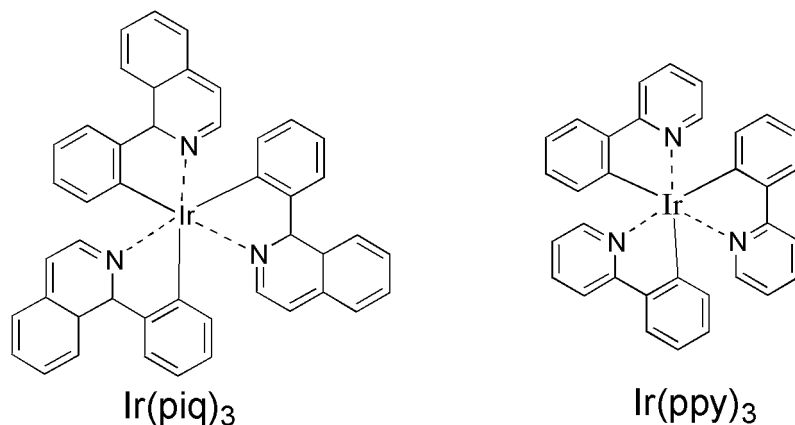


Figure 6.1. Chemical structure of the principal material studied, tris(1-phenylisoquinoline)iridium(III) – denoted as Ir(piq)₃, left. Shown for comparison is the prototypical Ir(ppy)₃, right.

It can be seen that Ir(piq)₃ is only slightly different when compared to the prototypical Ir(ppy)₃ molecule. The only difference between the materials is that Ir(piq)₃ contains a phenyl fused onto the pyridine of each ligand so creating the isoquinoline moiety.

Ir(piq)₃ shows relatively poor solubility, similar to Ir(ppy)₃, and this is explained due to the similar chemical structure of the two materials and the lack of any solubility enhancing additions to the molecule. The material was dissolved in THF at a concentration of 1 mg/ml. The optical absorption and photoluminescence (PL) spectra of Ir(piq)₃ in THF are shown in Figure 6.2. It can be seen that both the emission ($\lambda_{\text{peak}} = 625$ nm) and absorption spectra are different when compared with Ir(ppy)₃ ($\lambda_{\text{peak}} = 515$ nm). A direct comparison of the red-shifting of the absorption features of Ir(piq)₃ compared to Ir(ppy)₃ is shown in Figure 6.3.

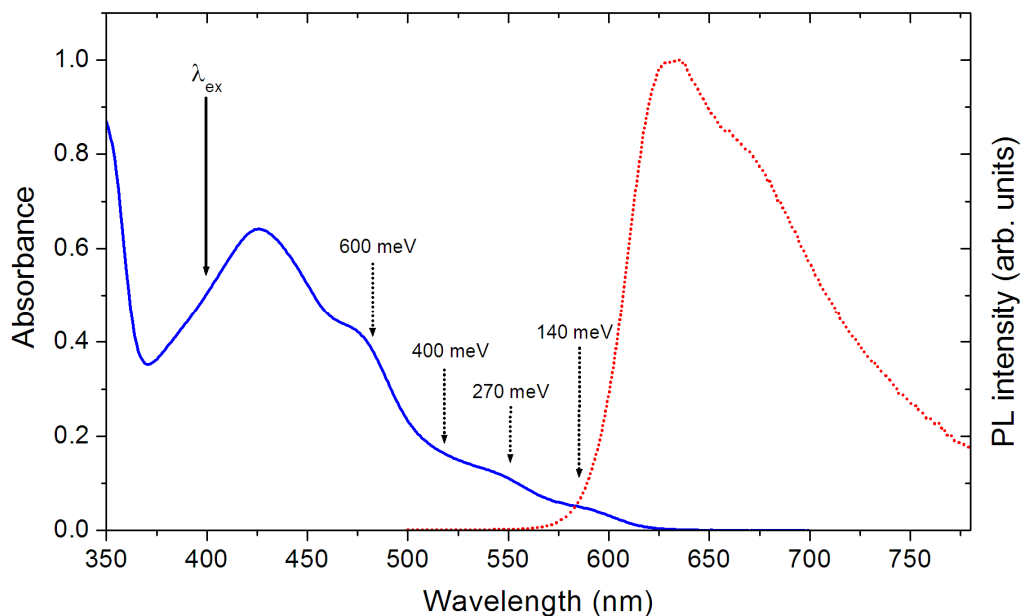


Figure 6.2. Optical absorption and photoluminescence spectra of Ir(piq)₃ in THF at a concentration of 1 mg/ml. The arrows indicate detection energies above the PL peak (dashed line) and the excitation wavelength (solid line) that studies were performed at.

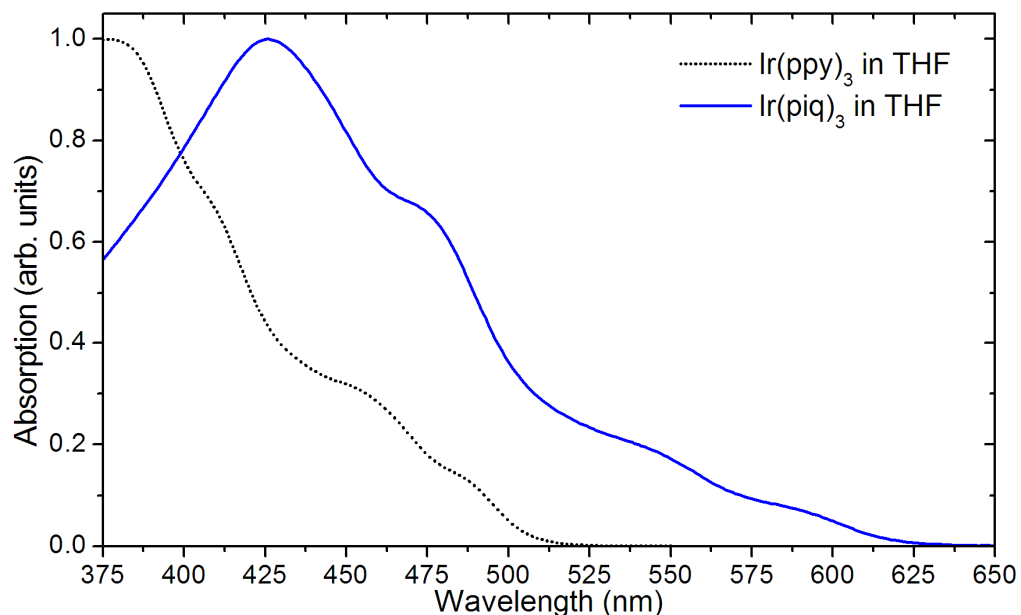


Figure 6.3. Normalised optical absorption spectrum of Ir(piq)₃ (solid blue line) when compared against Ir(ppy)₃ (dotted black line) indicating the ~ 0.4 eV redshift in features in Ir(piq)₃ caused by extra electron delocalisation. Both spectra are normalised to the peak of their MLCT absorption features for ease of comparison.

The red-shifting of features is a manifestation of the addition of the fused phenyl onto the ligands. This extends the electron delocalisation on the ligands compared to what would just be the case in Ir(ppy)₃, explaining the 0.4 eV shift in the PL peak that correlates with a approximate 0.4 eV shift in each of the MLCT absorption features.

Electronic excited states in Ir(piq)₃ have been assigned¹⁴ along similar lines to those features found in Ir(ppy)₃ and other iridium complexes. The lowest absorption feature, 575-625 nm, is assigned as the S₀ → ³MLCT transition and the 525-575 nm feature as a S₀ → ¹MLCT transition, with a least two further ¹MLCT states in the 375-525 nm region before strongly optically coupled π-π* states are observed < 375 nm. 400 nm excitation will therefore directly access the ¹MLCT manifold.

6.4 Ultrafast Luminescence Dynamics of Ir(piq)₃

Initial investigation of Ir(piq)₃ sought to establish the nature of the ultrafast processes that were occurring from the lowest ³MLCT state and thus luminescence dynamics were collected on the peak of the steady state PL spectrum (625 nm) and are shown in Figure 6.4.

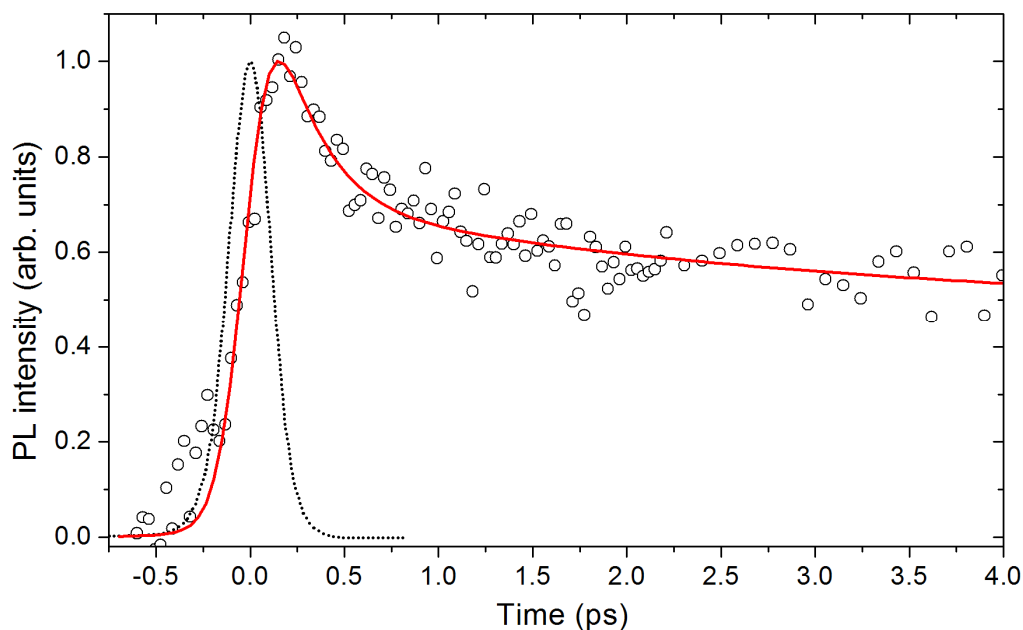


Figure 6.4. Ultrafast luminescence measurement of Ir(piq)₃ measured at 625 nm (the peak of the steady state emission spectrum). The dotted line indicates the instrument response function (260 fs FWHM) and the solid line indicates the best-fit of time constants 230 fs (50% of the total amplitude), 3 ps (17%) and a 33% nanosecond offset.

Two decay processes are observed, namely a 230 fs decay of 50% of the total amplitude, 3 ps decay (17%) and a long lived nanosecond offset (33%). It can therefore be stated that the steady state region has the same processes occurring that were observed in other iridium complexes (Chapters 4 and 5), namely population redistribution amongst the three electronic substates of the lowest ³MLCT state.

As the same dynamics were observed on the peak of the steady state PL spectrum it was hence of interest to recall and implement the vibrational dissipation observation that was used previously with dendrimer materials¹⁵ (Chapter 5), and so luminescence in Ir(piq)₃ was recorded at 140 meV of excess energy, which corresponds to a detection wavelength of 583 nm. Kinetics at this value of excess energy when compared with Ir(ppp)₃ are shown in Figure 6.5, with solid lines indicating best-fits for both datasets.

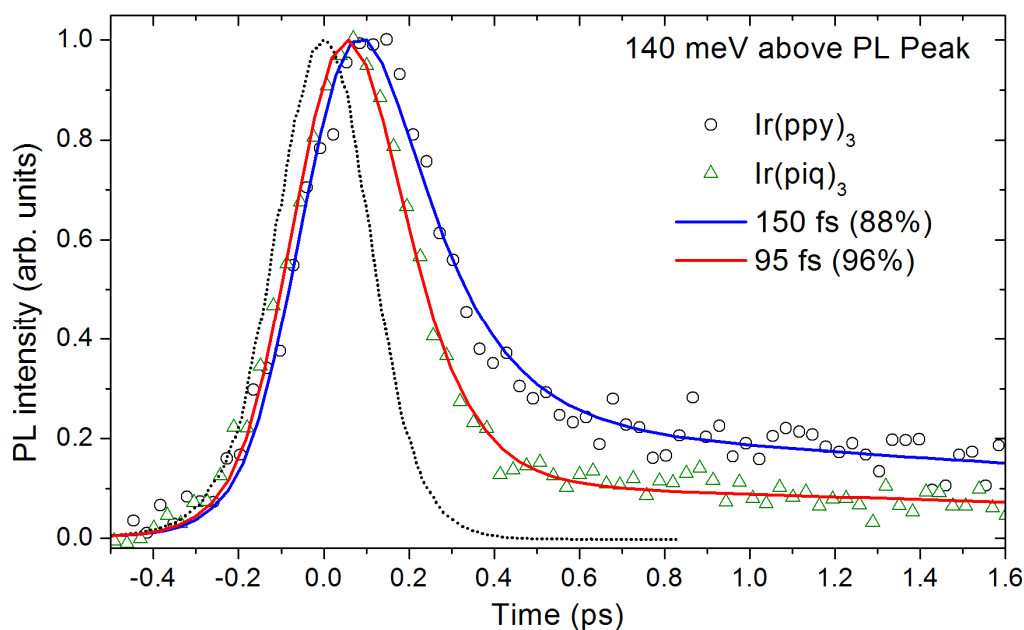


Figure 6.5. Ultrafast luminescence kinetics at a detection energy of 140 meV above the PL peak of Ir(piq)₃ (open triangles) and Ir(ppy)₃ (open circles). The dotted line indicates the IRF (260 fs FWHM). The solid lines indicate the best-fits for both datasets, with Ir(piq)₃ having a 95 fs decay representing 96% of the total amplitude and Ir(ppy)₃ having a 150 fs decay representing 88%. The rest of the decay in both datasets is accounted for by a 3 ps component. Copyright 2009 American Chemical Society,¹⁶ reproduced with permission of the rights holder.

It can easily be seen that the dynamics in Ir(piq)₃ are faster, with the femtosecond component fitting to a time constant of 95 fs versus the 150 fs found in Ir(ppy)₃. More of the decay amplitude is also represented by the femtosecond component in Ir(piq)₃ as well, with 96% occurring via ultrafast decay compared to 88% in Ir(ppy)₃.

The advantages of Ir(piq)₃, as discussed above, are the red-shifted features that allow access to luminescence detected from the singlet regions with upconversion spectroscopy – Raman signals from solvents preclude observation of luminescence below 480 nm in materials with limited solubility such as iridium cores. Luminescence at 550 nm, on the shoulder of the assigned ¹MLCT absorption feature is shown in Figure 6.6.

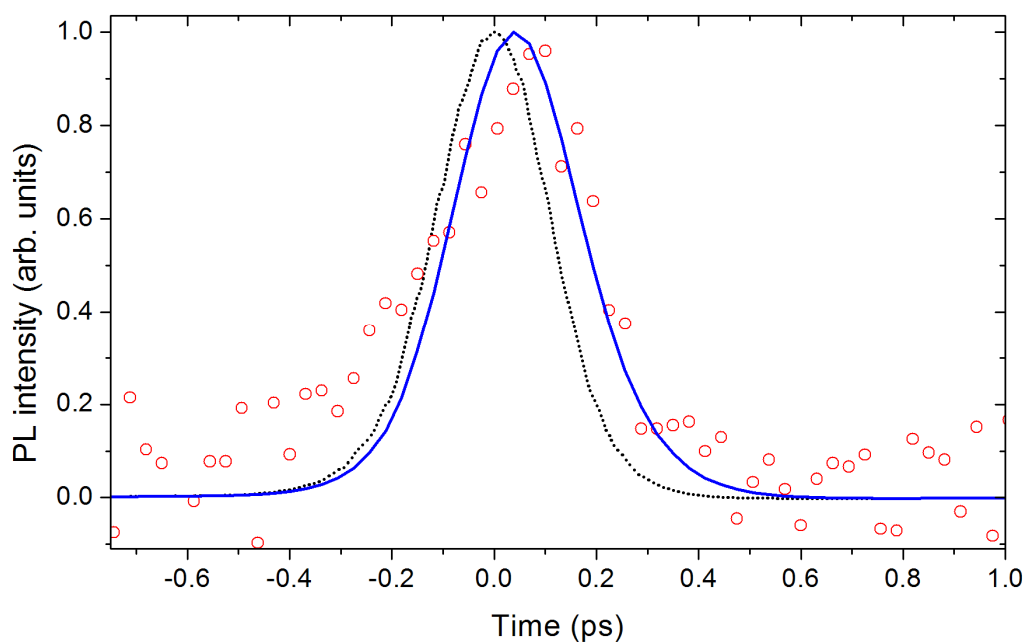


Figure 6.6. Ultrafast luminescence at a detection wavelength of 550 nm of $\text{Ir}(\text{piq})_3$ – representing a detection energy of 270 meV above the PL peak. The dotted line indicates the IRF (260 fs FWHM). While the dataset is noisy the best-fit was found to be a time constant of 70 fs (solid line) representing 100% of the decay. Copyright 2009 American Chemical Society,¹⁶ reproduced with permission of the rights holder.

As can be seen the recorded kinetics are of rather poor quality and have been fitted to give a time constant of 70 fs but the error of margin on this value would be quite substantive. To obtain a better observation of fluorescence, and thus a better measure on the ISC rate, the upconversion setup itself was substantially optimised (maximising optical routing and alignment to generate maximum luminescence and collect and upconvert as much of it as possible), and higher energy fluorescence was also looked at. The $\text{Ir}(\text{piq})_3$ absorption spectrum, Figure 6.2, indicates that at higher detection energies (400-525 nm) stronger optically coupled MLCT transitions exist, so emission from this region should show stronger luminescence, and therefore give better signal/noise when recording in this region.

Luminescence detected at 480 nm, on the peak of what is likely the second $^1\text{MLCT}$ state, and at 520 nm, on the red-side of that state, is shown in Figure 6.7.

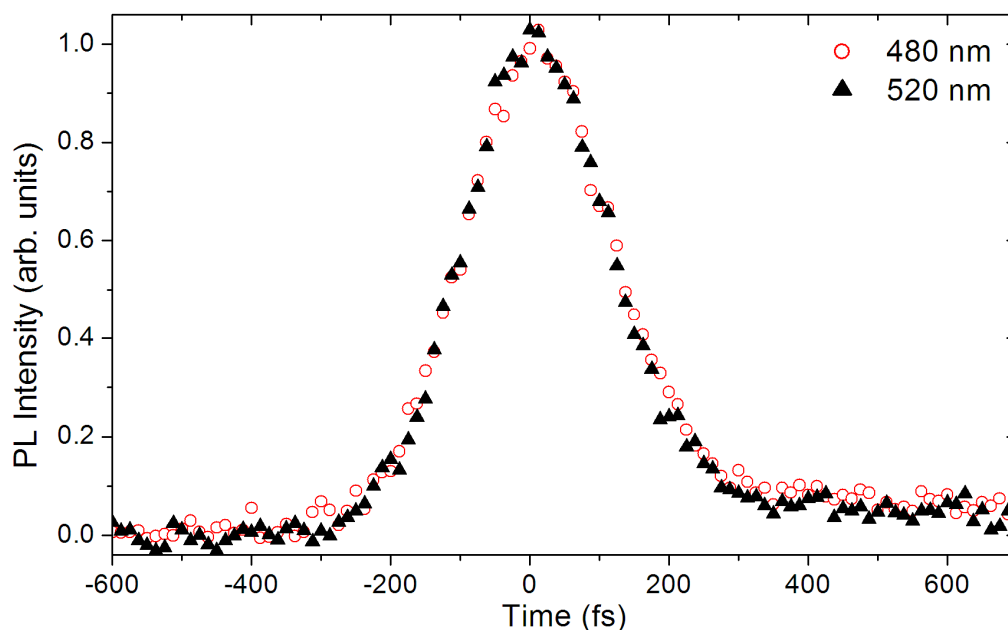


Figure 6.7. Ultrafast luminescence kinetics of Ir(piq)₃ at detection wavelengths of 480 nm (open circles) and 520 nm (closed triangles) indicating that they are identical to each other.

The two sets of kinetics appear to be identical, indicating they embody either emission from the same state or are representative of the same process. The kinetics at both wavelengths were averaged to produce better signal to noise and enable a tighter bound on fitting errors. The resultant kinetic trace and best-fit are shown in Figure 6.8.

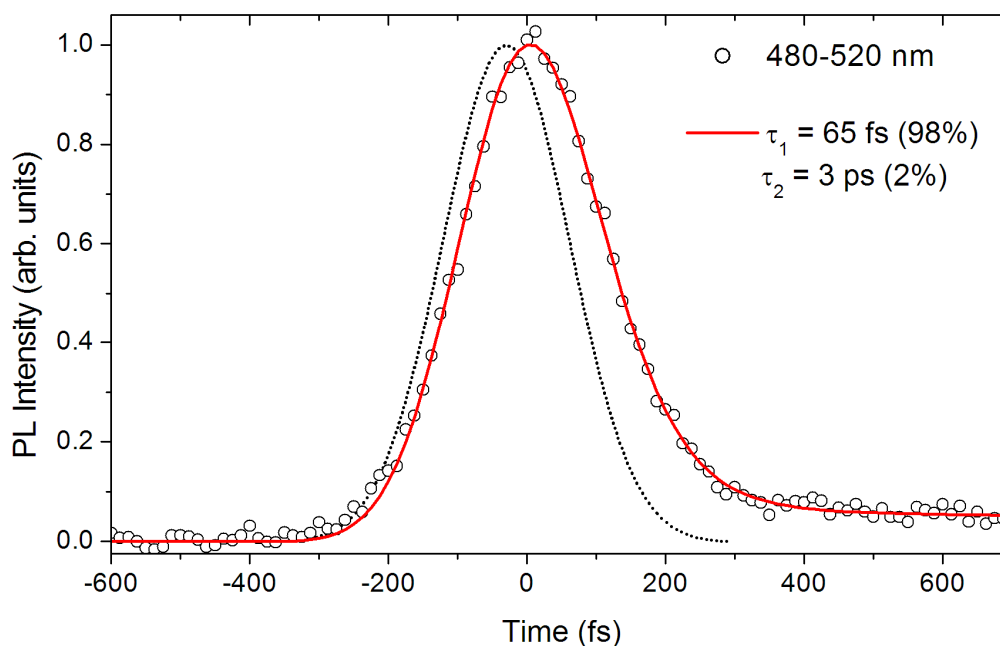


Figure 6.8. Ultrafast luminescence kinetics of Ir(piq)₃ in the region 480-520 nm. The kinetics from the two datasets in Figure 6.7 were averaged together to produce one dataset representing the region (open circles). The dotted line indicates the IRF (220 fs FWHM). The solid line is the best-fit of the dataset and gives a decay of 65 ± 5 fs representing 98% of the total decay, the other 2% of amplitude being fitted as a 3 ps component. The error in the femtosecond time constant was deduced from support plane analysis as discussed in the text.

The best-fit value was found to be 65 fs (98%) with a small (2%) 3 ps decay also present. The kinetics clearly have a high signal-to-noise and hence it was of interest to pursue a detailed error analysis to give as tight a bound as possible on the time constant. This was achieved with support plane analysis. The two averaged datasets (480 and 520 nm) were both acquired by averaging numerous scans, with standard error in the mean values calculated at each point in each dataset from the individual scans. Errors from each point in both datasets were then added in quadrature to give a final standard error in the mean value for each point in the final dataset. Fitting was then performed to find the reduced chi-square minimum, the errors at each point in each dataset being used to calculate the reduced chi-square values. Support plane analysis – the exploration of the reduced chi-squared (χ^2_{R}) surface – is regarded as one of the better ways of determining reasonable uncertainties of fitted parameters.

The support plane analysis was undertaken using calculated confidence intervals, as described by Lakowicz.¹⁷ Briefly, the confidence interval is described as the χ^2_{R} value at which the probability, P, is equal to 0.32, i.e. the value of the χ^2_{R} is one standard deviation away from the χ^2_{R} minimum. This value is defined by equation 6.1 below:¹⁷

$$F_x = \frac{\chi^2_{\text{R}}(\text{par})}{\chi^2_{\text{R}}(\text{min})} = 1 + \frac{p}{\nu} F(p, \nu, P) \quad [6.1]$$

where F_x is the multiplier on the χ^2_{R} minimum to give the value of χ^2_{R} at one standard deviation of error ($\chi^2_{\text{R}}(\text{par})$), p is the number of fitting parameters, ν is the degrees of freedom and $F(p, \nu, P)$ is the F-Statistic value with p parameters, ν degrees of freedom and a probability, P, of 0.32. Inputting the values found from the data used here, $p = 4$ and $\nu = 120$ gives an F-Statistic value of ~ 1.18 , which implies that $F_x = 1.039$. Thus given that the χ^2_{R} was found to be 1.0158, the one standard deviation value of χ^2_{R} is 1.0554. Uncertainty in a parameter can therefore be estimated by refitting the data while fixing the value of that parameter (leaving all others free), recording the χ^2_{R} value and finding when this becomes larger than the one standard deviation value calculated above. Visualization of the results of this procedure takes the form of a two dimensional plot of χ^2_{R} vs. parameter value, producing a parabola with a horizontal line indicating the error threshold, as shown in Figure 6.9.

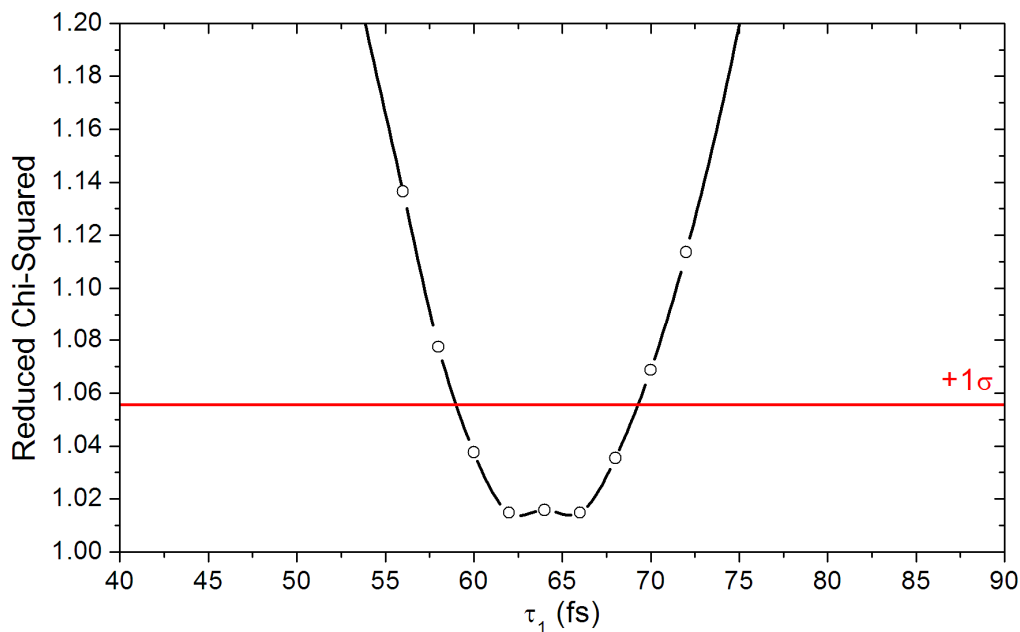


Figure 6.9. Reduced chi-square parabola with variation of τ_1 . All parameters in the fit of the 480-520 nm dataset as shown in Figure 6.8 were left free and τ_1 was varied with the reduced chi-square value noted at certain fixed values of τ_1 . A 1σ confidence limit is calculated as discussed in the text, and the intersection of the reduced chi-square parabola and the 1σ line give the error values as quoted of ± 5 fs.

The values of τ_1 where the 1σ line intersects with the parabola gives the error values for the parameter, hence τ_1 can be stated to be 65 ± 5 fs.

6.5 Ultrafast Transient Absorption Dynamics of Ir(piq)₃

Transient absorption measurements can help to identify and assign ultrafast excited state processes, however as has been seen with other iridium complexes (Chapters 4 and 5), excited state transient absorption kinetics may not show any imprint of the processes that are occurring due to an overlap of excited state features.

Transient absorption kinetics in Ir(piq)₃, however, show interesting dynamics on the ultrafast timescale. Shown in Figure 6.10 are the observed transient kinetics

when pumping at 400 nm and probing at both 600 and 675 nm. At all probe wavelengths the recorded signal is positive, representing excited state absorption.

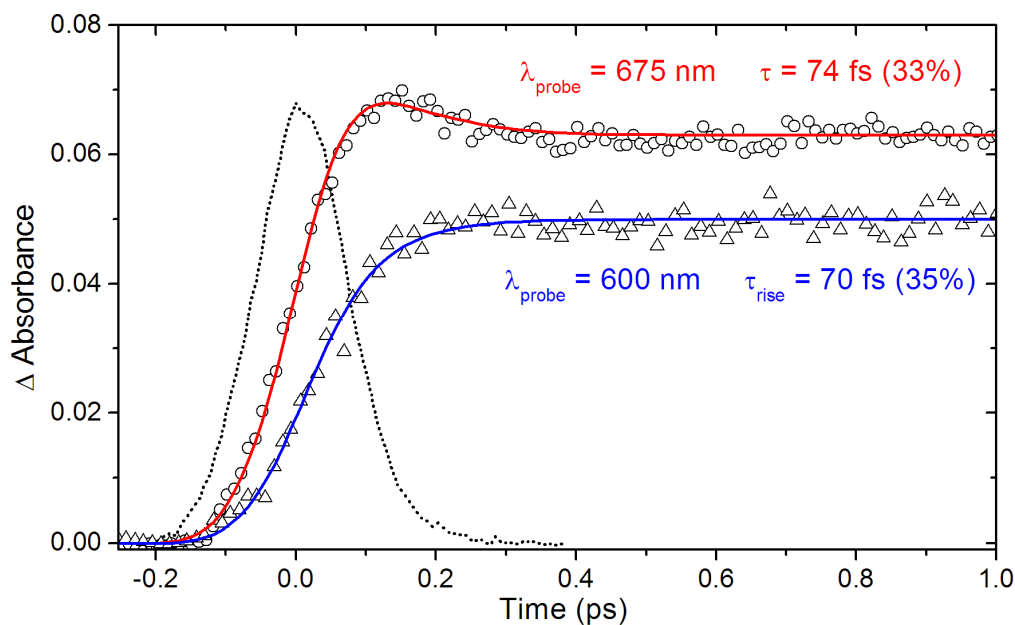


Figure 6.10. Recorded transient absorption signals of Ir(piq)₃ with $\lambda_{\text{pump}} = 400$ nm. The kinetics when probing at 600 nm (open triangles) and 675 nm (open circles) are shown. The dotted line indicates the instrument response function (185 fs FWHM) and the solid lines indicate the best fits with the time constants of the rise/decay as shown in the legend. Copyright 2009 American Chemical Society,¹⁶ reproduced with permission of the rights holder.

Fitting to the kinetics for 675 nm probe gives a decay of 74 ± 10 fs ($33 \pm 3\%$ amplitude) followed by a long lived nanosecond offset. The errors are deduced from the range of time constants and amplitudes that would still produce an acceptable fit. At 600 nm probe the kinetics fit to a rise-time constant of 70 ± 20 fs representing $35 \pm 15\%$ of the rise (the other 65% being instantaneous), with no decay being observed at all. Transient absorption dynamics were found to be unchanged out to long time periods, with a stable transient signal out to 200 ps shown in Figure 6.11. The transient was generally found to be unchanged out to ~ 500 ps, which was the upper limit on the delay line scanning range. Varying the probe wavelengths enables the reconstruction of the excited state absorption spectrum, as shown in Figure 6.12.

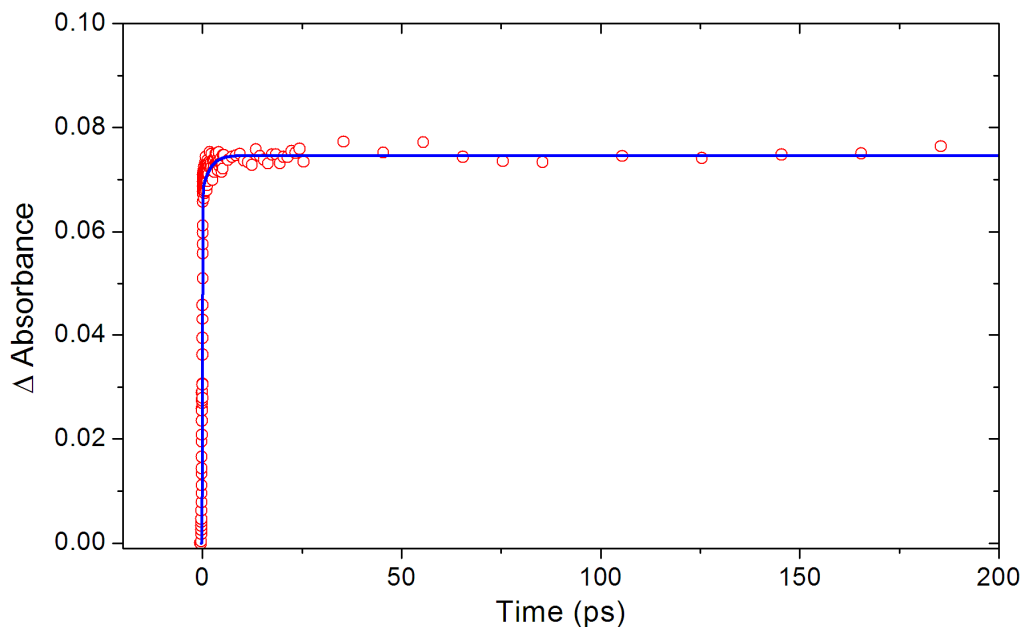


Figure 6.11. Transient absorption signal out to 200 ps of Ir(piq)₃ with $\lambda_{\text{pump}} = 400$ nm, $\lambda_{\text{probe}} = 630$ nm. After the initial formation of the transient, no dynamics are observed at all.

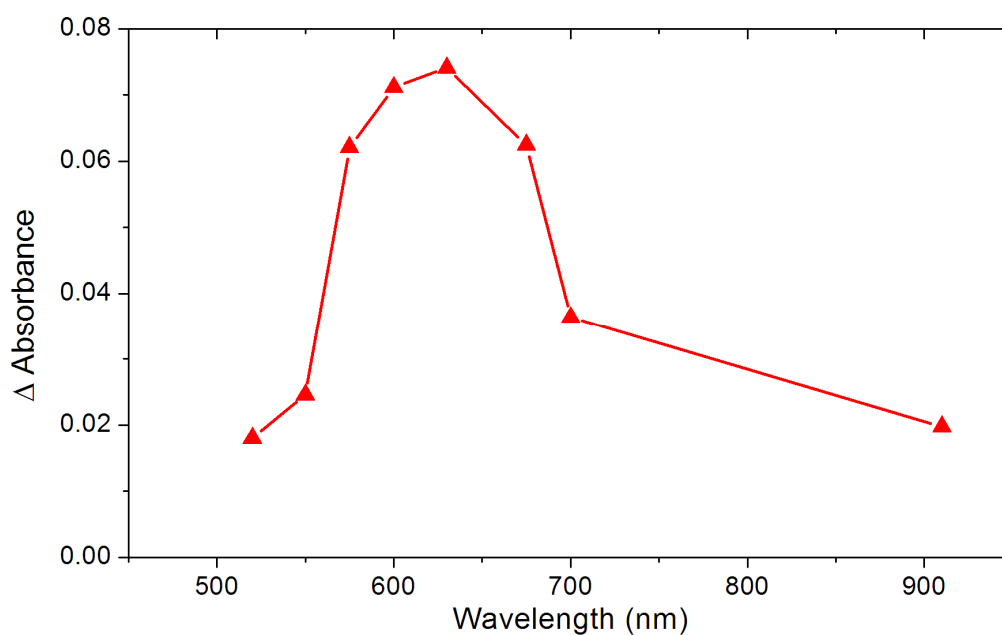


Figure 6.12. Excited state absorption spectrum of Ir(piq)₃ reconstructed from the transient signal values after ~ 500 fs. The spectrum shows a strong absorption feature centred ~ 625 nm with a tail extending out into the infra-red.

The excited state absorption spectrum shows some structure, with a clear peak coinciding with the steady state PL spectrum (625 nm) and falling off at shorter and longer wavelengths.

6.6 Interpretation of Ultrafast Dynamics

The results presented allow the elucidation of the intersystem crossing process in an iridium complex to be observed and characterised for the first time. Discussing the observed processes from low to high energy starting with observations of ultrafast luminescence from the lowest $^3\text{MLCT}$ state (Figure 6.4), the kinetics are as expected and interpreted as has previously been discussed in Chapter 4. That all materials looked at show the same decay process in the steady state PL region gives ever greater evidence that this is a process that is common to this class of materials and embodies population redistribution amongst the electronic substates of the lowest $^3\text{MLCT}$ state.

Observation of luminescence at 140 meV of excess energy, Figure 6.5, shows a clear and decisive conclusion when the dynamics are compared to the smaller $\text{Ir}(\text{ppy})_3$ molecule. Dissipation of excess energy at 140 meV is facilitated by intramolecular vibrational redistribution (IVR) and it is found that the decay time constant of IVR in $\text{Ir}(\text{piq})_3$ is 95 fs as compared to 150 fs in $\text{Ir}(\text{ppy})_3$. Looking at the molecular structure of the material itself the additional material in $\text{Ir}(\text{piq})_3$ as compared to $\text{Ir}(\text{ppy})_3$ is highlighted in red in Figure 6.13. It can be concluded that the extra material on the molecule enables faster dissipation of excess energy by IVR. More dissipation is found to occur by IVR (96%) when compared to $\text{Ir}(\text{ppy})_3$, (88%) as was also observed in the dendrimer materials as presented in Chapter 5. While the dendrimers showed no notable increase in the rate of IVR, with $\text{Ir}(\text{piq})_3$ however, the rate also shows a clear increase. The enhancement of the rate here is because the chemical additions are more strongly connected to the ligand. With the dendrimers the extra material, and vibrational dissipation, was mediated through a single C-C bond between the ligand and the dendron. Here,

however, the extra phenyl is fused onto the pyridine, creating a highly chemically integrated system and so the vibrational energy can redistribute unhindered within the extra material – indeed since the excited state will already sit on the entire phenylisoquinoline ligand area spatial redistribution is likely not required, just a redistribution from high to low frequency vibrational modes.

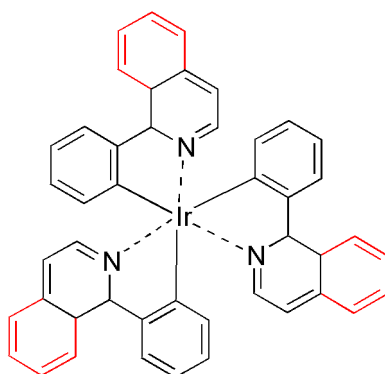


Figure 6.13. Chemical structure of Ir(pi-q)₃. Highlighted in red are the fused phenyl additions that turn the prototypical Ir(ppy)₃ molecule into the studied Ir(pi-q)₃.

Observation of intersystem crossing in iridium complexes, as was noted earlier, is not a trivial matter and has not previously been reported in any materials. The first attempt at observing the ¹MLCT → ³MLCT movement in Ir(pi-q)₃ was achieved by looking at luminescence at a detection wavelength of 550 nm. The absorption feature at this wavelength has been assigned as a ¹MLCT transition,¹⁴ and thus it was of interest to see what the luminescence dynamics were as they should represent fluorescence and thus the dynamics of the population leaving the ¹MLCT state to move to the ³MLCT manifold. Unfortunately the quality of the recorded luminescence at this wavelength was not especially good, Figure 6.6, however a best-fit on the kinetics can be made and gave a decay time constant of 70 fs.

At higher detection energies the ability to resolve fluorescence was substantially greater, attributed to the higher oscillator strengths of the electronic transitions as one moves to higher energy in the ¹MLCT manifold. The recorded kinetics,

Figure 6.7 and Figure 6.8, provided a much better bound on the rate of ISC. Deconvolution of the kinetics with the instrument response function indicates that the decays are not instrument limited, and best-fit to a time constant of 65 ± 5 fs with a support plane analysis giving the one standard deviation error values. This is therefore the observed ISC time constant in Ir(piq)₃, and its implications when viewed against other transition metal complex ISC times as discussed in Section 6.2 suggest that the rate of ISC in an iridium complex is of the same order as has previously been reported – 15-40 fs being reported in ruthenium.^{2, 3} The comparable time constants further confirms the view that there is no direct correlation between the mass of the central metal ion and the rate of ISC – iridium is heavier than ruthenium, yet ISC times are slightly slower.

The time constant of ISC observed in luminescence studies is confirmed with complementary transient absorption measurements. Unusual for an iridium complex, Ir(piq)₃ shows some change of its transient absorption on ultrafast timescales, Figure 6.10. Interpretation of these results, as is often the case with TA measurements, requires more care and thought than the obvious and direct assignments that can be made with luminescence measurements. Firstly, the recorded positive signal indicates that excited state absorption rather than stimulated emission is observed. What is then seen is that with 675 nm probe there is an instantaneous formation of the transient state followed by a 74 ± 10 fs decay. This decay represents $33 \pm 3\%$ of the total decay amplitude with the rest fitted as a long lived nanosecond transient. At 600 nm probe, however, 65% of the excited state forms instantaneously while the remaining $35 \pm 15\%$ forms with a rise-time of 70 ± 20 fs. Once formed the transient state is then unchanged out to at least 500 ps.

In interpreting these transient absorption dynamics it is first prudent to tie the two different probe wavelength kinetics together. Both have a process occurring with a time constant of ~ 70 fs so it would seem fair to attribute this time constant to the same mechanism. It is then a fair assumption to compare the dynamics in TA with those in the luminescence studies. As has been established in Chapter 4,

vibrational cooling and dissipation events within an electronic state are not likely to show in transient absorption kinetics due to the small degrees of change – when small amounts of relaxation occur within an electronic state, excited state absorption up to higher states is likely to be little affected. Thus the ~ 70 fs process observed with TA representing an electronic movement correlates well with the ~ 70 fs process observed in luminescence measurements that was assigned as ISC.

If the dynamics seen in the TA measurements at 600 and 675 nm probe wavelengths embody ISC it is pertinent to ask why they are as they are, i.e. why does this manifest itself as a rise-time in the transient formation at 600 nm probe and a decay at 675 nm probe. Without detailed knowledge of the excited state electronic structure in $\text{Ir}(\text{piq})_3$, which is unfortunately not available, exact reasoning for these processes is not possible, however excited state absorption of transition metal complexes with metal-ligand charge transfer excitation has been found to be dominated by $\pi\text{-}\pi^*$ absorption of the reduced ligand from 400-700 nm.¹⁸ It is also found that the highest occupied molecular orbital in iridium complexes comprises a mixture of the 5d orbital from the iridium ion and the π orbitals of the ligand.¹⁹⁻²² Hence upon photoexcitation with the formation of MLCT states there is a decrease in the electron density in the π orbital on the ligand. The electronic configuration is schematically represented in Figure 6.14.

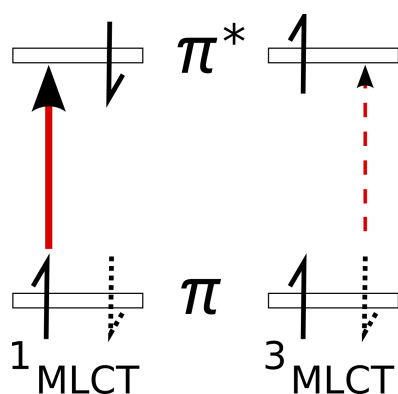


Figure 6.14. Schematic representation of the frontier ligand orbitals of Ir(piq)₃ upon photoexcitation to MLCT states. Due to the partial contribution to the MLCT states by π orbitals of the ligand there is a greater probability of excited state absorption from the singlet MLCT state as opposed to the triplet, explaining the observed decay in the transient seen when probing at 675 nm.

The dotted spin-down electron indicates that the MLCT state comprises partial π electron density (the other contributor being the 5d electron from the iridium ion). Since excited state absorption from the MLCT states, as is observed here, has to occur via a fully spin-allowed π - π^* transition there is thus a greater amount of excited state absorption (ESA) when in the ¹MLCT manifold as compared with the ³MLCT. The ~ 70 fs decay with 675 nm probe therefore embodies the movement of the population from the singlet to triplet MLCT state. The ~ 70 fs rise-time that is observed when probing at shorter wavelengths can hence be interpreted as a stronger excited state absorption from the ³MLCT state.

Recording the strength of the transient signals after 500 fs across multiple probe wavelengths enabled the reconstruction of the excited state absorption spectrum, Figure 6.12. With a departure from other iridium complexes the ESA spectrum shows some clear structure and it was of interest to overlay this feature with the steady state absorption and PL spectra to give better context for what was recorded, as shown in Figure 6.15.

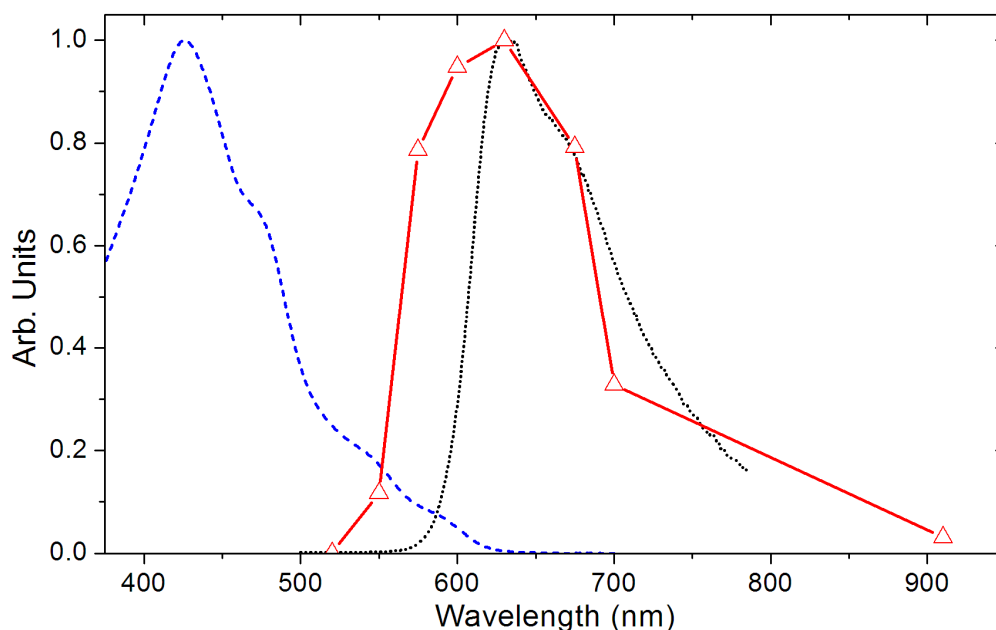


Figure 6.15. Excited state absorption spectrum (solid line and open triangle) of $\text{Ir}(\text{piq})_3$ displayed along with the material's steady state absorption (dashed line) and PL (dotted line) spectra. The ESA spectrum appears to follow the PL spectrum but this can be explained by a reduction in ESA at higher energy due to ground state bleaching, as indicated by the existence in the absorption spectrum at wavelengths < 600 nm.

While instinctively one might correlate the ESA spectrum with that of the steady state PL this is likely just as a result of ground state bleaching causing a drop in the transient signal < 600 nm, as indicated by the steady state absorption spectrum. The ESA spectrum therefore appears to actually follow the other investigated iridium complexes fairly closely, with a strong ESA at short wavelengths dropping off across the visible spectrum to leave a tail out into the infra-red. The small similar ligands of all these materials likely leaves this as a characteristic feature, and the strong ESA therefore precludes any simple mechanisms for achieving optical gain in these phosphorescent materials.

The work presented has therefore enabled the ultrafast evolution of the excited state in an iridium complex to be fully tracked for the first time. A schematic outline of the observed processes in is shown in Figure 6.16.

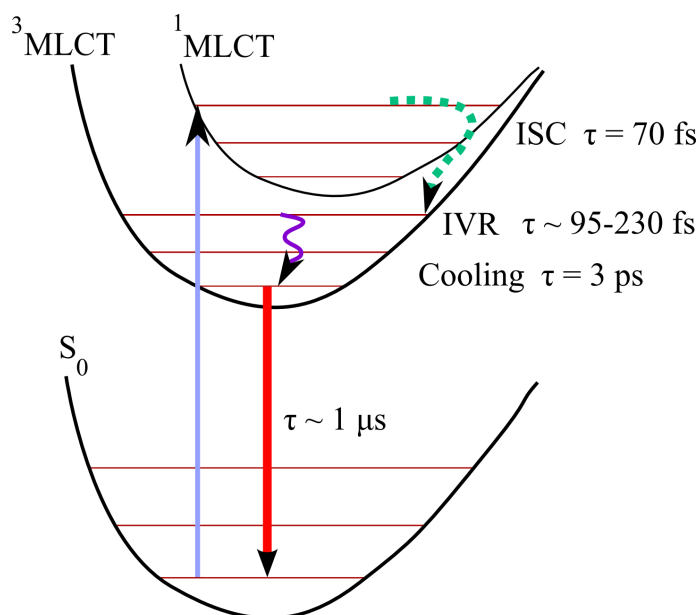


Figure 6.16. General schematic of the observed ultrafast processes in Ir(piq)₃. After initial excitation the ¹MLCT state is accessed and intersystem crossing to the ³MLCT manifold is found to proceed with a time constant of ~ 70 fs. Intramolecular vibrational redistribution and vibrational cooling to the surrounding solvent molecules proceeds on a 95-230 fs and 3 ps timescale to facilitate dissipation of excess energy, leaving the relaxed population in the lowest ³MLCT state to radiatively decay to the ground state on the microsecond timescale. Copyright 2009 American Chemical Society,¹⁶ reproduced with permission of the rights holder.

6.7 Conclusions

Observation of the ultrafast photophysical processes in the iridium complex Ir(piq)₃ has allowed a detailed evolution of the excited state decay mechanisms to be explored for the first time in this class of materials. The addition of a fused phenyl onto the pyridine of the ligand to create the isoquinoline moiety enables extra electron delocalisation and therefore red-shifting of optical transitions. This red-shifting moves ¹MLCT transitions lower in energy and therefore accessible for observation with upconversion spectroscopy, enabling clear observation of fluorescence from an iridium complex for the first time. A time constant of the decay of fluorescence of 65 ± 5 fs was observed and this embodies the ¹MLCT → ³MLCT population movement, i.e. the rate of intersystem crossing. Changes in the transient absorption dynamics with time constants ~ 70 fs have helped to support the ultrafast luminescence observations. A time constant of 70 fs for ISC in iridium complexes is consistent with the very fast evolution of the excited state that has been observed in other transition metal complexes and indicates that the highly spin-mixed nature of the singlet and triplet enables very efficient population transfer to the ³MLCT manifold. Once in the ³MLCT manifold the population is found to quickly relax to the lowest ³MLCT state. At 140 meV of excess energy Ir(piq)₃ shows a decay of the luminescence with a time constant of 95 fs representing 96% of the total decay (the other 4% being 3 picosecond vibrational cooling to the solvent). The 95 fs decay, embodying dissipation of excess energy by intramolecular vibrational redistribution is faster than when the decay at the same value of excess energy is monitored in Ir(ppy)₃, indicating that the larger ligands in Ir(piq)₃ enable faster dissipation of excess energy by IVR. Finally, once the population reaches the lowest ³MLCT state redistribution amongst the electronic substates is found to occur with time constants of 230 fs and 3 ps.

6.8 References

- [1] L.S. Forster, *Coordination Chemistry Reviews*, 2006. **250**(15-16): p. 2023-2033.
- [2] A.C. Bhasikuttan, M. Suzuki, S. Nakashima, and T. Okada, *Journal of the American Chemical Society*, 2002. **124**(28): p. 8398-8405.
- [3] A. Cannizzo, F. van Mourik, W. Gawelda, G. Zgrablic, C. Bressler, and M. Chergui, *Angewandte Chemie-International Edition*, 2006. **45**(19): p. 3174-3176.
- [4] W. Gawelda, A. Cannizzo, V.T. Pham, F. vanMourik, C. Bressler, and M. Chergui, *Journal of the American Chemical Society*, 2007. **129**(26): p. 8199-8206.
- [5] C. Bressler, C. Milne, V.T. Pham, A. ElNahhas, R.M. van der Veen, W. Gawelda, S. Johnson, P. Beaud, D. Grolimund, M. Kaiser, C.N. Borca, G. Ingold, R. Abela, and M. Chergui, *Science*, 2009. **323**(5913): p. 489-492.
- [6] Z. Abedin-Siddique, T. Ohno, K. Nozaki, and T. Tsubomura, *Inorganic Chemistry*, 2004. **43**(2): p. 663-673.
- [7] Z. Abedin-Siddique, Y. Yamamoto, T. Ohno, and K. Nozaki, *Inorganic Chemistry*, 2003. **42**(20): p. 6366-6378.
- [8] N.H. Damrauer, G. Cerullo, A. Yeh, T.R. Boussie, C.V. Shank, and J.K. McCusker, *Science*, 1997. **275**(5296): p. 54-57.
- [9] A. Cannizzo, A.M. Blanco-Rodriguez, A. El Nahhas, J. Sebera, S. Zalis, J.A. Vlcek, and M. Chergui, *Journal of the American Chemical Society*, 2008. **130**(28): p. 8967-8974.
- [10] G. Benko, J. Kallioinen, J.E.I. Korppi-Tommola, A.P. Yartsev, and V. Sundstrom, *Journal of the American Chemical Society*, 2002. **124**(3): p. 489-493.
- [11] K.C. Tang, K.L. Liu, and I.C. Chen, *Chemical Physics Letters*, 2004. **386**(4-6): p. 437-441.
- [12] G.J. Hedley, A. Ruseckas, and I.D.W. Samuel, *Chemical Physics Letters*, 2008. **450**(4-6): p. 292-296.

- [13] M.S. Lowry and S. Bernhard, *European Journal of Chemistry-A*, 2006. **12**(31): p. 7970-7977.
- [14] A. Tsuboyama, H. Iwawaki, M. Furugori, T. Mukaide, J. Kamatani, S. Igawa, T. Moriyama, S. Miura, T. Takiguchi, S. Okada, M. Hoshino, and K. Ueno, *Journal of the American Chemical Society*, 2003. **125**(42): p. 12971-12979.
- [15] G.J. Hedley, A. Ruseckas, Z. Liu, S.-C. Lo, P.L. Burn, and I.D.W. Samuel, *Journal of the American Chemical Society*, 2008. **130**(36): p. 11842–11843.
- [16] G.J. Hedley, A. Ruseckas, and I.D.W. Samuel, *Journal of Physical Chemistry A*, 2009. **113**(1): p. 2-4.
- [17] J.R. Lakowicz, *Principles of Fluorescence Spectroscopy*. 2nd ed. 1999: Kluwer Academic.
- [18] J.K. McCusker, *Accounts of Chemical Research*, 2003. **36**(12): p. 876-887.
- [19] P.J. Hay, *Journal of Physical Chemistry A*, 2002. **106**(8): p. 1634-1641.
- [20] E. Jansson, B. Minaev, S. Schrader, and H. Agren, *Chemical Physics*, 2007. **333**(2-3): p. 157-167.
- [21] K. Nozaki, *Journal of the Chinese Chemical Society*, 2006. **53**(1): p. 101-112.
- [22] T. Matsushita, T. Asada, and S. Koseki, *Journal of Physical Chemistry C*, 2007. **111**(18): p. 6897-6903.

7

Intramolecular Vibrational Redistribution Controls Internal Conversion in an Iridium Complex

What does a scanner see? he asked himself. I mean, really see? Into the head? Down into the heart? . . . see into me – into us – clearly or darkly? . . . if the scanner sees only darkly, the way I myself do, then we are cursed.

Philip K. Dick, *A Scanner Darkly*, 1977

7.1 Introduction

This chapter presents a detailed investigation of internal conversion (IC) between singlet metal-ligand charge transfer (MLCT) states in a deep red emitting iridium complex, Ir(dbfliq)₂acac. Three ¹MLCT states are identified and fluorescence from each of them is observed using upconversion spectroscopy. Global analysis of luminescence dynamics across the singlet emission region using a consecutive rate equation enables the time constants of IC for each state to be deduced. Time constants of decay from each singlet state are found to be dependent on the value of vibrational energy that is stored in the molecule. If less than 0.6 eV of energy is stored then IC, facilitated by intramolecular vibrational redistribution (IVR), is fast, 10-45 fs. If greater than 0.6 eV of vibrational energy is stored inside the molecule then IC slows down to 65-75 fs. It is therefore concluded that IVR, the dissipative mechanism that enables the wavepacket to reach the state crossing point, controls IC, as the rate of IVR dictates how quickly the population reaches the crossing point. As the vibrational energy stored in the molecule increases the

rate of IVR slows, with more stored energy forcing redistribution to lower frequency, slower, vibrational modes.

In Section 7.2 I provide a discussion of the process of non-radiative electronic decay, commonly called internal conversion, and the two main IC mechanisms that are identified, weak and strong coupling regimes. In Section 7.3 the steady state photophysical properties of the deep red emitting material under investigation are presented, including optical absorption and photoluminescence data and spectral fitting to both. In Section 7.4 the calculation of experimental transition dipole moments are shown, enabling the assignment of the identified spectral features. In Section 7.5 the primary ultrafast luminescence measurements are shown, detailing the implemented consecutive relaxation model and presentation of the globally analysed luminescence data. Decay associated fluorescence spectra for each of the identified singlet states are reconstructed from the results of global analysis and the effect of variation of the excitation energy is investigated. Detailed error analysis to support the assigned time constants is provided. In Section 7.6 discussion of the presented data is provided, outlining that IC is mediated by the amount of vibrational energy that is stored in the molecule and a schematic for the overall relaxation process through the three ¹MLCT states and across into the triplet manifold is shown. Finally in Section 7.7 the conclusions from this work are presented.

7.2 Internal Conversion: Non-radiative Electronic Relaxation

Internal conversion (IC) is defined as the non-radiative relaxation from one excited electronic state to another. The study of IC is an entire field in its own right and sits at the interface between fundamental chemistry and physics. Two regimes of internal conversion can be defined,¹ the weak coupling limit and the strong coupling case.

In the weak coupling limit, illustrated in Figure 7.1, the potential energy surfaces of the two electronic states, Denoted S_n and S_{n-1} , are little offset in vibrational space, and therefore the upper state can be thought of as sitting above and partially inside the lower state, akin to Russian nested dolls. A non-radiative electronic transition from the upper to lower state occurs due to the appropriate vibrational overlap between the two states – all non-radiative relaxation has to occur by vibrational pathways. When a large polyatomic molecule in a surrounding solvent medium is defined then large degeneracies of vibrational states exist and so an IC event becomes essentially irreversible as it is highly improbable that with a large number of final states degenerate with the initial that the system will return to the initial state.² IC in the weak coupling limit is governed by the so-called energy gap law,¹ where the probability of a non-radiative electronic transition is proportional to the energy gap, ΔE , between the initial and final state, hence closely spaced states have a high probability of IC, while significantly separated states (such as an $S_1 \rightarrow S_0$ transition, greater than ~ 1 eV) have lower probabilities.

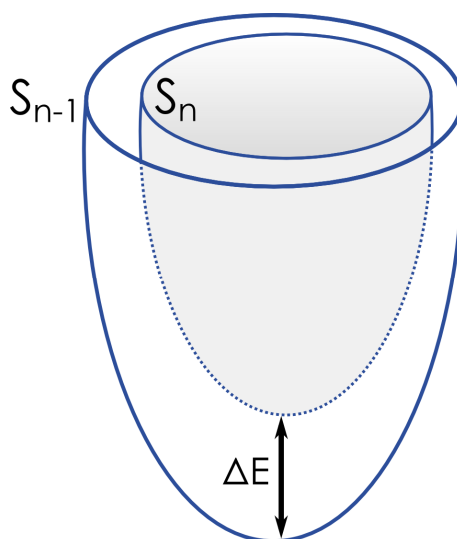


Figure 7.1. Schematic representation of the weak coupling case for internal conversion between two electronic states, S_n and S_{n-1} in vibrational space, redrawn from reference 1. S_n sits inside and somewhat above S_{n-1} with an energy gap, ΔE . Large overlap of the vibrational wavefunctions between the two states leads to non-radiative electronic decay.

In the strong coupling case, illustrated in Figure 7.2, the potential energy surface of the upper state, S_n , is now substantially shifted in vibrational space with regard to the lower state, S_{n-1} . The vibrational overlap between the two states is hence now much reduced, and therefore weak coupling IC is unlikely. The shift of the upper state, while reducing probability of weak coupling IC, has the consequence of creating an intersection between the upper and lower potential energy surfaces. Non-radiative relaxation can now occur via this intersection by strong coupling between the states, the intersection – or conical intersection as it is traditionally denoted³⁻⁷ – can enable very fast IC between the states once the population in the upper state reaches the crossing point as there is no barrier required for crossing, with the wavepacket already being in the correct place for a fast transition to the lower state.

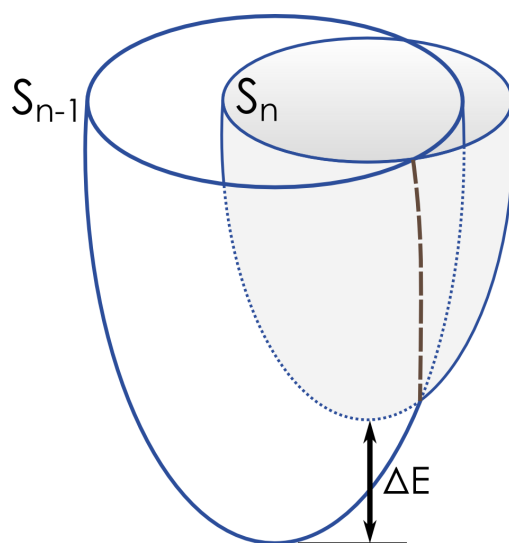


Figure 7.2. Schematic representation of the strong coupling case for internal conversion between two electronic states S_n and S_{n-1} in vibrational space, redrawn from reference 1. A large vibrational offset between the two states leads to poor overlap of the vibrational wavefunctions. Due to the offset between the two surfaces an intersection (dashed line) exists between the states, enabling fast internal conversion to occur.

A more detailed view of strong coupling IC is provided with an exemplar by Diao et al.⁸ on the $S_1 \rightarrow S_0$ IC event in azulene – the results of which are schematically shown in Figure 7.3, as reproduced from reference 8.

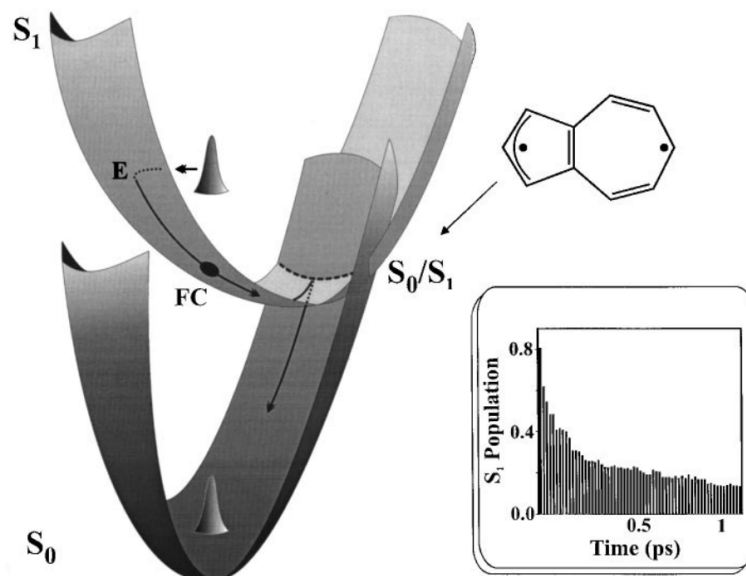


Figure 7.3. Schematic of the conical intersection between S_1 and S_0 in azulene, the chemical structure is shown top right, reproduced from reference 8. Vibrational relaxation occurs within S_1 to reach the crossing point, followed by relaxation within S_0 . Bottom right is a simulation of the population in S_1 when the excited state reaches the intersection, indicating that the population moves to S_0 with a characteristic time. Reproduced with permission of the rights holder.

Figure 7.3 shows the evolution of an excited state from the initially accessed upper state, before vibrational relaxation within the S_1 state to reach the conical intersection. Once at the intersection the population transfer between the states is modelled with a nonadiabatic dynamics simulation (inset histogram) and shown to have a characteristic time – the population can rapidly transfer back and forth between the states for some time before everything is finally in the lower state and relaxes down away from the intersection.

It is therefore obvious that the simple conventional photophysical description of internal conversion, as presented in a traditional Jablonski diagram, belies a very large and complex amount of quantum mechanical and vibrational detail that, as stated earlier, defines an entire field of science. A detailed quantum mechanical description of such processes in large polyatomic molecules, such as conjugated materials with strong visible optical transitions, is extremely difficult, owing to the large and complex nature of the molecule which creates complex potential energy surfaces.

The material presented here is just a qualitative overview of the two processes that non-radiative electronic decay can occur by. Lengthy and complex treatments, primarily theoretical, of these processes have been reported⁹⁻¹⁵ and experimental investigations have, even in recent times, been limited to studies of relatively simple small polyatomic molecules such as benzene^{16, 17} and azulene,⁸ and generally in the gas phase, owing to the great difficulty in observing internal conversion processes clearly.

Aside from a fundamental scientific interest in the process of internal conversion, the process and its mechanisms have important implications in a number of photophysical systems of merit. Protection of biological molecules from UV radiation^{18, 19} relies upon fast IC to convert potentially harmful electronic energy into heat in DNA molecules, reducing the effects of photodamage. Energy and charge transfer processes in artificial photosynthesis²⁰⁻²² and solar cells²³ can compete with IC, mediating more efficient energy conversion from higher energy excited states.²⁴

Internal conversion amongst excited metal-ligand charge transfer (MLCT) states is an almost completely unexplored area. One study of ultrafast processes in a ruthenium complex²⁵ observed three relaxation processes and assigned them as IC between three singlet states, however a careful and detailed presentation of the assignment was somewhat lacking and so it was not clear exactly what the identified processes truly represented. The highly spin-mixed nature of MLCT

states, facilitating a very fast movement to the lowest $^3\text{MLCT}$ state, mean that IC between excited states is difficult to observe with a high degree of certainty.

7.3 Photophysical Properties of a Deep Red Emitting Iridium Complex

7.3.1. *The Material Under Investigation*

The material chosen for studies of singlet IC processes was the deep red emitting heteroleptic iridium complex bis(2-(9,9-dibutylfluorenyl)-1-isoquinoline(acetylacetonate) iridium (III), denoted as $\text{Ir}(\text{dbfliq})_2\text{acac}$, structure shown in Figure 7.4. The material was purchased from American Dye Source Inc. and was used without further purification. $\text{Ir}(\text{dbfliq})_2\text{acac}$ was dissolved in tetrahydrofuran (THF) (spectrophotometric grade, Sigma Aldrich Co.) at a concentration of 2 mg/ml. The red emitting spectral properties are evident just from looking at the chemical structure as in addition to the isoquinoline moiety found in $\text{Ir}(\text{piq})_3$ (Chapter 6), the other half of the ligand has now been transformed into a fluorene unit, adding more conjugated material to further delocalise excited states and thus red-shift electronic transitions. Two long carbon butyl chains are attached to the fluorene unit and aid solubility. In this material one of the ligands is tied off as an electronically inactive acetylacetonate unit making this a heteroleptic complex.

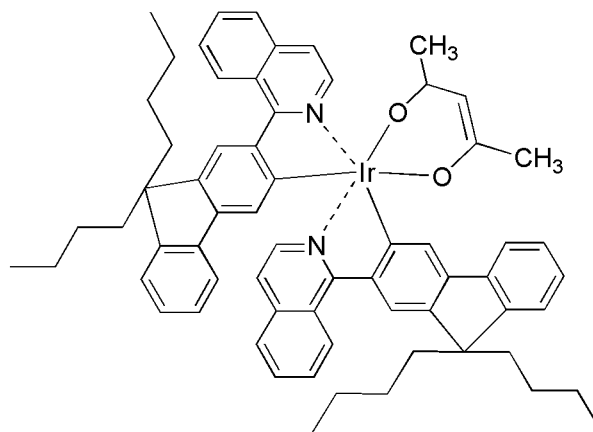


Figure 7.4. Chemical structure of bis(2-(9,9-dibutylfluorenyl)-1-isoquinoline(acetylacetonate) iridium (III), denoted as Ir(dbfliq)₂acac, that is used in these ultrafast photophysical studies.

The steady state optical absorption and photoluminescence (PL) spectra of Ir(dbfliq)₂acac are shown in Figure 7.5.

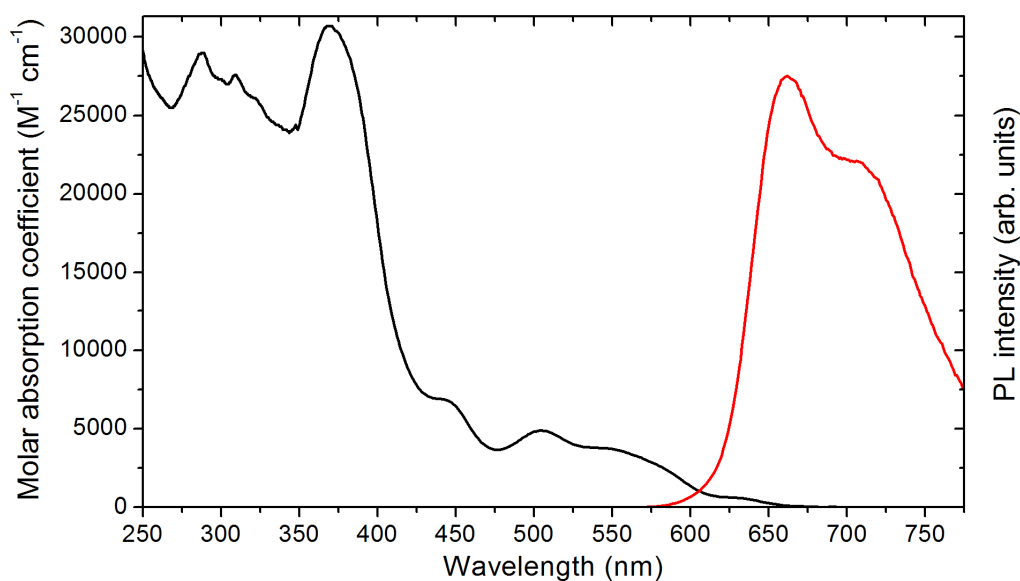


Figure 7.5. Optical absorption and photoluminescence ($\lambda_{\text{ex}} = 400 \text{ nm}$) spectra of Ir(dbfliq)₂acac in THF.

Noticeable features in the steady state spectra are the deep red emission from the material ($\lambda_{\text{peak}} = 660 \text{ nm}$) and the substantial structure that is visible in the absorption spectrum in the 400-600 nm region.

For full photophysical characterisation it was of interest to measure the natural lifetime and photoluminescence quantum yield (PLQY) of Ir(dbfliq)₂acac. A solution was prepared with an optical density of 0.1 at a wavelength of 400 nm and was degassed with three freeze-pump-thaw cycles. Measuring the PL spectrum of the material and comparing against a standard reference of a quinine sulphate solution enabled the PLQY of Ir(dbfliq)₂acac to be calculated to be 25%. The luminescence lifetime of the material was recorded using a time-correlated single photon counting setup and was measured to be 1 μs. Accordingly using equation 7.1 below, the radiative lifetime can be deduced, and was found to be 4 μs.

$$\tau_R = \frac{\tau_{PL}}{PLQY} \quad [7.1]$$

Ir(dbfliq)₂acac therefore shows efficient deep red emission and significant structural features in its absorption spectrum. It was hence of interest to employ spectral fitting to these features and to the PL spectrum to elucidate what likely transitions exist in the material and what the dominant vibrational mode is.

7.3.2 Spectral Fitting

Fitting can be performed on the PL spectrum to give an idea what the strongest vibrational mode coupled to the ³MLCT → S₀ optical transition is in Ir(dbfliq)₂acac. Taking the PL spectrum, multiplying the signal at each wavelength by the wavelength squared (to correct for the wavelength dependence in the monochromator in the fluorimeter, which has a linear dependence of bandwidths in the wavelength rather than energy scales) and converting to the energy scale enabled spectral fitting of the main features, taking care to ensure that the spacing between each the Gaussians was linked to ensure a vibrational progression is being fitted. Spacing between the vibronic Gaussians of 0.14 eV

was found to fit best. The best-fit parameters are shown in Table 7.1 and the fit is graphically presented in Figure 7.6, with residuals shown beneath the spectrum.

Transition	Central Energy (eV)	FWHM (eV)
$T_1 \rightarrow S_0$ (0-0)	1.88	0.14
$T_1 \rightarrow S_0$ (0-1)	1.74	0.15
$T_1 \rightarrow S_0$ (0-2)	1.6	0.15

Table 7.1. Fitting parameters of PL spectrum to the superposition of Gaussian functions, shown graphically in Figure 7.6, indicating central energy of Gaussian and full-width half maximum.

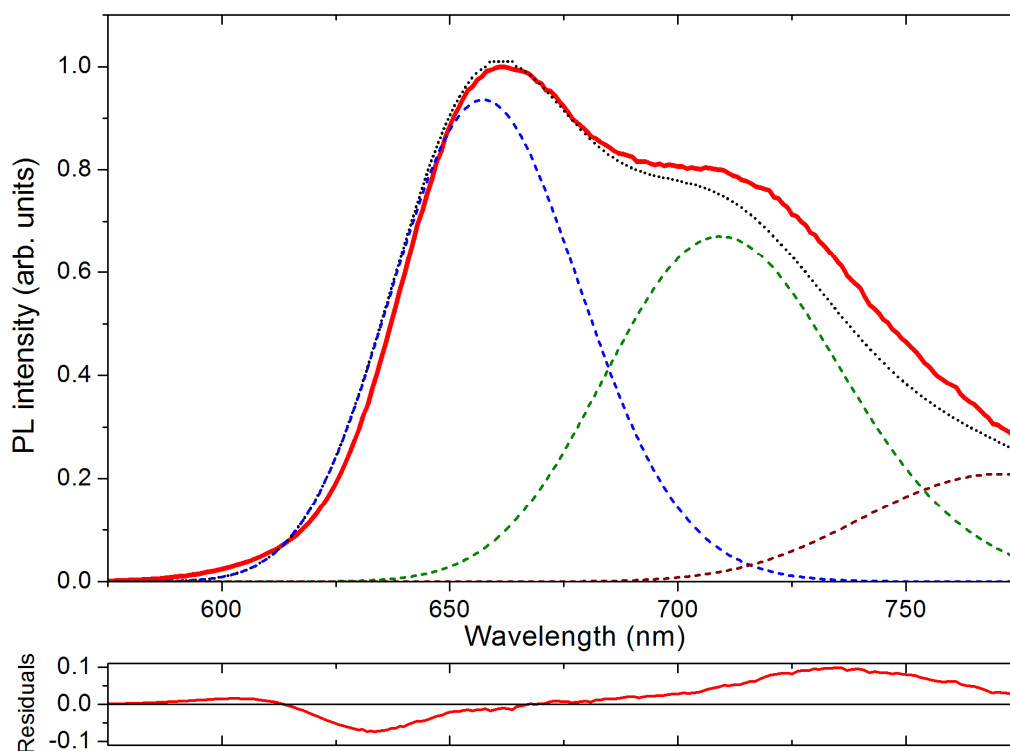


Figure 7.6. PL spectrum ($\lambda_{\text{ex}} = 400$ nm) of Ir(dbfliq)₂acac in THF (solid line). The fitted Gaussian functions to the PL spectrum are shown as dashed lines, representing the 0-0, 0-1 and 0-2 vibronic transitions, with the parameters shown in Table 7.1. The summation of the Gaussians is shown as a dotted line, indicating the relative goodness of the fit, with the residuals plotted below.

Fitting to the absorption spectrum can help elucidate what optical transitions exist in Ir(dbfliq)₂acac. As shown in Figure 7.5, the absorption spectrum shows

significant structure, indicative of multiple transitions, and in an effort to identify and assign these transitions it was desirable to fit multiple Gaussian functions to the data to attempt to reproduce the original spectrum. Fitting was performed with the spectrum converted to an energy scale (eV) and a sensible number of seed Gaussians of approximate amplitude and width were placed according to a visual inspection of the spectrum. Iterating to find the best-fit gave fitting parameters as shown in Table 7.2. The fit is graphically demonstrated in Figure 7.7, converted back to the wavelength scale, showing the individual Gaussians as solid lines and their summation as a dashed line on top of the originating absorption spectrum, with residuals shown below typically being ~ 1% of the total signal in the S_{1-3} region, indicating a very good fit was achieved.

Transition	Central Energy (eV)	FWHM (eV)
$S_0 \rightarrow L_2$	3.86	0.5
$S_0 \rightarrow L_1$	3.32	0.52
$S_0 \rightarrow S_3$	2.77	0.25
$S_0 \rightarrow S_2$	2.47	0.25
$S_0 \rightarrow S_1$	2.21	0.25
$S_0 \rightarrow T_1$	1.95	0.12

Table 7.2. Fitting parameters of absorption spectrum to the superposition of Gaussian functions, shown graphically in Figure 7.7, indicating the central energy of each Gaussian and its full-width half maximum.

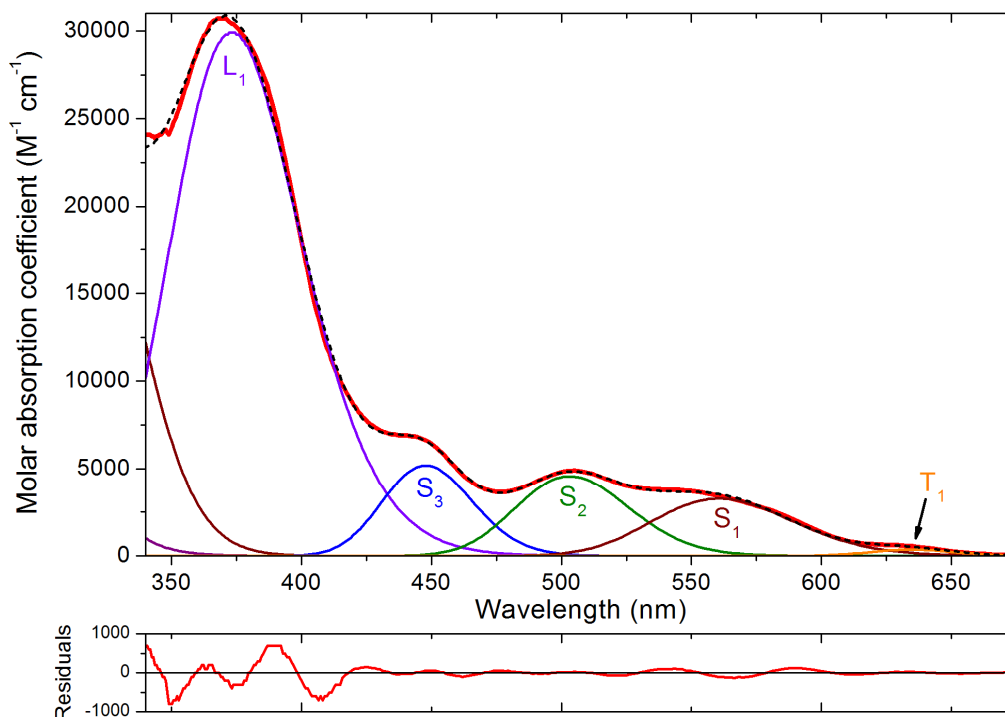


Figure 7.7. Optical absorption spectrum (red solid line) of Ir(dbfliq)₂acac in THF. The fitted Gaussians are shown, with one weak triplet peak identified (T₁), three stronger singlet peaks (S₁₋₃) and strong ligand centred peaks moving into the UV (L₁₊), with the associated fitting parameters shown in Table 7.2. The summation of the fit is shown as a black dashed line, indicating good reproduction of the absorption features. The residuals of the fit are shown below, with values in the identified S₁₋₃ region being ~ 1% of the total signal there.

One very weak state is identified (labelled T₁), three weak states (S₁₋₃) and multiple strong states in the UV (L₁₊). The S states are found to be 0.25 and 0.3 eV apart from each other and are almost equally strong.

The three identified S states became the focus of attention for this work. Their position and strength would generally lead them to be identified as ¹MLCT states, but assignment of such things normally occurs in common characterisation, traditionally achieved in a purely presumptive logical way, and normally under conditions where the true nature of the states is not of high importance to the characterisation that is reported. The spectral fitting performed here is suggestive that there are three Gaussian features, and that the three peaks are separated by ~ 0.25 eV, and narrower spacing, indicative of a vibronic progression of one

electronic state, would not produce an acceptable fit despite repeated attempts. This energy spacing is larger than that between vibronic peaks in the PL spectrum and this suggests transitions to separate distinguishable electronic states. More secure assignment of these three states could be made with further evidence that they are indeed ¹MLCT transitions, evidence that could be provided by looking at the transition dipole moments of the features.

7.4 Calculated Transition Dipole Moments: Assignment of Spectral Features

Transition dipole moment calculations were undertaken to help identify and support the assignments made to the features of the absorption spectrum. To test the validity of the calculated values it is first worth testing this approach by comparing calculated values for the ³MLCT state – comparing the oscillator strength calculated from the recorded emission against the absorption feature assigned as the ³MLCT state (T₁). Both these values can then be compared to theoretical numbers.

The oscillator strength, *f*, is defined by equation 7.2:²⁶

$$f = \frac{4\pi m_e \nu}{3e^2 \hbar} |\mu|^2 \quad [7.2]$$

where *m_e* is the mass of the electron, *ν* is the intensity weighted averaged emission frequency in hertz, *e* is the charge of an electron, *ħ* is planck's constant divided by 2π and *μ* is the transition dipole moment. For luminescence the dipole moment is defined by equation 7.3:^{27, 28}

$$\mu^2 = \frac{3\pi\epsilon_0 \hbar^4 c^3 \langle E^{-3} \rangle}{n_0 \tau_R} \quad [7.3]$$

where ϵ_0 is the vacuum dielectric constant, \hbar is planck's constant divided by 2π , c is the speed of light, n_0 is the refractive index of the solvent, τ_R is the radiative lifetime and $\langle E^{-3} \rangle$ is the intensity weighted average of the luminescence spectrum, defined by equation 7.4:

$$\langle E^{-3} \rangle = \frac{\int E^{-3} I(E) dE}{\int I(E) dE} \quad [7.4]$$

where E is the energy of the luminescence of intensity I in joules. The PLQY of Ir(dbfliq)₂acac is 0.25 and the radiative lifetime is 4 μ s, as stated in Section 7.3.1.

Hence for Ir(dbfliq)₂acac, taking the recorded PL spectrum, the refractive index of THF of 1.4 and using the radiative lifetime of 4 μ s, a dipole moment of 0.41 debye (D) for the emitting ³MLCT state is calculated, which gives an oscillator strength of 1.1×10^{-3} . Comparing this value with the number that can be calculated for the absorption spectrum feature T₁ identified using equation 7.5:²⁷

$$\mu^2 = 9.186 \times 10^{-3} n_0 \int \left[\frac{\epsilon(\nu)}{\nu} \right] d\nu \quad [7.5]$$

where n_0 is the refractive index of the solvent and the integral is the intensity weighted average of the identified absorption feature area when expressed as a molar absorption coefficient. The calculated value of the T₁ Gaussian is therefore 0.54 D, which gives an oscillator strength of 2.2×10^{-3} , a number in good agreement with the value calculated from the PL spectrum. These numbers are congruent with those reported for time dependent density functional theory (TDDFT) calculations by Nozaki on the prototypical Ir(ppy)₃ complex,²⁹ where an oscillator strength of $\sim 8.5 \times 10^{-4}$ is calculated for the highest triplet sublevel.

Utilising the absorption spectrum to calculate the oscillator strengths of the transitions is thus a valid approach and so the three S states of interest can be

looked at. Taking the three S states, S_{1-3} , as separate entities, the experimentally deduced transition dipole moments and oscillator strengths, f , are calculated from the absorption spectrum, with calculated numbers for all transitions provided in Table 7.3. The oscillator strengths for the S states are found to be on the order of 0.05 (a transition dipole moment of 2.5 D). If one were to treat all three features as representing a single electronic state, which is not thought to be the case, then the oscillator strength would be 0.17 (with a corresponding transition dipole moment of 4.22 D). Comparing these values with the numbers that have been reported in theoretical TDDFT studies provides evidence and support for the identification of three separate singlet MLCT states. In work by Hay³⁰ the oscillator strengths of the ten lowest MLCT singlet states of the $\text{Ir}(\text{ppy})_2\text{acac}$ complex are calculated, with the strongest found to be ~ 0.03 and in work by Jansson and co-workers,³¹ on $\text{Ir}(\text{ppy})_3$, the ten lowest singlet states are also calculated, with the strongest reported to be ~ 0.05 . These calculated numbers are in good agreement with the oscillator strengths that are found here for the identified $\text{Ir}(\text{dbfliq})_2\text{acac}$ singlet states, with both homo and heteroleptic complexes showing similar values. Therefore both theoretical studies find that the strongest singlet states are comparable with the experimental values for the S_{1-3} singlet states found here, and much smaller than the 0.17 that would be expected should the singlet region in $\text{Ir}(\text{dbfliq})_2\text{acac}$ be all one singlet state. Calculations on numerous other iridium complexes with differing ligands all show oscillator strengths of the lowest singlet states to be on the order of 0.05,³²⁻³⁷ indicating that this is likely a general feature of lowest singlet MLCT states in iridium complexes. Finally to confirm that the calculations performed here are within the expected range one can find the transition dipole moment and oscillator strength of the identified $L_1 \pi-\pi^*$ ligand centred transition. Based on the absorption spectrum the values found are $\mu = 8.04$ D and $f = 0.82$, and are numbers that are correct for a fully allowed $\pi-\pi^*$ transition, giving confidence to the MLCT values above.

Transition	Transition Dipole Moment (Debye)	Oscillator Strength	Assignment
$T_1 \rightarrow S_0$ (PL)	0.41	0.001	$^3\text{MLCT}$
$S_0 \rightarrow T_1$ (Abs.)	0.54	0.002	$^3\text{MLCT}$
$S_0 \rightarrow S_1$ (Abs.)	2.25	0.042	$^1\text{MLCT}$
$S_0 \rightarrow S_2$ (Abs.)	2.52	0.059	$^1\text{MLCT}$
$S_0 \rightarrow S_3$ (Abs.)	2.53	0.067	$^1\text{MLCT}$
$S_0 \rightarrow L_1$ (Abs.)	8.04	0.815	Ligand Centered

Table 7.3. Experimental transition dipole moments and oscillator strengths obtained using equations 7.2-7.5 of optical transitions identified in absorption and PL spectra.

The spacing and strengths of the identified S_{3-1} features all indicate, therefore, that they are separate electronic MLCT transitions. It is anticipated that the higher $^1\text{MLCT}$ states identified here would be, in smaller iridium complexes such as $\text{Ir}(\text{ppy})_3$, moved to higher energy, and thus hidden amongst the much more strongly absorbing ligand $\pi\text{-}\pi^*$ features. Hence $\text{Ir}(\text{dbfliq})_2\text{acac}$ gives a unique opportunity to study multiple $^1\text{MLCT}$ states in a transition metal complex which, due to their low energy and therefore accessibility with ultrafast luminescence spectroscopy, can give insights into the process of IC amongst singlet states.

7.5 Ultrafast Luminescence Measurements

7.5.1 Proposed Model: Consecutive Relaxation

Ultrafast luminescence dynamics can be observed in the wavelength region across all three identified S states. In consideration of the fact that three states exist and from an initial population in S_3 it is anticipated that the population will cascade down through each state sequentially, a consecutive relaxation model is used, i.e.

$S_3 \rightarrow S_2 \rightarrow S_1 \rightarrow T_1$. A custom fitting equation was implemented for this model, as shown in equation 7.6 and schematically represented in Figure 7.8, derived from consecutive rate equations.³⁸

$$F(t) = \left\{ \begin{array}{l} A_1 e^{-k_1 t} + A_2 \left[\frac{k_1}{k_2 - k_1} (e^{-k_1 t} - e^{-k_2 t}) \right] + \\ A_3 k_1 k_2 \left[\left(\frac{e^{-k_1 t}}{(k_2 - k_1)(k_3 - k_1)} \right) - \left(\frac{e^{-k_2 t}}{(k_2 - k_1)(k_3 - k_2)} \right) + \left(\frac{e^{-k_3 t}}{(k_3 - k_1)(k_3 - k_2)} \right) \right] \end{array} \right\} \otimes IRF \quad [7.6]$$

where A_n and k_n are the amplitude and rate-constant (reciprocal of time constant) of each component and the IRF represents convolution and temporal shift with respect to the instrument response function. The decay time constant of one process is used as the rise-time constant of the next (i.e. the S_3 decay is used as the S_2 rise-time).

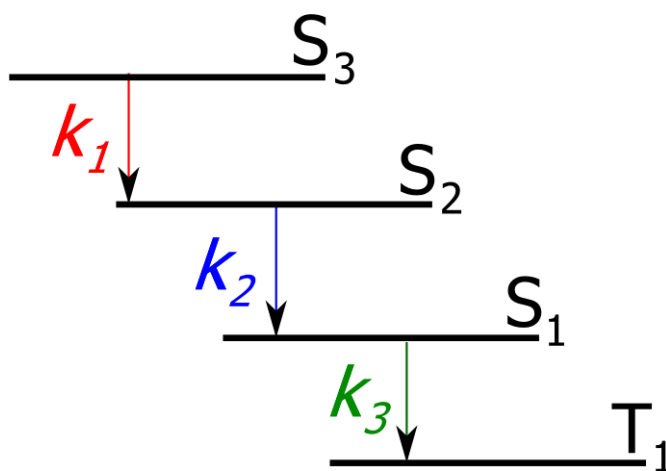


Figure 7.8. Schematic of the consecutive relaxation model used. Four states are defined and the sequential relaxation down through them drawn, with rate constants as shown.

Due to the overlap of each of the states, Figure 7.7, fitting to the luminescence dynamics has to take into account that emission at certain wavelengths (for example 530 nm) contains contributions from more than one state (for 530 nm, 50% S_2 and 50% S_1). To fit across a large number of datasets and with common

and co-dependent processes occurring global analysis, that is the simultaneous fitting of kinetics across multiple datasets to the same linked time constants, can help to both identify the associated time constants much quicker than manual iteration (swapping between datasets) and provide a better bound on the fitted time constant errors due to the large number of datasets.

7.5.2 Global Fitting to Luminescence Data

Global fitting was performed with the “Globals WE” software package developed at the Laboratory for Fluorescence Dynamics at the University of Illinois at Urbana-Champaign.³⁹

Ultrafast luminescence dynamics were observed in Ir(dbfliq)₂acac across the range 460-660 nm, with kinetics being recorded every 10 nm, covering the steady state PL region and the transitions to the three separate singlet states: S₁, S₂ and S₃. With 400 nm excitation Raman signals obscured true dynamics at wavelengths shorter than 480 nm, so to record the kinetics at 460 nm the excitation was moved to 380 nm – the lack of any Raman signal at this detection wavelength was confirmed by observing the dynamics from a sample cell filled solely with THF, with no signal being found. Global analysis with instrument response deconvolution was completed for 12 wavelengths across the ¹MLCT region, 460-580 nm. Global fitting was performed with all variables free and the exponential time constants linked. Sensible seed values were given for the time constants and individual amplitudes and the software then iterated to find the global reduced chi-squared minimum. An instantaneous formation of the population of the S₃ state (< 10 fs) from the initially excited L₁ state with 380/400 nm excitation was assumed, and this is confirmed by the lack of any observable rise in kinetics in the S₃ → S₀ transition region. While the custom fitting equation used (equation 7.6) defined three exponential decays to be used in the global fit, the luminescence decay at a particular wavelength could always be described by at most 2 exponentials.

The resultant global reduced chi-squared minimum fit showed τ_1 to have instrument limited emission with a time constant of ≤ 50 fs (represented by 460 nm dynamics in Figure 7.9) and it is shown in Section 7.5.4 that with consideration of emission intensity amplitudes that τ_1 must be < 20 fs.

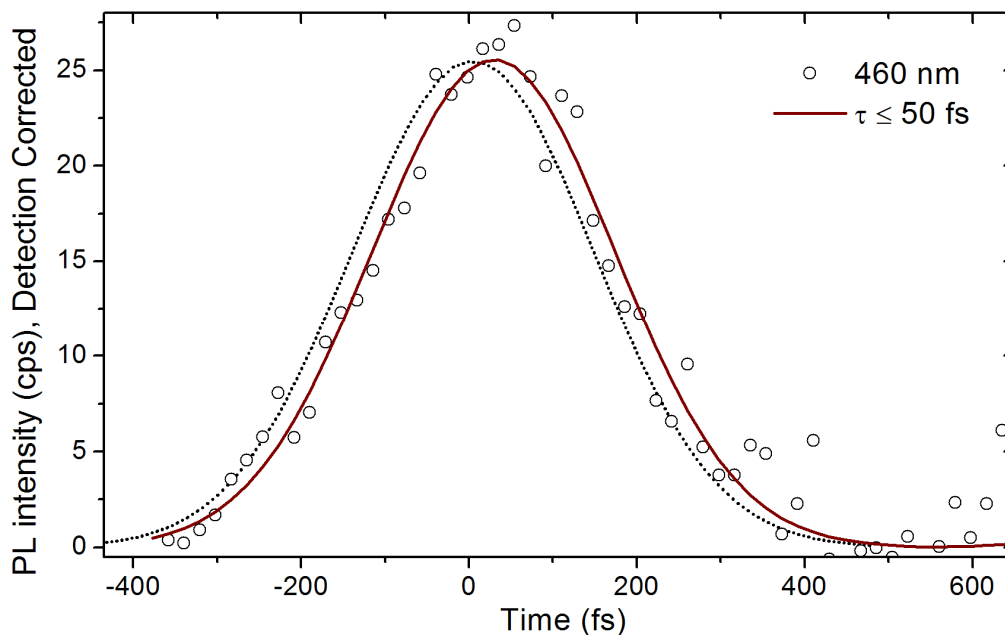


Figure 7.9. Ultrafast luminescence measurements of Ir(dbfliq)₂acac with 380 nm excitation and 460 nm detection. Deconvolution with the instrument response function (310 fs FWHM, dotted line) indicates that the emission is instrument limited, fitting to a time constant of 50 fs or less (solid line).

The lifetime of the second exponential decay, τ_2 , was found to be the only component (100%) at 500 nm, as shown in Figure 7.10, and the time constant was found to be 65 ± 7 fs where the stated error is the 1σ confidence level for the reduced chi-square error analysis (see Section 7.5.4). The third exponential component, τ_3 , was found to be 75 ± 12 fs, and dynamics at 570 nm (Figure 7.11) were found to consist of solely τ_3 decay (100%).

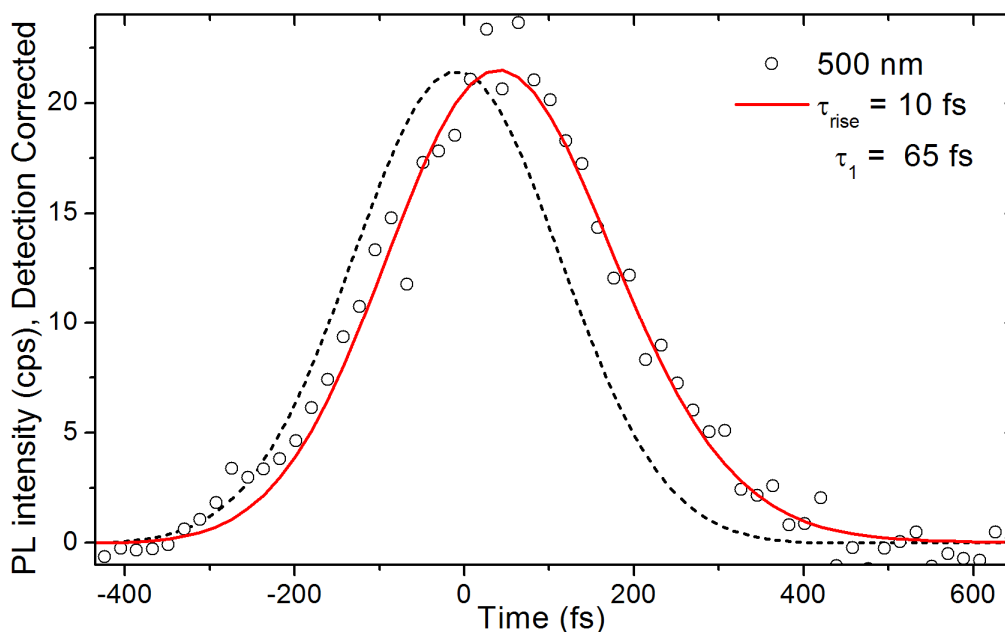


Figure 7.10. Ultrafast luminescence measurements of Ir(dbfliq)₂acac with 400 nm excitation and 500 nm detection. Upon global analysis deconvolution with the IRF (280 fs FWHM, dotted line) gives best-fit values of a 10 fs rise-time constant and a 65 fs decay time constant (solid line).

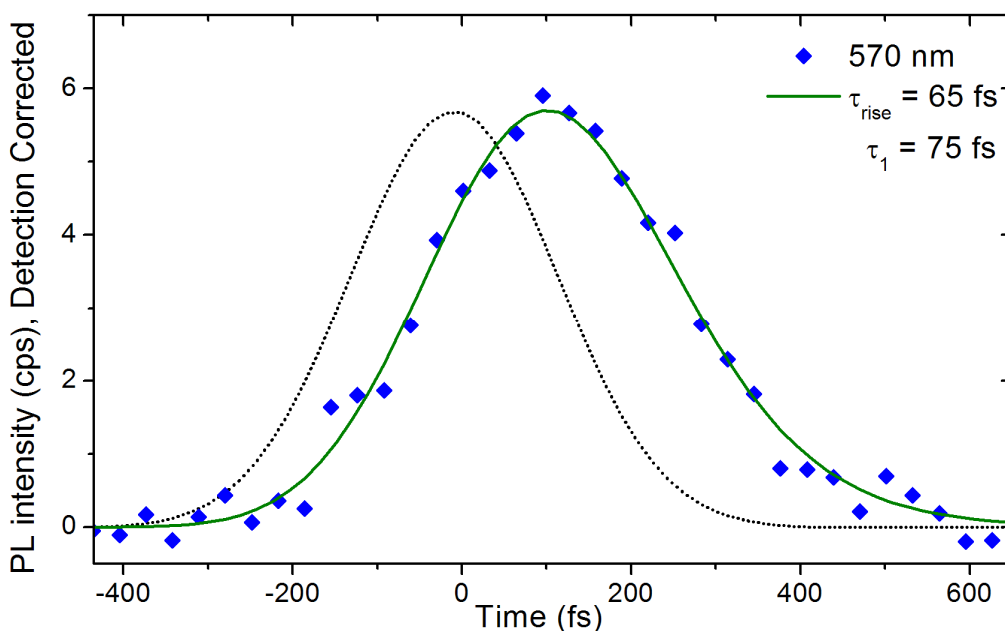


Figure 7.11. Ultrafast luminescence measurements of Ir(dbfliq)₂acac with 400 nm excitation and 570 nm detection. Upon global analysis deconvolution with the IRF (280 fs FWHM, dotted line) gives best-fit values of a 65 fs rise-time constant and a 75 fs decay time constant (solid line).

From these kinetics and global fitting we can therefore deduce that emission from S_3 decays in less than 50 fs, emission from S_2 , presupposing that the population is fed from S_3 , would have a rise-time constant equal to the lifetime of S_3 , and a decay time constant of 65 fs. Emission from S_1 has a rise-time constant of 65 fs (having been fed from S_2) and a decay time constant of 75 fs. Plots of fits with residuals at all wavelengths are shown in Figure 7.12 below, with a full table of results provided in Table 7.4.

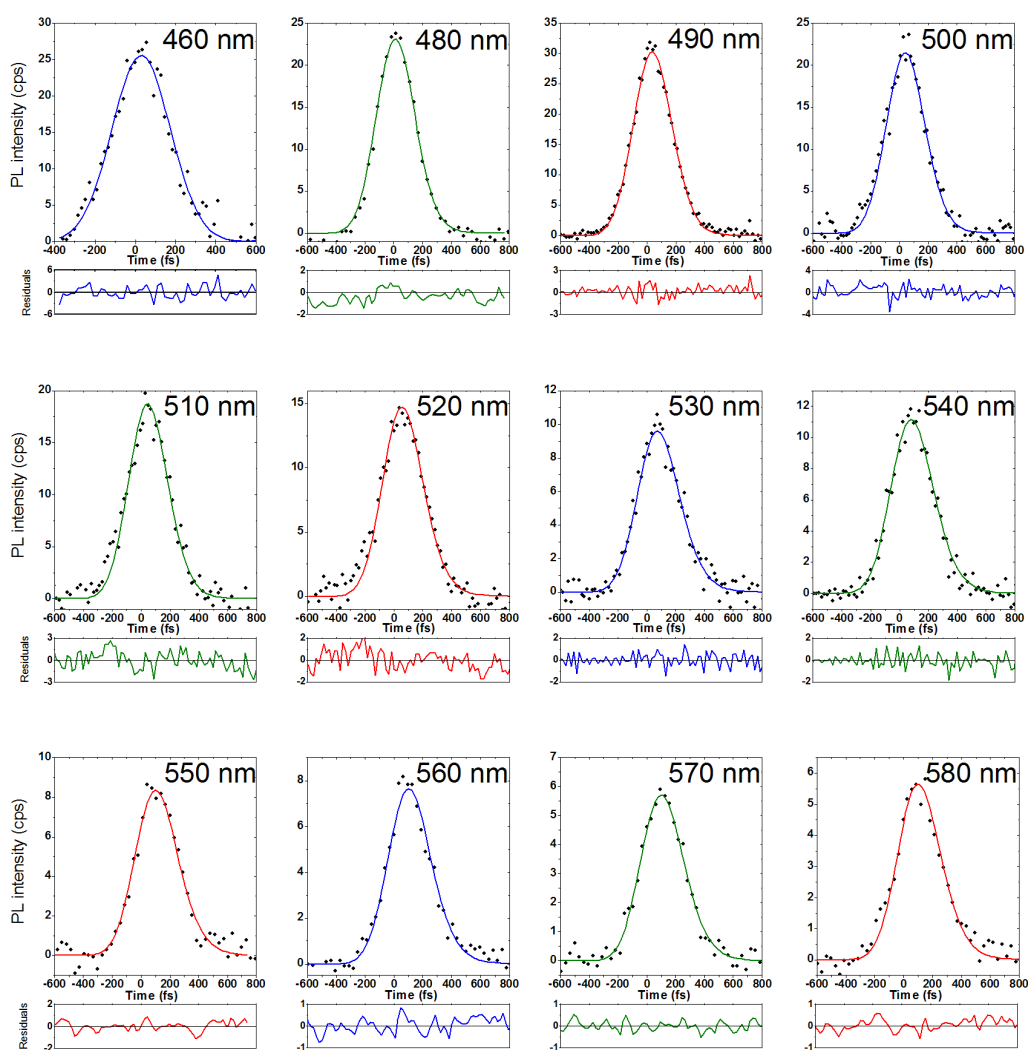


Figure 7.12. Ultrafast luminescence data (closed circles), global fits (solid lines) and residuals (beneath each window) for all 12 wavelengths that were globally analysed.

		τ_1 (fs)	τ_2 (fs)	τ_3 (fs)	Global $R\chi^2$
Global Variables →		10	65	75	1.37976
Emission Wavelength (nm)	Global Amplitude	A_1	A_2	A_3	Local $R\chi^2$
460	0.563	1	0	0	2.13177
480	0.88	0.462	0.538	0	1.88416
490	1	0.085	0.915	0	0.97182
500	0.687	0	1	0	1.71178
510	0.599	0	0.929	0.071	2.42487
520	0.469	0	0.727	0.273	1.98215
530	0.3	0	0.428	0.572	0.88047
540	0.345	0	0.318	0.682	1.29268
550	0.248	0	0	1	1.18026
560	0.227	0	0	1	1.02147
570	0.169	0	0	1	0.78864
580	0.168	0	0	1	1.01976

Table 7.4. Global Analysis best-fit parameters, overall and for each of the 12 wavelengths included in the global fit. The global amplitudes represent the multiplier on the individual amplitude components at each wavelength – all data as globally analysed was wavelength intensity sensitivity corrected for the instrument as discussed in the text.

Luminescence dynamics, therefore, allow us to ascertain that there is a decrease in the rate of internal conversion in the course of the relaxation to lower MLCT states. The relaxation also follows in an orderly manner, with a progression from higher to lower MLCT states. The observed luminescence dynamics in Ir(dbfliq)₂acac hence give an opportunity to obtain direct information on cascading relaxation processes involving several singlet MLCT states. To that end, it was of strong interest to utilise the amplitude information in each decay component at each wavelength that is provided by the global analysis to enable the construction of decay associated fluorescence spectra (DAFS) to glean information on the processes occurring amongst the singlet states – processes that have hitherto been difficult to deduce.

7.5.3 Decay Associated Fluorescence Spectra

Production of the DAFS for each decay component was carried out with correction for the wavelength dependence and detection sensitivity of the upconversion experimental setup with a white light source (Bentham IL7S), as detailed in Chapter 3. Correction for variation of the excitation wavelength (data at 460 nm was recorded with 380 nm excitation) was achieved by the use of Coumarin 102 laser dye solution, with count rates at both excitation wavelengths being recorded and a correction factor derived. Absorbance of the laser dye solution at both 380 and 400 nm was higher than 3, hence the derived correction factor accounted for the combined ratio in the upconversion and detection sensitivity when at two different excitation wavelengths. A further correction was applied to account for the difference in the absorbance of Ir(dbfliq)₂acac at 380 nm compared to 400 nm. Recording the fitted amplitudes across this wide spectral region based on the above parameters gives reconstructed spectra for each of the identified states, as shown in Figure 7.13.

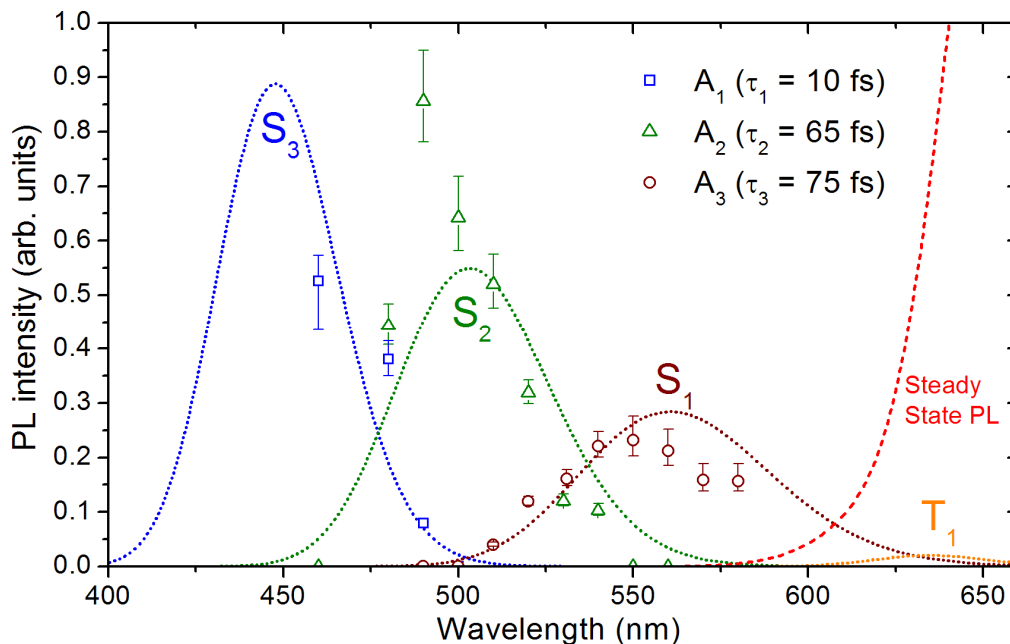


Figure 7.13. Amplitudes of fluorescence from S_3 , S_2 and S_1 excited states obtained from the global fit using equation 7.6 assuming a sequential relaxation process ($S_3 \rightarrow S_2 \rightarrow S_1$). The legend shows the time constant of relaxation for each of the individual states. Fluorescence intensities were corrected for the wavelength dependence sensitivity of the upconversion setup before fitting. Errors are obtained by utilising the time constant errors to produce the maximum and minimum amplitude values. The dotted lines show the predicted spectra of the non-relaxed fluorescence from each singlet state obtained from the Gaussian components of the absorption spectrum by applying a frequency cube correction according to equation 7.7.

For comparison with the already identified absorption features of the three singlet states, optical absorption and spontaneous emission can be related by Einstein's relation, where Einstein's A coefficient of spontaneous emission is related to the B coefficient of absorption for an electronic transition $ub \rightarrow la$ as shown in equation 7.7.²⁸

$$A_{ub \rightarrow la} = 8\pi h (\nu_{ub \rightarrow la})^3 n^3 c^{-3} B_{ub \rightarrow la} \quad [7.7]$$

where A and B are the coefficients, h is planck's constant, n is the refractive index, c the speed of light and ν is the $ub \rightarrow la$ transition frequency. It can be seen that the relationship between absorption and emission is dependent on the

transition frequency to the power of three, thus comparison of absorption and emission intensities requires multiplication of the central absorption frequency to the third power. Plotted in Figure 7.13 along with the reconstructed emission spectra are the three originating absorption Gaussians for each state, appropriately corrected. Errors for each emission point are also plotted and were deduced from the variations in the amplitude that were recorded at each wavelength when the associated errors in the relevant time constants were used to force the time constants at their extreme long/short values. The reconstructed spectra do not enforce what the amplitudes are across the entire range, i.e. the signal strength (and hence final amplitudes) at each wavelength are independent. The decay of S_3 , which solely from kinetics can only be said to be less than 50 fs, can be better defined when the S_3 DAFS is analysed. To position the S_3 DAFS with a similar amplitude to its Gaussian absorption feature a time constant of < 20 fs is found to be required (10 fs is used in Figure 7.13). DAFS plots with $\tau_1 = 10, 20, 30$ and 50 fs are shown in Figure 7.15 in Section 7.5.4 to indicate the poor reproduction of the S_3 spectrum with longer time constants.

When reconstructed with the full sequential decay model the DAFS show good agreement of the spectral position, shape and amplitudes when compared with the S_3 , S_2 and S_1 absorption Gaussians. Ultrafast luminescence at longer wavelengths, when detection moves into the steady state emission region (> 580 nm), shows slower dynamics. These wavelengths were not included in the global analysis due to the definite presence of long lived $^3\text{MLCT}$ emission, which is not accounted for with a sequential relaxation model. The decay time constants vary progressively, from residual 75 fs S_1 emission at 590 nm to 230 fs on the peak of the PL spectrum, Figure 7.14. Here emission is completely inside the $^3\text{MLCT}$ manifold and this, in addition to longer lived picosecond decay dynamics representing vibrational cooling to the surrounding solvent molecules, have previously been identified in this class of materials.⁴⁰

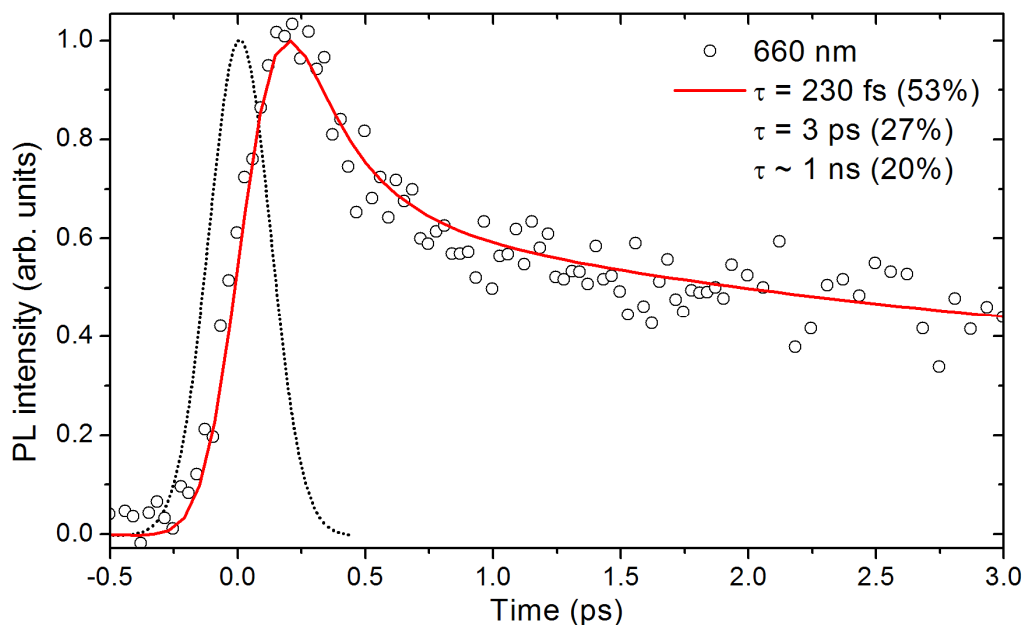


Figure 7.14. Ultrafast luminescence dynamics at 660 nm on the peak of the steady state PL spectrum for Ir(dbfliq)₂acac. The solid line indicates the fit, the IRF is shown as dotted line (280 fs FWHM). The kinetics fit best to a 230 fs decay component (53%), 3 ps decay (27%) and a nanosecond offset (20%).

7.5.4 Error Analysis

Global analysis of the recorded luminescence spectra in the wavelength range 460-580 nm produced a global reduced chi-square minimum with three time constants of < 50, 65 and 75 fs. Evidently these three time constants are closely spaced and hence careful error analysis is required to support the results presented.

Firstly the choice of three exponentials in the global fit is guided by the self-evident nature of the three identified states in the 460-580 nm fitting region. It is fully anticipated that all three states would contribute to the emission process and the lack of spectral overlap of the S₃ and S₁ Gaussians (Figure 7.7) gives guidance that it is unlikely that any intersection of these two states exists directly, therefore the excited state in S₃ will have to flow through S₂ before it can reach S₁ (and then on to T₁). It is important to note that while three time constants are used, kinetics at any one wavelength can be best described by at most two exponential decays.

Global fitting across the entire wavelength range with just two time constants would not produce an acceptable fit – the interdependence of the consecutive relaxation model (decay time constant at one wavelength is rise-time constant at another) creates constraints on the global fit and hence restriction to just two time constants leads to compromises that ensure the fit does not adequately reproduce the kinetics found in the data.

From the global fit the time constant of S_3 emission, τ_1 , can only be said to be instrument limited, i.e. < 50 fs (Figure 7.9) – the global reduced chi-square value was relatively insensitive to what value of τ_1 was used, although the best-fit was found to be ~ 10 fs but this did not solely provide enough support for stating this time constant with confidence. A better bound on the value was found by taking into consideration the amplitude of the recorded luminescence (fully corrected for the wavelength dependence of the upconversion setup). Requiring the S_3 emission to lie on or close to the S_3 absorption Gaussian indicates that $\tau_1 < 20$ fs, with a value of 10 fs used in the global analysis. The variation of the S_3 amplitude with variation of τ_1 is shown in Figure 7.15, showing the amplitudes produced for τ_1 values of 10, 20, 30 and 50 fs.

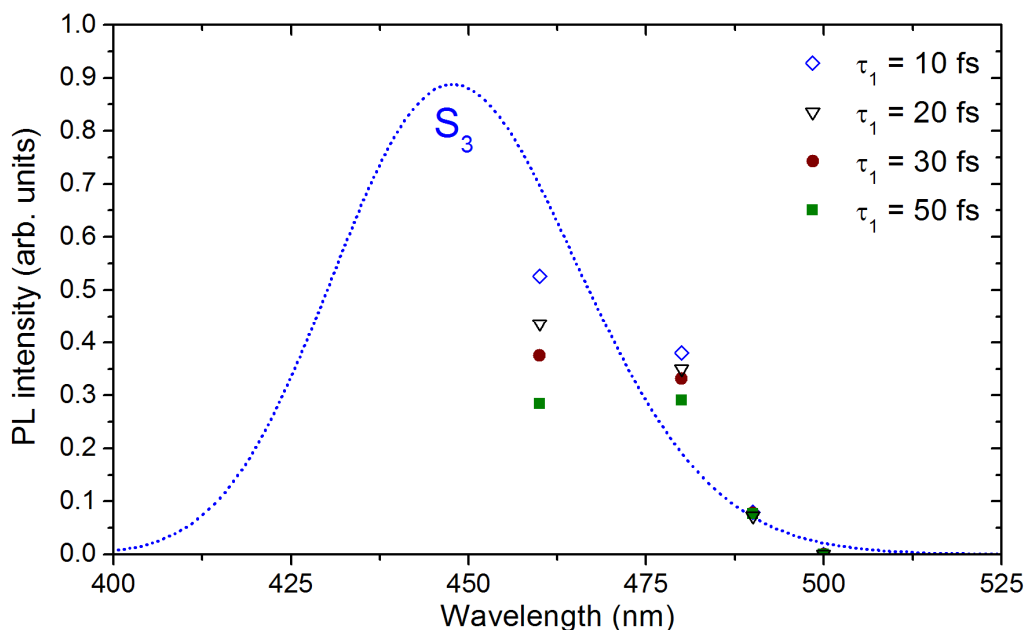


Figure 7.15. DAFS with variation of τ_1 . The open diamonds indicate a time constant of 10 fs, open triangles 20 fs, closed circles 30 fs and closed squares 50 fs. τ_1 is thus said to be < 20 fs based on the required time constants to produce amplitudes that follow the S_3 absorption Gaussian.

It can be seen that poor reproduction of the S_3 Gaussian exists when longer time constants are used.

The errors on τ_2 and τ_3 were deduced by use of support plane analysis, using the same reduced chi-square (χ^2_R) confidence interval methodology as defined in Chapter 6 and elsewhere⁴¹ – global analysis can help to generate a lower degree of uncertainty when a support plane analysis is undertaken, as the large number of combined datasets helps to reduce the uncertainty threshold. Briefly, the confidence interval is described as the χ^2_R value at which the probability, P , is equal to 0.32, i.e. the value of the χ^2_R is one standard deviation away from the global χ^2_R minimum. With a large number of datasets used in global analysis (and hence a large number of degrees of freedom) the one standard deviation increase that is required in the χ^2_R value is smaller – and hence the error bounds that can be placed on variables is smaller. The total number of data points across the 12 analysed datasets totals 924 and this, coupled with the number of parameters being fitted (9) gives a reduced-chi square multiplier of 1.00753, i.e. the increase

in the global reduced chi-square value from 1.37976 to 1.39015 gives the error bound. Variation of one parameter would produce a parabola with a one standard deviation confidence interval line; the intersection of the two would produce the errors. Here, however, there are two parameters of interest and therefore fixing one and fitting to find the χ^2_{R} minimum for both τ_2 and τ_3 produces a 7x9 matrix of χ^2_{R} values. This is graphically presented as a three dimensional contour plot, Figure 7.16. A ring can be traced (thick black line) at the one standard deviation contour, and this defines the errors for the two time constants, stated as ± 7 for τ_2 and ± 12 fs for τ_3 .

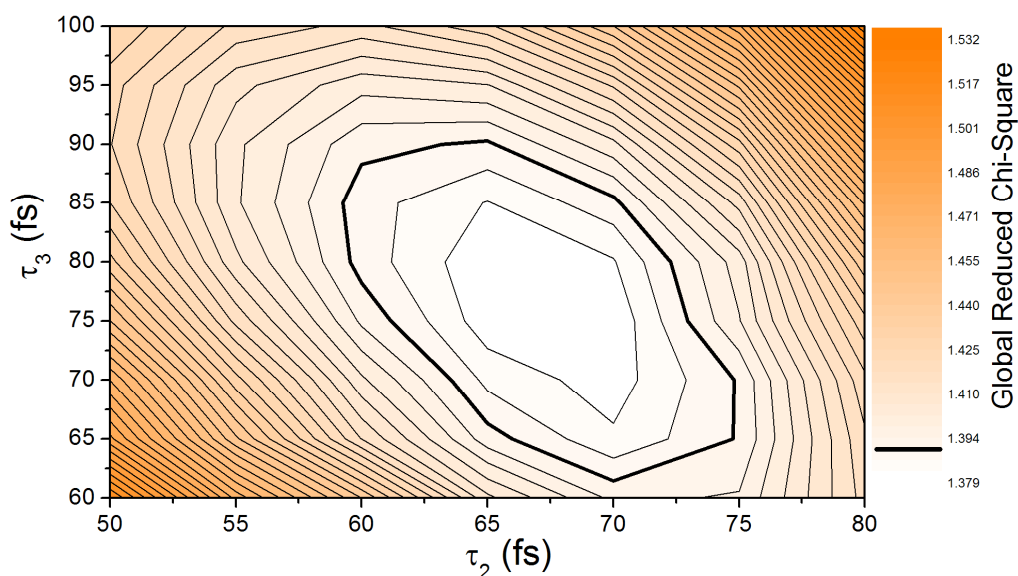


Figure 7.16. Contour plot of global reduced chi-square surface at $\tau_1 = 10$ fs when varying τ_2 and τ_3 with all other parameters left free. The global minimum of the surface is found to be at $\tau_2 = 65$ fs and $\tau_3 = 75$ fs. Quoted errors of ± 7 and ± 12 fs are derived from the increase in the reduced chi-square value of 1 standard deviation, as defined by F-Statistics, and is indicated with the thick black line.

In addition to providing the error bounds for τ_2 and τ_3 the contour plot also provides some supplementary evidence for the independence of these two variables as there is an anti-correlation in the direction of the surface. If the two time constants were actually representing the same process then the reduced chi-square surface should either show a symmetrical response or align itself with correlation between the two variables, i.e. the “direction” of the surface should

have a $y=x$ like form so that as τ_2 increases the surface supports an increase in τ_3 . Instead what is found is anti-correlation, i.e. a $y=1/x$ direction of the surface, such that as τ_2 increases τ_3 is confined to shorter time constants.

7.5.5 Variation of Excitation Wavelength

To investigate how the observed decay time-constants of internal conversion amongst the singlet states varied with differing amounts of energy stored inside the molecule the excitation energy was varied and the ultrafast luminescence dynamics monitored. Two variables were of interest, the time constants of S_2 and S_1 emission. Tuneability of the excitation source enabled excitation wavelengths from 380 to 425 nm to be used. S_1 emission at 550 nm was observed with 425 nm excitation and was found to be identical to that with 400 nm excitation, Figure 7.17, indicating that the time constant of S_1 emission was unchanged at 75 fs.

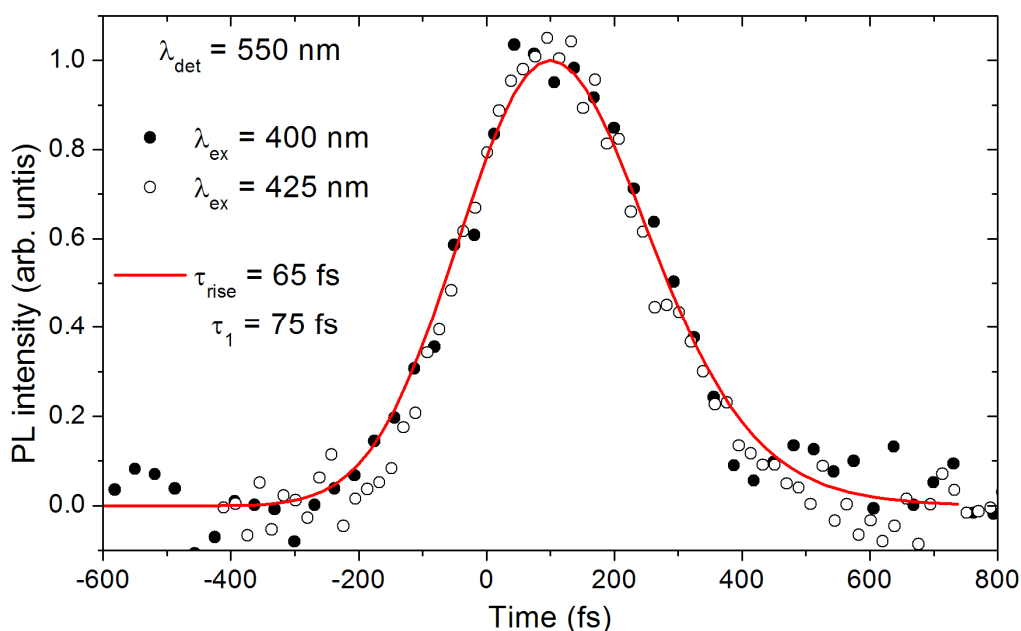


Figure 7.17. Ultrafast luminescence kinetics at 550 nm detection with variation of excitation wavelength: 400 nm (closed circles) and 425 nm (open circles). The best-fit (solid line) is found to be the same for both datasets, with a rise-time constant of 65 fs and a decay time-constant of 75 fs.

However observing S_2 emission at 500 nm with 415 nm excitation did show some change in dynamics. 415 nm excitation was required to enable Raman free observation of dynamics at 500 nm – this was confirmed by scanning a sample cell filled solely with THF and observing no signal. Comparison of the normalised recorded dynamics for 415 nm excitation with the values found using 400 nm excitation for 500 nm detection are shown in Figure 7.18 – the fit for the 400 nm excitation data is also shown. It can be seen that there is a small difference and kinetics with 415 nm excitation appear to be a little faster than with 400 nm.

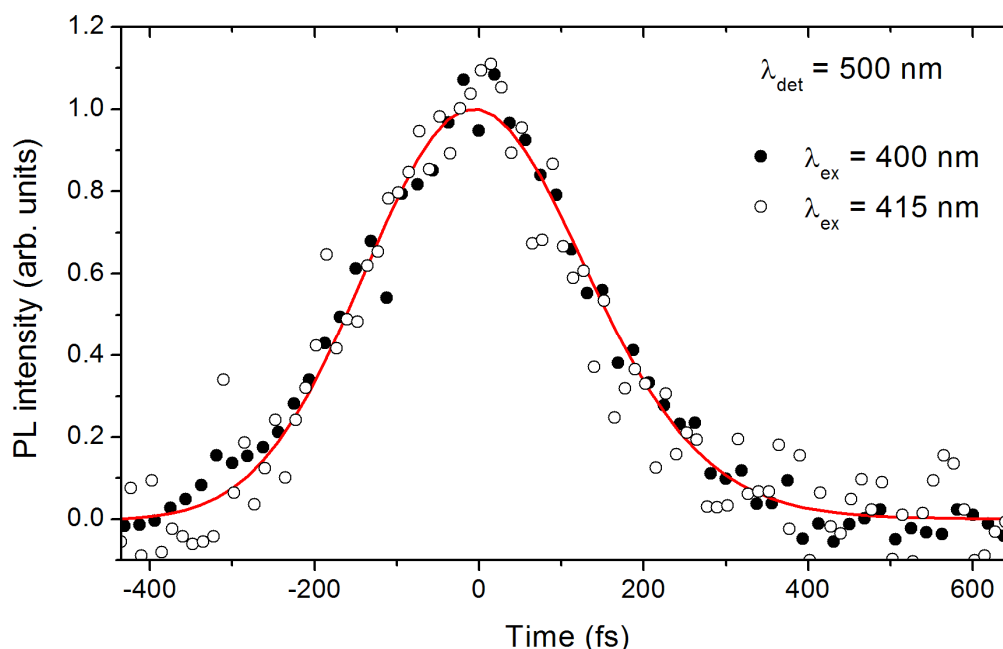


Figure 7.18. Ultrafast luminescence measurements with variation of excitation wavelength. Normalised kinetics with 400 nm (closed circles) and 415 nm (open circles) excitation at 500 nm detection. The Solid line is the 400 nm excitation data best-fit decay when convolved with the IRF (FWHM 280 fs) with a rise-time of 10 fs (100% of the rise) and a decay time constant of 65 fs. It can be seen that 415 nm excitation data (open circles) appears to be faster than the 400 nm data, with most points sitting inside the best-fit line.

Fitting to both datasets does show a decrease in the decay time-constant with longer excitation wavelength emission (65 fs down to ≤ 50 fs), but such values are somewhat poorly supported with single wavelength fitting due to the large potential error and so are not relied upon. What can instead be utilised to help

define the decrease in the time constant are the actual count rates of the recorded signals. Using the same method of excitation wavelength dependent correction factors already described above when used with 380 nm excitation, we can directly compare the amplitudes of 400 and 415 nm excitation emission at 500 nm, and this is shown (fully corrected for the upconversion setup's wavelength dependent sensitivity and the difference in Ir(dbfliq)₂acac's absorbance at both excitation wavelengths) in Figure 7.19.

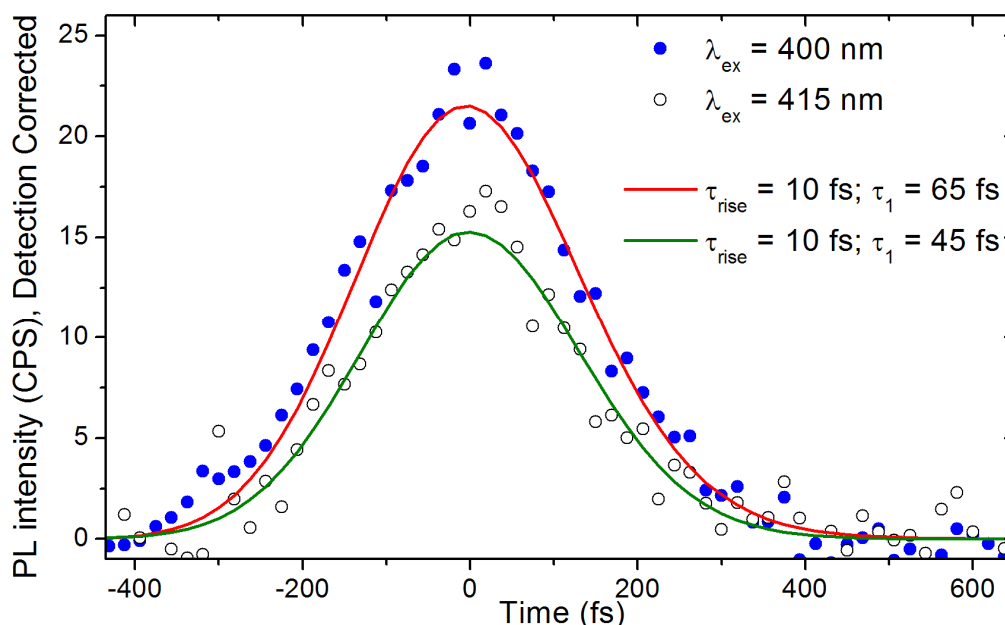


Figure 7.19. Ultrafast luminescence measurements with variation of excitation wavelength. The luminescence is detected at 500 nm with detection sensitivity corrections applied for 400 nm (closed circles) and 415 nm (open circles) excitation wavelengths. The solid lines are fits when convolved with the IRF. The kinetics are fully corrected for the upconversion sensitivity and excitation wavelength variation, hence when fitting with the same total amplitude the 415 nm data is required to have a shorter time constant (45 fs) compared to the 400 nm data (65 fs).

It can easily be seen that emission with 415 nm excitation produces a signal amplitude that is lower than with 400 nm excitation. Given the same state is being optically excited and the same state's emission is being recorded these amplitudes should be the same. The difference can therefore be accounted for in the time constants. If one requires that the fitted decay amplitudes for both sets of

kinetics are the same, utilising the sequential model and equations already discussed, then this forces the time constant of emission with 415 nm excitation to become shorter. The best-fit was hence found to be 45 ± 10 fs (the error being derived from the error in the amplitude at 500 nm and the error in the setup's wavelength dependent sensitivity correction factor).

7.6 Internal Conversion: Mediated by Energy Stored In The Molecule

Summarising the observed processes, the decay from the highest singlet state (S_3 to S_2) is found to be fast; however the exact rate of decay was not precisely defined for iridium complexes, due in no small part in the difficulty of achieving such time resolution. A time constant of < 20 fs is entirely congruent with the decay of the S_3 state, which occurs by conversion of electronic energy into vibrational energy of high frequency vibrational modes. In this report optical excitation actually initially accesses the L_1 state, however, one can state that the $L_1 \rightarrow S_3$ process will be very fast, justified by the lack of an observable rise-time in the S_3 kinetics and the small energy difference between the states. IC from S_2 to S_1 and ISC from S_1 to T_1 were found to be substantially slower (65 and 75 fs respectively) when excited with 400 nm. When less excitation energy was used to access L_1 (415 nm) the observed IC time constant for $S_2 \rightarrow S_1$ was found to decrease to 45 fs. However if the $S_1 \rightarrow T_1$ ISC time was observed with similar or even smaller values of excitation energy (425 nm) then it remained unchanged at 75 fs.

The rate of IC between excited electronic states of molecules can depend upon coupling strengths,⁴² the energy gap¹ and the shape of potential energy surfaces (PES) between states^{3, 8, 43} as well as the active vibrational modes of the molecule.⁴⁴ In this investigation of IC between singlet states in $\text{Ir}(\text{dbfliq})_2\text{acac}$ it is anticipated that the coupling strengths, energy gap, PES shapes and active vibrational modes of the molecule affecting IC between the three singlet states should all be similar because each singlet state shows similar optical coupling to

the ground state (oscillator strength) and similar absorption shapes. There must be, therefore, some other parameter that is controlling the rate of IC and slowing it down from < 20 to 75 fs over the course of its relaxation through the singlet states.

It is illustrative to plot the relaxation time from each state as a function of vibrational energy stored in the molecule, as shown in Figure 7.20, assuming that vibrational cooling to the solvent occurs on > 1 ps time-scale. This indicates that the rate of IC is fast when there is little energy stored in the molecule (bottom axis, < 0.6 eV) and with increasing values of stored energy the rate slows down. This relationship was tested when the excitation wavelength was varied, and the IC rates for S_2 and S_1 emission for 415 and 425 nm excitation respectively are shown as open circles. The 415 nm excitation data is especially helpful in aiding our understanding as it shows that $S_2 \rightarrow S_1$ IC, 65 fs with 400 nm excitation (0.62 eV of stored energy), decreases to 45 fs (0.5 eV of stored energy) – while this time-constant is not as fast as the < 20 fs value observed for the $S_3 \rightarrow S_2$ IC event (also with 0.5 eV of stored energy) it is faster than 65 fs, indicating that two distinct regimes can be identified, vibrationally unrestricted and restricted, where the amount of stored vibrational energy inside the molecule appears to control how fast IC events can occur. Time constants of relaxation within the $^3\text{MLCT}$ manifold are shown as open symbols and lie in the range of 150-230 fs. These are expected to be slower because the amount of energy being dissipated is small (top axis, < 0.1 eV) and involves very low frequency vibrational modes.⁴⁵

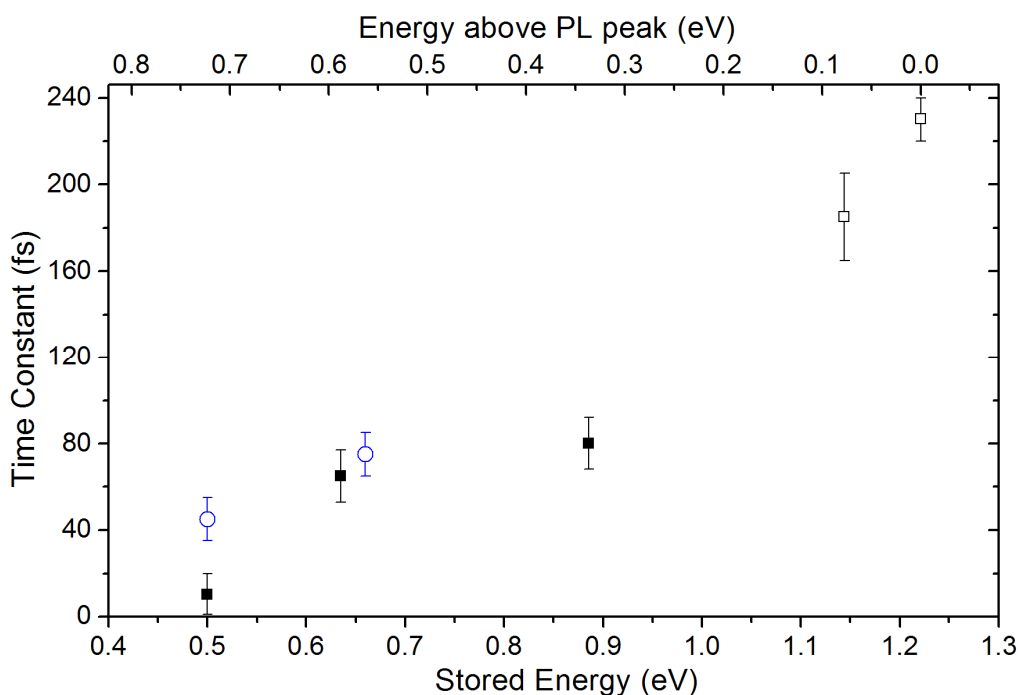


Figure 7.20. Relationship between the amount of vibrational energy stored in the molecule ($\lambda_{\text{ex}} - \lambda_{\text{det}}$) (bottom axis), or energy above the steady state PL peak ($\lambda_{\text{det}} - \lambda_{\text{peak}}$) (top axis) and the measured relaxation time constant for each state in Ir(dbfliq)₂acac, with open circles and closed squares representing IC between ¹MLCT states. Relaxation is facilitated by IVR and thus no energy is leaving the molecule, just being redistributed within it. Errors as deduced from fitting are shown. The open circles represent IC rates with variation of excitation energy as discussed in the text. The open squares lying at 1.15 and 1.2 eV of stored energy are identified as being hot triplet relaxation and population equilibration between the lowest ³MLCT state's electronic substates, respectively. The lowest substates are 100 cm⁻¹ or less apart, hence relaxation is through low frequency vibrational modes and hence is slower.

The rate of internal conversion from $S_3 \rightarrow S_2$ and $S_2 \rightarrow S_1$ has therefore been found to be dependent on the amount of vibrational energy stored inside the molecule. After proceeding into the S_2 state the population is found to decay with a time constant of 65 fs with 400 nm excitation. There therefore appears to be a substantial slowdown in the rate of IC from the $S_3 \rightarrow S_2$ to the $S_2 \rightarrow S_1$ events. The similar strength and shape of absorption transitions to both S_3 and S_2 states support that the potential energy surface (PES) can be only slightly shifted along the vibrational coordinate and there is thus little reason to presume that the rate of IC should change significantly. The considerable slowdown can be explained when the entire relaxation process is viewed as a whole. The $S_3 \rightarrow S_2$ crossing

occurs by dissipation of electronic energy into high frequency vibrational modes of the molecule and occurs on a time-scale of < 20 fs. The dominant vibrational modes of the molecule coupled to electronic transitions was found by fitting a vibrational progression to the PL spectrum to give a separation of 0.14 eV – this equates to a vibrational period of ~ 30 fs, and suggests a crossing time on the order of one half of a vibrational period or less. The question therefore arises as to why the $S_2 \rightarrow S_1$ crossing time is not just as fast. With 400 nm excitation the relaxation of $L_1 \rightarrow S_3 \rightarrow S_2$, however, has deposited ~ 0.6 eV of vibrational energy into high frequency vibrational modes, allowing it to occur very quickly. When it comes to enabling the next crossing event ($S_2 \rightarrow S_1$), the high frequency modes of the molecule appear to be saturated, and hence IVR, the process of vibrational energy flow from high to low frequency modes,^{46, 47} is required to clear them for acceptance of energy to facilitate the crossing, which explains the 65 fs time constant observed for the relaxation to S_1 . This is supported when the excitation wavelength was moved to 415 nm and the $S_2 \rightarrow S_1$ crossing event was observed to be 45 fs, which indicates that when there is less vibrational energy stored in the molecule (0.5 eV), some high frequency modes are still free to accept energy before requiring IVR to dissipate to lower frequency vibrational modes, hence the rate of IC will be faster.

Whether with 400 or 425 nm excitation, the $S_1 \rightarrow T_1$ ISC time constant is found to be 75 fs and indicates that with values of stored vibrational energy in the molecule > 0.6 eV the slowdown in the rate of decay plateaus at ~ 75 fs and implies that despite much more vibrational energy stored in the molecule (~ 0.9 eV) the rate of decay does not change significantly. One might expect that the rate would continue to decrease, however it appears that the clearance of high frequency vibrational modes to lower frequency by IVR is not saturated. This is not surprising with a large number of lower frequency modes that can take energy from the high frequency vibrational modes, hence the rate of IVR (and thus of ISC) remains at ~ 75 fs. The ISC time found here is confirmed with a complementary transient absorption measurement, Figure 7.21, where decay of the excited state absorption is observed with a time constant of 75 fs.

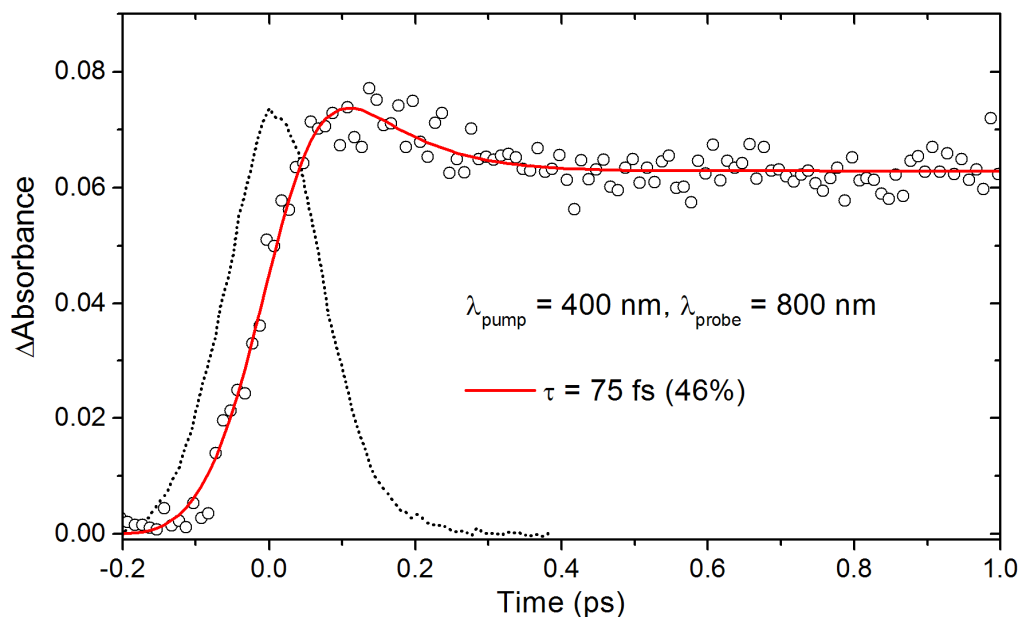


Figure 7.21. Ultrafast transient absorption kinetics ($\lambda_{\text{pump}} = 400$ nm, $\lambda_{\text{probe}} = 800$ nm) for Ir(dbfliq)₂acac. Deconvolution of the kinetics with the IRF (dotted line) gives a decay of 75 fs (46% amplitude).

Previous theoretical studies have shown that a true crossing of potential energy surfaces (PESs), a so-called conical intersection, enables much faster IC (by an order of magnitude) than an avoided surface crossing (nonadiabatic) when energy dissipation by IVR or cooling is included.⁴⁸ A schematic of a likely conical intersection between singlet state PES in the system under study is shown in Figure 7.22. The similar shapes and strengths of the $S_0 \rightarrow S_2$ and $S_0 \rightarrow S_3$ absorption transitions suggest that their PES will be similar in shape and that there will only be a small displacement in the nuclear coordinate between the states, making the conical intersection low in S_n and high in S_{n-1} . Very fast $S_3 \rightarrow S_2$ relaxation is also consistent with a conical intersection of the PES. In work by Gawelda et. al. on a tris-bipyridine iron complex⁴⁹ non-radiative relaxation between two states (in that case ISC) was proposed to occur by an avoided crossing, with a vibrational progression of the lowest ¹MLCT state being observed in its absorption spectrum. Here, however, no vibrational progression is seen – instead the three identified singlet electronic states appear as featureless Gaussians, indicating that they are significantly shifted in the vibrational coordinate, consistent with a conical intersection of the PES allowing IC via strong

coupling rather than an avoided crossing between them via weak coupling through overlap of the vibrational wavefunctions.

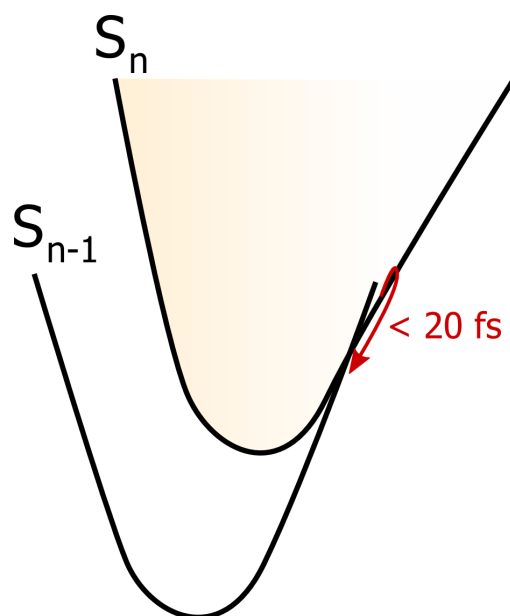


Figure 7.22. A sketch of two hypothetical potential energy surfaces with a conical intersection between them. Both PES have similar shapes and positions of their minimum in the nuclear coordinate. IC from one state to another occurs via a conical intersection and this was found, for the $S_3 \rightarrow S_2$ event, to be < 20 fs.

Figure 7.23 outlines the six main stages in the curve crossing events that are deduced from the experiments that have been undertaken with 400 nm excitation; each shows the proposed vibrational population distribution in the molecule, from high to low frequency modes at various points in the system's excited state evolution. First is panel 1, representing the system as it is in S_3 , showing some quantity of energy stored in high frequency modes (deposited there from the $L_1 \rightarrow S_3$ crossing) but broadly free of stored energy. Secondly, panel 2 shows the system immediately after the $S_3 \rightarrow S_2$ crossing event (< 20 fs), where a large amount of excess energy has been deposited in high frequency modes to facilitate movement to the crossing point. What follows after panel 2 is redistribution of that large amount of energy into lower frequency modes by IVR (65 fs). This is required to enable the movement to the $S_2 \rightarrow S_1$ crossing point, and the vibrational population of the system at this stage is shown in panel 3. Once high

frequency modes have cleared and are able to accept new energy depositions, movement to the crossing point can occur and so the $S_2 \rightarrow S_1$ crossing can take place. We do not know how fast the actual crossing event itself is, only that it is less than 65 fs, however given the similarity of all of the singlet states one might expect it to be similar to the $S_3 \rightarrow S_2$ time (i.e. < 20 fs). Panel 4 indicates the vibrational population distribution as it exists after having just entered S_1 , with a large amount of high frequency modes active having received energy from the motion towards the $S_2 \rightarrow S_1$ crossing. Panel 5 repeats the process of IVR (75 fs) from the saturated high frequency modes to lower frequency modes to enable acceptance of more high frequency dissipation energy. This time, however, the lower frequency modes are already somewhat populated; however this does not significantly slow the rate of IVR as there are still free accepting lower frequency modes available. ISC occurs from panel 5 to 6, and saturates the high frequency accepting modes once again and from here the excited state population is within the triplet manifold.

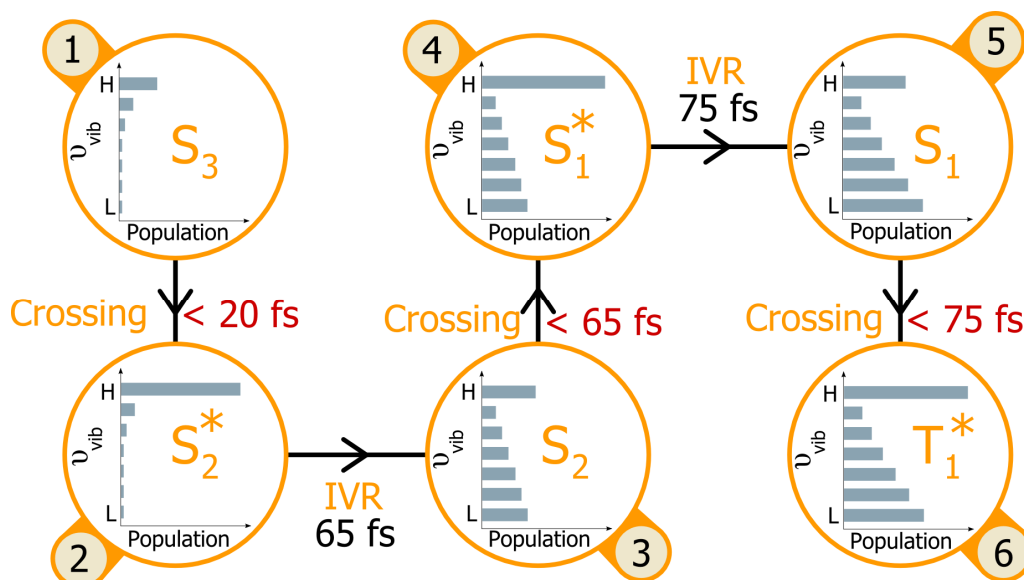


Figure 7.23. Schematic of ultrafast processes occurring in $\text{Ir}(\text{dbfliq})_2\text{acac}$. Shown is a diagrammatic view of the sequential relaxation model fitted to the data with 400 nm excitation, where S_n^* and T_n^* are vibrationally hot states. Shown in each bubble is the vibrational energy distribution of high (H) and low (L) frequency vibrational modes. Each crossing event deposits a large amount of energy into high frequency modes and this is then required to be redistributed by IVR to lower frequency modes before the excited state can move to the next crossing point, thus controlling the rate of IC. See the text for a full discussion of each panel.

As one moves across from S_1 into the T_1 (i.e. the $^3\text{MLCT}$) state there is a grow-in of a slower femtosecond emission that is associated with relaxation from within the $^3\text{MLCT}$ manifold. It is anticipated that in reality there would be a continuum of relaxation time constants across the region (i.e. relaxations high within the $^3\text{MLCT}$ manifold would be faster; and relaxations lower would be slower). Finally, as detection moves to still lower energy on the peak of the steady state PL spectrum (660 nm) the ultrafast kinetics show similar behaviour as has been observed in other iridium complexes.⁴⁰ Kinetics show two processes, 230 fs and 3 ps decays, and are assigned to population redistribution amongst the three substates of the lowest $^3\text{MLCT}$ excited state, facilitated by IVR and vibrational cooling to the bath.

7.7 Conclusions

The results presented here have given a unique opportunity to look at internal conversion amongst multiple ¹MLCT states in a transition metal complex for the first time. The experimental results presented show that in the complex Ir(dbfilq)₂acac the IC rate depends on the amount of vibrational energy stored in the molecule. When the amount of stored energy is < 0.6 eV the rate of IC from either the highest singlet MLCT state (S₃ → S₂) or the lower state (S₂ → S₁) is found to be fast, 10-45 fs, indicating that IC is an adiabatic process and that the crossing point between potential energy surfaces is reached by the wavepacket motion along the high frequency vibrational coordinate. Observed IC from S₂ to S₁, however, slows substantially when more vibrational energy is stored inside the molecule (> 0.6 eV), with a time constant of 65 fs being observed. Here IVR will have to dissipate energy to enable the crossing via the high frequency coordinate. This is also found in ISC from the lowest singlet MLCT state to the triplet, with a time constant of 75 fs. This suggests that the crossing rate depends on the availability of high frequency vibrational modes to accept the excess electronic energy. This feature is likely to be characteristic of transition metal complexes with a high density of electronic states. The wider implications of these results suggest that it might be possible to control rates of IC and ISC by molecular engineering of the chemical structure and molecular surroundings.

7.8 References

- [1] R. Englman and J. Jortner, *Molecular Physics*, 1970. **18**(2): p. 145-164.
- [2] G.W. Robinson and R.P. Frosch, *The Journal of Chemical Physics*, 1963. **38**(5): p. 1187-1203.
- [3] D.R. Yarkony, *Reviews of Modern Physics*, 1996. **68**(4): p. 985-1013.
- [4] D.R. Yarkony, *Journal of Physical Chemistry*, 1996. **100**(48): p. 18612-18628.
- [5] D.R. Yarkony, *Accounts of Chemical Research*, 1998. **31**(8): p. 511-518.
- [6] D.R. Yarkony, *Journal of Physical Chemistry A*, 2001. **105**(26): p. 6277-6293.
- [7] H. Koppel, W. Domcke, and L.S. Cederbaum, *Advances in Chemical Physics*, 1984. **57**: p. 59-246.
- [8] E.W.G. Diau, S. De Feyter, and A.H. Zewail, *Journal of Chemical Physics*, 1999. **110**(20): p. 9785-9788.
- [9] S. Perun, A.L. Sobolewski, and W. Domcke, *Journal of the American Chemical Society*, 2005. **127**(17): p. 6257-6265.
- [10] G.A. Worth and L.S. Cederbaum, *Annual Review of Physical Chemistry*, 2004. **55**: p. 127-158.
- [11] M. Garavelli, F. Bernardi, M. Olivucci, T. Vreven, S. Klein, P. Celani, and M.A. Robb, *Faraday Discussions*, 1998. **110**: p. 51-70.
- [12] F. Bernardi, M. Olivucci, and M.A. Robb, *Chemical Society Reviews*, 1996. **25**(5): p. 321.
- [13] V.M. Kenkre, A. Tokmakoff, and M.D. Fayer, *Journal of Chemical Physics*, 1994. **101**(12): p. 10618-10629.
- [14] J.V. Caspar and T.J. Meyer, *Journal of Physical Chemistry*, 1983. **87**(6): p. 952-957.
- [15] P. Avouris, W.M. Gelbart, and M.A. Elsayed, *Chemical Reviews*, 1977. **77**(6): p. 793-833.
- [16] B.R. Smith, M.J. Bearpark, M.A. Robb, F. Bernardi, and M. Olivucci, *Chemical Physics Letters*, 1995. **242**(1-2): p. 27-32.

- [17] P. Hobza, H.L. Selzle, and E.W. Schlag, *Journal of Physical Chemistry*, 1996. **100**(48): p. 18790-18794.
- [18] J.M.L. Pecourt, J. Peon, and B. Kohler, *Journal of the American Chemical Society*, 2001. **123**(42): p. 10370-10378.
- [19] H. Kang, B. Jung, and S.K. Kim, *Journal of Chemical Physics*, 2003. **118**(15): p. 6717-6719.
- [20] L.C. Sun, L. Hammarstrom, B. Akermark, and S. Styring, *Chemical Society Reviews*, 2001. **30**(1): p. 36-49.
- [21] J. Savolainen, R. Fanciulli, N. Dijkhuizen, A.L. Moore, J. Hauer, T. Buckup, M. Motzkus, and J.L. Herek, *Proceedings of the National Academy of Sciences of the United States of America*, 2008. **105**(22): p. 7641-7646.
- [22] M.R. Wasielewski, *Chemical Reviews*, 1992. **92**(3): p. 435-461.
- [23] G. Benko, J. Kallioinen, J.E.I. Korppi-Tommola, A.P. Yartsev, and V. Sundstrom, *Journal of the American Chemical Society*, 2002. **124**(3): p. 489-493.
- [24] J. Andersson, F. Puntoriero, S. Serroni, A. Yartsev, T. Pascher, T. Polivka, S. Campagna, and V. Sundstrom, *Chemical Physics Letters*, 2004. **386**(4-6): p. 336-341.
- [25] A.C. Bhasikuttan and T. Okada, *Journal of Physical Chemistry B*, 2004. **108**(34): p. 12629-12632.
- [26] P.W. Atkins, *Molecular Quantum Mechanics*. 2 ed. 1983: Oxford University Press.
- [27] R.S. Knox and H. van Amerongen, *Journal of Physical Chemistry B*, 2002. **106**(20): p. 5289-5293.
- [28] S.J. Strickler and R.A. Berg, *The Journal of Chemical Physics*, 1962. **37**(4): p. 814-822.
- [29] K. Nozaki, *Journal of the Chinese Chemical Society*, 2006. **53**(1): p. 101-112.
- [30] P.J. Hay, *Journal of Physical Chemistry A*, 2002. **106**(8): p. 1634-1641.
- [31] E. Jansson, B. Minaev, S. Schrader, and H. Agren, *Chemical Physics*, 2007. **333**(2-3): p. 157-167.

- [32] X. Gu, T. Fei, H.Y. Zhang, H. Xu, B. Yang, Y.G. Ma, and X.D. Liu, *European Journal of Inorganic Chemistry*, 2009(16): p. 2407-2414.
- [33] T. Liu, B.H. Xia, X. Zhou, Q.C. Zheng, Q.J. Pan, and H.X. Zhang, *Theoretical Chemistry Accounts*, 2008. **121**(3-4): p. 155-164.
- [34] B. Minaev, V. Minaeva, and H. Agren, *Journal of Physical Chemistry A*, 2009. **113**(4): p. 726-735.
- [35] X.N. Li, Z.J. Wu, Z.J. Si, H.J. Zhang, L. Zhou, and X.J. Liu, *Inorganic Chemistry*, 2009. **48**(16): p. 7740-7749.
- [36] Y.H. Lee and Y.S. Kim, *Thin Solid Films*, 2007. **515**(12): p. 5079-5083.
- [37] N.G. Park, G.C. Choi, J.E. Lee, and Y.S. Kim, *Current Applied Physics*, 2005. **5**(1): p. 79-84.
- [38] K.A. Connors, *Chemical Kinetics: The Study of Reaction Rates in Solution*. 1990: VCH Publishers.
- [39] J.M. Beechem and E. Gratton, *Proceedings of SPIE*, 1988. **909**: p. 77-81.
- [40] G.J. Hedley, A. Ruseckas, and I.D.W. Samuel, *Chemical Physics Letters*, 2008. **450**(4-6): p. 292-296.
- [41] J.R. Lakowicz, *Principles of Fluorescence Spectroscopy*. 2nd ed. 1999: Kluwer Academic.
- [42] K.F. Freed and J. Jortner, *Journal of Chemical Physics*, 1970. **52**(12): p. 6272.
- [43] M. Seel and W. Domcke, *Journal of Chemical Physics*, 1991. **95**(11): p. 7806-7822.
- [44] C. Canuel, M. Mons, F. Piuzzi, B. Tardivel, I. Dimicoli, and M. Elhanine, *Journal of Chemical Physics*, 2005. **122**(7).
- [45] G.J. Hedley, A. Ruseckas, Z. Liu, S.-C. Lo, P.L. Burn, and I.D.W. Samuel, *Journal of the American Chemical Society*, 2008. **130**(36): p. 11842-11843.
- [46] D.J. Nesbitt and R.W. Field, *The Journal of Physical Chemistry*, 1996. **100**(31): p. 12735-12756.
- [47] T. Elsaesser and W. Kaiser, *Annual Review of Physical Chemistry*, 1991. **42**(1): p. 83-107.

- [48] B. Balzer, S. Hahn, and G. Stock, *Chemical Physics Letters*, 2003. **379**(3-4): p. 351-358.
- [49] W. Gawelda, A. Cannizzo, V.T. Pham, F. vanMourik, C. Bressler, and M. Chergui, *Journal of the American Chemical Society*, 2007. **129**(26): p. 8199-8206.

8

Conclusions

Freedom is the freedom to say that two plus two make four. If that is granted, all else follows.

George Orwell, *Nineteen Eighty-Four*, 1949

Ultrafast photophysics provides the potential to truly understand the physics of chemical systems at a *molecular* level. Fundamental molecular processes occur on the femtosecond timescale, and using ultrafast tools can help to observe and understand these processes. If one can understand the processes then the possibility arises that one could control them.¹

This thesis has explored the ultrafast photophysics of a series of light emitting iridium complexes. Transition metal complexes can show very fast evolution of their excited state due to strong spin-orbit coupling and a high density of electronic states. The word “cascade” has been used² to refer to this fast evolution, indicating that the excited state population can be thought of as *flowing* down through these higher states, not necessarily even having time to fully establish itself in each one before it has reached the next. Internal conversion (IC), intersystem crossing (ISC) and vibrational relaxation are the three processes of merit, and it is these three processes that have been studied in some detail and described here for a number of iridium complexes.

In the ultrafast dynamics observed in different iridium complexes a commonality has been found, best exemplified by the themes running through Chapters 5, 6 and 7. The rate of intramolecular vibrational redistribution (IVR) appears to play a

major role in the ability of a molecule to dissipate excess energy on the ultrafast timescale – to the extent that the work in these three chapters indicate that IVR is an important, if not the most important, variable in controlling the rates of the evolution to the lowest excited state. A link can therefore be formed between the chemical structure of a material, the rate of vibrational dissipation, and the rate of electronic relaxation. This has been explored by observing the differences that adding dendrons (Chapter 5) or fused phenyl groups (Chapter 6) has on the ultrafast excited state evolution. Variation of the amount of vibrational energy stored in the molecule when observing internal conversion between states (Chapter 7) has enabled a detailed analysis of how IVR has a role in controlling the rates of electronic processes.

Taking the research as it has been presented, firstly the ultrafast dynamics of the prototypical iridium complex $\text{Ir}(\text{ppy})_3$ was investigated (Chapter 4). It was important to look at $\text{Ir}(\text{ppy})_3$ as it is the starting point for all light emitting iridium complexes, being the first material to be used and the most efficient in light emitting devices.^{3,4} Only one other ultrafast study on $\text{Ir}(\text{ppy})_3$ had been reported⁵ and few firm conclusions had been drawn. In the work completed here femtosecond luminescence measurements showed characteristic decay times across the spectral region of the steady state photoluminescence (PL) spectrum (representing emission from the lowest triplet metal-ligand charge transfer (MLCT) state) of 230 fs and 3 ps. These time constants were found to be independent of the solvent that the material was dissolved in or where on the steady state PL spectrum one observed emission (from the peak of the PL and lower in energy). Given that this emission has to be from the $^3\text{MLCT}$ state, and that the state actually consists of three electronic substates ($\sim 100 \text{ cm}^{-1}$ apart) due to zero-field splitting⁶ the conclusions were drawn that the 230 fs and 3 ps processes represented relaxation from the initially populated top substate to the two lower ones. These decay time constants were observed in steady state PL measurements for all iridium complexes that were studied, suggesting that this is a very general process common to many iridium complexes – and if one were to extend the conclusion further then it would imply that the zero-field splitting in all

materials studied was similar, a conclusion that is commensurate with the fact that all materials have similar phosphorescence efficiencies (a parameter that correlates with zero-field splitting).⁷

In the next chapter (Chapter 5) luminescence from Ir(ppy)₃ at a higher detection energy (140 meV above the PL peak) was compared against emission from that same amount of excess energy in two Ir(ppy)₃ cored dendrimers. Dendrimers are large macromolecules showing self-similar branching patterns to their structure. They were useful materials to study in this work because they allowed chemical additions to be made to a light emitting core without necessarily changing any of its electronic properties. Observing the emission at 140 meV of excess energy showed that the decays in both the core and dendrimers were best represented by two time constants of 150 fs, representing intramolecular vibrational redistribution (IVR), and 3 ps, representing vibrational cooling to the surrounding solvent molecules. While there was no measurable increase in the rate of IVR with the addition of the dendrons, there was an observed increase in the *amount* of excess energy dissipated by IVR, from 88% in Ir(ppy)₃ to 94% in the dendrimers. No increase in the rate may be seen due to the connection between the core and the dendron, though a single C-C bond, which will limit energy flow unless it is fully thermally activated.

The lack of any increase in the rate of IVR upon addition of material to the molecule with dendrimers contrasts with the observations in Ir(piq)₃ (Chapter 6). Here the extra material is a phenyl that is fused onto the pyridine of the ligand, ensuring that the excited state itself also covers the new additional chemical material. The time constant of IVR at 140 meV of excess energy was found to be 95 fs and represented 96% of the total decay. Clearly the rate of IVR has now increased, the fused phenyl enabling dissipation of excess energy to occur faster than in the smaller Ir(ppy)₃ molecule.

Also observed in Chapter 6 was fluorescence from an iridium complex for the first time. The red emitting properties of the material enabled light emission from

singlet states to be recorded. The decay time constant of fluorescence (thus embodying intersystem crossing) was found to be 65 ± 5 fs and was confirmed with complimentary transient absorption measurements which showed rise and decay features at a range of probe wavelengths of 70 fs. This made Ir(piq)₃ doubly unique, as Ir(ppy)₃ and the dendrimers had shown no dynamics in their transient absorption signals at all, indicating simply that ISC was likely to be < 100 fs. The ISC of 65 fs for Ir(piq)₃ sits well amongst the reported values for other transition metal complexes who have time constants of ISC ranging from < 20 fs in ruthenium⁸ to 3 ps in platinum complexes.⁹ There is still no absolute understanding of the rates of ISC, but in measuring this process in an iridium complex for the first time more evidence is provided to help in the process of understanding.

What is essentially the culmination of the work on iridium complexes was presented in Chapter 7, looking at excited state processes in a deep red emitting heteroleptic material, Ir(dbfliq)₂acac. The deep red spectral properties gave a unique opportunity to observe higher excited states and hence this section of work represented a substantial investment of time and analysis due to the distinctive properties that the material presented. The first piece of analysis that was undertaken was to assign and aid in the identification of three features in the absorption spectrum. Spectral fitting and transition dipole moment calculations were performed to support the assignment of these three features as three separate ¹MLCT states. This was an important ascription to make as the ultrafast emission was observed across the region of these features and so knowledge that three ¹MLCT states exist there was required to aid in subsequent analysis. The ultrafast luminescence measurements comprised of kinetics at 12 wavelengths and so global analysis was employed to give a greater confidence in the fitted parameters. A custom fitting equation was used that modelled a sequential relaxation down through the three ¹MLCT states. Global analysis indicated that the decay of the highest energy ¹MLCT state occurred with a time constant of 20 fs or less, the middle ¹MLCT state 65 ± 7 fs and the lowest ¹MLCT state was 75 ± 12 fs. These

times represent the time constants of IC (and in the last case ISC) and will be facilitated by the dissipation of excess energy by IVR.

Recasting the results on Ir(dbfliq)₂acac by looking at the rate of IC with respect to the amount of vibrational energy stored inside the molecule gave rise to the conclusion that with less than 0.6 eV of stored energy the rate of decay was fast, 10-45 fs, and with more than 0.6 eV it was slower at ~ 70 fs. This result was confirmed by varying the excitation wavelength and therefore changing the amount of stored energy that was present in the molecule when observing IC between the states – all indicating therefore that the rate of IC is defined by the rate of IVR. The movement of the population in a ¹MLCT state to reach the crossing point to the lower state is facilitated by high frequency vibrational modes, and if these modes become saturated then IVR to lower frequency modes must take place before movement to the crossing point can occur.

The wider implications of the work conducted during this PhD are to suggest that in transition metal complexes the molecule's vibrational properties can play an important role in the excited state evolution. Simple modification of a molecule to add new chemical components changes the vibrational properties (Chapters 5 and 6) and in so doing, therefore changes its ability to dissipate excess energy, thus changing the rates of electronic transitions. In some chemical and charge transfer reactions specific excited state energies and barriers are required to be surmounted, and so understanding of how vibrational energy controls the excited state evolution is important in perhaps being able to control these reactions.

While this work has presented a wide ranging view of ultrafast processes in iridium complexes there are of course many things that could be further explored. The excitation energy dependence experiments that were performed in Chapter 7 in particular have the potential to be significantly extended. Limitations on tuning of the Ti:Sapphire oscillator forbade a very detailed analysis of the excitation dependence of the ultrafast luminescence kinetics, especially interesting excitation wavelengths. For example, it would be of great interest to be able to excite

specifically to each of the S_{1-3} singlet states – monitoring the kinetics to see how the rates of IC and ISC vary. Raman free observations however, would of course be difficult to achieve. This highlights the second area of future work, achieving Raman free observations of ultrafast luminescence at detection energies close to the excitation energy. Dendrimers have proven themselves capable of doing this (Chapter 5) and a potential area of future research would be to utilise their advantageous solubility to explore ultrafast dynamics – particularly deep red emitters, whose properties indicate (Chapter 7) that detection of dynamics at higher energies can give detailed insight into dynamics and energy flow.

The body of work presented here represents a significant amount of ultrafast measurements on iridium complexes and it is hoped that the conclusions drawn can aid in the desire to reach understanding of the exact nature and factors governing ultrafast relaxation in transition metal complexes. As has been mentioned a few times, there was a surprising lack of research that had been conducted into the ultrafast photophysics of iridium complexes and it is hoped that the work reported here will motivate others to further explore these unique and fascinating systems.

8.1 References

- [1] A.H. Zewail, *Journal of Physical Chemistry A*, 2000. **104**(24): p. 5660-5694.
- [2] N. Damrauer, G. Cerullo, A. Yeh, T. Boussie, C. Shank, and J. McCusker, *Science*, 1997. **275**(5296): p. 54-57.
- [3] M.A. Baldo, S. Lamansky, P.E. Burrows, M.E. Thompson, and S.R. Forrest, *Applied Physics Letters*, 1999. **75**(1): p. 4-6.
- [4] C. Adachi, M.A. Baldo, M.E. Thompson, and S.R. Forrest, *Journal of Applied Physics*, 2001. **90**(10): p. 5048-5051.
- [5] K.C. Tang, K.L. Liu, and I.C. Chen, *Chemical Physics Letters*, 2004. **386**(4-6): p. 437-441.
- [6] W.J. Finkenzeller and H. Yersin, *Chemical Physics Letters*, 2003. **377**(3-4): p. 299-305.
- [7] H. Yersin and J. Strasser, *Coordination Chemistry Reviews*, 2000. **208**(1): p. 331-364.
- [8] A. Cannizzo, F. van Mourik, W. Gawelda, G. Zgrablic, C. Bressler, and M. Chergui, *Angewandte Chemie-International Edition*, 2006. **45**(19): p. 3174-3176.
- [9] Z. Abedin-Siddique, T. Ohno, K. Nozaki, and T. Tsubomura, *Inorganic Chemistry*, 2004. **43**(2): p. 663-673.

Appendix

Publications Arising from this Work

Everyone who receives the protection of society owes a return for the benefit.

John Stuart Mill, *On Liberty*, 1859

- Gordon J. Hedley, Arvydas Ruseckas and Ifor D.W. Samuel, “*Ultrafast Luminescence in Ir(ppy)₃*”, *Chemical Physics Letters*, **450** (4-6), 292-296 (2008).
- Gordon J. Hedley, Arvydas Ruseckas, Zehua Liu, Shih-Chun Lo, Paul L. Burn and Ifor D. W. Samuel, “*Iridium Metal Complexes as an Unambiguous Probe of Intramolecular Vibrational Redistribution*”, *Journal of the American Chemical Society*, **130** (36), 11842-11843 (2008).
- Gordon J. Hedley, Arvydas Ruseckas and Ifor D.W. Samuel, “*Ultrafast Intersystem Crossing in a Red Phosphorescent Iridium Complex*”, *Journal of Physical Chemistry A*, **113** (1), 2-4 (2009).
- Gordon J. Hedley, Arvydas Ruseckas and Ifor D.W. Samuel, “*Vibrational Energy Flow Controls Internal Conversion in a Transition Metal Complex*”, *Journal of Physical Chemistry A*, accepted for publication (2010).

"We are all afraid - for our confidence, for the future, for the world. That is the nature of the human imagination. Yet every man, every civilization has gone forward because of its engagement with what it has set itself to do. The personal commitment of a man to his skill, the intellectual commitment and the emotional commitment working together as one, has made the ascent of man."

Jacob Bronowski, *The Long Childhood, The Ascent of Man*, 1973

